Springer Proceedings in Physics 191

Giorgio Mantica
Ruedi Stoop
Sebastiano Stramaglia *Editors*

Emergent Complexity from Nonlinearity, in Physics, Engineering and the Life Sciences

Proceedings of the XXIII International Conference on Nonlinear Dynamics of Electronic Systems, Como, Italy, 7–11 September 2015

Springer

Springer Proceedings in Physics

Volume 191

The series Springer Proceedings in Physics, founded in 1984, is devoted to timely reports of state-of-the-art developments in physics and related sciences. Typically based on material presented at conferences, workshops and similar scientific meetings, volumes published in this series will constitute a comprehensive up-to-date source of reference on a field or subfield of relevance in contemporary physics. Proposals must include the following:

- name, place and date of the scientific meeting
- a link to the committees (local organization, international advisors etc.)
- scientific description of the meeting
- list of invited/plenary speakers
- an estimate of the planned proceedings book parameters (number of pages/articles, requested number of bulk copies, submission deadline).

More information about this series at http://www.springer.com/series/361

Giorgio Mantica · Ruedi Stoop
Sebastiano Stramaglia
Editors

Emergent Complexity from Nonlinearity, in Physics, Engineering and the Life Sciences

Proceedings of the XXIII International Conference on Nonlinear Dynamics of Electronic Systems, Como, Italy, 7–11 September 2015

Springer

Editors
Giorgio Mantica
Dipartimento di Scienza
ed Alta Tecnologia, Center
for Nonlinear and Complex Systems
Università dell'Insubria
Como
Italy

and

INFN
Milano
Italy

Ruedi Stoop
Institute of Neuroinformatics and Institute
for Computational Science
University of Zürich
Zurich
Switzerland

and

ETH Zürich
Zurich
Switzerland

Sebastiano Stramaglia
Dipartimento interateneo di Fisica
Michelangelo Merlin
Universita di Bari
Bari
Italy

and

INFN
Bari
Italy

ISSN 0930-8989 ISSN 1867-4941 (electronic)
Springer Proceedings in Physics
ISBN 978-3-319-47808-1 ISBN 978-3-319-47810-4 (eBook)
DOI 10.1007/978-3-319-47810-4

Library of Congress Control Number: 2016956831

Printed on acid-free paper

This Springer imprint is published by Springer Nature
The registered company is Springer International Publishing AG
The registered company address is: Gewerbestrasse 11, 6330 Cham, Switzerland

To the memory of Joseph Ford, on the twentieth anniversary of his passing

Preface

NDES2015 is the twenty-third Conference of the series *Nonlinear Dynamics in Electronic Systems*, which began in 1993 in Dresden (Germany) and whose 22nd edition took place in Albena, Bulgaria, in 2014. The conference was held in the magnificent ambiance of the Cloister of the Abbey of Sant'Abbondio, in Como, from September 7 to 11, 2015. It gathered about ninety participants from sixteen countries and five continents. Overall, there were sixteen invited and forty-six contributed talks.

Traditionally, the main theme of the conference has been the study of nonlinear oscillations in electronic circuits, with its many potential applications, but in recent years, these gatherings have covered much wider topics, from theoretical questions in pure dynamics to phenomena in complex networks: Here, synchronization has assumed an ever-increasing importance, not only in man-made, but also in biological systems, the human brain being perhaps the most tantalizing example. In NDES2015, the interdisciplinary aspect emerged clearly, as can be seen below and in the booklet of abstracts, available online at www.dfm.uninsubria.it/mantica/ndes15.

Como, Italy — Giorgio Mantica
Zurich, Switzerland — Ruedi Stoop
Bari, Italy — Sebastiano Stramaglia

Acknowledgements

The conference was organized as an activity of the *Center for Nonlinear and Complex Systems* of the Dipartimento di Scienza ed Alta Tecnologia, Università dell'Insubria, Como.

The Camera di Commercio di Como and the Alessandro Volta foundation, thanks to the Scientific Secretary Professor Giulio Casati, who also participated in the organization, provided financial support and secretarial services; Mariagiovanna Falasconi headed the administrative team.

All seminars were hosted in the Cloister of the Abbey of Sant'Abbondio in Como, courtesy of the Università dell'Insubria—thanks to the prorettore vicario professor Giuseppe Colangelo and to the Dipartimento di Diritto, Economia e Culture, direttore professoressa Laura Castelvetri. Logistic help on-site was provided skillfully by Sabrina Meroni and Pietro Catalano.

The Dipartimento di Scienza ed Alta Tecnologia of the Università dell'Insubria, Director Professor Stefano Serra Capizzano, provided financial support.

h.o.-COMPUTER Software GmbH, Amsterdamer Str. 91, Cologne, Germany, gracefully provided financial support: special thanks to Edmund Preiss and Harald Odendahl, who attended the conference.

The Istituto Nazionale di Fisica Nucleare, INFN, sezione di Milano, provided partial support for travel expenses, thanks to the Director Professor Alberto Santambrogio.

Upon application, the conference was awarded the label *EPS Sponsored* from the European Physical Association, which also funded the prize *best contribution from a young participant*, awarded by a committee composed of invited speakers to Tom Lorimer (University of Zürich and ETH Zürich, Switzerland).

The conference was also recommended by the Italian Associazione Caos e Complessità, thanks to the Director Professor Mario di Bernardo.

Florian Gomez and Tom Lorimer, at University of Zürich and ETHZ, helped with the organization and prepared the booklet of abstracts that was released before the conference.

Abirami Purushothaman at Springer was of great help in the final setup of this volume; it must be fully credited to Sabine Lehr, associate editor, if it appears in the series “Springer Proceedings in Physics.”

Last but not least, Andrea Spiriti, professor of history of art at the Università dell’Insubria, Varese, guided all participants in a scholarly commented visit to the Basilica of Sant’Abbondio, its cloister and the neighboring church of Saints Cosma and Damiano.

Contents

Contributors

Carlo Albert Eawag, Swiss Federal Institute of Aquatic Science and Technology, Dübendorf, Switzerland

Nicola Amoroso Dipartimento Interateneo di Fisica "Michelangelo Merlin", Università Degli Studi di Bari "Aldo Moro", Bari, Italy; Istituto Nazionale di Fisica Nucleare - Sezione di Bari, Bari, Italy

Alon Ascoli Institut für Grundlagen der Elektrotechnik und Elektronik, Technische Universität Dresden, Dresden, Germany

Andrey Babichev Jan and Dan Duncan Neurological Research Institute, Baylor College of Medicine, Houston, TX, USA; Department of Computational and Applied Mathematics, Rice University, Houston, TX, USA

Ronny P. Bartsch Keck Laboratory for Network Physiology, Department of Physics, Boston University, Boston, MA, USA; Department of Physics, Bar-Ilan University, Ramat Gan, Israel

Teresa Maria Altomare Basile Dipartimento Interateneo di Fisica "Michelangelo Merlin", Università Degli Studi di Bari "Aldo Moro", Bari, Italy; Istituto Nazionale di Fisica Nucleare - Sezione di Bari, Bari, Italy

Roberto Bellotti Dipartimento Interateneo di Fisica "Michelangelo Merlin", Università Degli Studi di Bari "Aldo Moro", Bari, Italy; Istituto Nazionale di Fisica Nucleare - Sezione di Bari, Bari, Italy

Damian Berger Institute of Neuroinformatics and Institute for Computational Science, University of Zürich, Zurich, Switzerland; ETH Zürich, Zurich, Switzerland

Alessandro Bertolino Dipartimento di Scienze Mediche di Base, Neuroscienze e Organi di Senso, Università Degli Studi di Bari "Aldo Moro", Bari, Italy; Azienda Ospedaliero-Universitaria Consorziale Policlinico, Bari, Italy; pRED, NORD DTA, F. Hoffman-La Roche Ltd., Basel, Svizzera

Giuseppe Blasi Azienda Ospedaliero-Universitaria Consorziale Policlinico, Bari, Italy

J.M. Byers US Naval Research Lab, Code 6395, Washington, DC, USA

T.L. Carroll US Naval Research Lab, Code 6392, Washington, DC, USA

Leon Chua Department of Electrical Engineering and Computer Sciences, University of California Berkeley, Berkeley, CA, USA

Jesus M. Cortes Biocruces Health Research Institute Barakaldo, Barakaldo, Spain; Departamento de Biologia Celular e Histologia, University of the Basque Country, Leioa, Spain; Ikerbasque: The Basque Foundation for Science, Bilbao, Spain

Yuri Dabaghian Jan and Dan Duncan Neurological Research Institute, Baylor College of Medicine, Houston, TX, USA; Department of Computational and Applied Mathematics, Rice University, Houston, TX, USA

Pasquale Di Carlo Dipartimento di Scienze Mediche di Base, Neuroscienze e Organi di Senso, Università Degli Studi di Bari "Aldo Moro", Bari, Italy

Massimiliano de Magistris Dipartimento di Ingegneria Elettrica e delle Tecnologie dell'Informazione, University of Naples FEDERICO II, Naples, Italy

Domenico Diacono Istituto Nazionale di Fisica Nucleare, sez. di Bari, Bari, Italy

Ibai Diez Biocruces Health Research Institute, Cruces University Hospital, Barakaldo, Spain

A.S. Dmitriev Kotelnikov Institute of Radio Engineering and Electronics of RAS, Moscow, Russia; Moscow Institute of Physics and Technology, Moscow Reg., Russia

E.V. Efremova Kotelnikov Institute of Radio Engineering and Electronics of RAS, Moscow, Russia; Moscow Institute of Physics and Technology, Moscow Reg., Russia

Tetsuro Endo Department of Electronics and Bioinformatics, Meiji University, Kawasaki, Japan

Salih Ergün ERARGE - Ergünler Co., Ltd. R&D Center, Beşiktaş, İstanbul, Turkey

Annarita Fanizzi Dipartimento Interateneo di Fisica "Michelangelo Merlin", Università Degli Studi di Bari "Aldo Moro", Bari, Italy

Luca Gerardo-Giorda Basque Center for Applied Mathematics, Basque Country, Bilbao, Spain

Jenny Held Eawag, Swiss Federal Institute of Aquatic Science and Technology, Dübendorf, Switzerland; Institute of Neuroinformatics and Institute for

Computational Science, University of Zürich, Zurich, Switzerland; ETH Zürich, Zurich, Switzerland

Shuya Hidaka Department of Electronics and Bioinformatics, Meiji University, Kawasaki, Japan

Naohiko Inaba Organization for the Strategic Coordination of Research and Intellectual Property, Meiji University, Kawasaki, Japan

Plamen Ch. Ivanov Keck Laboratory for Network Physiology, Department of Physics, Boston University, Boston, MA, USA; Harvard Medical School and Division of Sleep Medicine, Brigham and Women's Hospital, Boston, MA, USA

Sunghoon Joo Department of Bio and Brain Engineering, Korea Advanced Institute of Science and Technology (KAIST), Yuseong-gu, Daejeon, Republic of Korea

Karlis Kanders Institute of Neuroinformatics and Institute for Computational Science, University of Zürich, Zurich, Switzerland; ETH Zürich, Zurich, Switzerland

Andrey R. Kolovsky L.V. Kirensky Institute of Physics of Siberian Branch of Russian Academy of Sciencies, Krasnoyarsk, Russia

Julia M. Kroos Basque Center for Applied Mathematics, Basque Country, Bilbao, Spain

Marianna La Rocca Dipartimento Interateneo di Fisica "Michelangelo Merlin", Università Degli Studi di Bari "Aldo Moro", Bari, Italy

Aijing Lin Keck Laboratory for Network Physiology, Department of Physics, Boston University, Boston, MA, USA; Department of Mathematics, Beijing Jiaotong University, Beijing, China

Kang K.L. Liu Keck Laboratory for Network Physiology, Department of Physics, Boston University, Boston, MA, USA; Department of Neurology, Beth Israel Deaconess Medical Center, Harvard Medical School, Boston, MA, USA

Tom Lorimer Institute of Neuroinformatics and Institute for Computational Science, University of Zürich, Zurich, Switzerland; ETH Zürich, Zurich, Switzerland

Tommaso Maggipinto Dipartimento Interateneo di Fisica "Michelangelo Merlin", Università Degli Studi di Bari "Aldo Moro", Bari, Italy; Istituto Nazionale di Fisica Nucleare - Sezione di Bari, Bari, Italy

Samy Mailoud Sekkouri DiFeST, Università degli Studi di Parma, Parma, Italy

Alfonso Monaco Dipatimento di Fisica "M. Merlin", Istituto Nazionale di Fisica Nucleare, sez. di Bari, Bari, Italy

Anna Monda Department of Basic Medical Sciences, Neuroscience and Sense Organs, Università degli Studi di Bari "Aldo Moro", Bari, Italy

Yoonkey Nam Department of Bio and Brain Engineering, Korea Advanced Institute of Science and Technology (KAIST), Yuseong-gu, Daejeon, Republic of Korea

Daiki Ogusu Department of Electronics and Bioinformatics, Meiji University, Kawasaki, Japan

Marco Papalino Dipartimento di Scienze Mediche di Base, Neuroscienze e Organi di Senso, Università Degli Studi di Bari "Aldo Moro", Bari, Italy

Giulio Pergola Dipartimento di Scienze Mediche di Base, Neuroscienze e Organi di Senso, Università Degli Studi di Bari "Aldo Moro", Bari, Italy

Carlo Petrarca Dipartimento di Ingegneria Elettrica e delle Tecnologie dell'Informazione, University of Naples FEDERICO II, Naples, Italy

Munehisa Sekikawa Department of Mechanical and Intelligent Engineering, Utsunomiya University, Utsunomiya, Japan

Ruedi Stoop Institute of Neuroinformatics and Institute for Computational Science, University of Zürich, Zurich, Switzerland; ETH Zürich, Zurich, Switzerland

Sebastiano Stramaglia Dipartimento di Fisica, Università di Bari, Bari, Italy; INFN, Sezione di Bari, Bari, Italy

Sabina Tangaro Istituto Nazionale di Fisica Nucleare - Sezione di Bari, Bari, Italy

Andrea Tateo Dipatimento di Fisica "M. Merlin", Università Degli Studi di Bari "A. Moro", Istituto Nazionale di Fisica Nucleare, sez. di Bari, Bari, Italy

Ronald Tetzlaff Institut für Grundlagen der Elektrotechnik und Elektronik, Technische Universität Dresden, Dresden, Germany

Daniel Wechsler Institute of Neuroinformatics and Institute for Computational Science, University of Zürich, Zurich, Switzerland; ETH Zürich, Zurich, Switzerland

Sandro Wimberger DiFeST, Università degli Studi di Parma, Parma, Italy; Gruppo Collegato di Parma, INFN, Sezione di Milano Bicocca, Parma, Italy

Soudeh Yaghouti Dipartimento di Ingegneria Elettrica e delle Tecnologie dell'Informazione, University of Naples FEDERICO II, Naples, Italy

Introduction

After the conference, the editors solicited contributions to the proceedings and had them peer-reviewed. Out of these, seventeen papers were accepted and are collected herein: A brief description of their content is the best way to present the interdisciplinary, yet strongly coherent matter of this volume.

Part I, *Classical and Quantum Dynamics*, contains the most theoretically oriented investigations. On the classical side, this comprises three papers which describe, in order, new ways to identify chaotic attractors of ODE's, the study of complex bifurcations of delayed maps, and the comparison of fine details in the dynamics of Rulkov maps with those of biological examples. In the quantum domain, a new class of physical systems has surged to widespread attention: Bose condensates in optical lattices. Although physically different from electronic circuits, these systems share some of their mathematical characteristics and are promising of revolutionary applications. Moreover, they also permit to address the problem of the relation between classical and quantum dynamics. Two papers in this part investigate these deep questions.

Part II, *Chaotic Oscillations*, continues in the traditional mainstream of the conference with three papers on electronic circuits. They focus on applications boldly moving forward the state of the art: robust numerical simulations of TaO memristor nano-devices, ultrawide-band microwave chaotic generators implemented as SiGe-integrated circuits, and the cryptanalysis of random number generators based on chaotic circuits.

Part III, *Networks*, starts with yet another analysis of electronic circuits, now interconnected so to form a network. Here, collective behavior arises and is termed *emerging dynamics*, as in the title of this volume. The first paper presents theory and experiments on a configurable network of Chua's circuits, in which coupling strengths and configurations can be dynamically changed, thereby observing the onset of different synchronization patterns. The second paper studies a model of adaptive network, whose connection structure evolves in interaction with node dynamics, which in turn is influenced by the former, as in the usual framework.

Clearly, this model is intended to be a paradigm of neuronal cultures. Neuronal dynamics is also the focus of the third paper of this part, but starting point and aims are here reversed: A synthetic neural network is constructed with the goal of clustering groups of similar data in high-dimensional spaces. The paper describes a novel implementation of Hebbian learning, with potential application to bioinformatics.

Part IV, *Biological Dynamics*, is the most extended of the volume: It contains six papers. Indeed, biologically motivated research also permeated many papers in the previous parts, a fact which testifies both the increasing interest in biological applications and the undisputable superiority of the techniques of dynamics in tackling such problems. The first paper in this part is the lengthiest of this volume: It is an introduction to the concept of network physiology, in which organs and systems—albeit with vastly different characteristics and signal outputs—interact so to produce physiologic states and functions. A new technique, termed time-delay stability, is used to study the bursting activity of brain waves in different frequency domains, which reflects coordinated network interactions among organ systems that are essential to maintain health. The same theme is continued in the second paper, which studies the temporal excitation patterns that follow the passage of a depolarization wave on the cerebral cortex—that is associated with a drastic failure of brain homeostasis. A fascinating problem is addressed in the third paper: the stable internal representation of external spacial locations in the brain of mammals. By combining deep results in algebraic topology with a model of transient hippocampal network (in which the neural structure is subject to physiological reorganization), it is demonstrated that the large-scale spatial representation of the environment encoded by this network can remain stable. In the fourth paper, an undirected network is constructed from brain MRI scans, each node representing a macroscopic cortical location: This network is used to discriminate automatically patients with Alzheimer's disease and mild cognitive impairment. Yet another class of biological network is studied in the fifth paper of this part: It is defined by different gene expressions. The paper presents an algorithm for partitioning the network into different communities and for identifying the DRD2 gene coding for the D2 dopamine receptor. The sixth paper of the part presents a theoretical explanation of the experimental observation of the power-law distribution of time intervals between spikes in cultures of hippocampal neurons: It is demonstrated that it is due to the limited availability of resources that are being exhausted by the culture.

In closing this Introduction, we would like to quote a passage from Joseph Ford, who foresaw the far-reaching implications of dynamics, which are now blossoming and are well displayed in this volume dedicated to his memory:

> Over the centuries chaos has been blamed for every disaster visited on man from riots in the street to the heat death of the universe. Of course, not all of these accusations are false, for uncontrolled chaos can most assuredly be a devastating thing. Yet when controlled, the villainous chaos becomes gentle, useful, even enchanting. And why should it not be so; for in truth, chaos is merely dynamics freed from the shackles of order and predictability. Dynamical systems released to randomly explore their every possibility. Chaos can, therefore, provide us with a virtuoso display of exciting variety, a richness of choice,

a cornucopia of opportunity. Dare we hope that humans can harvest the richness without reaping the devastation? (in Directions in Chaos, Vol. 1, edited by Hao Bai-lin, World Scientific 1987).

Como, Italy — Giorgio Mantica
Zurich, Switzerland — Ruedi Stoop
Bari, Italy — Sebastiano Stramaglia
August 2016

List of Talks from NDES2015

Invited Talks

Stefano Boccaletti (ISC CNR Firenze, Italy) *Explosive synchronization of networked oscillators*

Leonid Bunimovich (Georgia Institute of Technology, Atlanta, USA) *On global stability of delayed and non-delayed networks*

Silvana Cardoso (Dept. of Chem. Eng. and Biotechnology, Cambridge University, UK) *Dynamics of buoyancy-driven flows in the Earth's subsurface and in the ocean*

Thomas L. Carroll (US Naval Res. Labs, Washington DC, USA) *Nonlinear systems characterization using phase space density*

Julyan Cartwright (CSIC Granada, Spain) *Chemobrionics: Nonlinear dynamics, electronic systems, and the origin of life*

Ned Corron (U.S. Army Redstone Arsenal, AL, USA) *Chaos in optimal communication waveforms*

Egidio D'Angelo (Dip. Scienze del sistema nervoso, Università di Pavia, Italy) *Spatiotemporal dynamics of neuron activity in brain microcircuits*

Lucilla de Arcangelis (Dip. Fisica, Seconda Università di Napoli, Italy) *Correlations in the brain*

Hans J. Herrmann (Computational Physics, ETH Zürich, Switzerland) *Rolling and synchronization in dense packings of spheres*

Plamen Ch. Ivanov (Physics Department, Boston University and Division of Sleep Medicine, Harvard Medical School, USA) *Network physiology: How complex physiologic organ systems dynamically interact*

Gregor Jotzu (Institute for Quantum Electronics, ETH Zürich, Switzerland) *Exploring topological and magnetic order with ultracold fermions in optical lattices*

Andrey R. Kolovsky (L.V. Kirensky Institute of Physics, Siberian Branch of Russian Academy of Sciences, Russia) *Treating many-body quantum systems by means of classical mechanics*

Pietro Lio' (Dept. of Computer Science, Cambridge University, UK) *Hierarchical block matrices as looking glasses for multi-scale biology*

Daniele Marinazzo (Gent University, Belgium) *Conserved Ising model on the human connectome*

Lou Pecora (US Naval Res. Labs, Washington DC, USA) *Symmetries, cluster synchronization, and isolated desynchronization in complex networks*

Norbert Stoop (Department of Mathematics, MIT, Cambdrige MA, USA) *Rayleigh-Benard instability in curved elastic bilayer systems: Wrinkles, dimples, and the early universe*

Special Seminar

Andrea Spiriti (Università dell'Insubria, Varese, Italy) *The Abbey and the Cloister of Sant'Abbondio and the Church of the Saints Cosma and Damiano*

Contributed Talks

(delivered by the first author mentioned)

Carlo Albert (Eawag, Swiss Federal Institute of Aquatic Science and Technology, Switzerland) *Bayesian parameter inference for stochastic differential equation models*

Yuri V. Andreyev et al. (Moscow Institute of Physics and Technology, State University, Russia) *Ultrawideband chaotic transmitter panel*

Alon Ascoli et al. (Technische Universität Dresden, Dresden, Germany) *Continuous and differentiable approximation of a TaO memristor model for robust numerical simulations*

Sergey Belyakin et al. (State University of Moscow, Russia) *Stabilization of hyperbolic Plykin attractor by the Pyragas method*

Damian Berger et al. (University of Zürich and ETH Zürich, Switzerland) *Power laws as the result of exponentially decaying spiking frequency during synchronized activity*

Fausto Borgonovi (Università Cattolica, Brescia, Italy) *Quantum transport in light-harvesting systems*

Zeynep Çağıl et al. (Sakarya University, Turkey) *Chaos synchronization between finance and Rikitake systems by active control with unknown parameters*

Barış Cevher et al. (Sakarya University, Turkey) *Synchronization of chaotic three time scales brushless DC motor system by means of one state passive controller*

Shunda Chen et al. (Center for Nonlinear and Complex Systems, Università dell'Insubria, Como Italy) *Thermal conduction and thermoelectricity in one-dimensional nonlinear systems*

Yuri Dabaghian (Rice University and Duncan Neurological Research Institute, Houston, USA) *Robust spatial memory maps in flickering neuronal networks: a topological model*

Massimiliano de Magistris et al. (Università di Napoli, Italy) *Experiments on clustering and synchronous patterns in a configurable network of chaotic oscillators*

Roberto R. Deza et al. (IFIMAR, UNMdP-CONICET, Mar del Plata, Argentina) *Controlling the range of a Schmitt trigger's switching oscillations by means of external noise and nonlinear feedback*

Federica Di Michele et al. (Università dell'Aquila, Italy) *A simplified mathematical model for nano-bio interface*

Elena V. Efremova, A.S. Dimitrev (Moscow Institute of Physics and Technology, State University, Russia) *Ultrawideband microwave 3–7 GHz chaotic oscillator implemented as SiGe integrated circuit*

Salih Ergün (ERARGE - Ergunler Co., Ltd. R&D Center, Turkey) *Cryptanalysis of a random number generator based on a chaotic oscillator*

Stefan Glüge et al. (Zürich University of Applied Sciences, Switzerland) *Detecting influences—a network analysis of the European bond market based on partial mutual information*

Florian Gomez et al. (University of Zürich and ETH Zürich, Switzerland) Frequency-sharpening and scale-invariance in a system of forcing-coupled Hopf oscillators

Jenny Held et al. (University of Zürich and ETH Zürich, Switzerland) *Hebbian learning clustering using networks of Rulkov neurons*

Karlis Kanders et al. (University of Zürich and ETH Zürich, Switzerland) *Simulating neural oscillations with map-based neurons*

A.S. Karavaev et al. (Saratov Branch of the Institute of Radio Engineering and Electronics of Russian Academy of Sciences, Russia) *Phase and frequency locking in complex model of blood pressure dynamics*

Uğur Erkin Kocamaz et al. (Uludağ University, Turkey) *Non-identical chaos anti-synchronization via passive control*

Danil Kulminskiy et al. (Saratov Branch of the Institute of Radio Engineering and Electronics of Russian Academy of Sciences, Russia) *Chimera states in ensembles of time-delayed feedback oscillators with the mean field*

Hiroyuki Kusano et al. (Hosei University, Tokyo, Japan) *Analysis of digital maps based on simple feature quantities*

Marianna La Rocca et al. (Università di Bari, Italy) *Multiplex network based features for early Alzheimer characterization*

Tom Lorimer et al. (University of Zürich and ETH Zürich, Switzerland) *Saturation effect produces deviations from power law statistics in real-world networks*

Volodymyr Maistrenko et al. (National Scientific Centre for Medical and Biotechnical Research, Kyiv, Ukraine) *Cloning of 3D chimera states*

Ludovico Minati et al. (Istituto Neurologico Carlo Besta, Milano and Center for Mind/Brain Sciences, Università di Trento, Italy) *Nonlinear dynamics and low-frequency fluctuations in network hubs: tentative analogy between the resting human brain and coupled single-transistor chaotic oscillators*

Anna Monda et al. (Università di Bari, Italy) *Complex network for DRD2 gene community identification in schizophrenia*

Yasuo Murata et al. (Hosei University, Tokyo, Japan) *Hyperchaos and synchronization in paralleled power converters*

Daiki Ogusu, Tetsuro Endo (Meiji University, Kawasaki, Japan) *Complex bifurcations of Arnol'd tongues generated in three-coupled delayed logistic maps*

O.I. Olusola et al. (University of Lagos, Nigeria) *Experimental investigation of chaos synchronization in nonlinear oscillators via cyclic coupling*

Yuko Osana et al. (Tokyo University of Technology, Japan) *Chaotic quaternionic multidirectional associative memory with adaptive scaling factor of refractoriness*

Thomas Ott et al. (Zürich University of Applied Sciences, Switzerland) *A spin physics-based framework for hybrid recommendation systems*

A.I. Panas et al. (Kotel'nikov Institute of Radio Engineering and Electronics of Russian Academy of Sciences, Fryazino Branch, Russia) *Modified microwave chaotic Colpitts oscillator*

Andrey A. Polezhaev (P. N. Lebedev Physical Institute of the Russian Academy of Sciences, Moscow, Russia) *Mechanisms of complex pattern formation in chemical systems*

Vladimir Ponomarenko et al. (Saratov Branch of the Institute of Radio Engineering and Electronics of Russian Academy of Sciences, Russia) *Method of generalized synchronization detection without using an auxiliary system approach*

Mikhail Prokhorov et al. (Saratov Branch of the Institute of Radio Engineering and Electronics of Russian Academy of Sciences, Russia) *Recovery of couplings and parameters of elements in networks of time-delay systems*

Leonardo Ricci et al. (Università di Trento, Italy) *New tools to determine the optimal embedding of a time series*

Raffaello Seri (Università dell'Insubria, Varese, Italy) *Conditions for persistence of stochastic processes*

Veronika Stolbova et al. (Potsdam Institute of Climate Impact Research, Germany) *Prediction of the Indian Summer Monsoon as a spatially organized critical transition*

Arūnas Tamaševičius et al. (Center for Physical Sciences and Technology, Vilnius, Lithuania) *Stabilization of steady states in an array of the coupled FitzHugh–Nagumo oscillators*

Vahid Tavakkoli et al. (Klagenfurt University, Austria) *A novel recurrent neural network based ultra-fast, robust and scalable solver for time varying matrix inversion*

Ylmaz Uyaroğlu et al. (Sakarya University, Turkey) *Controlling chaotic permanent magnet synchronous motor with a single state speed feedback controller*

Daniel Wechsler et al. (University of Zürich and ETH Zürich, Switzerland) *Emergence of complex structure and behavior from elementary adaptive network automata*

Sandro Wimberger (Università di Parma, Italy) *Transport and non-equilibrium dynamics with cold atoms*

Xiyun Zhang (University of Potsdam, Germany) *Explosive synchronization in complex network*

Part I
Classical and Quantum Dynamics

Nonlinear Systems Characterization Using Phase Space Density

T.L. Carroll and J.M. Byers

1 Introduction

The description and analysis of chaotic attractors is an evolving field. Much of this work is concerned with modeling and prediction of dynamical systems [2, 6, 11, 13, 20]. Finding a model of the actual vector field is probably the most efficient way to describe a dynamical system, but finding a model without knowing the proper functional form is computationally difficult and sensitive to noise. If the goal is only to characterize, but not to predict, then studies of the geometry of the attractor may be useful. Such techniques have been used for many years [3, 9, 12, 14, 17, 22]. More recently, graph theory has been used to characterize attractors as networks [8], although with the exception of networks based on recurrences, it's not clear what the physical significance of the network is.

The shape of a chaotic attractor is well defined and not subject to prediction errors, but there are few tools for describing this shape [19, 22]. In this work, we describe the shape of a chaotic attractor by partitioning the attractor into regions of different densities. It is well known that the probability measure of a dynamical system reflects its long term behavior in phase space [9, 10]. For some dynamical systems, such as complex electronic circuits, or driven structures, it isn't mathematically tractable to generate a model for the system [21, 23], so characterizing the attractor without including details of the dynamics is all that is possible. In the work described here, the attractor is partitioned into regions that each contain the same amount of information. We measure information by estimating the probability distribution of points in a given region and using a statistical quantity to show that this distribution can be

T.L. Carroll (✉)
US Naval Research Lab, Code 6392, Washington, DC20375, USA
e-mail: thomas.carroll@nrl.navy.mil

J.M. Byers
US Naval Research Lab, Code 6395,Washington, DC 20375, USA
e-mail: jeff.byers@nrl.navy.mil

G. Mantica et al. (eds.), *Emergent Complexity from Nonlinearity, in Physics, Engineering and the Life Sciences*, Springer Proceedings in Physics 191,
DOI 10.1007/978-3-319-47810-4_1

distinguished from a uniform random distribution. We then use common statistical methods to compare densities in corresponding regions of different attractors. In previous work, it was established that density can be used to compare attractors [4]. The current method extends the range of application of density based methods to attractors that are not similar to each other, and it does away with an arbitrary parameter by using the data itself to determine how to create a histogram for the attractor.

2 Density in Phase Space

We begin by embedding a time series s into a d dimensional phase space using the method of delays [1]. For each point in s, a vector $\mathbf{s}(i)$ is defined as $\mathbf{s}(i) = \{s(i), s(i+\tau), \ldots s(i+(d-1)\tau)\}$. The embedding dimension d and the delay τ may be found by any one of a number of standard methods [1].

A histogram of the embedded attractor in the phase space is then created. The phase space is divided into bins, and the bin locations and sizes are recorded, as well as the number of points in each bin. The bins may have different sizes.

2.1 Determining Partitions

We choose to subdivide, or partition, the attractor based on whether subdividing a part of the attractor yields more information than not subdividing. The partition A is composed of elements, or bins, a_j;

$$\mathbf{A} = \bigcup_{\mathbf{k=1}}^{\mathbf{K}} \mathbf{a_k}. \tag{1}$$

We measure information by counting the number of attractor points m_k that fall into each of our K bins. We then estimate the most likely values of the probabilities $\pi_k, k = 1 \ldots K$ for finding a point in each bin. We ask how these probabilities differ from simply having the same probability in each bin. We could use the number of counts m_k in each bin as a measure of probability, but there can be considerable variation in the values of m_k for a particular set of π_k's, particularly if the total number of points observed is small. Our statistical measure must take into account this uncertainty. If the set of π_k's differs significantly from what we would expect from a uniform distribution, then dividing a region into K bins gives us more information than not subdividing.

Partitioning the attractor might seem to be loosing spatial information, since we are grouping points into bins. Because of the information criteria for choosing bin size however, we subdivide the attractor until the set of points in each bin can't be

distinguished from a uniform distribution over the same space, so we are finding the minimum size bins that contain information about the attractor.

In most cases, the final bins found using this information criteria won't be all the same size- some regions of the attractor contain structure at smaller length scales than other parts. The size of the final bins will also depend on the number of data points, as more data will allow us to better see small scale variations.

2.2 Information Criteria

We observe some number of points m_k in each bin. It is possible that the points on the attractor are distributed randomly over the partition $\mathbf{A}$, in which case the probability π_k of finding a point in bin k is constant for all values of k. Statistically, we could have observed different numbers of points in the different bins even though the probabilities of finding a point were the same for all bins. Based on the set of counts m_k, we need statistical tools to tell us by how much the most likely set of probabilities for each bin differs from a uniform distribution over all bins.

Given the set of probabilities π_k, the likelihood of observing a particular set of counts m_k is given by the multinomial distribution

$$\text{Mult}(\mathbf{m}|\boldsymbol{\pi}) = M! \prod_{k=1}^{K} \frac{(\pi_k)^{m_k}}{m_k!} \text{ s.t.} \sum_{k=1}^{K} m_k = M \text{ and } \sum_{k=1}^{K} \pi_k = 1. \tag{2}$$

Initially we don't know anything about the probabilities π_k. Given a set of parameters α_k, the Dirichlet distribution [7] gives the probability of a particular set of π_k's.

$$p(\boldsymbol{\pi}|\boldsymbol{\alpha}) = \text{Dir}(\boldsymbol{\pi}|\boldsymbol{\alpha}) = \frac{\Gamma\left(\sum_k \alpha_k\right)}{\prod_k \Gamma(\alpha_k)} \prod_k \pi_k^{\alpha_k - 1}, \tag{3}$$

where Γ is the gamma function and the α_k's are adjustable parameters. Assuming no prior knowledge about the π_k's, we use the maximum entropy prior distribution, for which all α_k's $= 1/2$.

Combining the prior probabilities from (3) with the observed m_k's substituted into (2) using Bayes theorem yields an updated Dirichlet distribution:

$$\text{Dir}(\boldsymbol{\pi}|\boldsymbol{\alpha}') \propto \text{Mult}(\mathbf{m}|\boldsymbol{\pi}) \cdot \text{Dir}(\boldsymbol{\pi}|\boldsymbol{\alpha}). \tag{4}$$

The prior Dirichlet distribution of (3) and the updated Dirichlet distribution of (4) may be compared by means of a Kullback–Leibler divergence [15]. For two probability distributions p and q, the Kullback–Leibler divergence is the number of bits needed to encode the probability distribution p using samples from q. As an example, if p was the alphabet and q was a binary code, then $D_{KL}(p||q)$ would be

the number of bits needed to encode the alphabet. The Kullback–Leibler divergence is described by

$$D_{KL}(p||q) \equiv \sum_{k=1}^{K} p\,(k) \ln\left(\frac{p\,(k)}{q\,(k)}\right). \tag{5}$$

In a longer work [5] we show how (3)–(5) may be combined to give an analytic result that gives the Kullback–Liebler divergence between the updated Dirichlet distribution (4) and a the prior Dirichlet distribution of (3). The divergence is

$$\begin{aligned} &D_{KL}\left(\mathrm{Dir}(\boldsymbol{\pi}\,|\boldsymbol{\alpha}')||\mathrm{Dir}(\boldsymbol{\pi}\,|\boldsymbol{\alpha})\right) = \\ &\tfrac{1}{\ln 2}\sum_{k=1}^{K}\left[(m_k - \rho_0 V_k)\cdot\psi\left(m_k + \tfrac{1}{2}\right) - \ln\Gamma\left(m_k + \tfrac{1}{2}\right) + \ln\Gamma\left(\rho_0 V_k + \tfrac{1}{2}\right)\right] \end{aligned} \tag{6}$$

where $\rho_0 = \sum_{k=1}^{K} m_k \Big/ \sum_{k=1}^{K} V_k$, where V_k is the volume of an individual bin. The function ψ is the digamma function, while α is the set of parameters in the prior distribution, and α' is the updated set of parameters. Equation (6) represents the amount of information we gain by dividing the data into K bins.

We also need to add a partitioning penalty to the information difference function. Dividing the data into K bins creates information; if $K = 4$, for example, it requires two bits to specify each of the four bins, so for the penalty function we use $L(\Theta) = K \cdot \log_2 K$. The final information criterion is then

$$R(\mathbf{X}, \Theta) = \frac{D_{KL}\left(\mathrm{Dir}(\boldsymbol{\pi}\,|\boldsymbol{\alpha}'_P)||\mathrm{Dir}(\boldsymbol{\pi}\,|\boldsymbol{\alpha}'_C)\right) - L(\Theta)}{K}. \tag{7}$$

The units of $R(\mathbf{X}, \Theta)$ are bits/bin. We may set a reasonable threshold: if $R(\mathbf{X}, \Theta) > 1$ bit, then partitioning the data into K bins gives more information than treating the data as a constant distribution over the same volume.

3 Identifying Sprott Attractors

Sprott [18] found a family of 19 different chaotic attractors defined by 3-dimensional ODE's with one or two quadratic nonlinearities. This group of attractors is a useful test set for our attractor comparison methods.

Each set of ODE's for the Sprott attractors was integrated using a 4th order Runge-Kutta integrator with a time step of 0.01. The integrator output was decimated by keeping every 50th point to produce a time series. Time series of 20,000 points were embedded in a three dimensional space with an embedding delay of two points. Figure 1 is a plot of the embedded attractor for the Sprott C system. The Sprott attractors were partitioned by initially dividing the phase space into two bins/axis, for a total of eight bins. The information criterion $R(\mathbf{X}, \Theta)$ (7) was found by counting the num-

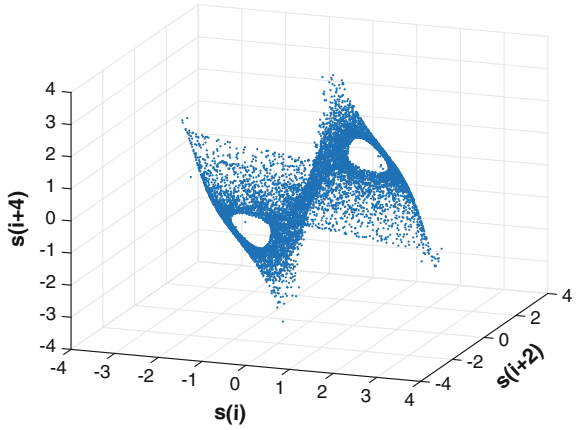

Fig. 1 Embedded time series signal for the Sprott C attractor with an embedding delay of 2

ber of points in each of the eight bins (the m_k values). For the initial division, $R(\mathbf{X}, \Theta)$ was much greater than one bit/bin, so each of the eight bins was further partitioned into eight bins. The initial set of eight bins can be denoted as (1), (2), (3) . . . (8). At the next level, bin (1) is divided into bins (1, 1), (1, 2), (1, 3) . . . (1, 8). In order to determine whether a further subdivision is required, $R(\mathbf{X}, \Theta)$ is computed using the number of points in the bins (1, 1), (1, 2), (1, 3) . . . (1, 8). If $R(\mathbf{X}, \Theta) > 1$bit, each of the bins at this level are again subdivided, and the process continues until $R(\mathbf{X}, \Theta) < 1$bit. In the same manner, all the other top level bins are also subdivided. The final bins may have different sizes.

The result of top down partitioning for the Sprott C attractor is shown in Fig. 2. The partitioning yielded 2427 total bins of different sizes. The density of the bin with the highest density is ρ_{max}. Figure 2a shows all the bins for the partitioned attractor whose density is $>0.1\rho_{max}$, Fig. 2b shows bins with densities from $10^{-1}\rho_{max}$ to $10^{-2}\rho_{max}$, Fig. 2c shows bins with densities from $10^{-2}\rho_{max}$ to $10^{-4}\rho_{max}$, and Fig. 2d shows bins with densities $<10^{-4}\rho_{max}$.

3.1 Comparing Densities

Once attractors have been partitioned, they can be compared by comparing densities at the same locations in their respective phase spaces. The Kullback–Leibler divergence (6) can be used to for this comparison, but there can be situations where one attractor has a finite density at a particular location while the other attractor has zero density. As a result, the Kullback–Leibler divergence can't be used to compare densities for such a location. To avoid this problem, we use the Jensen–Shannon divergence [16] to compare attractors. The Jensen–Shannon divergence is a symmetrized version of the Kullback–Leibler divergence:

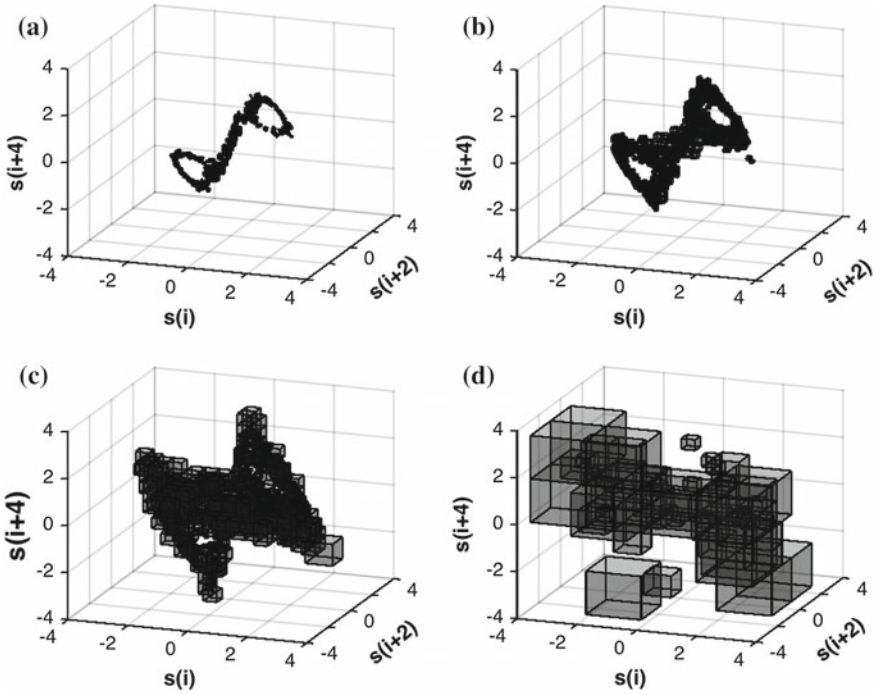

Fig. 2 Histogram bins found by top down partitioning of the Sprott C attractor. The highest density is ρ_{max}. **a** Shows all the bins for the partitioned attractor whose density is $>0.1\rho_{max}$, **b** shows bins with densities from $10^{-1}\rho_{max}$ to $10^{-2}\rho_{max}$, **c** shows bins with densities from $10^{-2}\rho_{max}$ to $10^{-4}\rho_{max}$, and **d** shows bins with densities $<10^{-4}\rho_{max}$

$$D_{JS}(p\,\|q) = \sum_{k=1}^{K} \frac{1}{2}\left[\log\left(\frac{p(k)}{0.5(p(k)+q(k))}\right) p(k) + \log\left(\frac{q(k)}{0.5(p(k)+q(k))}\right) q(k)\right] \tag{8}$$

3.2 Distinguishing Attractors

We want to build up statistics on how well we can distinguish the 19 Sprott attractors, so for each attractor we generate a time series of 200,000 points and divide each time series into ten parts of 20,000 points each. We embed the 20,000 point times series in three dimensions with an embedding delay of two points, and apply the top down partitioning method to create bins to divide the phase space into local regions in which the attractor density appears constant Fig. 2 shows an example of these regions. The embedded Sprott attractors are denoted $\mathbf{S}(i, j)$, where $i = 1 \ldots 19$ indicated the particular Sprott system and $j = 1 \ldots 10$ indicates the part of the time series.

For each bin, indexed by k, the density of points in that bin ρ_k is found by dividing the number of points in the bin, m_k, by the volume of the bin. The density is converted to an empirical probability by normalizing each ρ_k by the sum of all the ρ_k's for the entire attractor.

We choose a bin on one attractor $a_h(i_1, j_1), i_1 = 1 \ldots 19, j_1 = 1 \ldots 5$ where i_1 indicates the particular Sprott system, and j_1 indicates a part of the time series for that Sprott system. We look for the bins $a_k(i_2, j_2), i_2 = 1 \ldots 19, j_2 = 6 \ldots 10$ that overlap in phase space with $a_h(i_1, j_1)$. The overlapping region is the intersection

$$V_{hk}(i_1, j_1, i_2, j_2) = V[a_h(i_1, j_1) \cap a_k(i_2, j_2)] \; k = 1 \ldots N_k \tag{9}$$

where $V[]$ means the phase space volume, and N_k is the total number of bins on $\mathbf{S}(i_2, j_2)$. The probabilities for overlapping bins h and k are

$$\begin{array}{l} \pi(h)_{hk}(i_1, j_1, i_2, j_2) = V\left[a_h(i_1, j_1) \bigcap a_k(i_2, j_2)\right] \rho_h(i_1, j_1) \\ \pi(k)_{hk}(i_1, j_1, i_2, j_2) = V\left[a_h(i_1, j_1) \bigcap a_k(i_2, j_2)\right] \rho_k(i_2, j_2) \end{array} \tag{10}$$

The Jensen–Shannon divergence is calculated as

$$\begin{array}{l} D(h,k)_{JS}(i_1, j_1 \| i_2, j_2) = \\ \frac{1}{2}\left[\begin{array}{l} \log\left(\frac{\pi(h)_{hk}(i_1, j_1, i_2, j_2)}{0.5(\pi(h)_{hk}(i_1, j_1, i_2, j_2) + \pi(k)_{hk}(i_1, j_1, i_2, j_2))}\right)\pi(h)_{hk}(i_1, j_1, i_2, j_2) \\ + \log\left(\frac{\pi(h)_{hk}(i_1, j_1, i_2, j_2)}{0.5(\pi(h)_{hk}(i_1, j_1, i_2, j_2) + \pi(k)_{hk}(i_1, j_1, i_2, j_2))}\right)\pi(k)_{hk}(i_1, j_1, i_2, j_2) \end{array}\right] \end{array} \tag{11}$$

The Jensen–Shannon divergence between $\mathbf{S}(i_1, j_1)$ and $\mathbf{S}(i_2, j_2)$ is the sum

$$D_{JS}(i_1, j_1 \| i_2, j_2) = \sum_{h=1}^{N_h} \sum_{k=1}^{N_k} D(h,k)_{JS}(i_1, j_1 \| i_2, j_2) \tag{12}$$

The number of errors in identification n_e is given by

$$n_e = \sum_{i_1=1}^{19} \sum_{j_1=1}^{5} \sum_{j_2=1}^{5} H(i_1, j_1, j_2) \tag{13}$$

where $H(i_1, j_1, j_2)$ is defined as

$$\begin{array}{l} if \\ \quad \min\left(D_{JS}(i_1, j_1 \| i_2, j_2) \; i_2 = 1 \ldots 19\right) < D_{JS}(i_1, j_1 \| i_2, j_2) \\ \quad H(i_1, j_1, j_2) = 1 \\ else \\ \quad H(i_1, j_1, j_2) = 0 \end{array} \tag{14}$$

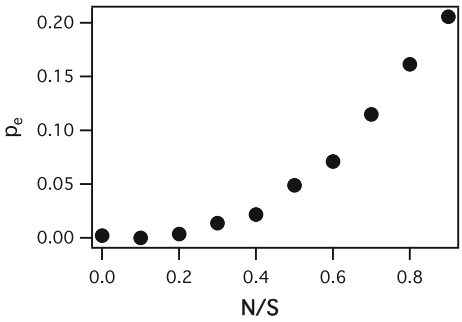

Fig. 3 Probability of error p_e in identifying the 19 Sprott systems when additive noise is present. N/S is the noise level divided by the signal level

The error fraction is n_e divided by the total number of comparisons. For the $19 \times 5 \times 5$ comparisons between Sprott attractors with no noise, only one identification failed.

3.3 Noise Considerations

Rarely in the real world do we have access to a noise free signal, so the attractor density partitioning method must also be robust to added noise. When noise is added to a signal and the result is normalized, the amplitude of the actual signal is reduced. In order for the densities such as that shown in Fig. 2 to properly overlap, the density for the noisy signal must be rescaled so that the actual signal covers the same region of phase space as the noise-free signal. It is complicated to calculate the size of this rescaling, however, as it depends on the relative statistics of the noise and the signal. In order to avoid this complication, we add noise with the same amplitude and spectrum to the original noise free signal.

For this noise study, bandpass filtered noise with the same amplitude and spectrum was added to both $\mathbf{S}(i_1, j_1)$ and $\mathbf{S}(i_2, j_2)$. The noise spectrum occupied the same frequency range as the spectra of the Sprott systems.

Figure 3 shows the error rate for identifying the Sprott attractors when noise was added to all signals.

Figure 3 shows a slight drop in the probability of error for small noise levels. Beyond that, the probability of error increases to about 20% when the noise is as large as the signal.

4 Conclusions

We have demonstrated a density-based method for comparing chaotic attractors. The method yields a single number that tells us how different two attractors are. It is easier to compare attractors, as an attractor for a chaotic system is a stable object, while individual trajectories are sensitively dependent on initial conditions. For many

applications where prediction is not desired, density can give a useful comparison between attractors. In order to estimate densities, we used an algorithm based on a statistical comparisons to coarse-grain the attractor into the smallest spatial scales that contained structure that could be distinguished from a uniform distribution of points in phase space. This coarse-graining reduced the size of the data set, speeding up any computation that depended on the attractor density.

References

1. Abarbanel, H.D.I., et al.: The analysis of observed chaotic data in physical systems. Rev. Mod. Phys. **65**, 1331–1392 (1993)
2. Brown, R., et al.: Modeling and synchronizing chaotic systems from time-series data. Phys. Rev. E **49**, 3784–3800 (1994)
3. Buzug, T., Pfister, G.: Optimal delay time and embedding dimension for delay-time coordinates by analysis of the global static and local dynamical behavior of strange attractors. Phys. Rev. A **45**, 7073 (1992)
4. Carroll, T.L.: Attractor comparisons based on density. Chaos **25**, 013111 (2015)
5. Carroll, T.L., Byers, J.M.: Grid-based partitioning for comparing attractors. Phys. Rev. E **93**, 042206 (2016)
6. Casdagli, M.: Nonlinear prediction of chaotic time series. Physica D **35**, 335–356 (1989)
7. Cover, T.M., Thomas, J.M.: Elements of Information Theory. Wiley, New York (2006)
8. Donner, R.V., et al.: Recurrence-based analysis by means of complex network methods. Int. J. Bifurc. Chaos **21**, 1019–1046 (2011)
9. Eckmann, J.-P., Ruelle, D.: Ergodic theory of chaos and strange attractors. Rev. Mod. Phys. **57**, 617–656 (1985)
10. Farmer, J.D.: Information dimension and the probabilistic structure of chaos. Z. Naturforsch. A (Astrophysik, Physik und Physikalische Chemie) **37A**, 1304–1325 (1982)
11. Farmer, J.D., Sidorowich, J.J.: Predicting chaotic time series. Phys. Rev. Lett. **59**, 845–848 (1987)
12. Grassberger, P., Procaccia, I.: Measuring the strangeness of strange attractors. Physica D: Nonlinear Phenom. **9**, 189–208 (1983)
13. Hunt, B.R., et al.: Efficient data assimilation for spatiotemporal chaos: a local ensemble transform Kalman filter. Physica D **230**, 112–126 (2007)
14. King, G.P., et al.: Phase portraits from a time series: a singular system approach. Nucl. Phys. B - Proc. Suppl. **2**, 379–390 (1987)
15. Kullback, S., Leibler, R.A.: On information and sufficiency. Ann. Math. Stat. **22**, 79–86 (1951)
16. Menendez, M.L., et al.: The Jensen–Shannon divergence. J. Frankl. Inst. **334B**, 307–318 (1997)
17. Packard, N.H., et al.: Geometry from a time series. Phys. Rev. Lett. **45**, 712–716 (1980)
18. Sprott, J.C.: Some simple chaotic flows. Phys. Rev. E **50**, 647–650 (1994)
19. Suetani, H., et al.: Manifold learning approach for chaos in the dripping faucet. Phys. Rev. E **86**, 036209 (2012)
20. Sugihara, G., May, R.M.: Nonlinear forecasting as a way of distinguishing chaos from measurement error in time series. Nature **344**, 734–741 (1990)
21. Todd, M.D., et al.: Using chaotic interrogation and attractor nonlinear cross-prediction error to detect fastener preload loss in an aluminum frame. Chaos: An Interdiscip. J. Nonlinear Sci. **14**, 387–399 (2004)
22. Tufillaro, N.B., et al.: Template analysis for a chaotic NMR laser. Phys. Rev. A **44**, R4786–R4788 (1991)
23. Wood, J., et al.: A behavioral modeling approach to nonlinear model-order reduction for RF/Microwave ICs and systems. IEEE Trans. Microw. Theory Tech. **52**, 2274–2284 (2004)

Complex Bifurcation of Arnol'd Tongues Generated in Three-Coupled Delayed Logistic Maps

Daiki Ogusu, Shuya Hidaka, Naohiko Inaba, Munehisa Sekikawa and Tetsuro Endo

Abstract This study investigates quasi-periodic bifurcations and Arnol'd resonance webs generated in a three-coupled delayed logistic map. Complex bifurcation structure is generated when a conventional Arnol'd tongue transits to a higher-dimensional Arnol'd tongue. We discovered that, at least, two periodic attractors coexist in the conventional Arnol'd tongue which can bifurcate to two one-tori via doubly-folded Neimark–Sacker bifurcation.

1 Summary

The partial and complete synchronization of three or higher frequency quasi-periodic oscillations has recently been studied extensively [1]. Vitolo et al. clarified that two types of bifurcation routes from a two-dimensional torus to a three-dimensional torus exists [2]. One is a quasi-periodic Hopf (QH) bifurcation, and the other is a quasi-periodic saddle-node (QSN) bifurcation. The Arnol'd resonance web is a phenomenon that was discovered and defined by Broer et al. [1] in the numerical

D. Ogusu (✉) · S. Hidaka · T. Endo
Department of Electronics and Bioinformatics, Meiji University, Kawasaki 214-8571, Japan
e-mail: ce51011@meiji.ac.jp

S. Hidaka
e-mail: ce41083@meiji.ac.jp

T. Endo
e-mail: endoh@meiji.ac.jp

N. Inaba
Organization for the Strategic Coordination of Research and Intellectual Property, Meiji University, Kawasaki 214-8571, Japan
e-mail: naohiko@yomogi.jp

M. Sekikawa
Department of Mechanical and Intelligent Engineering, Utsunomiya University, Utsunomiya 321-8585, Japan
e-mail: sekikawa@cc.utsunomiya-u.ac.jp

G. Mantica et al. (eds.), *Emergent Complexity from Nonlinearity, in Physics, Engineering and the Life Sciences*, Springer Proceedings in Physics 191,
DOI 10.1007/978-3-319-47810-4_2

analysis of a map, where regions generating invariant closed curves (ICCs) corresponding to two-dimensional tori in vector fields extend in many directions in the invariant torus-generating region like a web.

One of the major concerns in this field is the problem how a conventional Arnol'd tongue transits to a higher dimensional Arnol'd tongue near QH bifurcation curves. Takens and Wagener provided a bifurcation diagram near the parameter regions [3], and Kuznetsov and Meijer conducted Lypunov analysis [4]. The simplest one may be the transition from a conventional Arnol'd tongue to a two-dimensional torus-Arnol'd tongue via Neimark–Sacker bifurcation [5]. More complex one was reported by Broer et al. [6].

In this study, we conduct a Lyapunov analysis for a three-coupled delayed logistic map expressed by the following form:

$$
\begin{aligned}
F(x_n, y_n, z_n, & \; x_{n+1} = y_n, \\
w_n, u_n, v_n)^\top : & \; y_{n+1} = B_1 y_n(1 - x_n) + \varepsilon_1 w_n + \varepsilon_2 v_n, \\
& \; z_{n+1} = w_n, \\
& \; w_{n+1} = B_2 w_n(1 - z_n) + \varepsilon_3 v_n + \varepsilon_4 y_n, \\
& \; u_{n+1} = v_n, \\
& \; v_{n+1} = B_3 v_n(1 - u_n) + \varepsilon_5 y_n + \varepsilon_6 w_n.
\end{aligned}
\tag{1}
$$

We classify the phenomena in Fig. 1. If the largest Lyapunov exponent is negative, the attractor is defined as periodic, and is denoted by orange in the Lyapunov diagrams shown later. If the largest Lyapunov exponent is positive, the attractor is defined as chaotic, and is denoted by red in the diagram. Because the objective dynamics is discrete, the attractor is torus if the largest Lyapunov exponent λ_1 equals zero. If only λ_1 is zero, the attractor is called invariant one-torus (IT_1) corresponding to a two-torus in vector fields, which is denoted by blue in the diagrams. The three-torus and four-torus abbreviated as IT_2 and IT_3, respectively are defined as in Fig. 1.

We use such abbreviation as shown in Fig. 2 for the several types of bifurcations. Throughout this study, a Neimark–Sacker bifurcation is abbreviated by NS, a saddle-node bifurcation is abbreviated by SN, a quasi-periodic Hopf bifurcation from IT_1 to IT_2 is abbreviated by QH, and a quasi-periodic saddle-node bifurcation from IT_1 to IT_2 is denoted by QSN. A quasi-periodic Hopf bifurcation from IT_2 to IT_3 is denoted by QH_2 and a quasi-periodic saddle-node bifurcation from IT_2 to IT_3 is denoted by QSN_2.

Map	Vector fields	Lyapunov exponents	Color
Periodic (IT_0)	Periodic	$\lambda_1 < 0$	orange
Invariant one-torus (IT_1)	Two-torus	$\lambda_1 = 0, \lambda_2 < 0$	blue
Invariant two-torus (IT_2)	Three-torus	$\lambda_1 = \lambda_2 = 0, \lambda_3 < 0$	black
Invariant three-torus (IT_3)	Four-torus	$\lambda_1 = \lambda_2 = \lambda_3 = 0, \lambda_4 < 0$	dark green
Chaos	Chaos	$\lambda_1 > 0$	red

Fig. 1 Correspondence of terminologies and colors

Bifurcations	Abbreviated terms
Neimark-Sacker bifurcation from IT_0(periodic) to IT_1	NS
Saddle-node bifurcation from IT_0(periodic) to IT_1	SN
Quasi-periodic Hopf bifurcation from IT_1 to IT_2	QH
Quasi-periodic saddle-node bifurcation from IT_1 to IT_2	QSN
Quasi-periodic Hopf bifurcation from IT_2 to IT_3	QH_2
Quasi-periodic saddle-node bifurcation from IT_2 to IT_3	QSN_2

Fig. 2 Abbreviations for the several types of bifurcations

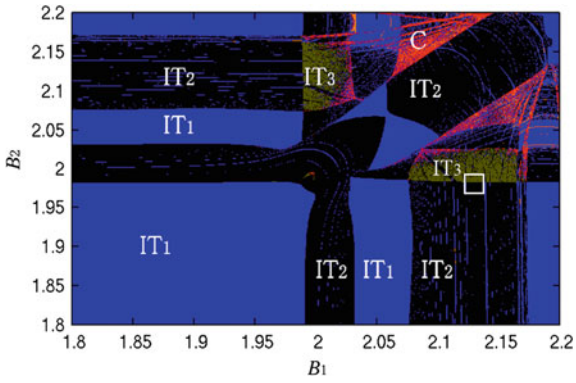

Fig. 3 Global view of Lyapunov diagram of (1) for $\varepsilon_1 = 0.01$, $\varepsilon_2 = 0.002$, $\varepsilon_3 = 0.001$, $\varepsilon_4 = 0.02$, $\varepsilon_5 = 0.01$, $\varepsilon_6 = 0.01$, and $B_3 = 2.05$

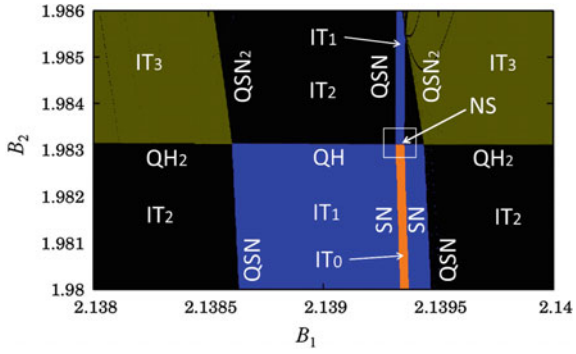

Fig. 4 Magnified view of the *square* region of the Lyapunov diagram in Fig. 3. Parameters are the same as those in Fig. 3

Figure 3 shows a global view of Lyapunov diagram of the three coupled delayed logistic maps shown in (1). In the figure, horizontal and vertical axes are parameters B_1 and B_2, respectively. The Lyapunov exponents are calculated using the procedure presented by Shimada and Nagashima [7]. The region marked IT_1 is the region where an invariant one-torus is generated. In the same manner, IT_2, IT_3, and C denote the regions where an invariant two-torus, an invariant three-torus, and chaos are generated, respectively. We pay attention to the square region.

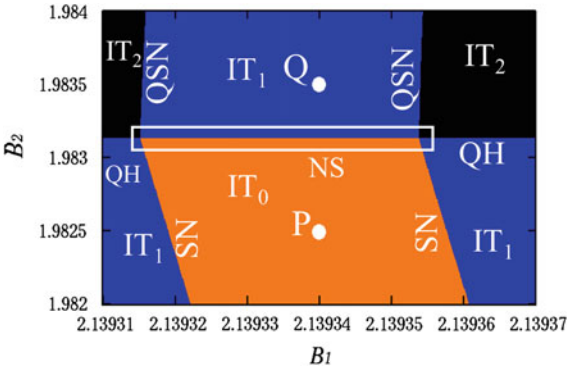

Fig. 5 Further magnified view of the *square* region of the Lyapunov diagram in Fig. 4. Parameters are the same as those in Fig. 3. The *squared* region is used after

Figure 4 shows the magnified view of the square region in Fig. 3. As seen in the figure, the IT_1 Arnol'd tongue transits to the IT_2 Arnol'd tongue via QH or QSN. We focus on bifurcation structure where a conventional (IT_0) Arnol'd tongue bifurcates to invariant one-torus (IT_1) Arnol'd tongue through a Neimark–Sacker bifurcation. At first glance, this bifurcation structure appears to be a simple transition. However, the bifurcation structure is complex according to our numerical results.

Figure 5 shows a further magnified view of the square region of the Lyapunov diagram in Fig. 4. Our concern is what kind of bifurcation occurs when a parameter is moved from P to Q across NS. Figure 6a shows the periodic attractors obtained at the point marked $P : (B_1, B_2) = (2.13934, 1.9825)$ in Fig. 5. Figure 6b shows a magnified view of the square region in Fig. 6a. Note that two attractors coexist in the IT_0 Arnol'd tongue at P. One is denoted as red crosses and the other is denoted as green crosses, each of which consists of a periodic attractor with a period of 93. Figure 7 shows coexisting two invariant one-tori (IT_1) obtained at $Q : (B_1, B_2) = (2.13934, 1.9835)$. The coexisting periodic attractors at P bifurcate to two invariant one-tori through a Neimark–Sacker bifurcation. To the best of our knowledge, this is a novel bifurcation structure. The reason is explained below.

Figure 8a shows a doubly-folded Neimark–Sacker bifurcation curve obtained by magnifying the squared region in Fig. 5. Figure 8b shows the schematic in Fig. 8a. The skyblue curves denote Neimark–Sacker bifurcation of the stable periodic points, and the brown curves denote Neimark–Sacker bifurcation of the unstable periodic points. Note that the bifurcation curves of the unstable periodic points do not affect bifurcation of the attractors. There are four stable SN bifurcation lines on the both side of the stable and unstable NS bifurcation curves. They are tangent to the NS bifurcation curves at four points at which codimension-two bifurcation occurs. Note that the Neimark–Sacker bifurcation curve is doubly twisted. This bifurcation structure explains the coexisting periodic solutions (IT_0) and coexisting invariant one-tori (IT_1). In the region below the stable NS curves, stable coexisting two periodic solutions are observed, and they bifurcate to invariant one-tori via two Neimark–Sacker bifurcations. Since Neimark–Sacker bifurcation is doubly folded, existence of four codimension-two bifurcation points are naturally explained.

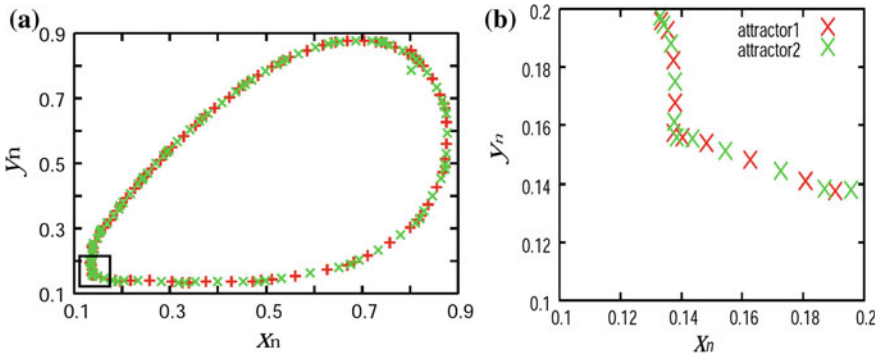

Fig. 6 Coexisting two periodic attractors with period of 93 obtained at a *point* marked $P : (B_1, B_2) = (2.13934, 1.9825)$ in Fig. 5. Parameters are given in Fig. 3. **a** Whole view **b** magnified view of the *squared* region

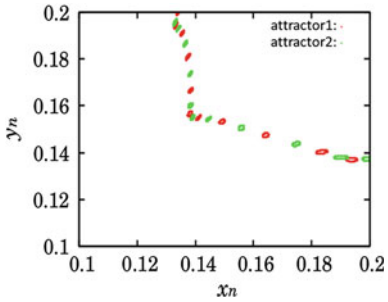

Fig. 7 Magnified diagram of a part of the coexisting two invariant one-tori for $Q : (B_1, B_2) = (2.13934, 1.9835)$ after NS bifurcation

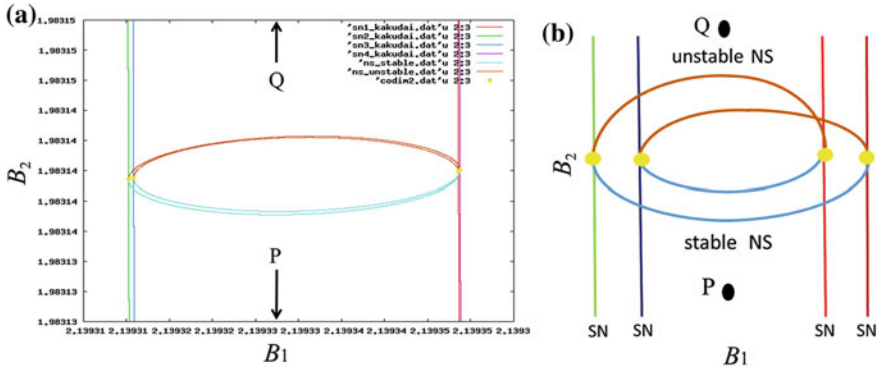

Fig. 8 A doubly-folded Neimark–Sacker bifurcation curve. Two *skyblue* curves present the stable NS bifurcation, and *two brown* curves the unstable NS bifurcation. **a** Magnified diagram of the *square* region in Fig. 5, **b** schematic of **a**

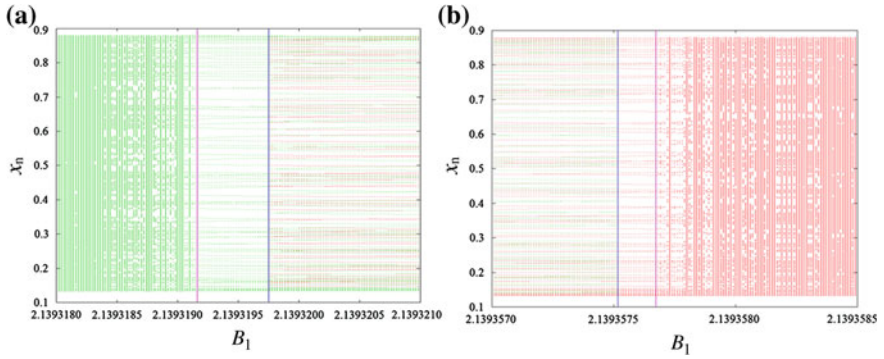

Fig. 9 One-parameter bifurcation diagrams for two solutions denoted *red* and *green* with $B_2 = 1.9825$. Other parameters are given in Fig. 3. **a** Parameter B_1 is decreased from P. The IT_0 *red* attractor disappears on the *blue line* via SN bifurcation, while the IT_0 *green* attractor gives rise to SN cycle bifurcation on the *red line* to become one-torus IT_1 attractor. **b** Parameter B_2 is increase from P. The IT_0 *green* attractor disappears on the *blue line* via SN bifurcation, while the IT_0 *red* attractor gives rise to SN cycle bifurcation on the *red line* to become one-torus IT_1 attractor

We will explain this bifurcation as follows when the parameter is changed from P to Q. At the parameter P, we obtain two coexisting periodic attractors with a period 93. When the parameter is increased across one of two skyblue curves, one of two periodic attractors presents a NS bifurcation to become IT_1, and the other one remain as IT_0. If the parameter is increased more across two skyblue curves two solutions bifurcate to become IT_1. Therefore, we observe two IT_1 as shown in Fig. 7.

Figure 9 shows a one-parameter bifurcation diagram where we use two initial points at parameter P. In Fig. 9a, we trace the two IT_0 solutions from P to the left direction. One of two periodic attractors in red disappears at SN bifurcation on the blue line. On the other hand, the periodic solution in green bifurcates to one-torus (IT_1) on the red line via a saddle-node cycle bifurcation.

In contrast, Fig. 9b shows a one-parameter bifurcation diagram where we trace the solution from P to the right. In this case, the periodic solution in green disappears at the SN bifurcation point on the blue line. Furthermore, the periodic solution in red bifurcates to one-torus (IT_1) through a saddle-node cycle bifurcation on the red line.

2 Conclusion

In this study, we investigated quasi-periodic bifurcations generated by a three-coupled delayed logistic map. We discovered two coexisting periodic solutions with period 93 in an Arnol'd tongue. By varying the bifurcation parameter to left and to right in the IT_0 Arnol'd tongue, first, a saddle-node bifurcation occurs by which one of the periodic solutions disappear, and next a saddle-node cycle bifurcation occurs through which a periodic solution bifurcates to an invariant-torus.

References

1. Broer, H., Simó, C., Vitolo, R.: The Hopf-saddle-node bifurcation for fixed points of 3D-diffeomorphisms: the Arnol'd resonance web. Bull. Belg. Math. Soc. Simon Stevin **15**, 769–787 (2008)
2. Vitolo, R., Broer, H., Simó, C.: Quasi-periodic bifurcations of invariant circles in low-dimensional dissipative dynamical systems. Regul. Chaot. Dyn. **16**, 154–184 (2011)
3. Takens, F., Wagener, F.O.O.: Resonances in skew and reducible quasi-periodic Hopf bifurcations. Nonlinearity **13**, 377–396 (2000)
4. Kuznetsov, Y.A., Meijer, H.G.E.: Remarks on interacting Neimark–Sacker bifurcations. J. Differ. Equ. Appl. **12**, 1009–1035 (2006)
5. Sekikawa, M., Inaba, N., Kamiyama, K., Aihara, K.: Three-dimensional tori and Arnold tongues. Chaos **24**, 013017 (2014)
6. Broer, H., Simó, C., Vitolo, R.: Hopf saddle-node bifurcation for fixed points of 3D-diffeomorphisms: analysis of a resonance 'bubble'. Physica D **237**, 1773–1799 (2008)
7. Shimada, I., Nagashima, T.: A numerical approach to ergodic problem of dissipative dynamical systems. Prog. Theor. Phys. **61**, 1605–1616 (1979)

Phase Response Properties of Rulkov Model Neurons

Karlis Kanders and Ruedi Stoop

Abstract Neurons communicate using patterns of impulses (action potentials); practically all these patterns can, upon suitably chosen parameters, be reproduced by Rulkov's phenomenological, low-dimensional, map-based neuron models. Here, using phase response curves, we show that Rulkov map neurons also respond to transient pulse stimulation in a way that is compatible with the biological examples. This is important because Rulkov maps are computationally very inexpensive, allowing to perform large-scale simulations of the brain.

1 Introduction

To perform neural network simulations on scales relevant to the brain, one needs biologically plausible neuron models and sufficient computational power to simulate interactions between a large number of such elements. The two-dimensional map models by Rulkov [1–3] and one model by Izhikevich [4] provide such phenomenological, low-dimensional, discrete-time spiking neuron models and, while being computationally extremely inexpensive [5], offer a rich repertoire of responses.

Both mentioned modeling frameworks are built upon fast, spiking subsystems that mimick the cell membrane voltage behavior, whereas slow, regulatory subsystems turn the spiking on and off; both approaches can be fitted rather well to the experimentally recorded responses of pyramidal neurons and interneurons exhibiting regular spiking, spike rate adaptation, bursting etc. [2, 6]. The design of the Rulkov neuron models is directly based on discrete map dynamics, whereas the Izhikevich's model

K. Kanders (✉) · R. Stoop
Institute of Neuroinformatics and Institute for Computational Science,
University of Zürich, Winterthurerstr. 190, 8057 Zurich, Switzerland
e-mail: kkanders@ini.phys.ethz.ch

R. Stoop
e-mail: ruedi@ini.phys.ethz.ch

K. Kanders · R. Stoop
ETH Zürich, Zurich, Switzerland

G. Mantica et al. (eds.), *Emergent Complexity from Nonlinearity, in Physics, Engineering and the Life Sciences*, Springer Proceedings in Physics 191,
DOI 10.1007/978-3-319-47810-4_3

is a system of ordinary differential equations integrated using an Euler scheme (with the time step usually chosen to equal 0.5 or 1 ms). Situations are known, however, where network simulations of Izhikevich's neurons depend strongly on the exact value of the time step [7]. To avoid this problem, for the present study we will use Rulkov neurons.

The specific question that we aim to answer in this work, is whether the Rulkov model will be able to reflect fine-grained neurobiological details embodied in the phase response curves (PRC) of real biological neurons. PRC describe how transient input to a regularly spiking neuron affects the length of its interspike intervals [8, 9]. Neurons can either be driven to regular spiking by endogenous mechanisms, or by a large number of small-scale uncorrelated input that in the Gaussian central limit can be approximated by a constant driving current. The collective dynamics of networks composed of such elements can be strongly dependent on their phase response properties [10, 11], making PRC an important feature of neuron models. In real neurons, PRC shapes reflect the dynamics of the various membrane ion channels. Here, we show that the main characteristics of realistic PRC can be modeled with astounding reliability by the simple maps proposed by Rulkov [1, 2].

2 Methods

2.1 Neuron Models

The first neuron model by Rulkov [1] that we will use is given by the equations

$$x_{n+1} = \begin{cases} \frac{\alpha}{1-x_n} + u & x_n \leq 0, \\ \alpha + u & 0 < x_n < \alpha + u \text{ and } x_{n-1} \leq 0, \\ -1 & x_n \geq \alpha + u \text{ or } x_{n-1} > 0, \end{cases} \tag{1}$$

$$y_{n+1} = y_n - \mu(1 + x_n) + \mu\sigma + \mu\beta^y I_n, \tag{2}$$

where $u = y_n + I_n$ (Fig. 1). The fast variable x_n models the cell membrane potential, while y_n is a regulatory subsystem, the evolution speed of which is governed by parameter μ (usually set to a small value of the order of 10^{-3}). For $\alpha > 4$, the model is capable of bursting; in the present study, we will, however, restrict ourselves to the spiking regime. External stimulation pulses were applied via the current I_n, which at perturbation time is the perturbation strength K, and is zero otherwise. The effect of the perturbation on y_n can be controlled by the scaling parameter β^y (normally kept at $\beta^y = 1$).

This two-dimensional map has one fixed point, at coordinates $x^* = -1 + \sigma$, $y^* = x^* - \frac{\alpha}{1-x^*}$. As σ is increased above some threshold value, this fixed point loses stability and, in the suspension, a stable cycle appears through a subcritical

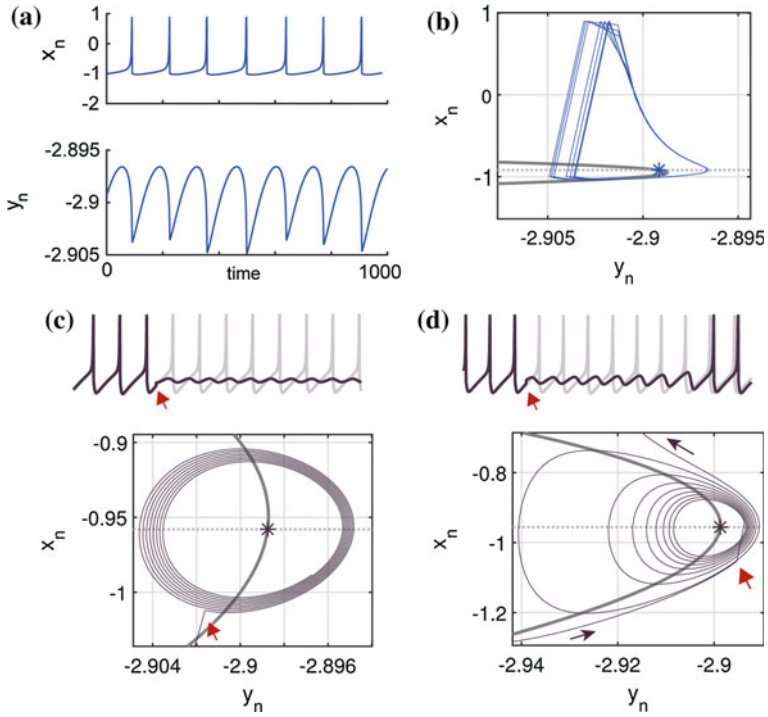

Fig. 1 Original Rulkov map [1]. **a** Spiking regime. **b** State space trajectory of the iterated map. The solid *gray line* is the x_n nullcline $y_n = x_n - \alpha/(1 - x_n)$; the *dotted gray line* is the y_n nullcline $x_n = -1 + \sigma$. The location of the fixed point is denoted by a star. **c** Bistability obtained for σ slightly smaller than σ_{th}. *Top* Original and perturbed x_n trace; *bottom* state space trajectory; perturbation locations are indicated by *red arrows*. **d** Temporary silencing for σ just above σ_{th}. Model parameters: **a**, **b** $\alpha = 3.8$, $\mu = 0.001$, $\sigma = 0.08$; **c**, **d** $\alpha = 3.8$, $\mu = 0.008$, $\sigma_{th} \approx 0.043$; $\sigma = 0.042$ (**c**), 0.044 (**d**)

Andronov-Hopf bifurcation [12]: the map transitions from silence to spiking behavior. The threshold σ can be found by setting, at the fixed point, the determinant of the map's Jacobian equal to 1, which yields $\sigma_{th} = 2 - \sqrt{\frac{\alpha}{1-\mu}}$. The model shows hysteresis, where the spiking becomes stable at values of σ slightly below σ_{th}. For some range of σ, this causes bistability: a perturbation of a spiking system can drive the latter to the fixed point, silencing it in this way (Fig. 1c). This effect has been observed in the central nervous system, for example, in spinal motorneurons and in cerebellar Purkinje cells [13, 14]. Upon increasing σ, a perturbation can temporarily suppress spiking but the system will recover due to the central fixed point's instability (Fig. 1d). Based on the publication date, this first model of Rulkov will be referred to as the *original Rulkov map*.

The second Rulkov model that we analyze has a very similar fast subsystem, with, however, $u = y^{rs} + I_n + \beta^{hp} I_n^{hp}$. The slow subsystem is replaced by a model of

a hyperpolarizing current following an action potential [2]

$$I_{n+1}^{hp} = \gamma^{hp} I_n^{hp} - \begin{cases} g^{hp}, & \text{spike at } n\text{-th step} \\ 0, & \text{otherwise.} \end{cases} \tag{3}$$

This two-dimensional map reaches the spiking behavior through a fold bifurcation. Parameter y^{rs} controls the distance between the nullclines of x_n and I_n^{hp} (which is simply the line $I_n^{hp} = 0$). The smaller this distance, the lower is the spiking frequency. Parameter γ^{hp} controls the decay of the I_n^{hp} variable, having a value between 0 and 1. The threshold y^{rs} above which the neuron spikes, can be found by setting the maximum of the x_n nullcline to 0, i.e., $\frac{1}{\beta^{hp}}(x_n - \frac{\alpha}{1-x_n} - y^{rs}) = 0$ for $x_n = 1 - \sqrt{\alpha}$ (the location of the nullcline's maximum). This yields $y_{th}^{rs} = 1 - 2\sqrt{\alpha}$. In [2], the hyperpolarizing version was used to model fast spiking interneurons without spike rate adaptation. The parameters g^{hp} and γ^{hp} can, however, be adjusted to also cover accommodating behaviour. In contrast to the original neuron model of Rulkov, this model is an integrator [6], which means that it does not exhibit subthreshold oscillations and simply relies, for spike emission, on high frequency stimulation. In the rest of the text, this version will be referred to as the *hyperpolarizing Rulkov map*.

2.2 Phase Response Curves

Our PRC presented below are obtained numerically by perturbing the state variables during the interspike interval and recording the length of the perturbed interval (the first order phase response) as well as the length of the subsequent interval (second order phase response). The first order PRC, PRC_1, is calculated as

$$PRC_1(K, \phi) = \frac{T - T(K, \phi)}{T}, \tag{4}$$

where T is the interspike interval of an unperturbed neuron and $T(K, \phi)$ is the perturbed interspike interval length. K is the strength of the perturbation; as $K \approx 0.10$ is approximately the strength of synaptic inputs used in the large-scale simulations in [2], this value was used as the default perturbation strength. In the case of inhibitory perturbations, K was simply multiplied by -1. Our perturbations covered the duration of one time step, phase ϕ is determined as $\phi = t/T$, where t is the time step at which the perturbation is applied, measured from the beginning of the interspike interval. For the original Rulkov map, PRC were averaged over 10 simulation runs, because at some parameter values we observed a slight jitter of the interspike interval length. For the hyperpolarizing Rulkov map, the spiking period is stable, and multiple runs were, therefore, not necessary.

Second order PRC, PRC_2, are calculated as

$$PRC_2(K, \phi) = \frac{T - T'(K, \phi)}{T}, \tag{5}$$

where $T'(K, \phi)$ is the length of the interspike interval following the directly perturbed interval. If there are no higher order effects, we will therefore have $T'(K, \phi) = T$ and $PRC_2(K, \phi) = 0$. For the rest of the text, we will refer to first and second order phase response curves simply as PRC_1 and PRC_2, respectively, where our understanding should be that both of them depend both on the phase at which the perturbation is applied and on the perturbation strength.

The neuron models that we use do not exhibit an absolute refractory period (as its length would depend on the reference time scale that can vary from 0.5 to several ms per one time step). However, it is easy to see that such an addition would simply result in a vanishing PRC_1 for the duration of the absolute refractory period.

Measuring the relative phase advances, PRC are dimensionless. A positive value indicates that the spike following a perturbation arrives faster; a negative value indicates that the next spike is delayed. PRC that are essentially only positive or only negative are called type-1, whereas PRC that exhibit phase advances as well as phase delays are called type-2. This classification matches a widely accepted classification by Hodkgin [15], where neurons are distinguished by their current-frequency curves and their membrane excitability. Type-1 PRC are usually observed for the Class-I neurons that undergo a fold bifurcation to the spiking state and, as the suprathreshold input current is decreased, spike with arbitrarily low frequencies. Type-2 PRC are associated with Class-II neurons that undergo Andronov-Hopf bifurcations and exhibit a jump in the frequency-current curve [6]. In experiments, the PRC of a particular neuron can switch between the two types, for example, in response to neuromodulators [16], or change in spiking frequency [17]. This switching of the PRC type need, however, not be accompanied by a corresponding change in the spiking threshold dynamics (see Results below). For the biophysical basis of the different types of threshold dynamics and thus the resulting types of PRC, see [18].

3 Results and Discussion

In the following sections, we work out for each of the two Rulkov models the characteristic PRC type, and demonstrate how PRC can be modified via model parameters to obtain desired effects. We will show that with simple modifications of the existing models we can achieve responses that are very similar to the experimental observations of cortical neurons.

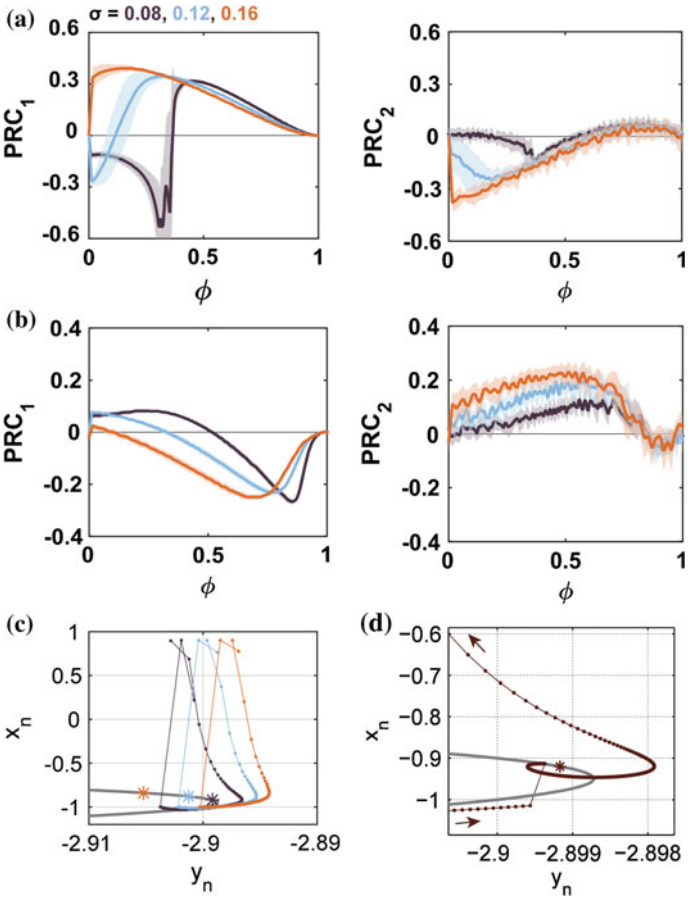

Fig. 2 Examples of first and second order phase response curves of the original Rulkov neuron model for **a** excitatory and **b** inhibitory perturbations. *Shaded* area is the standard deviation due to the jitter of the interspike interval. **c** The distance between the limit cycle and the unstable focus (denoted by a *star*) increases for larger σ values. **d** Example of an excitatory perturbation at $\phi = 0.34$ of the neuron with $\sigma = 0.08$. Model parameters: $\alpha = 3.8$, $\mu = 0.001$, $\beta^y = 1$; perturbation strength, $K = 0.10$

3.1 Original Rulkov Map: Type-2 PRC

The original Rulkov model (1, 2) exhibits for a certain parameter range a type-2 phase response curve: In Fig. 2a, b, separate regions of positive and negative PRC values emerge reliably. This is consistent with the claim that map changes from silent to spiking behavior via a (suspended) Andronov-Hopf bifurcation [12]. The shape of the first order PRC_1 changes with increasing σ, ultimately switching from type-2 to type-1 behavior (see also Fig. 3a). The obtained PRC type depends on the location of the limit cycle in the state space. The eigenvalues of the Jacobian at the fixed point

scale proportionally with σ and, therefore, for smaller σ values the unstable focus is less repelling and the limit cycle is closer to the nullcline of x_n (Fig. 2c). This permits the original Rulkov model to exhibit the counter-intuitive effect of an excitatory perturbation extending the interspike interval by pushing the state vector into a region where the evolution of the system is slower, and in the opposite direction (Fig. 2d). For large σ, the fixed point is more repelling and the limit cycle is further away from the nullcline, which renders the prediction of the effect of the perturbation simpler. The Rulkov model also covers the phenomenon of an early inhibitory pulse shortening the interspike interval (Fig. 2b). This is a prominent observation in cortical neurons [19] that has been attributed to the inactivation of voltage dependent, slow potassium conductances [20]. For the Rulkov model, the phenomenon can be explained by an increase of the evolution speed of the y_n variable, due to the term $-\mu(1 + x_n)$ in 2.

Often, the perturbed trajectory returns to the original limit cycle sufficiently fast de novo [21], but also the opposite case is observed. Higher order effects should, in particular, be taken into account in studies of phase locking and synchronization of large sets of neurons, and second order effects have been observed for vertebrate [22] and invertebrate [23] animal neurons. For examples of generated non-trivial second order PRC_2 see Fig. 2a, b right. Whereas negligible higher order effects allow for more convenient theoretical analysis, methods to deal with more complicated cases have been developed as well [24].

It is possible to reduce a PRC_2 for some range of σ by increasing the parameter μ which makes the dynamics of y_n faster (Fig. 3). Increase in μ also enlarges the region of σ values for which the PRC_1 is type-2. The amplitude of PRC_1 decreases, but this to some extent can be balanced by increasing the parameter β^y that amplifies the effect of the perturbation on the y_n variable. The trade-off to increasing μ is thus a reduced range of possible spiking periods (Fig. 3d).

The effect of the perturbation strength, K, on the PRC is shown in Fig. 4. Overall, the amplitude of the PRC scales predictably with K, albeit not entirely in a linear manner, as the skewness of the PRC changes to some extent. For strong excitatory perturbations, a type-2 PRC_1 eventually switches to type-1.

For the previous results, perturbations were applied at a fixed strength during a single time step. A more realistic synaptic input would be distributed more broadly in time and depend on the distance between x_n and the reversal "potential" of the synapses (see [2] for biologically more plausible implementations). Overall, PRC of a more realistic excitatory stimulation would, however, not be much different, because the resting level of the neuron is far away from the reversal potential of excitatory synapses, whereas inhibitory PRC could be rather attenuated if the inhibitory reversal potential were close to the resting level.

In this section, we have shown that the original Rulkov map is a rather powerful model when it comes to phase responses. It can exhibit a phase response curve of type-2 – a property often observed in cortical pyramidal neurons [16, 17, 19]. The shape and amplitude of the PRC can be easily modified using in particular the model parameters σ and β^y, and second order effects can be controlled to some extent via the parameter μ. It has been demonstrated that in conditions similar to the central nervous system in vivo, where neurons are 'bombarded' with many synaptic inputs

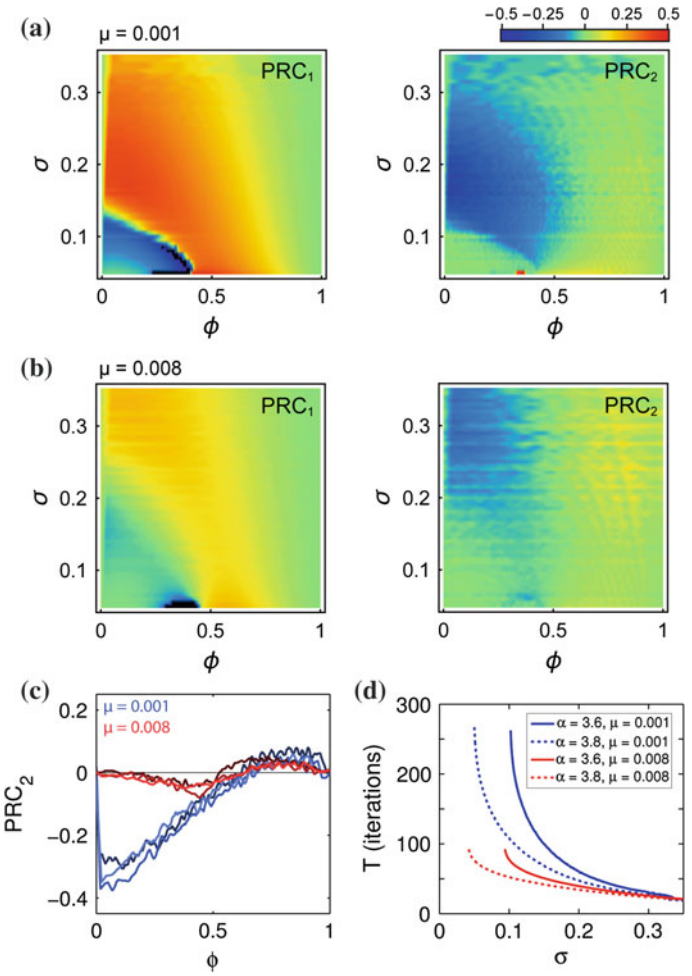

Fig. 3 **a** Excitatory PRC_1 (*left*) and PRC_2 (*right*) heat maps of the phase response amplitudes (values below −0.5 are shown in *black*). Model parameters: $\alpha = 3.8$, $\mu = 0.001$, $\beta^y = 1$, $K = 0.10$. **b** Same as **a**, but with $\mu = 0.008$ and $\beta^y = 5$. **c** An increase in μ may significantly diminish PRC_2. Comparison between Rulkov models of the same periodicity (T = 45, 60, 75; *darker colors* indicate larger T). **d** Parameter μ controls the attainable range of spiking periods; a change in α leaves the range practically unchanged

causing tonic depolarization, it is more likely for them to be of Class-II [25], implying that type-2 PRC could be quite common. However, there are also modeling cases that only require a type-1 PRC neuron model. In the next section we will show that for such situations, the hyperpolarizing Rulkov map is a good choice.

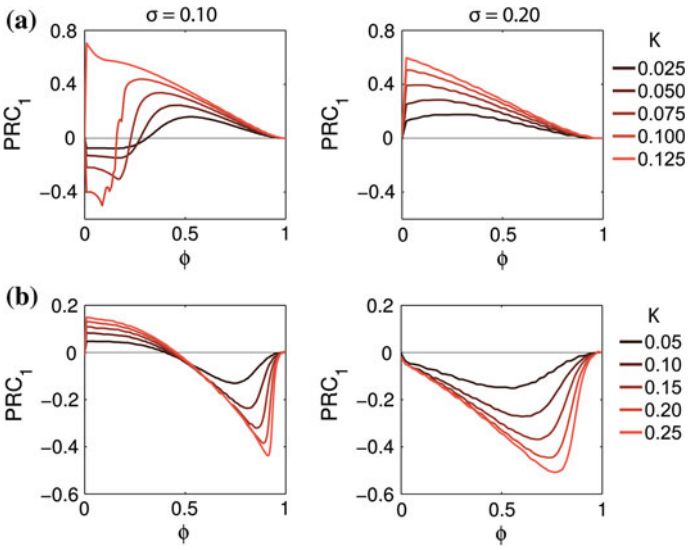

Fig. 4 Effect of different perturbation strengths, K, for the original Rulkov model, for **a** excitatory and **b** inhibitory perturbations (averages). Model parameters: $\alpha = 3.8$, $\mu = 0.001$, $\beta^y = 1$, $\sigma = 0.10$ (*left*), 0.20 (*right*)

3.2 The Hyperpolarizing Rulkov Model: Type-1 PRC

Hyperpolarizing Rulkov maps (1, 3) generally exhibit strictly type-1 PRC_1 (Fig. 5a, b) and essentially flat PRC_2 (not shown). Perturbations arriving at early phases have a negligible effect and PRC peaks are always bent towards late phases. This is because the map 'sticks' to the x_n nullcline (see Fig. 5c) and a perturbation along the x_n axis would rapidly decay back to the nullcline. As a function of the spiking period, a PRC's amplitude could be either increasing or decreasing, depending on the parameters y^{rs} and γ^{hp}. If the decay parameter γ^{hp} is held constant and the period is lowered by increasing y^{rs}, then the amplitude decreases with higher spiking frequencies. The opposite happens if y^{rs} is held constant (i.e., the nullcline does not change its position) and the period is lowered by decreasing γ^{hp} – the amplitude of the PRC increases and the maximum shifts towards smaller phases (Fig. 5a, b right). This difference can be understood by observing the map's trajectory in state space. In Fig. 5c, two trajectories are shown of the same period. The orange trajectory with smaller γ^{hp} (i.e., faster decay of I_n^{hp}) spends more time at the maximum of the nullcline and is more susceptible to perturbations. Hence, if one needs to exhibit distinct spiking periods, the sensitivity can be adjusted by using different combinations of γ^{hp} and y^{rs} (Fig. 5d).

Another way to calibrate the hyperpolarizing model's sensitivity is by means of a small modification of 3 that permits the perturbation to also affect variable I_n^{hp}

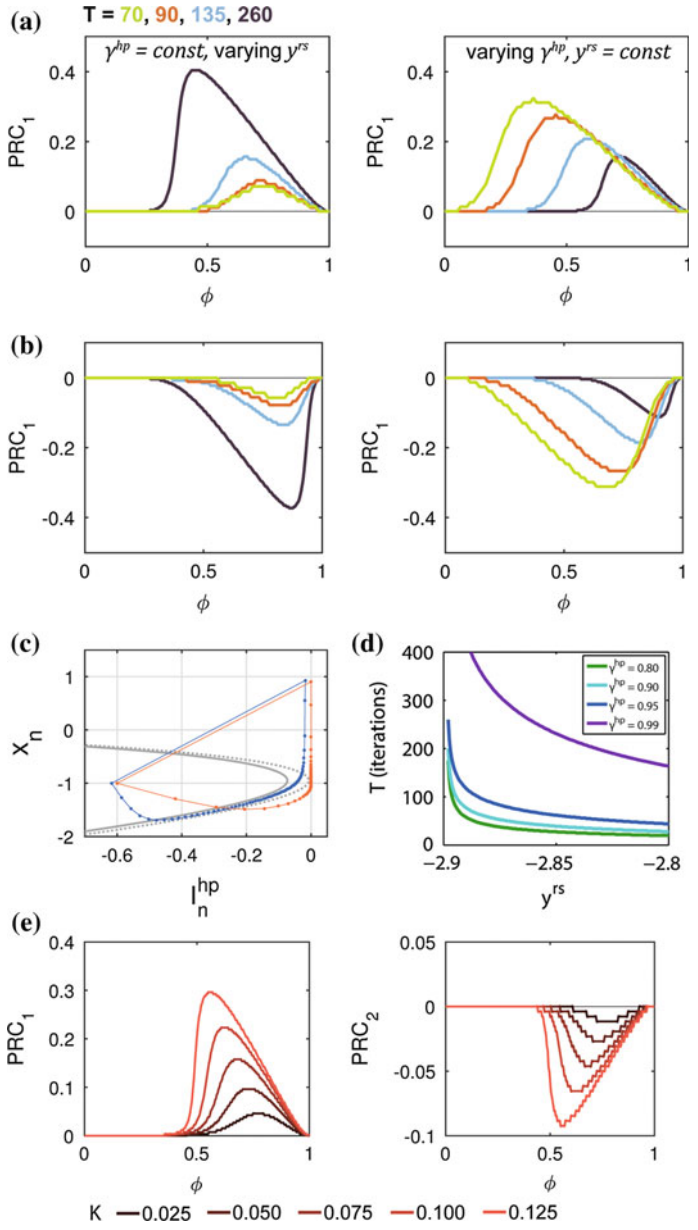

Fig. 5 Hyperpolarizing Rulkov model. PRC_1 for **a** excitatory and **b** inhibitory perturbations; $PRC_2 = 0$. The spiking period is varied either by changing y^{rs} (*left*) or γ^{hp} (*right*). **c** Two limit cycles from **a** of identical period, $T = 70$. The *orange* map has a larger y^{rs} and a smaller γ^{hp}. **d** Spiking period as a function of y^{rs} for different γ^{hp}. **e** Excitatory PRC with second order effects for different perturbation strengths. Model parameters: **a** $\alpha = 3.8$, $\beta^{hp} = 0.5$, $g^{hp} = 0.6$, $\gamma^{hp} = 0.95$, $y^{rs} = -2.862, -2.880, -2.893, -2.898$; **b** same as **a** except $y^{rs} = -2.895$, $\gamma^{hp} = 0.7, 0.85, 0.938, 0.976$; **e** $\alpha = 3.8$, $\beta^{hp} = 0.5$, $g^{hp} = 0.03$, $\gamma^{hp} = 0.995$, $y^{rs} = -2.89$

$$I_{n+1}^{hp} = \gamma^{hp} I_n^{hp} + \beta^p I_n - \begin{cases} g^{hp}, & \text{spike at } n\text{-th step} \\ 0, & \text{otherwise.} \end{cases} \tag{6}$$

Here, I_n is a perturbation term similar to that of 2 and the variable β^p can be used to calibrate the effectiveness of the perturbation. This modification makes the map more responsive, while PRC_2 still is negligible (not shown).

Second order effects can be induced by tuning γ^{hp} very close to 1. This will slow down the decay of I_n^{hp} and, therefore, generate a contribution to the next interspike interval. In order to not be confronted with excessively long spiking periods, the parameter g^{hp} can be reduced. An example of the hyperpolarizing Rulkov map with second order effects is shown in Fig. 5e. Very similar PRC are observed for rat pyramidal neurons [22, 26]. In [27], such type-1 PRC were modeled using the adapting theta neuron model (a system of two ordinary differential equations). Because of its felicitous phase response properties, the hyperpolarizing Rulkov map can be used as a numerically exact and computationally efficient alternative to such modeling.

3.3 *Periodic Forcing of Rulkov Maps*

In this section we provide an example from theoretical neuroscience where PRC are of particular significance: the case of periodically forced oscillators [8, 21, 28]. Let us start from a neuron spiking with period T, due to an endogenous process or a small-scale background input. This neuron now receives strong periodic perturbations (e.g., from a synchronized neuronal population nearby). Circle maps can be used to describe the result of such an interaction in terms of the evolution of the phase differences between the neuron itself and its input source. For this system, the phase return map is defined as

$$\phi_{i+1} = \phi_i + \Omega - g(K, \phi_i) \quad \text{modulo } 1, \tag{7}$$

where ϕ_i is the phase of the spiking neuron at which the perturbation arrives, $\Omega = T_p/T$ is the ratio of the perturbation period and the intrinsic spiking period of the neuron, and $g(K, \phi_i) = 1 - PRC(K, \phi_i)$. The phase return map can be used to predict the possible phase lockings and their dynamical stability, which in turn depends on the shape of the PRC. Using this approach, Stoop et al. [21] retrieved Arnol'd tongues from inhibitory and from excitatory interactions that successfully predicted the experimental observations. Here, we test whether Rulkov map neurons respond to periodic forcing similarly to the biological neurons.

In the previous sections we established that Rulkov maps can model a wide variety of phase responses. Surprisingly, the modeling of measured PRC reported for pyramidal neurons in the rat neocortex [21] turned out to be more challenging than expected because of three constraints: excitatory PRC should be predominantly of type-1, whereas inhibitory PRC should be of type-2 and the second order effects

should be minimal. With the original Rulkov map, it was possible to satisfy the first two requirements (at parameter values $\alpha = 3.8$, $\sigma = 0.15$, $\mu = 0.001$), but second order effects were not negligible (see Fig. 2). Second order effects could be diminished by increasing μ, but only at the cost of rendering the excitatory PRC_1 more biphasic (see Fig. 3). To simultaneously satisfy the three constraints, a tentative "best of both worlds" model was created, by combining the slow subsystems of the original and of the hyperpolarizing Rulkov map, respectively, as

$$y_{n+1} = \gamma y_n - \mu(1 + x_n) + \mu\sigma + \mu\beta^y I_n - \\ - \begin{cases} g^{hp}, & \text{spike at } n\text{-th step} \\ 0, & \text{otherwise.} \end{cases} \tag{8}$$

The introduced decay term γ controls the "memory" of the y_n variable and, therefore, minimizes the second order effects if required. There is still the possibility of counter-intuitive phase responses, because of the term depending on x_n. Finally, the reset term g^{hp} permits to move the state variable further away from threshold and to increase the time during which the state vector is in the vicinity of the x_n nullcline. In the following case we leave $g^{hp} = 0$.

The combined map (1 with $u = y_n + I_n + y^{rs}$ and 8) can satisfy the mentioned constraints, albeit at the cost of a larger number of tunable parameters compared to the previously discussed models. We leave the detailed analysis of the map to another investigation; the main purpose here was to serve as an example for demonstrating how the slow subsystem can be modified to obtain desired properties.

In Fig. 6 we demonstrate that the combined map can qualitatively model the experimental observations of [21]. The obtained Arnol'd tongues have a similar structure, including the skewness and a possible chaotic behavior for strong inhibitory perturbations (positive Lyapunov exponents $\lambda = \lim_{n\to\infty} \frac{1}{n} \Sigma_i^n \ln|P'(\phi_i)|$, where $P(\phi_i)$ is given by 7). There are also positive Lyapunov exponents for strong excitatory interaction, but PRC at high K values ($K > 0.25$) slightly differ from the experimental PRC. In the experimental setting, such large perturbation strengths, however, would already relate to damaged cells [29].

In Fig. 7 we show that such phase return maps successfully predict phase locking. The simulations of periodic forcing of the map agree well with the predictions from the bifurcation diagram, obtained from first order PRC only. In this particular case, period-2 phase locking was very stable, whereas period-1 and period-3 were somewhat more noisy. This variability could be caused by a slight jitter of the spiking period and an accumulation of the second order effects over a longer period of time.

The average period of the limit cycle in this case is rather short (32 iterations), which constrains the set of perturbation periods that can be tested in the simulations, i.e., Ω can only be changed in relatively large steps of $\simeq 0.03$. In such a case, if the spiking period of the neuron is slightly jittered and the support of Ω for a particular periodicity is not sufficiently large, some variability will be inherited, and high-periodicity phase-locking might not be observable at all. This can be considered as

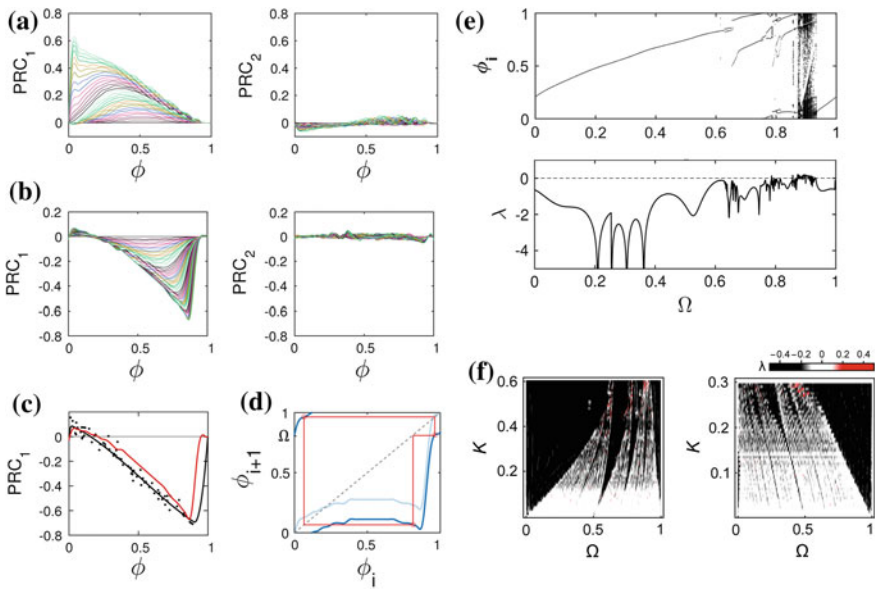

Fig. 6 Periodic forcing of a Rulkov neuron. **a** Excitatory and **b** inhibitory PRC with very small second order effects ($K \in [0, 0.3]$ in **a** and $K \in [0, 0.6]$ in **b**). **c** Comparison between the experimentally obtained inhibitory PRC (*black*) [21] and the Rulkov model (*red*). **d** Corresponding phase return map to **c** with period-3 orbit ($\Omega = 0.838$). In the background the phase return map with $\Omega = 0$ is shown with a *lighter color*. **e** Bifurcation diagram (*top*) and corresponding Lyapunov exponents (*bottom*) obtained from a polynomial fit to the phase return map (**d**). Chaotic interaction ($\lambda > 0$) is possible for some interval of Ω. **f** Arnol'd tongues for inhibitory (*left*) and excitatory (*right*) interaction obtained using spline interpolated phase return maps; *color* codes for λ values. Spline interpolation is faster than manual fitting but it gives rise to some spurious positive λ. Model parameters: $\alpha = 3.8$, $\sigma = 0.2$, $\mu = 0.01$, $\gamma = 0.91$, $\beta^y = 1$, $y^{rs} = -2.89$; $K = 0.6$ for **c**–**e**

a caveat to using map models. However, a more rigorous exploration of the matter might still come up with a slower spiking map with similar phase response properties.

4 Conclusions

In our work, we have provided evidence that the neuron models proposed by Rulkov [1, 2] are well suited for modeling biologically plausible neural networks. Besides their capability of reproducing realistic firing patterns, these maps also capture the main qualities of the phase responses to pulse perturbations: the original Rulkov model from [1] can reproduce the phase response properties of Class-II neurons, while the hyperpolarizing map from [2] can reproduce phase response curves characteristic to Class-I neurons. Using the parameters of the model, desired particularities of the phase responses can be achieved easily. In addition, we have demonstrated

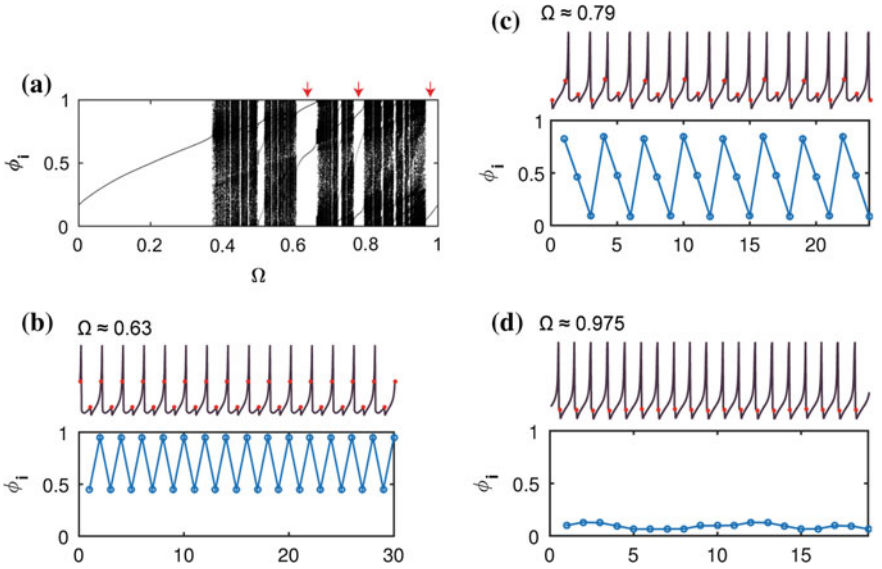

Fig. 7 Bifurcation diagram (**a**) can successfully predict period-2 **(b)**, period-3 **(c)** and period-1 **(d)** phase locking in the simulations of periodic inhibitory perturbations ($K = 0.25$). Perturbation events are marked by the *red circles*

that small modifications of the Rulkov model can provide such a system with the ability to respond realistically to periodic stimuli, which supports the expectation that a network of such elements will exhibit realistic activity.

References

1. Rulkov, N.: Modeling of spiking-bursting neural behavior using two-dimensional map. Phys. Rev. E **65**, 041922 (2002)
2. Rulkov, N.F., Timofeev, I., Bazhenov, M.: Oscillations in large-scale cortical networks: map-based model. J. Comput. Neurosci. **17**, 203–223 (2004)
3. Shilnikov, A.L., Rulkov, N.F.: Subthreshold oscillations in a map-based neuron model. Phys. Lett. A **328**, 177–184 (2004)
4. Izhikevich, E.M.: Simple model of spiking neurons. IEEE Trans. Neural Netw. **14**, 1569–1572 (2003)
5. Girardi-Schappo, M., Tragtenberg, M.H.R., Kinouchi, O.: A brief history of excitable map-based neurons and neural networks. J. Neurosci. Methods **220**, 116–130 (2013)
6. Izhikevich, E.M.: Dynamical Systems in Neuroscience: The Geometry of Excitability and Bursting. The MIT Press, Cambridge (2007). Chapter 8
7. Long, L.N., Fang, G.: A Review of Biologically Plausible Neuron Models. AIAA Paper No. 2010-3540, AIAA InfoTech@Aerospace Conference (2010)
8. Glass, L., Mackey, M.C.: From Clocks to Chaos. Princeton University Press, Princeton (1988)
9. Smeal, R.M., Ermentrout, G.B., White, J.A.: Phase-response curves and synchronized neural networks. Philos. Trans. R. Soc. Lond. B. Biol. Sci. **365**, 2407–2422 (2010)

10. Hansel, D., Mato, G., Meunier, C.: Synchrony in excitatory neural networks. Neural Comput. **7**, 307–337 (1995)
11. Achuthan, S., Canavier, C.C.: Phase-resetting curves determine synchronization, phase locking, and clustering in networks of neural oscillators. J. Neurosci. **29**, 5218–5233 (2009)
12. Shilnikov, A.L., Rulkov, N.F.: Origin of chaos in a two-dimensional map modelling spiking-bursting neural activity. Int. J. Bifurcat. Chaos **13**, 3325–3340 (2003)
13. Hounsgaard, J., Kiehn, O.: Ca++ dependent bistability induced by serotonin in spinal motoneurons. Exp. Brain Res. **57**, 422–425 (1985)
14. Loewenstein, Y., Mahon, S., Chadderton, P., Kitamura, K., Sompolinsky, H., Yarom, Y., Häusser, M.: Bistability of cerebellar Purkinje cells modulated by sensory stimulation. Nat. Neurosci. **8**, 202–211 (2005)
15. Hodgkin, A.: The local electric changes associated with repetitive action in a non-medullated axon. J. Physiol. **107**, 165–181 (1948)
16. Stiefel, K.M., Gutkin, B.S., Sejnowski, T.J.: Cholinergic neuromodulation changes phase response curve shape and type in cortical pyramidal neurons. PLoS One **3**, e3947 (2008)
17. Tsubo, Y., Takada, M., Reyes, A.D., Fukai, T.: Layer and frequency dependencies of phase response properties of pyramidal neurons in rat motor cortex. Eur. J. Neurosci. **25**, 3429–3441 (2007)
18. Prescott, S.A., De Koninck, Y., Sejnowski, T.J.: Biophysical basis for three distinct dynamical mechanisms of action potential initiation. PLoS Comput. Biol. **4**, e1000198 (2008)
19. Schindler, K.A., Bernasconi, C., Stoop, R., Goodman, P.H., Douglas, R.J.: Chaotic spike patterns evoked by periodic inhibition of rat cortical neurons. Z. Naturforsch **52**, 509–512 (1997)
20. Bernasconi, C.A., Schindler, K., Stoop, R., Douglas, R.: Complex response to periodic inhibition in simple and detailed neuronal models. Neural Comput. **11**, 67–74 (1999)
21. Stoop, R., Schindler, K., Bunimovich, L.A.: When pyramidal neurons lock, when they respond chaotically, and when they like to synchronize. Neurosci. Res. **36**, 81–91 (2000)
22. Reyes, A., Fetz, E.: Effects of transient depolarizing potentials on the firing rate of cat neocortical neurons. J. Neurophysiol. **69**, 1673–1683 (1993)
23. Oprisan, S.A., Prinz, A.A., Canavier, C.C.: Phase resetting and phase locking in hybrid circuits of one model and one biological neuron. Biophys. J. **87**, 2283–2298 (2004)
24. Martignoli, S., Stoop, R.: Phase-locking and Arnold coding in prototypical network topologies Discrete Cont. Dyn-B **9**, 145–162 (2008)
25. Prescott, S.A., Ratté, S., De Koninck, Y., Sejnowski, T.J.: Pyramidal neurons switch from integrators in vitro to resonators under in vivo-like conditions. J. Neurophysiol. **100**, 3030–3042 (2008)
26. Reyes, A., Fetz, E.: Two modes of interspike interval shortening by brief transient depolarizations in cat neocortical neurons. J. Neurophysiol. **69**, 1661–1672 (1993)
27. Gutkin, B.S., Ermentrout, G.B., Reyes, A.D.: Phase-response curves give the responses of neurons to transient inputs. J. Neurophysiol. **94**, 1623–1635 (2005)
28. Stoop, R., Schindler, K., Bunimovich, L.A.: Noise drive neocortical interaction: a simple generation mechanism for complex neuron spiking. Acta Biotheor. **48**, 149–171 (2000)
29. Stoop, R., Schindler, K., Bunimovich, L.A.: Neocortical networks of pyramidal neurons: from local locking and chaos, to global locking and synchronization. Nonlinearity **13**, 1515–1529 (2000)

Treating Many-Body Quantum Systems by Means of Classical Mechanics

Andrey R. Kolovsky

Abstract Many-body physics of identical particles is commonly believed to be a sovereign territory of Quantum Mechanics. The aim of this contribution is to show that it is actually not the case and one gets useful insights into a quantum many-body system by using the theory of classical dynamical systems. In the contribution we focus on one paradigmatic model of many-body quantum physics - the Bose–Hubbard model which, in particular, describes interacting ultracold Bose atoms in an optical lattice. We show how one can find/deduce the energy spectrum of the Bose–Hubbard model by using a kind of the semiclassical approach.

1 Introduction

The semiclassical methods are known to be a powerful tool in studying quantum systems. They use information about classical dynamics of the system to predict its quantum dynamics or find the energy spectrum. Besides practical aspect, these methods also contribute to our understanding of subtle relation between the quantum and classical mechanics – an issue which might be even more important. Until now the overwhelming majority of semiclassical studies have been done for single-particle problems. Yet, there is other type of problems which can be addressed by using the same kind of ideas – these are dynamical and spectral properties of an ensemble of identical particles. In this contribution we shall give an example of application of 'semiclassical methods' to one of the paradigm models of the many-body physics – the Bose–Hubbard (BH) model. This model describes, in particular, ultracold bosonic atoms optical lattices [7], with a unique for the many-body physics experimental control over the model parameters [6].

A.R. Kolovsky (✉)
L.V. Kirensky Institute of Physics of Siberian Branch of Russian Academy of Sciencies, 660036 Krasnoyarsk, Russia
e-mail: andrey.r.kolovsky@gmail.com

G. Mantica et al. (eds.), *Emergent Complexity from Nonlinearity, in Physics, Engineering and the Life Sciences*, Springer Proceedings in Physics 191,
DOI 10.1007/978-3-319-47810-4_4

2 Bose–Hubbard Model

Denoting by $\hat{a}_l$ and $\hat{a}_l^\dagger$ the bosonic annihilation and creation operators, $[\hat{a}_l, \hat{a}_{l'}^\dagger] = \hbar\delta_{l,l'}$, and by $\hat{n}_l = \hat{a}_l^\dagger \hat{a}_l$ the number operator, the Bose–Hubbard Hamiltonian reads

$$\widehat{H} = \sum_{l=1}^{L} \varepsilon_l \hat{n}_l - \frac{J}{2} \sum_{l=1}^{L} \left(\hat{a}_{l+1}^\dagger \hat{a}_l + h.c. \right) + \frac{U}{2} \sum_{l=1}^{L} \hat{n}_l (\hat{n}_l - 1) \ . \tag{1}$$

In this Hamiltonian ε_l are the on-site energies, J is the hopping matrix element, and U the microscopic interaction constant. Having in mind cold Bose atoms in the one-dimensional optical lattice, the constant U is mainly determined by the s-wave scattering length for neutral atoms, and the constant J by the lattice depth [7]. In laboratory experiments both the scattering length and the lattice depth can be varied in large intervals, which affords practically arbitrary ratio U/J. Notice, that the Hamiltonian (1) preserves the total number of particles (atoms), which we denote by N.

A remark concerning the boundary condition is in order. We assume a uniform system (i.e., no spatial dependence for the on-site energies), for which we shall use the periodic boundary condition if $L \geq 3$. In this case the Hamiltonian (1) can be rewritten in terms of the operators $\hat{b}_k$ and $\hat{b}_k^\dagger$,

$$\hat{b}_k = \frac{1}{\sqrt{L}} \sum_l \exp\left(i \frac{2\pi k}{L} l \right) \hat{a}_l \ , \quad \hat{b}_k^\dagger = \left(\hat{b}_k \right)^\dagger \ . \tag{2}$$

Unlike the operators $\hat{a}_l$ ($\hat{a}_l^\dagger$), which annihilate (create) an atom in the Wannier states, operators (2) annihilate or create an atom in the Bloch states. Using the transformation (2) and dropping the first term in the Hamiltonian (1) (which is a constant for a uniform system) we have

$$\widehat{H} = -J \sum_k \cos\left(\frac{2\pi k}{L} \right) \hat{b}_k^\dagger \hat{b}_k + \frac{U}{2L} \sum_{k_1,k_2,k_3,k_4} \hat{b}_{k_1}^\dagger \hat{b}_{k_2}^\dagger \hat{b}_{k_3} \hat{b}_{k_4} \tilde{\delta}(k_1 + k_2 - k_3 - k_4) \ , \tag{3}$$

where $\tilde{\delta}$ is the periodic δ-function, i.e., $\tilde{\delta}(k)$ equals unity if k is a multiple of L and zero otherwise. Depending on the addressed question this form of the BH model might be more convenient than (1). In particular, it follows from (3) that for $U = 0$ the eigen-energies of the BH Hamiltonian are given by the equation,

$$E_j = -J \sum_k \cos\left(\frac{2\pi k}{L} \right) n_k \ , \quad \sum_k n_k = N \ . \tag{4}$$

The total number of eigen-energies E_j obviously coincides with dimension of the Hilbert space,

$$\mathcal{N} = \frac{(N+L-1)!}{N!(L-1)!}\ , \tag{5}$$

which is obtained by counting all possible distributions of N atoms among L wells.

It is very difficult task to find energies E_j if U differs from zero. As it will be explained below, in general case we cannot find them analytically[1] while numerically we are restricted to rather small system size because the dimension of the Hilbert space grows exponentially with L and N. A way around these problems is to use 'semiclassical methods', where one is not bounded with small N and L. To this end we introduce the classical counterpart of the quantum BH model.

3 Classical Bose–Hubbard Model

Formally, the classical counterpart of the quantum BH model is obtained by rescaling the Hamiltonian (1) with respect to N and identifying the creation and annihilation operators with c-number. This gives

$$H = -\frac{J}{2}\sum_{l=1}^{L}(a_{l+1}^{*}a_l + c.c.) + \frac{g'}{2}\sum_{l=1}^{L}|a_l|^4\ , \tag{6}$$

where the constant $g' = UN$ is called the macroscopic interaction constant, to distinguish it from the microscopic interaction constant U. The Hamiltonian (6) generates classical trajectories according to the Hamilton equation of motion,

$$i\frac{d}{dt}a_l = \frac{\partial H_0}{\partial a_l^{*}} = -\frac{J}{2}\,(a_{l+1} + a_{l-1}) + g'|a_l|^2 a_l\ , \tag{7}$$

which is known in the physical literature as the Discrete Nonlinear Schrödinger Equation (DNLSE). Let us remark that the conservation law for particle number takes the form of the norm conservation: $\sum_{l=1}^{L}|a_l|^2 = 1$.

Historically, (7) was deduced by using the mean-field approach, where the complex amplitudes a_l have the meaning of order parameters. For this reason the classical Hamiltonian (6) is often referred to as the mean-field Hamiltonian. In the rest of this section we justify the Hamiltonian (6) rigorously, without appealing to the mean-field approximation. We shall follow an approach based on the notion of the Husimi function.[2]

[1] This should be opposed to the Fermi–Hubbard model, where the spectrum can be found analytically by using the Betha ansatz.

[2] A similar approach is based on the notion of the Wigner function [12–14]. The Husimi function, however, has an advantage that it is positively defined.

Given $|\Psi(t)\rangle$ to be the many-body wave function of the quantum Hamiltonian, the Husimi function is defined as

$$f(\mathbf{a}, t) = |\langle \mathbf{a}|\Psi(t)\rangle|^2 \ , \tag{8}$$

where $|\mathbf{a}\rangle$ are the so-called coherent $SU(L)$ states [11],

$$\big|\mathbf{a}\big\rangle = \frac{1}{\sqrt{N!}}\left(\sum_{l=1}^{L} a_l \hat{a}_l^\dagger\right)^N |vac\rangle \ .$$

Note that the Husimi function (8) is a function of L complex amplitudes a_l and the time t. In terms of the Husimi function (8) the Schrödinger equation for the wave function $|\Psi(t)\rangle$ takes the form

$$\frac{\partial f}{\partial t} = \{H, f\} + O\left(\frac{1}{N}\right) \ , \tag{9}$$

where $\{\ldots,\ldots\}$ denotes the Poisson brackets, the c-number Hamiltonian H is given in (6) and we refer the reader to the work [16] for the explicit form of terms which are inverse proportional to N. The crucial point in the presented derivation of the classical Hamiltonian is that (9) formally coincides with equation on the Husimi function of a single-particle system if one identifies $1/N$ with the Planck constant.[3] Thus one can use the common semiclassical theory to study the BH model. This theory relates the energy spectrum of the quantum BH model (1) to the phase-space structure of the classical BH model (6). We shall give examples in the subsequent sections.

To conclude this section we also display the classical counterpart of the Hamiltonian (3):

$$H = -J\sum_{k=} \cos\left(\frac{2\pi k}{3}\right) b_k^* b_k + \frac{g}{2}\sum_{k_1,k_2,k_3,k_4} b_{k_1}^* b_{k_2}^* b_{k_3} b_{k_4} \tilde{\delta}(k_1 + k_2 - k_3 - k_4) \ , \tag{10}$$

where $g = UN/L$. Notice that the macroscopic interaction constant g in (10) differs from the above introduced constant g' by the factor L. Often one uses the constant g also in (7). In this case, however, the amplitude a_l are normalized to L but not to unity. To be certain, we shall characterize interactions by the constant $g = UN/L$ and restrict ourselves by the parameter region where $g \leq J$.

[3] The effective Planck constant $\hbar_{eff} = 1/N$ should not be mismatched with the fundamental Planck constant $\hbar$ which we set to unity from now on. We also mention that within the discussed formalism a_l and a_l^* are the canonical variables, i.e., one does not interpret them as order parameters.

4 Bose–Hubbard Dimer

We proceed with examples, where the simplest case corresponds to $L = 2$ – the so-called BH dimer. Noticing that the BH system has two independent integrals of motion – the energy and the norm – we immediately conclude that the dimer is an integrable system. In fact, using the action-angle variables, $a_l = \sqrt{I_l}\exp(i\theta_l)$, and taking into account conservation of the norm, $I_1 + I_2 = 1$, the original system of two degrees of freedom reduces to the following effective system of one degree of freedom,

$$H_{eff} = gI^2 - J\sqrt{1 - I^2}\cos(\theta)\ , \quad |I| \leq 1\ , \tag{11}$$

where $I = (I_2 - I_1)$ and $\theta = \theta_2 - \theta_1$.[4] For $g \neq 0$ the phase portrait of the system (11) resembles that of the mathematical pendulum. Small oscillations of this pendulum have the frequency

$$\Omega = \sqrt{J^2 + 2gJ}\ , \tag{12}$$

which is know in the physical literature as the Josephson frequency. We mention, in passing, that Josephson's oscillations of cold atoms in a two-site optical potential were observed in the experiment [1].

Quantizing the effective system (11) in terms of $\hbar_{eff} = 1/N$ one obtains the energy spectrum of the BH dimer. As follows from the above analogy with the pendulum, the low-energy spectrum of the BH dimer should be equidistant with the level spacing given by the Josephson frequency Ω, and the high-energy spectrum should consist of doubly degenerate levels, which correspond to the clockwise and counterclockwise rotations of the pendulum. These expectations are fully confirmed by the numerical analysis. Figure 1a shows the energy spectrum of the BH dimer as the function of the macroscopic interaction constant g for $N = 40$ where, to facilitate the comparison, we rescale the spectrum by using the Josephson frequency (12). The high- and low-energy regions, which are separated by the 'quantum separatrix', are clearly seen in Fig. 1a. Let us also mention that in the limit $N \to \infty$ the density of state diverges at the separatrix [2].

5 Bose–Hubbard Trimer

The case $L = 3$ is more complicated because the classical BH trimer is a non-integrable system with mixed phase space. It is largely an open question about the volumes of regular and chaotic components for a given energy shell $H(\mathbf{a}) = E$.

[4] Using one more canonical transformation, $b_1 = (a_1 + a_2)/\sqrt{2}$ and $b_2 = (a_1 - a_2)/\sqrt{2}$, one gets a different form of the effective Hamiltonian, which is similar to (14) in Sect. 5. Naturally, this does not affect the final results.

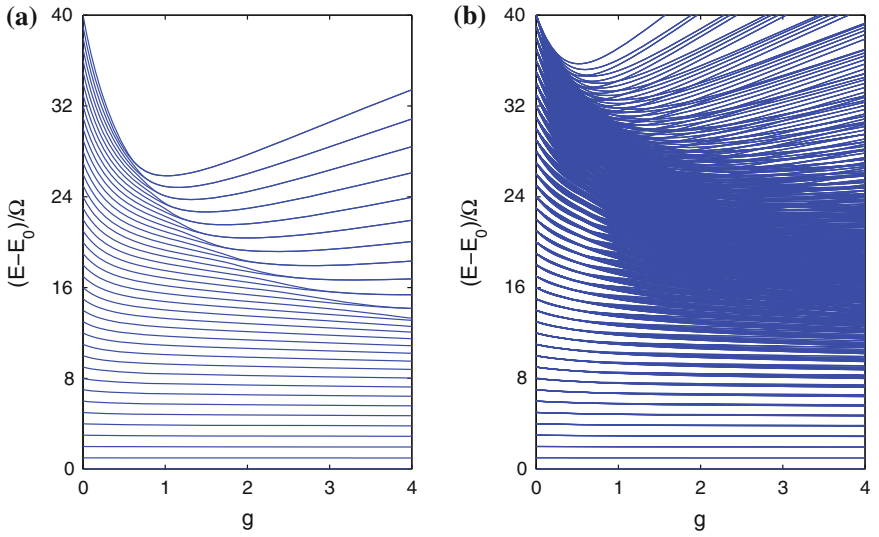

Fig. 1 Energy spectrum of the 2-site BH model, *left*, and the 3-site BH model, *right*, for $N = 40$. The energy is measured relative to the ground energy E_0 and scaled with respect to the frequency Ω given in (12) and (15), respectively. The value of the hopping matrix element $J = 1$

However, we can prove that the chaotic component vanishes at low energies and, hence, we are left with a stability island.

The proof involves several steps. First we rewrite the Hamiltonian (10) for $L = 3$ in terms of the canonical variables b_k and b_k^*. This gives

$$H = -J \sum_{k=-1}^{1} \cos\left(\frac{2\pi k}{3}\right) b_k^* b_k + \frac{g}{2} \sum_{k_1,k_2,k_3,k_4=1}^{-1} b_{k_1}^* b_{k_2}^* b_{k_3} b_{k_4} \tilde{\delta}(k_1 + k_2 - k_3 - k_4) \ .$$

Next we switch to the action-angle variables, $b_k = \sqrt{I_k}\exp(i\phi_k)$, and explicitly take into account that $\sum_k I_k = 1$. This reduces our system of three degrees of freedom to the system of two degrees of freedom:

$$\begin{aligned} H = (\delta + g)(I_{-1} + I_{+1}) + 2gI_0\sqrt{I_{-1}I_{+1}}\cos(\phi_{-1} + \phi_{+1}) \\ -g(I_{-1}I_{+1} + I_{-1}^2 + I_{+1}^2) + 2g\sum_{\pm} I_{\mp}\sqrt{I_0 I_{\pm 1}}\cos(2\phi_{\mp 1} - \phi_{\pm 1}) \ , \end{aligned} \tag{13}$$

where $\delta = J[1 - \cos(2\pi/3)]$, $I_0 = 1 - I_{-1} - I_{+1}$ and the phases $\phi_{\pm 1}$ of variables $b_{\pm 1}(t)$ are measured with respect to the phase of $b_0(t)$. The low-energy dynamics of the system (13), which is associated with the low-energy spectrum of the quantum system, implies $I_{\pm 1} \ll I_0$. Keeping in the Hamiltonian (13) only the terms linear in $I_{\pm 1}$, and using one more canonical transformation,

$$I = I_{+1} + I_{-1} \ , \quad \theta = (\phi_{+1} + \phi_{-1})/2 \ ,$$
$$M = (I_{+1} - I_{-1})/2 \ , \quad \vartheta = \phi_{+1} - \phi_{-1} \ ,$$

we end up with the effective Hamiltonian which locally describes the low-energy stability island:

$$H_{eff} = (\delta + g)I + g\sqrt{I^2 - 4M^2}\cos(2\theta) \ , \quad |M| \leq I/2 \ . \tag{14}$$

Note that H_{eff} does not include phase ϑ and, hence, the action M is a constant of motion.

The obtained Hamiltonian (14) suffices to find the low-energy spectrum of the 3-site BH model. To do this we integrate the system (14) by introducing new action, $\tilde{I} = (1/2\pi) \oint I(\theta, E)d\theta$, and resolving the latter equation with respect to the energy. We get $E = \Omega \tilde{I}$ where

$$\Omega = \sqrt{\delta^2 + 2g\delta} \ . \tag{15}$$

Finally, we quantize actions $\tilde{I}$ and M in units of the effective Planck constant $\hbar_{eff} = 1/N$. This gives equidistant set of energy levels $E_n = E_0 + \Omega n$, with $(n + 1)$ degeneracy of the nth level. It should be stressed that the equidistant spectrum is an approximation which is valid until some critical energy E_{cr}. If we go to higher energy the spectrum becomes nonlinear and the degeneracy is removed, see Fig. 1b. It is also seen in Fig. 1b that for high energies $E \approx E_0 + \Omega N/2$ the regular spectrum coexists with an irregular spectrum, which is consistent with the fact that high-energy energy shells of the classical 3-site system contain both regular and chaotic components.

6 Many-Site Bose–Hubbard Model

For $L \gg 1$ the role of chaos becomes even more important. Now majority of eigenstates of the BH model are chaotic states in the sense of Quantum Chaos [5, 15]. To clarify the meaning of 'majority of states' we discuss the density of states $\rho(E)$ of the quantum BH model for $L \gg 1$.

Let us for the moment $U = 0$. Then the spectrum is known analytically, see (4). It follows from this equation that $\rho(E)$ has the region of support $|E| \leq JN$ and is peaked around $E = 0$, see Fig. 2a.[5] As g is increased the whole distribution shifts to the right by the mean interaction energy $E_{int} = gN$ and becomes profoundly asymmetric, see panels (b) and (c) in Fig. 2. To relate the depicted distributions to the classical BH model we scale the energy E and $\rho(E)$ with respect to N and use the Weyl law. This gives

[5] Slight asymmetry of $\rho(E)$ with respect to $E = 0$ is related to the fact that L is odd. For even L (for example $L = 6$) the distribution is perfectly symmetric, i.e., $\rho(E)$ is an even function of E.

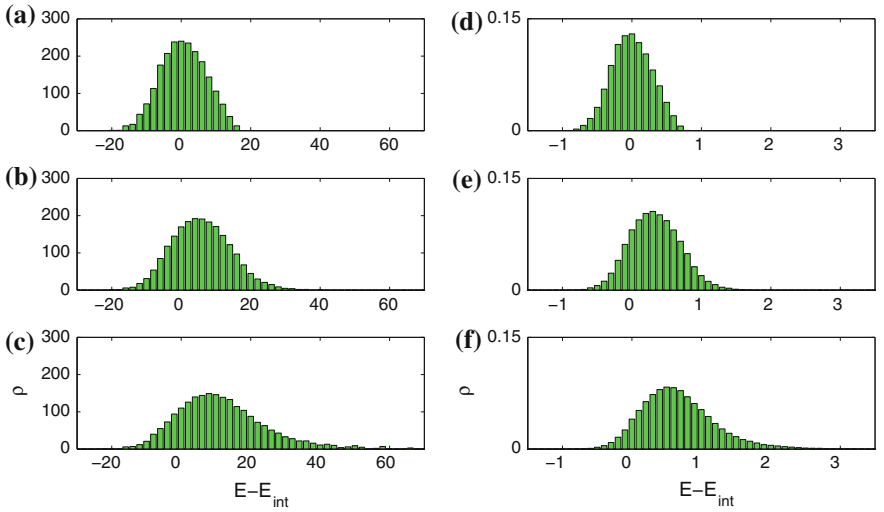

Fig. 2 Density of states of the 5-site BH model for $N = 20$, panels **a**–**c**, as compared to the classical 'density of states', panels **d**–**f**. The energy is measured with respect to the mean interaction energy $E_{int} = gN$. The macroscopic interaction constant $g = 0$, panels **a** and **d**, $g = 1$, panels **b** and **e**, $g = 2$, panels **c** and **f**. The hopping matrix element $J = 1$

$$\lim_{N\to\infty} N\frac{\rho(E/N)}{\mathscr{N}(N)} = \rho_{cl}(E)\ , \tag{16}$$

where $\mathscr{N}$ is given in (5), $\rho_{cl}(E)$ is the phase-space volume of the energy shell $H(\mathbf{a}) = E$ of the classical BH model, and we implicitly assume that $\rho_{cl}(E)$ is normalized to unity (i.e., $\int \rho_{cl}(E)\mathrm{d}E = 1$). For the considered $g = 0, 1, 2$ the classical density of states $\rho_{cl}(E)$ is shown in the panels (d–f) in Fig. 2. A nice agreement with the quantum density of states indicates that $N = 20$ is already large enough to drop the limit sign in (16). Let us also mention that for $L \gg 1$ and $g \ll J$ the function $\rho_{cl}(E)$ can be well approximated by the following simple equation,

$$\rho_{cl}(E) = B\exp\left(A\sqrt{1-\frac{E^2}{J^2}}\right)\ , \tag{17}$$

where $A = A(L)$ is the fitting parameter and B the normalization coefficient. We shall use (17) together with (16) to approximate the density of states of the quantum BH model when performing statistical analysis of its energy spectrum.

The next step is to identify the borders of chaos in Fig. 2. To answer this question we again appeal to the classical BH model. Here the critical energy or, more exactly, crossover interval can be found by using Monte-Carlo simulations. In more details, we randomly generate initial condition $\mathbf{a}(t = 0)$, evolve it in time by solving DNLSE, and determine whether the trajectory is regular or chaotic. It was found that for $L \geq 5$

and $g \sim J$ the crossover interval is close to the energy of the ground $E_0 \equiv E_{min} \approx -J + g/2$, which corresponds to the extended initial condition $a_l(t=0) \approx 1/\sqrt{L}$. For example, for $L = 5$ and $g = 1$ the crossover interval is $E_{min} + 0.05J < E < E_{min} + 0.15J$. It should be mentioned that there is another crossover interval which is close to the maximal energy $E_{max} \approx gL$, which corresponds to the localized initial condition $a_l(t=0) \approx \delta_{l,l'}$.[6] In the context of cold atoms, however, only the lower critical energy is of interest because the right tail of the density of states of the single-band BH model usually overlaps with the spectrum originating from the second band of the many-bands BH model.

7 Statistical Analysis of the Energy Spectrum

As stated in Sect. 6, all states of the quantum BH model in the central part of the distribution $\rho(E)$ are chaotic states. This can be proved by statistical analysis of the eigenfunctions and eigen-energies, where the simplest test is the distribution $P(s)$ of the normalized distances s between two nearest energy levels,

$$s = (E_{j+1} - E_j)\rho(E_j) \ . \tag{18}$$

If the states are chaotic, this distribution should obey the Wigner–Dyson statistics,

$$P(s) = \frac{\pi}{2} s \exp\left(-\frac{\pi}{4} s^2\right) \ . \tag{19}$$

The Wigner–Dyson statistics is usually opposed to the the Poisson statistics,

$$P(s) = \exp(-s) \ , \tag{20}$$

which is typical for integrable systems. We note that in the numerical analysis it is more convenient to compare not distributions themselves but the integrated distributions

$$I(s) = \int_0^s P(s')\mathrm{d}s' \ . \tag{21}$$

The solid line in the lower panel in Fig. 3 shows the integrated level-spacing distribution (21) for $L = 5$, $N = 19$, and $g = 1$, where energies are taken from the energy interval marked by the thick line in the upper panel.[7] An excellent agreement

[6] Regular localized solutions of DNLSE are known as discrete solitons or breathers [4].

[7] For the periodic boundary conditions (which are used throughout the paper) the quantum BH model possesses additional, pure quantum integral of motion – the total quasimomentum $\kappa = 2\pi k/L$. Thus the whole spectrum can be decomposed into L independent spectra labeled by κ. In Fig. 3 we choose $\kappa = 2\pi/L$ subspace. The results for other κ look similar, except the case $\kappa = 0$ where one should take into account the odd-even symmetry of the eigenstates.

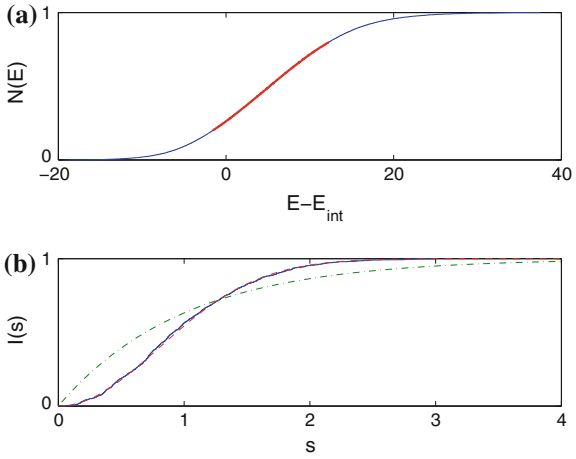

Fig. 3 Integrated density of states of the 5-site BH model for $g = 1$ and $N = 19$ (*thin blue line* in the *upper panel*), and the integrated level-spacing distribution $I(s)$ (*solid blue line* in the *lower panel*) as compared to the integrated Wigner–Dyson distribution (*dashed red line*) and the integrated Poisson distribution (*dash-dotted green line*). The hopping matrix element $J = 1$. The energies are taken from the interval marked by the *thick red line* in the *upper panel*, that comprises 60 presents of the total number of states $\mathscr{N} = 1771$

with the Wigner–Dyson distribution is noticed. Let us mention that this excellent agreement of the numerical data with (19) also indicates the relative volume of the chaotic component in the classical BH model to be close to unity in the considered energy interval. In this way the quantum and classical analysis of the BH model compliment each other. Furthermore, calculating $P(s)$ for different g and approximating the result by the Berry–Robnik distribution,[8] we can estimate the relative volumes of regular and chaotic components in the classical BH model. In particular, in the considered case $L = 5$ the distribution $P(s)$ changes from almost perfect Poisson for $g = 0.1$ to almost perfect Wigner–Dyson for $g = 0.5$. Thus a transition to the developed chaos in the classical BH model (in the considered energy interval, of course) happens at $g = 0.5$.

To conclude this section we briefly discuss the energy interval $E_0 < E < E_{cr}$, where the energy spectrum is regular. We can find this regular spectrum by generalizing the approach of Sect. 5. In fact, the effective Hamiltonian (14) describes the coupling of the mode $k = 0$ with the modes $k_1 = 1$ and $k_2 = -1$. If $L > 3$ the mode $k = 0$ is also coupled to the modes $k_1 = k$ and $k_2 = -k$. Repeating the analysis of Sect. 5 we come to the effective Hamiltonian of the form (14) where the parameter $\delta = J[1 - \cos(2\pi/3)]$ is substituted by the parameter $\delta_k = J[1 - \cos(2\pi k/L)]$. Thus the low energy spectrum of the system is given by a sum of equidistant spectra with the frequencies

[8] Berry–Robnik's statistics gives level-spacing distribution for a system with mixed phase space and interpolates between Poisson and Wigner–Dyson statistics.

$$\Omega_k = \sqrt{2g\delta_k + \delta_k^2}\ , \quad \delta_k = J[1 - \cos(2\pi k/L)]\ . \tag{22}$$

If we restrict ourselves by small $k \ll L$, the frequencies (22) are approximated by

$$\Omega_\kappa = \sqrt{2g}\kappa\ , \quad \kappa = 2\pi k/L\ , \tag{23}$$

which is nothing else as the Bogoliubov dispersion relation for elementary excitations of the Bose–Einstein condensate.

8 Conclusion

The presented results give the following picture of quantum-classical correspondence between the classical (6) and quantum (1) BH systems.

The low-energy trajectories of the classical system are regular and encircle the $2L$-dimensional invariant torus. Topologically, this multi-dimensional torus is a tensor product of $L/2$ four-dimensional tori defined by the effective Hamiltonians (14) with δ substituted by $\delta_k = J[1 - \cos(2\pi k/L)$. Quantizing these tori in terms of the effective Planck's constant $\hbar_{eff} = 1/N$ we obtain the lower-energy spectrum of the quantum system, which for $L \gg 1$ coincides with the Bogoliubov spectrum of elementary excitations above the ground state. Notice that, since we restrict ourselves to values of the macroscopic interaction constant g of the same order as the hopping matrix element J and assume $N \gg 1$, we have $U \ll J$. Thus the ground state of the system is a super-fluid state. It is an open question whether one can extend the semiclassical analysis into the region of large g, where the ground state of the system is a Mott insulator.

As we go to higher energies the invariant tori become gradually destroyed. This means that energy shells of the classical BH model contain both the regular and chaotic components and, depending on the initial condition, the classical trajectory is either regular or chaotic. With respect to the quantum BH model this is the most subtle case because the energy spectrum becomes a mixture of the regular spectrum, which is a reminiscent of the Bogoliubov spectrum, and an irregular spectrum.

With further increase of the energy the classical BH model shows a transition to the developed chaos and the spectrum of the quantum system becomes fully irregular. To avoid any misinterpretations we note that the term 'irregular' does imply the eigen-energies to be random numbers. On the contrary, there are important correlations between positions of the energy levels which are reflected, in particular, in the Wigner–Dyson distribution for distances between the nearest levels. Because the same correlations are present for eigenvalues of a random matrix, the meaning of the term 'irregular' is similarity of the spectrum with spectrum of random matrices.

In the work we focussed on the energy spectrum and did not pay much attention to the eigenfunctions. It was shown in [8] that eigenfunctions of the BH model also possess universal properties reflected, in particular, in the Breit–Wigner distribu-

tion for the local density of states. This has important consequences for transport phenomena with cold atoms. For example, if we address Bloch oscillations[9] of interacting Bose atoms, we find that they irreversibly decay [3, 10]. Remarkably, this quantum dynamics is perfectly reproduced by solving classical (9) on the truncated Husimi function [9]. This result provides one more example of successful treating of a many-body system by means of classical mechanics.

References

1. Albiez, M., Gati, R., Fölling, J., Hunsmann, S., Cristiani, M., Oberthaler, M.K.: Direct observation of tunneling and nonlinear self-trapping in a single bosonic Josephson junction. Phys. Rev. Lett. **95**(1), 010,402 (2005)
2. Bastidas, V.M., Engelhardt, G., Perez-Fernandez, P., Vogl, M., Brandes, T.: Critical quasienergy states in driven many-body systems. Phys. Rev. A **90**, 063628 (2014)
3. Buchleitner, A., Kolovsky, A.R.: Interaction-induced decoherence of atomic Bloch oscillations. Phys. Rev. Lett. **91**, 253,002 (2003)
4. Campbell, D.K., Flach, S., Kivshar, Y.S.: Localizing energy through nonlinearity and discreteness. Phys. Today **57**(1), 43–49 (2004)
5. Giannoni, M.-J., Voros, A., Zinn-Justin, J.: Chaos and Quantum Physics. North-Holland, Amsterdam (1991)
6. Jaksch, D., Zoller, P.: The cold atom Hubbard toolbox. Annals of Phys. **315**, 52 (2005)
7. Jaksch, D., Bruder, C., Cirac, J., Gardiner, C., Zoller, P.: Cold bosonic atoms in optical lattices. Phys. Rev. Lett. **81**, 3108 (1998)
8. Kolovsky, A.R.: Conductivity with cold atoms in optical lattices. J. of Stat. Mech.: Theory and Exp. **2009**, P02,018 (2009)
9. Kolovsky, A.R., Korsch, H.J., Graefe, E.M.: Bloch oscillations of Bose-Einstein condensates: Quantum counterpart of dynamical instability. Phys. Rev. A **80**, 023,617 (2009)
10. Meinert, F., Mark, M.J., Kirilov, E., Lauber, K., Weinmann, P., Gröbner, M., Nägerl, H.C.: Interaction-induced quantum phase revivals and evidence for the transition to the quantum chaotic regime in 1d atomic Bloch oscillations. Phys.Rev. Lett. **112**, 193,003 (2014)
11. Perelomov, A.M.: Generalized Coherent States and their Applications. Springer, Berlin Heidelberg New York London Paris Tokyo (1986)
12. Polkovnikov, A.: Phase space representation of quantum dynamics. Annals of Phys. **325**, 1790 (2010)
13. Sinatra, A., Lobo, C., Castin, Y.: The truncated Wigner method for Bose-condensed gases: Limits of validity and applications. J. of Phys. B: At. Mol. Opt. Phys. **35**, 3599 (2002)
14. Steel, M.J., Olsen, M.K., Plimak, L.I., Drummond, P.D., Tan, S.M., Collett, M.J., Walls, D.F., Graham, R.: Dynamical quantum noise in trapped Bose-Einstein condensates. Phys. Rev. A **58**, 4824 (1998)
15. Stöckmann, H.J.: Quantum Chaos. Cambridge University Press, Cambridge (1999)
16. Trimborn, F., Witthaut, D., Korsch, H.J.: Exact number conserving phase-space dynamics of the M-site Bose–Hubbard model. Phys. Rev. A **77**, 043,631 (2008)

[9]Bloch oscillations are dynamical response of the system to an external static field. For non-interacting atoms these would be periodic oscillation of the mean atomic momentum with the Bloch frequency which is proportional to the field strength.

Mean-Field Transport of a Bose-Einstein Condensate

Samy Mailoud Sekkouri and Sandro Wimberger

Abstract The expansion of an initially confined Bose-Einstein condensate into either free space or a tilted optical lattice is investigated in a mean-field approach. The effect of the interactions is to enhance or suppress the transport depending on the sign and strength of the interactions. These effects are discusses in detail in view of recent experiments probing non-equilibrium transport of ultracold quantum gases.

1 Introduction

Since the first realization of Bose-Einstein condensates in 1995 with ultracold alkali atoms [1], experiments with ultracold quantum gases have launched a vast research field for investigating the quantum nature of matter with an unprecedented experimental precision [2, 3]. One of the directions investigated today is concerned with the quantum transport of ultracold matter. Pioneering here are the recent experimental results by the two groups at ETH [4] and at NIST [5]. Many transport scenarios of ultracold bosons and fermions were studied starting from a microscopic (many-body) description [6, 7]. In a more general setting, mean-field quantum transport of a Bose-Einstein condensate was investigated in the context of Bloch oscillations and tunneling in Wannier-Stark systems [8, 9], of barrier tunneling [10], of disorder, [11], or of time-dependent potentials [12]. In almost all of the experimental realizations, so far, what has been studied was essentially the expansion of a cloud of cold atoms which is controlled by external fields and interactions. Along the same lines, we propose in this contribution a relatively simple method to prepare the initial state, namely within an steep harmonic trap. Transport occurs when the trap is opened

S. Mailoud Sekkouri · S. Wimberger (✉)
DiFeST, Università degli Studi di Parma, Via G. P. Usberti 7/a, 43124 Parma, Italy
e-mail: sandro.wimberger@fis.unipr.it

S. Mailoud Sekkouri
e-mail: samy.mailoudsekkouri@studenti.unipr.it

S. Wimberger
Gruppo Collegato di Parma, INFN, Sezione di Milano Bicocca, 43124 Parma, Italy

G. Mantica et al. (eds.), *Emergent Complexity from Nonlinearity, in Physics, Engineering and the Life Sciences*, Springer Proceedings in Physics 191,
DOI 10.1007/978-3-319-47810-4_5

in one direction. We investigate in detail how the particle current in such a setup depends on the interactions, which we treat in mean-field approximation following the celebrated Gross-Pitaevskii equation [13, 14].

2 Our Transport Setup

The dynamics of a Bose-Einstein condensate in mean-field approximation is described by the Hamiltonian

$$H = \frac{p^2}{2m} + V_{\text{int}}(r,t) + V_{\text{ext}}(r,t)\,. \tag{1}$$

The interatomic potential of a cold dilute gas of bosons is replaced by the effective mean-field interaction

$$V_{\text{int}}(r,t) = g_{3D}|\psi(r,t)|^2\,, \tag{2}$$

where the coupling constant $g_{3D} = \frac{4\pi\hbar a_s}{M}N$ is determined by the number of atoms N, their mass M, and the two-body s-wave scattering length a_s. The wave function is then normalized to unity. Please note that the strength and the sign of a_s can be controlled quite well in the experiment [2, 14]. We restrict here to a quasi one-dimensional situation, in which the condensate is well confined in the two transverse directions. Such a reduction essentially leads to a rescaling of the coupling constant. This rescaling depends on the precise geometry of the trapping potentials. A standard argument [2] reduces g_{3D} to its one-dimensional version $g_{1D} = 2\hbar\omega_\perp a_s$, where the transverse confinement frequency $\omega_\perp$ is assumed to be large compared to the longitudinal one.

To simplify the problem, we express all quantities in the units of the longitudinal harmonic oscillator confinement with frequency ω at $t = 0$. This means that we express $p \to \tilde{p} \equiv p(\hbar\omega m)^{-\frac{1}{2}}$ and $x \to \tilde{x} \equiv x\left(\frac{\omega m}{\hbar}\right)^{\frac{1}{2}}$. In this units, the Hamiltonian for $t = 0$ now reads

$$\tilde{H}(\tilde{x},\tilde{p};t=0) \;=\; \frac{1}{2}\tilde{p}^2 \;+\; \tilde{g}_{1D}|\tilde{\psi}(\tilde{x},\tilde{t})|^2 \;+\; \frac{1}{2}(\tilde{x}-\tilde{x}_0)^2\,, \tag{3}$$

and for $t > 0$ correspondingly

$$\tilde{H}(\tilde{x},\tilde{p};t>0) \;=\; \frac{1}{2}\tilde{p}^2 \;+\; \tilde{g}_{1D}|\tilde{\psi}(\tilde{x},\tilde{t})|^2 + \frac{1}{2}\Theta(\tilde{x}_0-\tilde{x})(\tilde{x}-\tilde{x}_0)^2 \tag{4}$$

$$-\;\Theta(\tilde{x}-\tilde{x}_0)\left[\tilde{F}\tilde{x} + \tilde{A}\sin^2(\tilde{K}(\tilde{x}-\tilde{x_0}))\right]. \tag{5}$$

The initially prepared state and the potentials are sketched in Fig. 1. The sinusoidal term in (4) describes an optical lattice into which the condensate can expand. $\tilde{A}$ is the amplitude of the lattice and $\tilde{K} = \pi/\tilde{d}_{\text{L}}$ determines its spatial period $\tilde{d}_{\text{L}}$. The linear

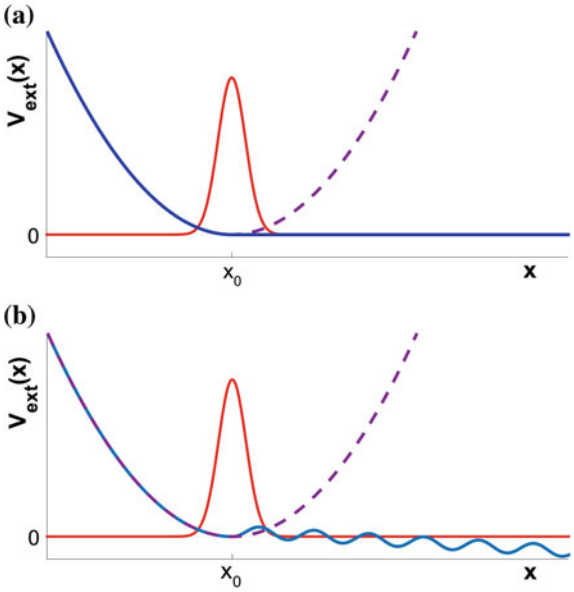

Fig. 1 Sketch of the experiments we are proposing. The initial state (*red solid lines*) is prepared within an harmonic trap (*blue lines* for $x < x_0$ and *viola dashed lines* for $x > x_0$). The trap is released on the right part of x_0 to zero, which makes the initial wavepacket move towards the right. We investigate two exemplary cases: without any external potential seen in **a** and with a tilted periodic lattice seen in **b**. The total external potential at $t > 0$ is plotted by the overall *blue lines* in both cases

potential with force $\tilde{F}$ controls the tilt of the lattice. In the next section we study the temporal evolution in the sketched setups, in particular the dependence of the atomic currents (towards the right) on the interaction strength $\tilde{g}_{1D}$. In the following we drop the tildes for simplicity, with the additional convention $g \equiv \tilde{g}_{1D}$.

3 Numerical Results

Our main observable for the study of the mean-field transport of the condensate is the following probability current density

$$j(x,t) = \frac{1}{2i}\left[\psi^*(x,t)\frac{\partial\psi(x,t)}{\partial x} - \psi(x,t)\frac{\partial\psi^*(x,t)}{\partial x}\right]. \tag{6}$$

The current will obviously depend on the precise nature of the interaction (attractive or repulsive) and its strength. We integrate the nonlinear Schrödinger equation determined by (4), using a finite difference spatial representation of the wave function

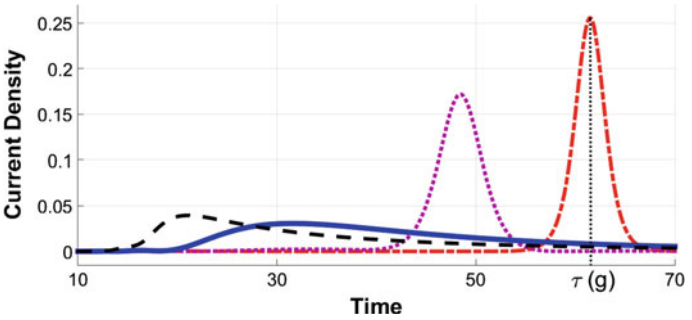

Fig. 2 The particle current as a function of time at $x = 2x_0$ for the following values of interaction strength from left to right: $g = 2$ (*black dashed line*), $g = 0$ (*blue solid line*), $g = -1$ (*viola dotted line*), and $g = -2$ (*red dot-dashed curve*). We observe clear maxima of the currents, whose position on the time axis (denoted by τ) is determined by the sign and the strength of the nonlinearity. The lattice parameters are $A = 1$, $d_{\mathrm{L}} = 4$ and $F = 0.043$

and a norm-preserving Crank-Nicholson integrator, see e.g. [15] for details on the integration scheme. For a grid-step size of Δx, the time-dependent current at the grid point x_n is given by

$$j(x_n, t) = \frac{i}{2\Delta x}[\psi^*(x_n + \Delta x, t)\psi(x_n, t) - \psi^*(x_n, t)\psi(x_n + \Delta x, t)]\,. \quad (7)$$

3.1 Case (a): Directed Free Expansion

For the case of the free expansion towards the right (case (a) in Fig. 1), we first plot the current density as a function of the interaction strength g at the point $x = 2x_0$, with $x_0 = 20.5$, please see Fig. 2. At this fixed position, the probability current as a function of time shows a characteristic maximum, whose position on the time axis is determined by g.

For repulsive interactions ($g > 0$), the wave packet tends to expand faster due to the additional repulsive potential term in (3). For the attractive case ($g < 0$), the opposite happens and the wave packet tends to stabilize and the expansion is slowed down. Figure 3 shows the same results for a window of positions from $x = x_0$ to $x \approx 60$ (above which the wave function is absorbed in order to avoid artificial back reflections). Interestingly, but not too surprisingly, the dispersion in the spatial-temporal plane (x, t) is minimized by strong attractive interactions. Here the current maximum is very stable and the dynamics of the condensate is almost free of dispersion similar to a solitonic motion, see Fig. 3(d).

In order to quantify the effect of the nonlinearity g, we plot the dependence of the times τ when the maximum density is reached at $x = 2x_0$ in Fig. 4. While the qualitative behavior of the enhanced expansion and the slowdown for positive and

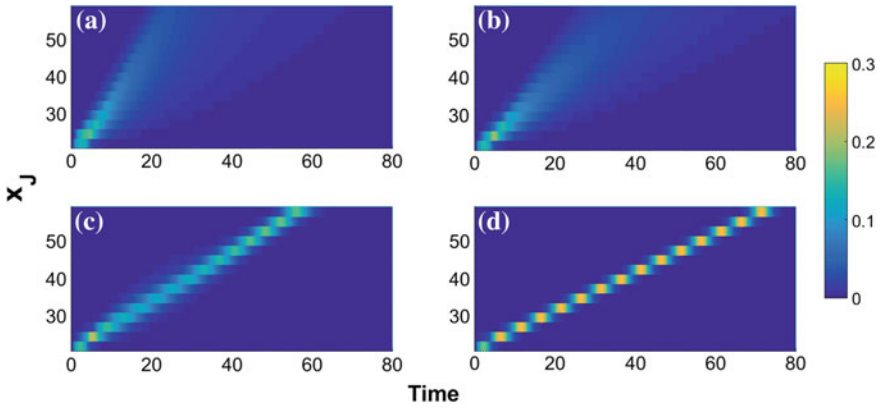

Fig. 3 Heat map of the current density $j(x,t)$ as in Fig. 1 but for a window of positions $x = x_J$. The two-dimensional plots show that repulsive interactions enhance the transport, see panel **a** for $g = 2$, while attractive interactions slow it down, see panel **c** for $g = -1$ and **d** for $g = -2$. **b** is the reference case without interactions. As an interesting side effect, the dispersion in the spatial-temporal plane (x,t) is minimized by strong attractive interactions, see panel **d**, corresponding to the *dot-dashed line* in the previous figure

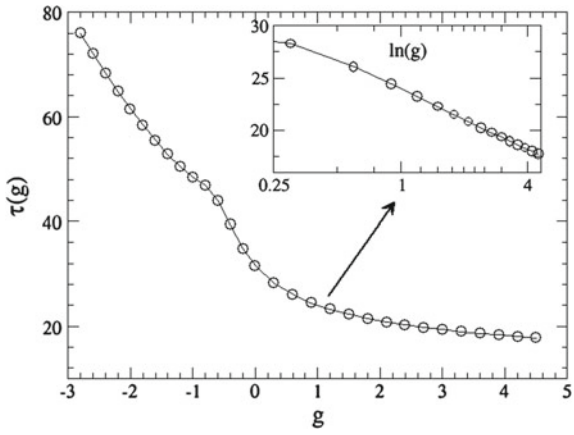

Fig. 4 The times $\tau(g)$ of maximal current at position $x = 2x_0$ extracted from data sets such as shown in Fig. 2 and for the same lattice parameters as there. For positive nonlinearities g, the scaling of the enhancement of the expansion seems logarithmic (see *inset*). For negative g, the expansion is slowed down a lot, which can be seen by the steep increase of the curve for decreasing $g < 0$

negative g, respectively, is clear (see also [16]), we have no analytic explanation so far for the precise form of the observed scaling of $\tau(g)$ seen in Fig. 4.

3.2 *Case (b): Expansion into a Wannier-Stark Lattice*

Optical lattices are by now a standard tool for the control of the motion of Bose-Einstein condensates [3]. The presence of an optical lattice slows down the expansion into it, while a constant negative tilt accelerates an initially localized wave packet

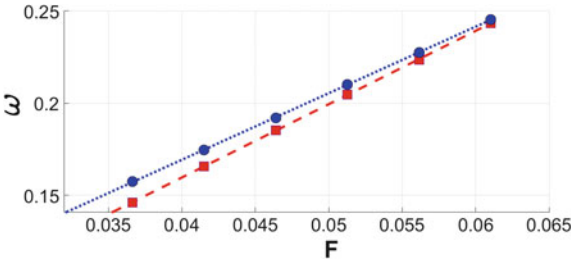

Fig. 5 Oscillation frequency ω at $g = 0$ versus. the Stark force F for the case with left confinement (*blue symbols* connected by *dotted line*) and without it (*red symbols* connected by *dashed line*). In both cases, the scaling is linear as expected. The presence of the left part of the harmonic trap affects only the slope. The lattice parameters are $A = 1$ and $d_L = 4$

towards the right. However, when both potential are present simultaneously, c.f. our setup shown in Fig. 1(b), the situation is less clear. A tilted lattice problem defines the Wannier-Stark system, which was investigated with Bose condensates in great detail before, see e.g. [8, 9]. In this system, again an initially localized wave packet remains localized but it oscillates with a characteristic Bloch frequency ω_B given by the constant level distance of the energy spectrum (arising from the constant spatial tilt). In our units, $\omega_B = F d_L$, where d_L is the lattice spacing. This linear scaling of the oscillation frequency with the Stark force F is seen also in our expansion problem in the absence of interactions ($g = 0$). Because of the presence of the harmonic confinement on the left, the proportionality factor is slightly lower than one, as seen in Fig. 5 (blue symbols connected by the dotted line). Releasing also the left part of the trap, we instead observe the correct pre factor one, please see the red symbols in Fig. 5. The frequencies are extracted from the current oscillations to the right of (but close to) x_0 after a short initial transient, necessary for the wave packet to adapt to the presence of the tilted lattice.

More interesting is the oscillatory behavior in the presence of interactions. We investigate again both cases of repulsive and attractive nonlinearity. The frequencies are extracted as described above from the current oscillations. Our results are shown in Fig. 6. A repulsive interaction with $g > 0$ increases the oscillation frequency. For not too large positive g, this increase is linear, and we will come up with an intuitive explanation below. For large nonlinearities a saturation is observed, see $g > 1$ in Fig. 6. Here the repulsion leads to a fast expansion which in turn decreases the density again. More complex is the case of attractive interactions with $g < 0$. For small $|g| < 1$, the Bloch-like oscillations are rather stable. For large $|g| > 1$, again the nonlinearity potential dominates the dynamics, in the sense that the nonlinear term is larger than the kinetic term in (4). Here interaction-induced oscillations with a frequency $\omega \propto |g|$ occur. In this latter case, the density remains large during the evolution because of the attractive forces, and the theory developed by Kolovsky in [17] applies. There our observed linear scaling of the oscillation frequency with the nonlinear coupling parameter is theoretically predicted.

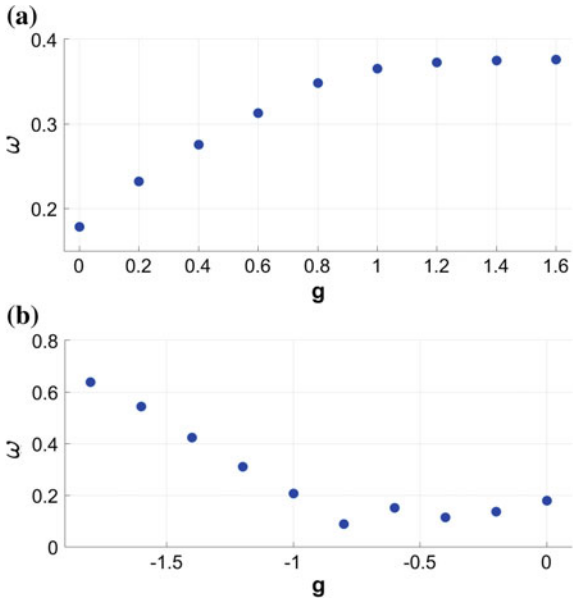

Fig. 6 Bloch-like oscillation frequency ω as a function of the nonlinear coupling constant g. While an attractive interaction ($g < 0$, see **a**) slows down the oscillations in the region $-0.8 < g < 0$, a repulsive one, see **b**, increases the frequency. For large negative $g < -1$, the nonlinear potential dominates the dynamics and interaction-induced oscillations with a frequency $\omega \propto |g|$ occur. The lattice parameters are the same as in the previous figure

In the following we concentrate on the case of repulsive interactions. Here we can explain the initial linear increase in the oscillation frequency seen Fig. 6(b) by the local level shift induced by the nonlinear potential term in (4). This shift depends on the densities in the lattice sites which is largest in the "central" well centered at x_0 (at least at and close to $t = 0$). This shift then leads to an effective increase of the difference ΔE of the two energy levels in the neighboring wells, and consequently to a larger oscillation frequency. We may estimate

$$\Delta E \approx g \int_{d_L} dx |\psi(x,t)|^2 . \tag{8}$$

Because of the oscillations, we take the times t of maximal density differences in the two wells for computing the above estimate. In principle, we can redo the effect of the nonlinear potential by rescaling the Stark force from F to $F - F'$, where $F' \approx \Delta E / d_L$. This reduces the problem to the noninteracting one with the same Block-like oscillation frequency determined just by F alone. Corresponding numerical simulation for the current density are shown in Figs. 7 and 8. The former plot nicely corroborates the effective compensation of the nonlinear potential in the temporal oscillations of the current. The latter figure highlights the good compensation comparing the currents globally in the spatial-temporal plane $(x > x_0, t)$.

Of course, our estimate given in (8) is a bit too rough in order to be perfect for all times (in particular because of the time-dependence of the process). Yet, this possibility of controlling the dynamics of a Bose-Einstein condensate is quite interesting. We refer to similar situations where the effect of the interaction was

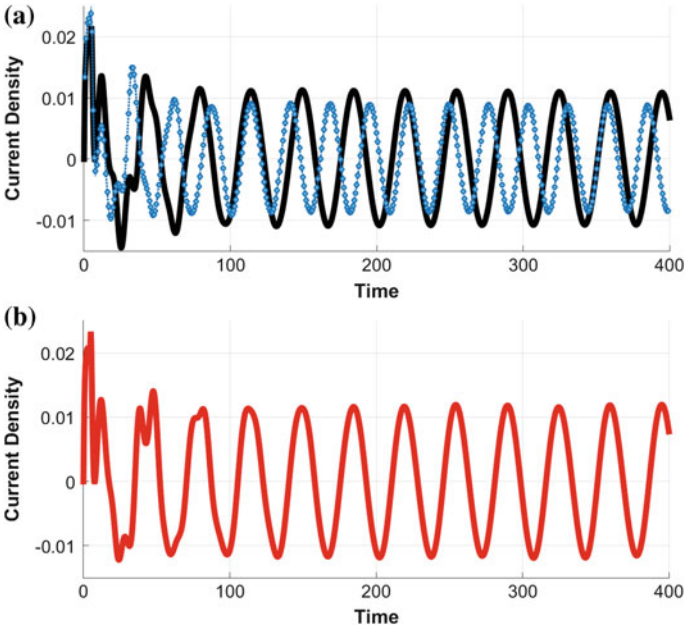

Fig. 7 Temporal evolution of the current to the right but close to x_0 for the three cases: **a** $g = 0$, $F = 0.043$ (*black solid line*), $g = 0.2$, $F = 0.043$ (*blue symbols*), and **b** $g = 0.2$, $F = 0.043 - F' = 0.029$ (*red solid line*). In **b** the nonlinear shift of the local energy level (where the atomic density is large) is corrected by a reduction of the Stark force with $F' = 0.029$. We observe good agreement between the oscillation frequencies of the *black* (**a**) and the *red* (**b**) curves. The lattice parameters are chosen as in the previous two figures

approximately cancelled by applying appropriate external potentials in theory [18] and an actual experiment at Innsbruck [19].

4 Conclusions and Perspectives

We propose a rather simple experiment to probe the effect of interparticle interactions in the non-equilibrium dynamics of a Bose-Einstein condensate. We have seen that the time-dependent atomic current towards the right can be well controlled in our setup. Interactions enhance or suppress the transport or the oscillations depending on their sign and their strength.

Preliminary computations on a full three dimensional evolution with strong confinement in the transverse dimensions seem to confirm our one-dimensional results (provided that the geometry of the confinement is matched such as to guarantee the same effective nonlinearity along the longitudinal direction). Interesting would be the case of an effective two-dimensional problem under so-called pancake confine-

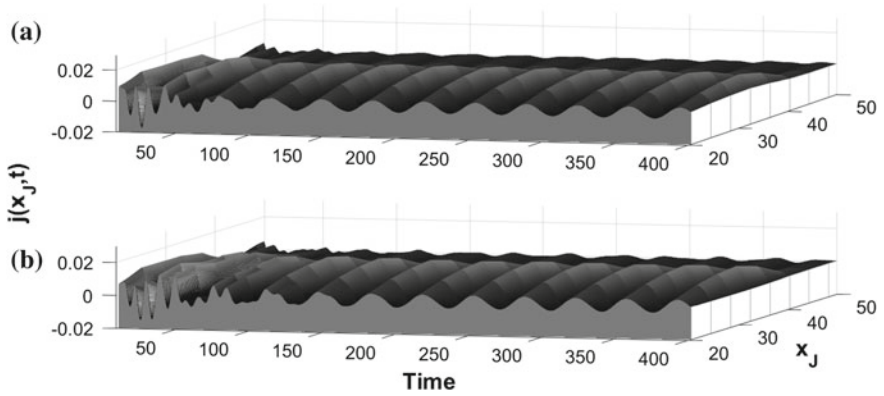

Fig. 8 Temporal evolution of the current as a function of position $x = x_J$ and time t. Shown are in panel **a** the data for the some parameters as in Fig. 7a at $g = 0$, and in panel **b** as in Fig. 7b. As noted previously the two cases are very similar due to the compensation of the effect of the nonlinearity in **b**

ment as recently studied in the context of mean-field transport in Kaiserslautern [20]. Here both directions are equally important and the expansion and transport of the condensate may be controlled even along both dimensions simultaneously.

Acknowledgements We are very grateful for support by the FIL 2014 program of Parma University. Moreover, SW thanks the organizers of the NDES 2015 conference for their kind invitation and the wonderful meeting at Como.

References

1. Cornell, E.A., Wieman, C.E.: Rev. Mod. Phys. **74**, 875 (2002); Ketterle, W.: Rev. Mod. Phys. **74**, 1131 (2002)
2. Lewenstein, M., Sanpera, A., Ahufinger, V., Damski, B., Sen(De), A., Sen, U.: Adv. Phys. **56**, 243 (2007); Bloch, I., Dalibard, J., Zwerger, W.: Rev. Mod. Phys. **80**, 885 (2008)
3. Grimm, R., Weidemüller, M., Ovchinnikov, Y.B.: Adv. At. Mol. Opt. Phys. **42**, 95 (2000); Morsch, O., Oberthaler, M.: Rev. Mod. Phys. **78**, 179 (2006)
4. Brantut, J.- P., Meineke, J., Stadler, D., Krinner, S., Esslinger, T.: Sci. **337**, 1069 (2012); Krinner, S., Stadler, D., Husmann, D., Brantut, J.- P., Esslinger, T.: Nat. **517**, 64 (2015); Husmann, D., Uchino, S., Krinner, S., Lebrat, M., Giamarchi, T., Esslinger, T., Brantut, J.- P.: Sci. **350**, 1498 (2015)
5. Eckel, S., Lee, J.G., Jendrzejewski, F., Murray, N., Clark, C.W., Lobb, C.J., Phillips, W.D., Edwards, M., Campbell, G.K.: Nat. **506**, 200 (2014)
6. Gutman, D.B., Gefen, Y., Mirlin, A.D.: Phys. Rev. B **85**, 125102 (2012); Bruderer, M., Belzig, W., Phys. Rev. A **85**, 013623 (2012); Nietner, C., Schaller, G., Brandes, T.: Phys. Rev. A **89**, 013605 (2014); Marcos, F.G., Platero, G., Nietner, C., Schaller, G., Brandes, T.: Phys. Rev. A **94**, 023622 (2016); Papoular, D.J., Pitaevskii, L.P., Stringari, S., Quantized conductance with bosonic atoms, preprint arXiv:1510.02618
7. Ivanov, A., Kordas, G., Komnik, A., Wimberger, S.: Eur. Phys. J. B **86**, 345 (2013)

8. Morsch, O., Müller, J.H., Cristiani, M., Ciampini, D., Arimondo, E.: Phys. Rev. Lett. **87**, 140402 (2001); Roati, G., de Mirandes, E., Ferlaino, F., Ott, H., Modugno, G., Inguscio, M.: Phys. Rev. Lett. **92**, 230402 (2004); Ferrari, G., Poli, N., Sorrentino, F., Tino, G. M.: Phys. Rev. Lett. **97**, 060402 (2006); Sias, C., Zenesini, A., Lignier, H., Wimberger, S., Ciampini, D., Morsch, O., Arimondo, E.: Phys. Rev. Lett. **98**, 120403 (2007); Gustavsson, M., Haller, E., Mark, M.J., Danzl, J.G., Rojas-Kopeinig, G., Nägerl, H.-C.: Phys. Rev. Lett. **100**, 080404 (2008); Zenesini, A., Sias, C., Lignier, H., Singh, Y., Ciampini, D., Morsch, O., Mannella, R., Arimondo, E., Tomadin, A., Wimberger, S.: New J. Phys. **10**, 053038 (2008); Zenesini, A., Lignier, H., Tayebirad, G., Radogostowicz, J., Ciampini, D., Mannella, R., Wimberger, S., Morsch, O., Arimondo, E.: Phys. Rev. Lett. **103**, 090403 (2009); Haller, E., Hart, R., Mark, M.J., Danzl, J.G., Reichsöllner, L., Nägerl, H.-C.: Phys. Rev. Lett. **104**, 200403 (2010)
9. Wimberger, S., Mannella, R., Morsch, O., Arimondo, E., Kolovsky, A.R., Buchleitner, A.: Phys. Rev. A **72**, 063610 (2005); Witthaut, D., Graefe, E.M., Wimberger, S., Korsch, H.J.: Phys. Rev. A **75**, 013617 (2007); Rapedius, K., Elsen, C., Witthaut, D., Wimberger, S., Korsch, H.J.: Phys. Rev. A **82**, 063601 (2010)
10. Paul, T., Richter, K., Schlagheck, P.: Phys. Rev. Lett. **94**, 020404 (2005); Gattobigio, G.L., Couvert, A., Reinaudi, G., Georgeot, B., Guéry-Odelin, D.: Phys. Rev. Lett. **109**, 030403 (2012)
11. Lucioni, E., Deissler, B., Tanzi, L., Roati, G., Zaccanti, M., Modugno, M., Larcher, M., Dalfovo, F., Inguscio, M., Modugno, G.: Phys. Rev. Lett. **106**, 230403 (2011)
12. Lignier, H., Sias, C., Ciampini, D., Singh, Y., Zenesini, A., Morsch, O., Arimondo, E.: Phys. Rev. Lett. **99**, 220403 (2007); Arimondo, E., Ciampinia, D., Eckardt, A., Holthaus, M., Morsch, O.: Adv. AMOP **61**, 515 (2012); Salger, T., Kling, S., Denisov, S., Ponomarev, A.V., Hänggi, P., Weitz, M.: Phys. Rev. Lett. **110**, 135302 (2013)
13. Leggett, A.J.: Rev. Mod. Phys. **73**, 307 (2001)
14. Pethick, C.J., Smith, H.: Bose-Einstein Condensation in Dilute Gases. Cambridge University Press, Cambridge (2002); Pitaevskii, L., Stringari, S.: Bose-Einstein Condensation. Oxford University Press, Oxford (2003)
15. Cerboneschi, E., Mannella, R., Arimondo, E., Salasnich, L.: Phys. Lett. A **249**, 495 (1998); Wimberger, S., Mannella, R., Morsch, O., Arimondo, E.: Phys. Rev. Lett. **94**, 130404 (2005)
16. Holland, M.J., Cooper, J.: Phys. Rev. A **53**, R1954 (1996); Holland, M.J., Jin, D.S., Chiofalo, M.L., Cooper, J.: Phys. Rev. Lett. **78**, 3801 (1997); Adhikari. S.K.: J. Phys. B At. Mol. Opt. Phys. **36**, 3951 (2003)
17. Kolovsky, A.R.: Phys. Rev. Lett. **90**, 213002 (2003)
18. Micciché, S., Buchleitner, A., Lillo, F., Mantegna, R., Paul, T., Wimberger, S.: New J. Phys. **15**, 033033 (2013)
19. Gustavsson, M., Haller, E., Mark, M.J., Danzl, J.G., Hart, R., Daley, A.J., Nägerl, H.-C.: New J. Phys. **12**, 065029 (2010)
20. Labouvie, R., Santra, B., Heun, S., Wimberger, S., Ott, H.: Phys. Rev. Lett. **115**, 050601 (2015)

Part II
Chaotic Oscillations

Continuous and Differentiable Approximation of a TaO Memristor Model for Robust Numerical Simulations

Alon Ascoli, Ronald Tetzlaff and Leon Chua

Abstract This paper proposes the introduction of appropriate continuous and differentiable approximations to discontinuous and piecewise differentiable functions respectively adopted in state equation and Ohm's based law of the mathematical model of an extended memristor recently fabricated at Hewlett Packard labs. The study of this model is particularly timely because the material at the basis of the relative memristor device, i.e. Tantalum oxide, has been recently classified, together with Hafnium oxide, as one of the most plausible candidates for a large-scale manufacturing of memory resistive devices, especially for memory applications. However, recent studies have demonstrated that the adoption of discontinuous and/or piecewise differentiable functions in the differential algebraic equation set describing the complex dynamics of these devices may be the source of serious convergence issues in standard software packages. This calls for an impeding necessity to ameliorate mathematical descriptions of real memristors. In this paper we present a thorough study which aims at deriving the most appropriate set of continuous and differentiable approximants to the discontinuous and piecewise differentiable functions of the TaO memristor model.

A. Ascoli (✉) · R. Tetzlaff
Institut für Grundlagen der Elektrotechnik und Elektronik, Technische Universität Dresden, Dresden, Germany
e-mail: alon.ascoli@tu-dresden.de

R. Tetzlaff
e-mail: ronald.tetzlaff@tu-dresden.de

L. Chua
Department of Electrical Engineering and Computer Sciences, University of California Berkeley, Berkeley, CA, USA
e-mail: chua@eecs.berkeley.edu

G. Mantica et al. (eds.), *Emergent Complexity from Nonlinearity, in Physics, Engineering and the Life Sciences*, Springer Proceedings in Physics 191,
DOI 10.1007/978-3-319-47810-4_6

1 Introduction

The introduction of memristors [1] into the realm of electrical circuit elements is promising to revolutionize the world of electronics in the years to come. Several challenges have to be yet overcome before a large-scale deployment of this nonlinear dynamical device in the integrated circuit market, but some companies [2] have already engineered memristor-based circuits and systems which either outperform or complement the functionalities of state-of-the-art hardware solutions. The performance of the device is usually evaluated by taking into account a number of factors. For example, in memory applications [3] the most important quality measure are nonlinearity, off-to-on resistance ratio, endurance, retention, and sensitivity to process/voltage supply/temperature fluctuations. Recently, materials have been ranked in terms of the scores memristors based upon them attain for each of these attributes. Tantalum oxide (TaO) is one of the first materials in the table [4]. It is therefore worth to analyse the corresponding memristors, aiming at understanding the nonlinear dynamics [5] emerging in these nanoscale structures [6]. Recently a TaO memristor was manufactured and modeled at Hewlett Packard labs [7]. According to the latest classification [8], this nano device belongs to the class of extended memristors [9]. The mathematical description descends directly from physics laws, and is very accurate. Therefore it may be taken as reference for simulations on circuits and systems containing these memristors. However, discontinuous and piecewise differentiable functions respectively appear in state equation and Ohm's based law of the model. It was recently revealed that serious convergence issues may arise in software packages for the numerical integration of differential algebraic equations (DAE) [10] in case the model contains discontinuous and/or piecewise differentiable functions. It is therefore opportune to look for a proper continuous and differentiable approximation to the original mathematical description of the TaO memristor. This paper first introduces classes of possible continuous and differentiable kernels for the replacement of the discontinuous and piecewise differentiable functions present in the original model, and then carries out a detailed investigation aimed at selecting the most appropriate approximations. The resulting continuous and differentiable DAE set accurately captures the dynamics of the original model, and does not suffer from convergence issues, even in circuits employing a large number of memristors. This study complements recent research developments on numerical techniques for simulations on memristor devices, circuits, and systems [11].

2 Model

In 2013 Hewlett Packard announced the manufacturing of a novel memristor nano device based upon TaO [7]. The corresponding mathematical model, revealing the high degree of nonlinearity inherent into the two-terminal element, is the combination of a differential equation governing the evolution of the state $x \in [0, 1]$, namely

Table 1 TaO memristor model parameter values

$A\,/s^{-1}$	$\sigma_{off}\,/V$	x_{off}	$\beta\,/A^{-1}V^{-1}$
10^{-10}	$1.3 \cdot 10^{-2}$	$4 \cdot 10^{-1}$	500
$B\,/s^{-1}$	σ_{on}		x_{on}
$1 \cdot 10^{-4}$	$4.5 \cdot 10^{-1}$		$6 \cdot 10^{-2}$
$\sigma_p\,/A^{-1}V^{-1}$	$G_m\,/S$	$a\,/S$	$b\,/V^{-\frac{1}{2}}$
$4 \cdot 10^{-5}$	$2.5 \cdot 10^{-2}$	$7.2 \cdot 10^{-6}$	4.7

$$\frac{dx}{dt} = f(x, v_m) = \left[A \sinh\left(\frac{v_m}{\sigma_{off}}\right) \exp\left(-\frac{x_{off}^2}{x^2}\right) \exp\left(\frac{1}{1+\beta_m i_m v_m}\right) \right. \\ \left. \text{step}(-v_m) \right] + \left[B \sinh\left(\frac{v_m}{\sigma_{on}}\right) \exp\left(-\frac{x^2}{x_{on}^2}\right) \exp\left(\frac{i_m v_m}{\sigma_p}\right) \text{step}(v_m) \right], \quad (1)$$

where $\text{step}(\cdot) = \frac{1+sign(\cdot)}{2}$ is the unit step function, and of an algebraic constraint relating current i_m through the device to voltage v_m across it, i.e.

$$i_m = W(x, v_m) v_m. \quad (2)$$

Here $W(x, v_m)$ denotes the memductance function, expressed by

$$W(x, v_m) = G_m x + a \exp\left(b\sqrt{|v_m|}\right)(1 - x), \quad (3)$$

where $|\cdot|$ denotes the modulus function. The memristor may be classified as a first-order voltage-controlled extended memristor according to the latest classification [12]. The model parameters, reported in Table 1, shall be used throughout the analysis presented in this paper.

3 Continuous and Differentiable DAE Set

The convergence properties of standard software packages for numerical integration of DAE sets may be negatively affected by the presence of discontinuity and/or piecewise differentiability in the models [10]. The mathematical description for the TaO memristor, provided in Sect. 2, adopts the modulus function in the expression for the memductance, given in (3), and the step function in the definition of the state equation, reported in (1). We propose to replace the modulus function with a differentiable approximating kernel falling within the following class:

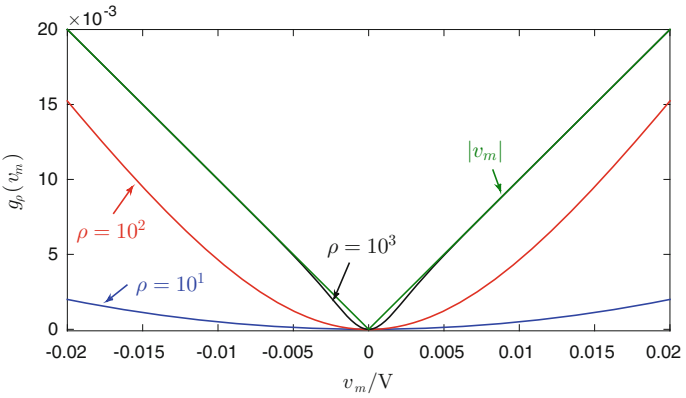

Fig. 1 Plots of $g_\rho(v_m)$ versus v_m for $\rho \in \{10^1, 10^2, 10^3\}$. The piecewise differentiable function, the proposed kernels are approximating functions of, is also shown

$$g_\rho(\cdot) = (\cdot)\left(\frac{1}{1+\exp(-\rho\,\cdot)} - \frac{1}{1+\exp(\rho\,\cdot)}\right), \tag{4}$$

where $\rho \in \mathbb{R}_+$ defines the concavity of $g_\rho(\cdot)$ in the origin. Illustrative plots of the approximating kernels for $\rho \in \{10^1, 10^2, 10^3\}$ and of the original piecewise differentiable modulus function are shown in Fig. 1 as a function of the memristor voltage.

The selection of the most appropriate differentiable kernel from the class proposed in (4) is based upon the capability of the resulting memductance function approximation to track with satisfactory accuracy the static behaviour of the nano device [7]. Here static behaviour denotes the device mode of operation under constant state, when the memristor acts in general as a nonlinear resistor. This mode is under way as long as the control voltage is applied for a sufficiently small time interval and assumes properly low values, so that any state change from the initial condition $x(0) = x_0$ may be neglected. As a result, one may analyze just Ohm's based law (2) with $x = x_0$ without taking care for the state equation. Further, it is opportune to remark that the value of the concavity parameter in the function $g_\rho(\cdot)$ has a significant influence on the static behaviour only for state values close to the lower bound, and for $|v_m| \approx 0\,\mathrm{V}$. Considering a non-disruptive memristor control voltage range, specifically $[-0.3, 0]\,\mathrm{V}$, dashed line curves in Fig. 2 illustrate, under values for ρ equal to 10^1(plot(a)), 10^2 (plot(b)), and 10^3 (plot(c)), the static behaviour of the nanoscale element resulting from the use of the approximating kernel $g_\rho(\cdot)$ for the modulus function $|\cdot|$ in (3). The numerical results referring to a state initial condition set to 0, 10^{-4}, 10^{-3}, and 10^{-2} are highlighted in red, black, blue, and pink respectively. In each plot the numerical solutions, resulting from the adoption of the modulus function, are also shown for comparison purposes as solid curves (the association between colours and initial states is the same as for the dashed curves).

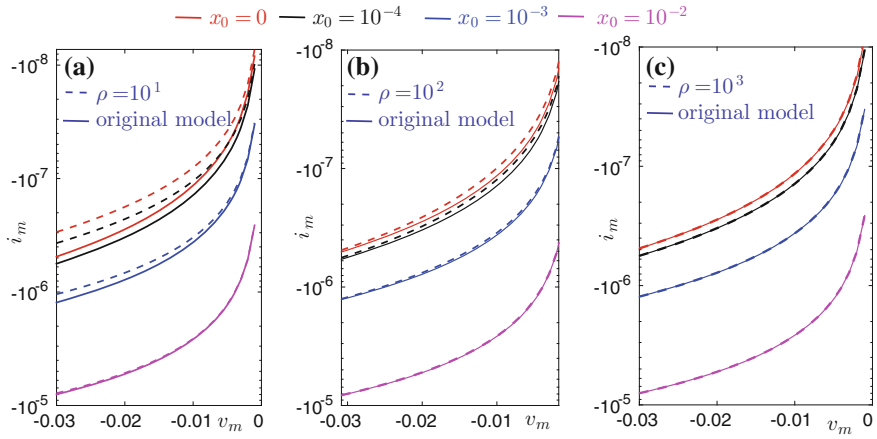

Fig. 2 Current–voltage characteristics observed under the assumption that the excitation signal has a sufficiently small amplitude, and is applied for a properly limited amount of time so that the resulting memristor state change from the initial condition is negligible. The state value at time $t = 0\,\mathrm{s}$ takes values in $\{0, 10^{-4}, 10^{-3}, 10^{-2}\}$. The solid and dashed curves respectively refer to the use of the piecewise differentiable and differentiable versions of the memductance function. In the latter case the concavity parameter ρ is chosen equal to 10^1, 10^2, and 10^3 in plots **a**, **b**, and **c** respectively

The dashed curves better match the solid ones in plot (c). It follows that, among the elements of the kernel class expressed by equation (4), the one with $\rho = 10^3$ represents a near optimal differentiable approximation to the modulus function. In order to confirm the appropriateness of this choice for ρ, we then examined the graphs of i_m versus v_m over the same memristor control voltage range as in Fig. 2 for a set of initial states uniformly spaced in the existence domain [0, 1]. An accurate agreement between the numerical results referring to the original piecewise differentiable memductance function and to the proposed differentiable approximation with $\rho = 10^3$ in $g_\rho(\cdot)$ was observed. Next, we propose to substitute the step function step$(\cdot)$ in the state equation with a continuous kernel within the class expressed by

$$f_k(\cdot) = \frac{1}{1 + \exp(-k\,\cdot)}, \tag{5}$$

where $k = f_k'(0)$, and the superscript $'$ denotes differentiation with respect to the argument. With reference to Fig. 3, where the horizontal axis reports the memristor voltage, the pink trace is the graph of the unit step function, while black, red, and blue curves depict the shape of the approximating kernel $f_k(\cdot)$, given in equation (5), under values for k set to 30, 40, and 50 respectively.

At this stage investigations aiming at choosing the most suitable candidate kernel for an accurate continuous approximation of the function step$(\cdot)$, responsible for the

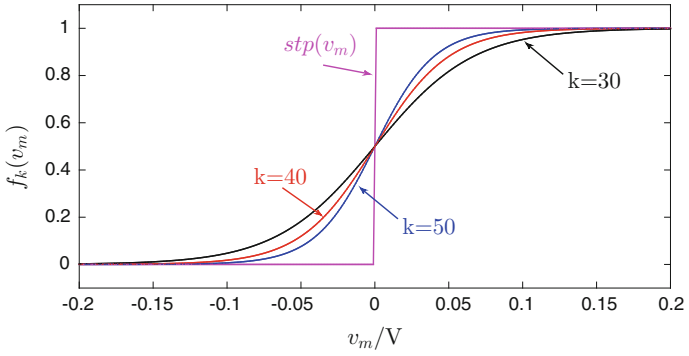

Fig. 3 Graphs of unit step function step(·) (a) and proposed approximating kernel $f_k(\cdot)$ for $k \in \{30, 40, 50\}$. The independent variable is the memristor voltage

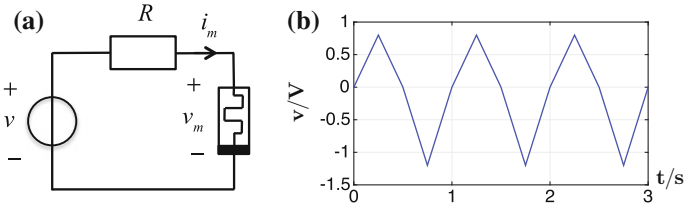

Fig. 4 **a** Circuit under test for the selection of the most appropriate kernel for an accurate continuous approximation of the unit step function. **b** Asymmetric shape of the voltage waveform sourced by the voltage generator

memristor transition between on and off state, are performed. A circuit composed of the series combination between a linear resistor of value $R = 70.1\,\Omega$ and the TaO memristor was excited through the application of a triangular waveform generated by a standard voltage source v. Plots (a) and (b) in Fig. 4 respectively show test circuit and excitation signal. The latter is characterized by a period $T = 1\,\text{s}$, and, most importantly, exhibits distinctly-valued amplitudes, i.e. 0.8 V and 1.2 V, under positive and negative polarity respectively.

In the simulations of Fig. 5 the state initial condition is set to $x_0 = 0.065$. Plot (a) shows the steady state pinched hysteresis loops emerging in the memristor current–voltage plane from numerical integration of the model Eqs. (1) and (2) upon replacement of the unit step function, appearing in the state equation, with the continuous kernel given in (5), and of the modulus function in the memductance expression contained in Ohm's based law with the approximating kernel $g_\rho(\cdot)$ with $\rho = 10^3$. The black, pink, and blue traces respectively refer to values for k set to 30, 40, and 50. Adopting the discontinuous function within differential (1), and the piecewise differentiable modulus function in the memductance expression (3) within Ohm's based law (2), the corresponding numerical result is plotted in red in Fig. 5(b). Among the traces of plot (a), the blue one most closely tracks the numerical result derived

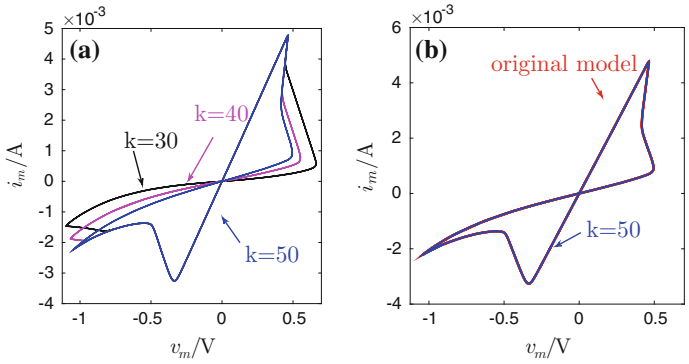

Fig. 5 **a** Memristor current–voltage pinched hysteresis loops observed at steady state upon numerical integration of the TaO memristor model with differentiable kernel $g_\rho(\cdot)$ with $\rho = 10^3$ replacing $|\cdot|$ in (2) and continuous function $f_k(\cdot)$ substituting $step(\cdot)$ in (1). Traces referring to values of k set to 30, 40, and 50 are respectively shown in *black*, *pink*, and *blue*. The latter one best agrees with the pinched hysteresis loop, drawn in *red* in plot **b** and obtained from the numerical solution to the original discontinuous and piecewise differentiable model proposed by HP engineers (see Fig. 6 in [7]). The *blue curve* from plot **a** is also graphed in plot **b** to highlight the accuracy of the approximation. See the text for details on test circuit, input, and initial condition

from the discontinuous and piecewise differentiable DAE set, as is evident from the observation of plot (b), where it is superimposed over the red trajectory.

Therefore, from the class of kernels expressed by (5), the one chosen for the continuous approximation to the step function has k equal to 50.

The accuracy of the proposed continuous and differentiable variant of the HP TaO memristor model was confirmed through an extensive number of simulations covering distinct test circuits, inputs and initial conditions.

Let us show an exemplar from the investigations. Test circuit, and state initial condition are kept unaltered as compared to the simulation of Fig. 5. The input waveform driving the resistor-memristor series circuit shares the same attributes with the signal of Fig. 4(b), except for the period which is swept here in $\{1, 10^{-2}, 10^{-4}, 10^{-6}, 10^{-8}\}$ s so as to analyse the frequency dependence of the steady state pinched hysteresis loops in the memristor current–voltage plane. As expected, the pinched hysteresis loops shrink as the input period decreases. The numerical results in plot (a) refer to the numerical integration of the original discontinuous and piecewise differentiable model Eqs. (1) and (2), while the curves in plot (b) were derived through numerical solution of the approximated DAE set, where $f_k(\cdot)$ with $k = 50$ replaces step$(\cdot)$ in the state equation, and $g_\rho(\cdot)$ with $\rho = 10^3$ substitutes $|\cdot|$ in the memductance expression within Ohm's based law. Each curve in plot (b) matches accurately the corresponding curve in plot (a) (Fig. 6).

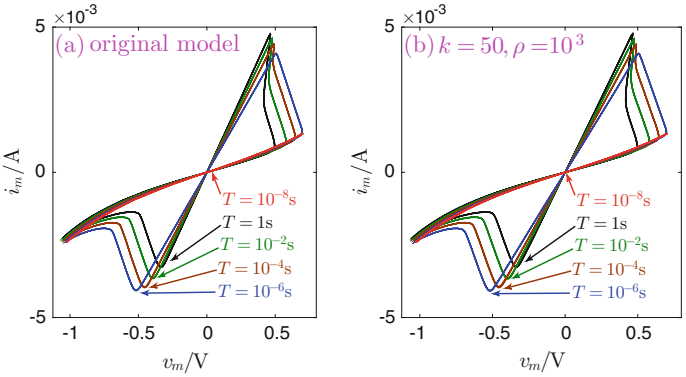

Fig. 6 Monotonic decrease in lobe area of the steady state memristor current–voltage pinched hysteresis loop with the frequency of excitation. The text provides details on test circuit, input source, and state initial condition. Numerical results descending from solution of discontinuous and piecewise differentiable model and proposed continuous and differentiable variant are respectively illustrated in plots **a** and **b**

4 Conclusions

The availability of reliable models of real memristors [13] is a key preliminary requirement for a comprehensive investigation of their utilization in integrated circuit design [14]. Hewlett Packard engineers have recently developed an accurate model, based on physics laws, for a Tantalum oxide extended memristor manufactured in house. Convergence issues may arise in the numerical integration of the model due to the presence of discontinuous and piecewise differentiable functions in state equation and Ohm's based law respectively. This paper introduces a continuous and differentiable approximation to the original TaO memristor model for robust numerical simulations. The approximated differential algebraic equation set supports the analysis of multi-memristor circuits, which is crucial for the exploration of the full potential of the promising Tantalum oxide nano-device in future electronics applications.

Acknowledgements The authors would like to acknowledge the contribution and the networking support of the EU COST Action IC1401. This work has been partially supported by the Czech Science Foundation under grant No. 14 − 19865*S*, Czech Republic. The authors sincerely thank J. P. Strachan, J. J. Yang, and S. Williams for insightful discussions on the HP TaO memristor.

References

1. Chua, L.O.: Memristor: the missing circuit element. IEEE Trans. Circuit Theory **18**(5), 507–519 (1971)
2. http://www.crossbar-inc.com

3. Vontobel, P.O., Robinett, W., Kuekes, P.J., Stewart, D.R., Straznicky, J., Williams, R.S.: Writing to and reading from a nano-scale crossbar memory based on memristors. Nanotechnol. **20**, 425204 (2009). doi:10.1088/0957-4484/20/42/425204. 21pp
4. Mikolajick, T., Slesazeck, S., M*ä*hne, H., Wylezich, H., Shuai, Y., You, T., Schmidt, H.: Resistive switching: from basic switching mechanisms to device application. In: Workshop on Memristor Science & Technology, European Conference on Design, Automation & Test in Europe (DATE), 2014
5. Corinto, F., Ascoli, A., Gilli, M.: Nonlinear dynamics of memristor oscillators. IEEE Trans. Circuits Syst.-I **58**(6), 1323–1336 (2011). doi:10.1109/TCSI.2010.2097731
6. Chua, L.O.: Resistance switching memories are memristors. Appl. Phys. A **102**, 765–783 (2011). doi:10.1007/s00339-011-6264-9
7. Strachan, J.P., Torrezan, A.C., Miao, F., Pickett, M.D., Yang, J.J., Yi, W., Medeiros-Ribeiro, G., Williams, R.S.: State dynamics and modeling of tantalum oxide memristors. IEEE Trans. Electron Devices **60**(7), 2194–2202 (2013)
8. Chua, L.O.: If It's Pinched, It's a Memristor. Special Issue on Memristive Devices, Semiconductor Science and Technology, September 2014
9. Ascoli, A., Corinto, F., Tetzlaff, R.: A class of versatile circuits, made up of standard electrical components, are memristors. Int. J. Circuit Theory Appl. **44**, 127–146 (2015). doi:10.1002/cta.2067
10. Biolek, D., Di Ventra, M., Pershin, Y.V.: Reliable SPICE simulations of memristors, memcapacitors and meminductors. Radioengineering **22**(4), 945–968 (2013)
11. Ascoli, A., Tetzlaff, R., Biolek, Z., Kolka, Z., Biolkov*á*, V., Biolek, D.: The art of finding accurate memristor model solutions. IEEE J. Emerg. Sel. Top. Circuits Syst. **5**(2), 133–142 (2015). doi:10.1109/JETCAS.2015.2426493
12. Chua, L.O.: Everything you wish to know about memristors but are afraid to ask. Radioengineering **24**(2), 319–368 (2015)
13. Ascoli, A., Slesazeck, S., M*ä*hne, H., Tetzlaff, R., Mikolajick, T.: Nonlinear dynamics of a locally-active memristor. IEEE Trans. Circuits Syst.-I **62**(4), 1165–1174 (2015). doi:10.1109/TCSI.2015.2413152
14. Ascoli, A., Corinto, F., Tetzlaff, R.: Generalized boundary condition memristor model. Int. J. Circuit Theory Appl. **44**(1), 60–84 (2015). doi:10.1002/cta.2063

Ultrawideband Microwave 3–7 GHz Chaotic Oscillator Implemented as SiGe Integrated Circuit

E.V. Efremova and A.S. Dmitriev

Abstract Structure of chaotic generator is proposed that provides chaotic oscillations with required form of signal spectrum. A model system on 0.25-μm SiGe component library is developed, and IC layout is designed. An experimental sample of microwave chaotic source with bipolar transistor as the active element is fabricated with 0.25-μm SiGe process. The system demonstrates generation of ultrawideband chaotic oscillations of 3–7 GHz frequency range. Results of numerical simulation and experimental study of the chip are analyzed.

1 Introduction

At present, a great interest is attracted to the use of ultrawideband (UWB) signals for wireless communications. A set of signal types is offered, e.g., ultrashort pulses, chirps, OFDM-signals, etc. [1–6]. One of the promising types of information carriers for UWB wireless communications is UWB chaotic radio pulse [7]. This type of signals is included in standards IEEE 802.15.3a (Ultrawideband Wireless Personal Area Networks) [8] and IEEE 802.15.6 (Wireless Body Area Networks) [9]. Several generations of communication devices based on chaotic technology are already developed [10]. Potential application areas are local personal networks, sensor networks, mobile devices, etc. UWB equipment intended for use in such areas employs an unlicensed 3.1–10.6 GHz frequency range to transmit data in communication networks composed of a huge number of transceivers. Appearance of such tasks stimulates active development of carrier sources, i.e., generators of microwave chaotic signals.

E.V. Efremova (✉) · A.S. Dmitriev
Kotelnikov Institute of Radio Engineering and Electronics of RAS, Moscow, Russia
e-mail: efremova@cplire.ru

A.S. Dmitriev
e-mail: chaos@cplire.ru

E.V. Efremova · A.S. Dmitriev
Moscow Institute of Physics and Technology, Dolgoprudnyi,
Moscow Reg., Russia

G. Mantica et al. (eds.), *Emergent Complexity from Nonlinearity, in Physics, Engineering and the Life Sciences*, Springer Proceedings in Physics 191,
DOI 10.1007/978-3-319-47810-4_7

Prospects of a wide use of microwave chaos in wireless communication systems depend on possibility of constructing chaotic generators with preassigned characteristics. Consumer electronics and sensor networks impose restrictions on the properties of chaotic transceivers. Chaotic generators for such applications must produce a UWB chaotic signal in a prescribed frequency band with rather smooth power spectrum envelope and prescribed power spectral density. At the same time, such devices must be compact, have low power consumption and repeatable characteristics. Ideally, chaotic generator must be implemented as a chip.

By now, basic principles of synthesizing low-dimensional oscillators with preassigned power spectrum are already developed [11, 12]. In particular, these principles work well for oscillators with a transistor as the active element. Computer simulation methods for microwave chaotic sources with actual element characteristics taken into account were developed [13]. Using these methods, a number of lumped-component generators for various frequency bands were designed [13, 14].

The next step to be done is implementation of UWB microwave chaotic generators as microchips. A peculiarity of such systems is very small size of micro-chips in comparison with the characteristic wavelength of generated signal. So, they cannot contain any distributed elements, they must be lumped-parameter systems. Moreover, there are rather strong restrictions on element values. From practical point of view, only small-value inductances can be used. Another feature of passive elements on the die is strong nonideality, especially high ohmic losses. Also, elements interact through the chip substrate, which significantly complicates the original oscillator structure.

An IC chaotic microwave oscillator on SiGe technology was first developed in [15, 16]. Experimental IC generator provided chaotic oscillations of 3–8 GHz frequency band with 50 μW signal power.

At the same time, for practical use (including UWB communications) chaotic oscillators with higher power output and more smooth spectrum envelope are demanded. Solving this problem is the aim of the present work.

2 Oscillator Model

Chaotic oscillator circuit, based on a single-transistor active element and a passive quadripole closed in the feedback loop, was used. As was shown earlier, choosing parameters of the passive quadripole, one can form the power spectrum of the generator output signal [13].

This approach was used in the design of UWB chaotic generator. Electric circuit of the proposed generator is presented in Fig. 1. The proposed structure is shown to produce chaotic oscillations in a wide parameter range, whereas the frequency band is defined by frequency selective properties of the passive quadripole in the feedback loop and the output signal tap circuit.

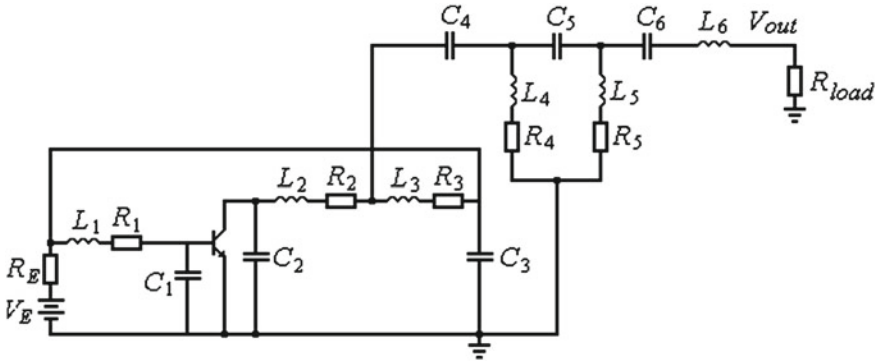

Fig. 1 Electric circuit of chaotic generator

Silicon-germanium (SiGe) 0.25-μm technology was taken for IC fabrication. The reasons were a possibility to use a bipolar transistor and sufficiently high boundary frequency, which was an important characteristic for chaotic oscillators.

To design and simulate generator microchip, we used Cadence IC software. This is a standard specialized tool for full-cycle microchip design, from electric circuit to fabric-ready topology. It allows us to use the component libraries given by manufacturers and to adapt the system to a concrete technology process.

Thus, the first stage of generator design is deduction of schematic circuit diagram. At the next stage, ideal elements of the generator circuit are replaced with models of bipolar transistor and passive components from SiGe 0.25-μm process library. Passive elements from the process library are described by equivalent schemes, that take into account substrate leakage current, skin-effect, etc. To simulate the bipolar transistor, a high-dimensional SPICE-model is used, that takes into account frequency and nonlinear effects.

Realistic inductive elements have non-zero resistance, whereas base-emitter and emitter-collector junctions have capacitances. Model elements from the technology library comply with these factors. To obtain generation at high frequencies, capacities C_1 and C_2 must be small. Decreasing these values leads to the situation when they become comparable to the capacities of base-collector, base-emitter junctions. At the same time, the active resistance of the inductor is quite big, so there is no need in additional resistors. This allows us to simplify the system and employ the capacities of base-emitter and emitter-collector junctions as capacitors C_1 and C_2 of the generator circuit, and replace resistances R_1, R_2, R_3, R_4, R_5 with active resistances of the corresponding inductors.

To test generator experimentally, the oscillator IC is placed in QFN16 package. Since the package can affect the dynamics of the oscillator, it is reasonable to take its impact into account at the stage of crystal design, in order to compensate possible negative effects. With this purpose, an equivalent circuit of the package was added to the oscillator model.

3 Simulation

After replacing the ideal elements with elements from the technological library, the system was simulated to calculate time-domain and spectral characteristics of generated oscillations. For communication applications the spectrum of chaotic generator as a UWB signal source must be smooth enough within the operation frequency range. Moreover, the chaotic mode must be stable under small variations of the voltage supply. To achieve this property, the system component values are selected in such a way as to obtain wide parameter area, in which chaotic mode with smooth spectrum envelope is realized. As a result, a chaotic oscillator with nonideal active and passive elements is synthesized, that generates chaotic oscillations in 3–7 GHz frequency band.

In the generator model, as the supply voltage is increased the following bifurcations take place. First, periodic oscillations of the main frequency are excited (Fig. 2a), then a frequency grid appears (Fig. 2b, c) and then comes continuous spectrum (Fig. 2d, e), that corresponds to chaotic mode. The transition from regular to chaotic mode occurs through a cascade of period-doubling bifurcations. A further voltage increase leads to destruction of the chaotic mode (Fig. 2f).

Synthesized generator model provides generation of chaotic oscillations in the frequency band $F = 3$–7 GHz. The power is about $P = 1.6$ mW at supply voltage $V_E = 2$ V and current consumption $I = 26$ mA. Largest Lyapunov exponent of the mode is equal to 0.1.

At the last stage of developing chaotic generator, microchip topology is designed (Fig. 3), based on the synthesized oscillator with nonlinear elements.

Design of microchip topology consists of placing the system elements on silicon substrate and connecting these elements with connection pads. Insertion of the pads and interaction of the elements via substrate make essential effect on the system dynamics. This effect can be seen in Fig. 4.

Here the result of the system dynamics simulation is shown for the same parameter set as in Fig. 2d, but with some artifacts taken in consideration. Actually, in this case the effect of parasitic capacitance was taken into account. Though the frequency range and power consumption remain almost the same, the power spectrum envelope (Fig. 4b) becomes non-uniform and the output power decreases. Speaking of the microchip topology, artifacts can lead to not only degradation of spectral characteristics of the chaotic signal, but to destruction of the chaotic mode itself. It is especially sensitive to resistive effects. That is why at the last stage of simulation, element arrangement on the substrate must be optimized in order to minimize the influence of topology artifacts on generator characteristics. Also, the system parameters must be corrected to compensate effect of unavoidable topology artifacts.

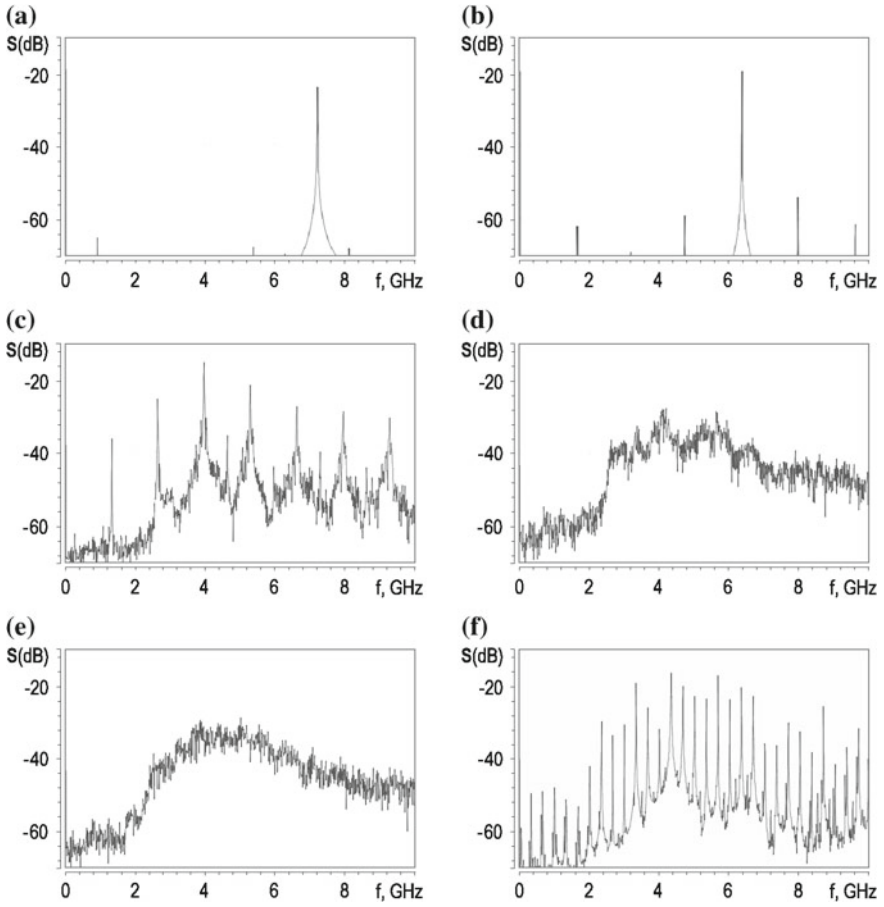

Fig. 2 Model. Power spectrum density of SiGe 0.25 μm generator IC versus frequency, **a** $V_E = 0.8$ V, **b** $V_E = 1.16$ V, **c** $V_E = 1.7$ V, **d** $V_E = 1.8$ V, **e** $V_E = 2.0$ V, **f** $V_E = 2.3$ V

4 Experiment

A set of experimental samples of SiGe microchips was fabricated according to the developed model. The chip area was about 1.6 sq. mm. For experimental studies the chip was placed in a plastic package, the chip pins were connected with the package terminals with thin wires.

Experimental investigation of the microchip shows that with increasing supply voltage periodic oscillations are excited first at about 2 GHz. After that a frequency grid appears in the power spectrum (Fig. 5a), that consists of the main frequency and its odd and even harmonics. This is followed by a set of period-doubling bifurcations (Fig. 5b, c) and transition to a chaotic mode with ragged power spectrum envelope (Fig. 6a). After that goes an area in which regular and chaotic modes change each

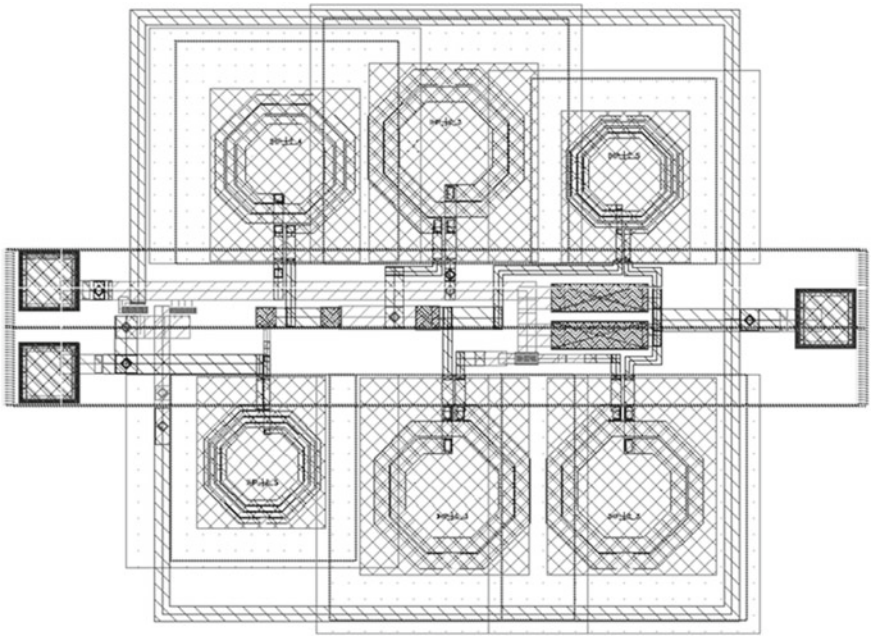

Fig. 3 Integrated circuit topology

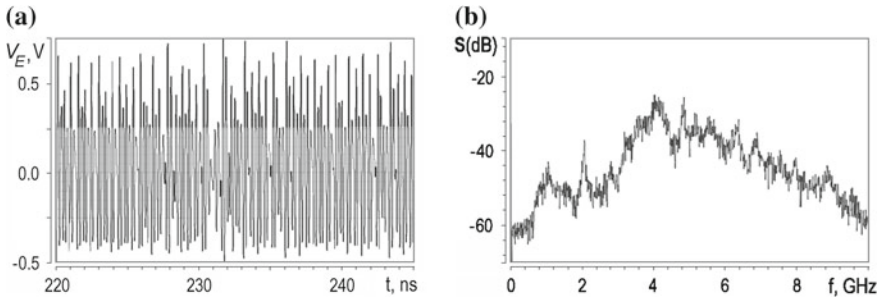

Fig. 4 Waveform and power spectrum density of a chaotic mode of the generator model (parasitic capacitance is taken into account) at $V_E = 2\,\text{V}$

other, and finally the system comes to a mode with continuous power spectrum (Fig. 6b). Further voltage increase leads to destruction of the chaotic mode (Fig. 6c). Comparison of Fig. 2 and Figs. 5 and 6 show that, as a whole, the scenarios of dynamic mode evolution in the model and the experimental system coincide. Signal power spectra occupy the same frequency range, the transition from regular to chaotic modes occurs through cascade of period doubling bifurcations. Note that the region of chaotic modes (with the power spectrum in Fig. 6c) is quite large, about $\Delta V_E = 0.35\,\text{V}$.

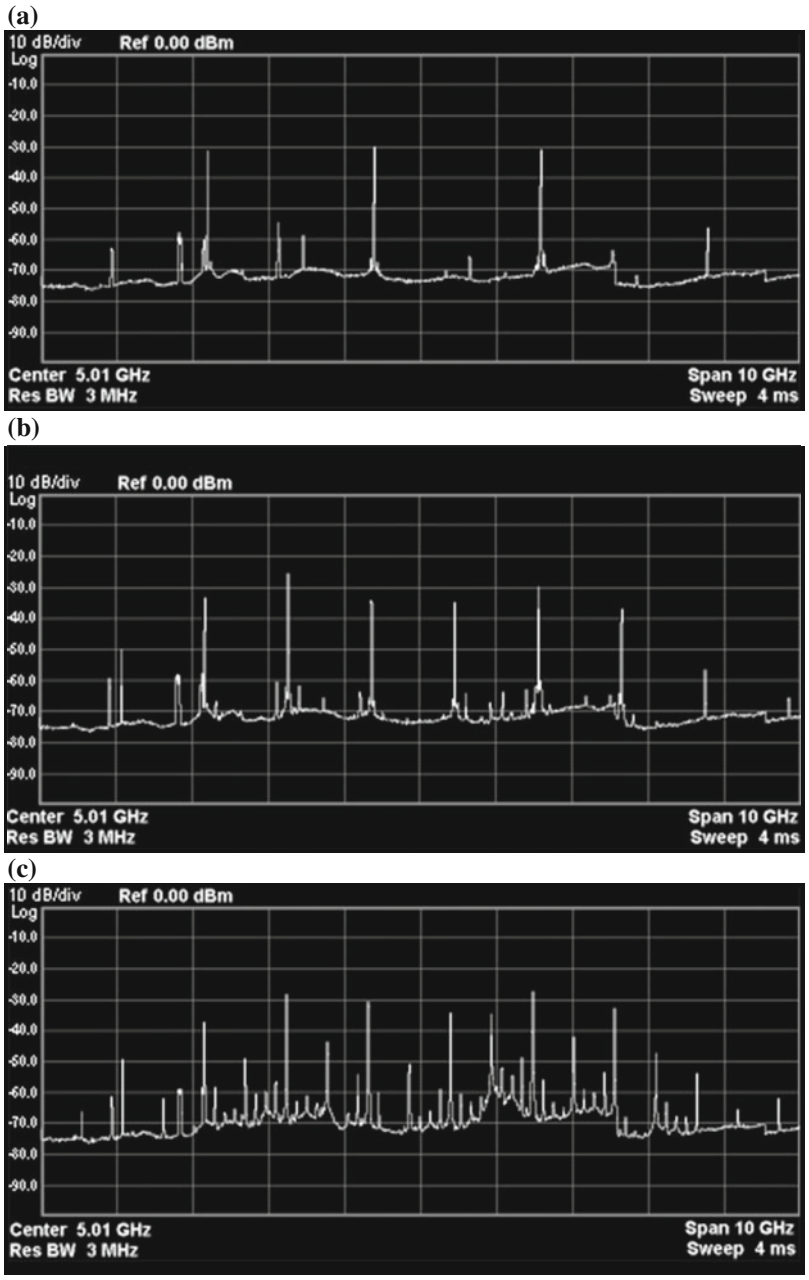

Fig. 5 Experiment. Power spectrum density of IC generator on SiGe 0.25 μm versus frequency, **a** $V_E = 0.93$ V, **b** $V_E = 1.01$ V, **c** $V_E = 1.08$ V. X-axis step is 1 GHz, Y-axis step 10 dB

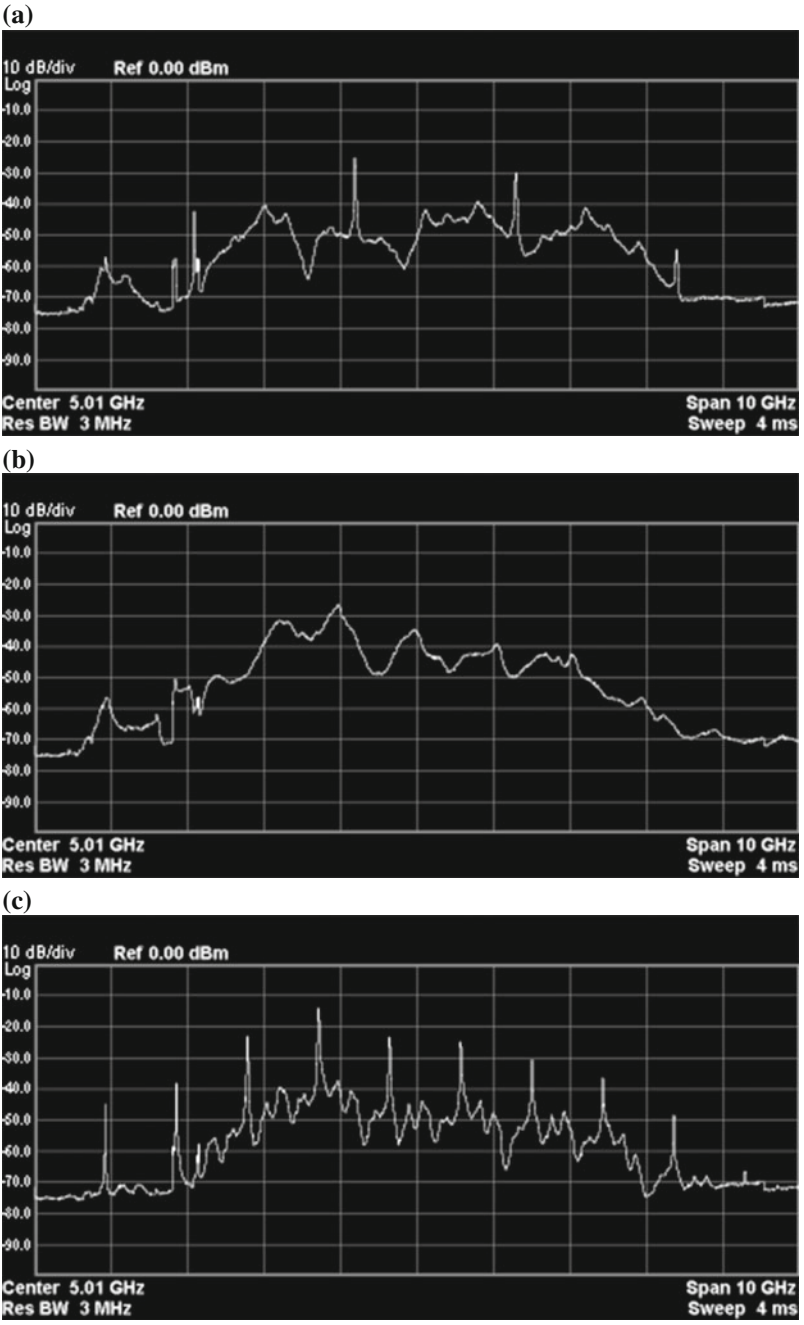

Fig. 6 Experiment. Power spectrum density of IC generator on SiGe 0.25 μm versus frequency, **a** $V_E = 1.28\,\text{V}$, **b** $V_E = 2.1\,\text{V}$, **c** $V_E = 2.36\,\text{V}$. X-axis step is 1 GHz, Y-axis step 10 dB

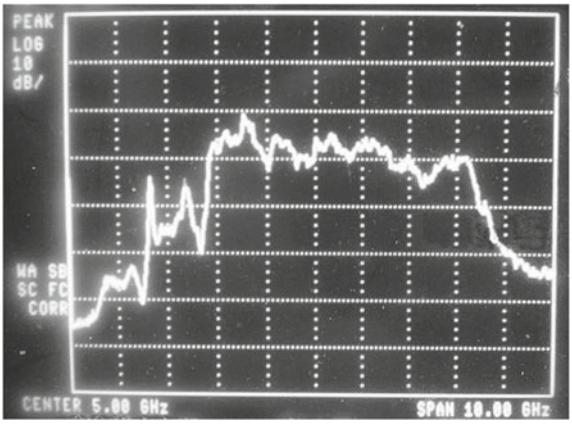

Fig. 7 Power spectrum of chaotic mode of the generator from [14]. X-axis step is 1 GHz, Y-axis step 10 dB

In operation mode, at supply voltage $V_E = 2.1$ V, the generator produces chaotic oscillations in the frequency band 3–7 GHz (Fig. 6c). This agrees with the simulation results. Current consumption in this mode is $I = 26$ mA, which is close to the calculated $I = 24$ mA. Output signal power is about $P = 300\,\mu$W.

Earlier an SMT (surface-mount technology) lumped-component generator of 3–8 GHz chaotic oscillations (Fig. 7) was developed and investigated [14]. The signal power of this system was about 300 μW. So, the proposed and developed IC chaotic oscillator demonstrates spectral and power characteristics close to those of the SMT generator.

5 Conclusions

SiGe microchip was developed and fabricated. It generates ultrawideband microwave chaotic oscillations of 3–7 GHz frequency band. Experimental results are in good agreement with simulation, which justifies the approach and opens ways for mass production of UWB microwave chaotic generator chips. This, in turn, allows design and mass production of consumer communication devices based on UWB chaotic signals on modern microelectronic technology.

In addition to 3–7 GHz frequency band, other areas of microwave range are also in demand. So, development of integrated UWB chaotic generators for different frequency ranges becomes an actual task. Generators of UWB microwave oscillations can be used in numerous applications such as wireless personal and sensor networks, mobile robots, etc.

Acknowledgements This study is supported in part by the Russian Science Foundation (project 16-19-00084).

References

1. Win, M.Z., Scholtz, R.A.: IEEE Commun. Lett. **2**(2), 36 (1998)
2. A tutorial on ultra wideband technology, IEEE 802.15 Working group submission. IEEE, New York (2005). http://grouper.ieee.org/groups/802/15/pub/2000/Mar00/00082r1P802-15_WG-UWB-Tutorial-1-XtremeSpectrum.pdf Accessed 25 Feb 2016
3. TG4a proposal for low rate DS-UWB (DS-UWB-LR). IEEE, New York (2005). http://grouper.ieee.org/groups/802/15/pub/2005/15-05-0021-00-004a-low-rate-ds-uwb-tg4a.ppt Accessed 25 Feb 2016
4. Lampe J.: Introduction to chirp spread spectrum (CSS) technology. IEEE, New York (2004). http://grouper.ieee.org/groups/802/15/pub/2004/15-04-0353-00-004a-chirp-spread-spectrum-technology.ppt Accessed 25 Feb 2016
5. Gerrits, J., et al.: EURASIP J. Adv. Sign. Proc. **3**, 382 (2005)
6. Multi-band OFDM physical layer proposal for IEEE 802.15 task group 3a. IEEE, New York (2003). http://www.ieee802.org/15/pub/2003/Jul03/03268r2P802-15_TG3a-Multi-band-CFP-Document.pdf Accessed 25 Feb 2016
7. Dmitriev, A.S., et al.: J. Comm. Technol. Electron. **46**(2), 207 (2001)
8. IEEE Standard for Information technology Telecommunications and information exchange between systems Local and metropolitan area networks Specific requirements; Part 15.4: Wireless Medium Access Control (MAC) and Physical Layer (PHY) Specifications for Low-Rate Wireless Personal Area Networks (WPANs); Amendment 1: Add Alternate PHYs, (2007)
9. IEEE 802.15.6-2012. IEEE standard for local and metropolitan area networks - Part 15.6: wireless body area networks. (2012). http://standards.ieee.org/about/get/802/802.15.html Accessed 25 Feb 2016
10. Dmitriev, A.S., et al.: J. Comm. Technol. Electron. **58**(12), 1113 (2013)
11. Dmitriev, A.S., et al.: Int. J. Bifurc. Chaos **6**(5), 851 (1996)
12. Dmitriev, A.S., Efremova, E.V.: Transistornye generatory chaosa s zadannoi formoi spectra moschnosty kolebanii (Transistor chaos generators with prescribed shape of power spectrum). Radiotekhnika. **8**, 67 (2005)
13. Dmitriev, A.S., et al.: J. Comm. Technol. Electron. **52**(10), 1137 (2007)
14. Dmitriev, A.S., et al.: Tech. Phys. Lett. **40**(2), 1 (2014)
15. Dmitriev, A.S., et al.: Tech. Phys. Lett. **35**(12), 1090 (2009)
16. Dmitriev, A.S., et al.: J. Comm. Technol. Electron. **55**(7), 765 (2010)

Cryptanalysis of a Random Number Generator Based on a Chaotic Oscillator

Salih Ergün

Abstract This paper introduces an algebraic cryptanalysis of a random number generator (RNG) based on a chaotic oscillator. An attack system is proposed to discover the security weaknesses of the chaos-based RNG. Convergence of the attack system is proved using master slave synchronization scheme where the only information available are the structure of the RNG and a scalar time series observed from the chaotic oscillator. Simulation and numerical results verifying the feasibility of the attack system are given. The RNG does not fulfill NIST-800-22, Diehard and Big Crush statistical test suites, the previous and the next bit can be predicted, while the same output bit sequence of the RNG can be reproduced.

1 Introduction

People have needed to keep their critical data secure since they began to communicate with each other. Over the last decades there has been an increasing emphasis on using tools of information secrecy. Certainly, random number generators (RNGs) have more prominently positioned into the focal point of research as the core component of the secure systems. Although many people are even unaware that they are using them, we use RNGs in our daily business. If we ever obtained money from a bank's cash dispenser, ordered goods over the internet with a credit card, or watched pay TV we have used RNGs. Public/private key-pairs for asymmetric algorithms, keys for symmetric and hybrid crypto-systems, one-time pad, nonces and padding bytes are created by using RNGs [1].

Being aware of any knowledge on the design of the RNG should not provide a useful prediction about the output bit sequence. Even so, fulfilling the requirements for secrecy of cryptographic applications using the RNG dictate three secrecy criteria as a "must": 1. The output bit sequence of the RNG must pass all the statistical tests

S. Ergün (✉)
ERARGE - Ergünler Co., Ltd. R&D Center, Şair Nedim Cad. No:50/5,
34357 Beşiktaş, İstanbul, Turkey
e-mail: salih.ergun@erarge.com.tr

G. Mantica et al. (eds.), *Emergent Complexity from Nonlinearity, in Physics, Engineering and the Life Sciences*, Springer Proceedings in Physics 191,
DOI 10.1007/978-3-319-47810-4_8

of randomness; 2. The previous and the next random bit must be unpredictable [2] and; 3. The same output bit sequence of the RNG must not be able to be reproduced [3].

An important principle of modern cryptography is the Kerckhoff's assumption [3], states that the overall security of any cryptographic system entirely depends on the security of the key, and assumes that all the other parameters of the system are publicly known. Cryptanalysis is the complementary of cryptography. Interaction between these two branches of cryptology form modern cryptography which has become strong only because of cryptanalysis revealing weaknesses in existing cryptographic systems.

There are four fundamental random number generation methods out of all RNG designs reported in the literature: 1. Amplification of a noise source [4, 5]; 2. Jittered oscillator sampling [6, 7]; 3. Discrete-time chaotic maps [8, 9] and; 4. Continuous-time chaotic oscillators [10, 11]. Although the use of discrete-time chaotic maps in the realization of RNG has been widely accepted for a long period of time, it has been shown during the last decade that continuous-time chaotic oscillators can also be used to realize RNGs [10, 11]. In particular, a so-called RNG based on a continuous-time chaotic oscillator has been proposed in [10].

In this paper we target the RNG reported in [10] and further propose an attack system to discover the security weaknesses of the targeted system. The strength of a cryptographic system almost depends on the strength of the key used or in other words on the difficulty for an attacker to predict the key. On the contrary to recent RNG design [11], where the effect of noise generated by circuit components was analyzed to address security issue, the target random number generation system [10] pointed out the deterministic chaos itself as the source of randomness.

Advances in computing power necessitate a continuous chase between security and attacks. Together with constantly increasing communication rates, increases in computing power eventually reveals the need for more secure and fast RNGs. In comparison with RNGs based on the other common techniques, which are advantageous in the sense that true random behavior can be mathematically proven, it is seen that RNGs based on continuous-time chaotic oscillators can offer much higher data rates. Following up in this direction, we investigate the usefulness of the proposed attack methods for the security analysis of chaos based RNG designs.

The organization of the paper is as follows. In Sect. 2 the target RNG system is described in detail; In Sect. 3 an attack system is proposed to cryptanalyze the target system and its convergence is proved; Sect. 4 illustrates the numerical results with simulations which is followed by concluding remarks.

2 Target System

Chaotic oscillators are categorized into two groups: discrete-time or continuous-time, respectively regarding on the evolution of the dynamical systems. In comparison with RNGs based on discrete-time chaotic sources it appears that RNGs

based on continuous-time chaos can be implemented using less complex and more robust structures, particularly due to the absence of successive sample-and-hold and multiplier stages.

In target random number generation system [10], a continuous-time double-scroll-like chaotic attractor is utilized as the core of the RNG. This chaotic system is derived from the negative-gm LC tank oscillator and expressed by the following (1):

$$\begin{aligned}
\dot{x_1} &= ax_1(s_1 - 1) - y_1 \\
\dot{y_1} &= x_1 - z_1 \\
\dot{s_1} &= c - \tfrac{a}{2}[(s_1 - 1)^2 + x_1^2] \\
2\dot{z_1} &= y_1 - 2z_1 + k \begin{cases} b & if\ x_1 \geq x_{sat} \\ \sqrt{2ab}x_1\sqrt{1 - (\frac{x_1}{\sqrt{2}x_{sat}})^2} & if\ |x_1| < x_{sat} \\ -b & if\ x_1 \leq -x_{sat} \end{cases}
\end{aligned} \tag{1}$$

The equations in (1) generate chaos for different sets of parameters. The chaotic attractor shown in Fig. 1 is obtained from the numerical analysis of the system with $a = 0.4$, $b = 0.15$, $c = 0.8$ and $k = 8$.

Target random number generation mechanism is illustrated in Fig. 2 where bit generation method is based on jittered oscillator sampling technique. As depicted in Fig. 2 output of a fast oscillator is sampled on the rising edge of a jittered slower clock using a D flip-flop where the jittered slow clock is realized by the sum of triangular wave and a chaotic signal.

In this design, if the fast and the slower clock frequencies are known as well as the starting phase difference ΔT, the output of the fast oscillator, sampled at the rising edge of the jittered slower clock, can be predicted. It can be shown that the output

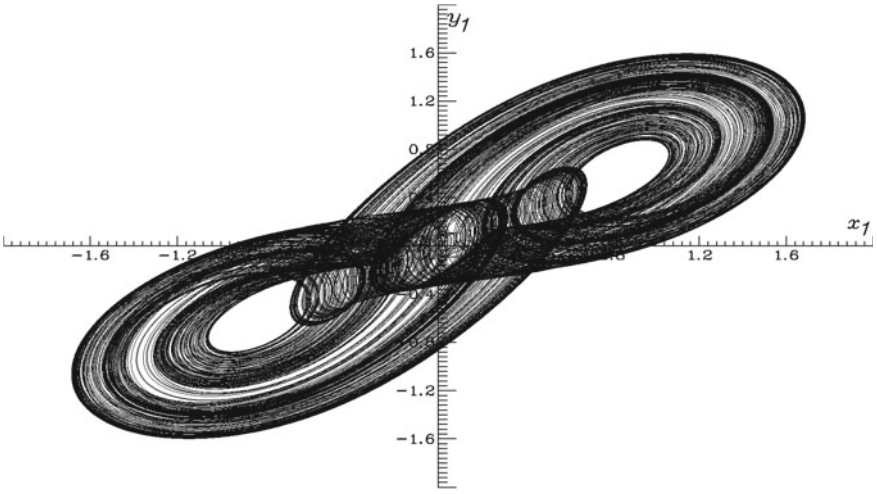

Fig. 1 Numerical analysis results of the chaotic system for $a = 0.4$, $b = 0.15$, $c = 0.8$ and $k = 8$

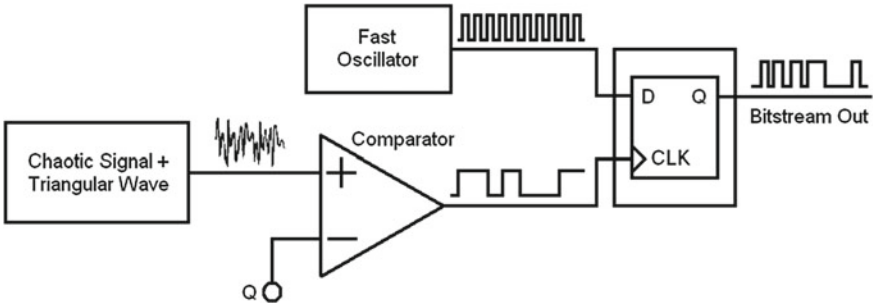

Fig. 2 Target random number generation system

bit sequence $S_{(bit)i}$ is the inverse of least significant bit of the ratio between the total periods of the jittered slower clock and period of the fast clock:

$$S_{(bit)i} = \left(\frac{\lfloor \frac{(\sum_{j=1}^{i} T_{slow\ j}) - \Delta T}{T_{fast}/2} \rfloor mod 2}{(2d_{fast})} \right)' \tag{2}$$

where $T_{fast} = \frac{1}{f_{fast}}$, f_{fast}, d_{fast} are the period, frequency and the duty cycle of the fast clock, respectively, and the periods of the jittered slower clock $T_{slow\ j}$ are obtained at times t satisfying:

$$s(t) = x_1(t) + tw(t) = Q\ with\ \frac{ds}{dt} > 0 \tag{3}$$

where $x_1(t)$ is the chaotic signal, $tw(t)$ is the triangular wave signal and Q is the threshold value used to generate slower clock. We have numerically verified that, for high $\frac{f_{fast}}{f_{slow\ center}}$ ratios, the effect of ΔT becomes negligible and the mean value (m_{output}) of the output sequence S_{bit} approaches the fast clock duty cycle d_{fast} where frequency of the triangular-wave, corresponding to mean frequency of the jittered slower clock $f_{slow\ center}$, determines the throughput data rate (f_{rng}). It should be noted that, anyone who knows the chaotic signal output can reproduce the same output bit sequence.

The authors of [10] have preferred to use FIPS-140-1 [12] statistical test suite in order to analyze output randomness of their chaos-based RNG design. However, NIST-800-22 [13], Big Crush [14] and Diehard [15] statistical test suites which are available at the publication date of target paper [2] weren't applied to output bit stream of the target RNG. It should be noted that, the target random number generation system [2] doesn't satisfy the third secrecy criteria, which states that "RNG must pass all the statistical tests of randomness."

3 Attack System

After the seminal work on chaotic systems by Pecora and Carroll [16], synchronization of chaotic systems has been an increasingly active area of research [17]. In this paper, convergence of attack and target systems is numerically demonstrated using master slave synchronization scheme by means of feedback method [17]. In order to provide an algebraic cryptanalysis of the target random number generation system a attack system is proposed which is given by the following (4):

$$\begin{aligned}
\dot{x_2} &= ax_2(s_2 - 1) - y_2 \\
\dot{y_2} &= x_2 - z_2 + d(y_1 - y_2) \\
\dot{s_2} &= c - \tfrac{a}{2}[(s_2 - 1)^2 + x_2^2] \\
2\dot{z_2} &= y_2 - 2z_2 + k \begin{cases} b & if\ x_2 \geq x_{sat} \\ \sqrt{2ab}x_2\sqrt{1 - (\frac{x_2}{\sqrt{2}x_{sat}})^2} & if\ |x_2| < x_{sat} \\ -b & if\ x_2 \leq -x_{sat} \end{cases}
\end{aligned} \tag{4}$$

where d is the coupling strength between the target (master) and attack (slave) systems and the only information available are the structure of the target random number generation system and a scalar time series observed from y_1.

In this paper, we are able to construct the attack system expressed by the (4) that synchronizes ($y_2 \rightarrow y_1$ for $t \rightarrow \infty$) where t is the normalized time. We define the error signals as $e_x = x_1 - x_2$, $e_y = y_1 - y_2$ and $e_z = z_1 - z_2$ where the aim of the attack is to design the coupling strength such that $|e(t)| \rightarrow 0$ as $t \rightarrow \infty$.

The master slave synchronization of attack and target systems is verified by the conditional Lyapunov Exponents (CLEs), and as firstly reported in [16], is achievable if the largest CLE is negative. CLEs for the attack system are calculated from the set of ordinary differential equations given in (4) where standard QR decomposition method of Eckmann and Ruelle (Reviews of Modern Physics, 1985) is used.

In Fig. 3, largest CLE graph is drawn as a function of coupling strength d while a scalar time series is observable from y_1. As drawn in the figure, when $0.66 < d < 0.99$ then the largest CLE is negative and hence identical synchronization of target and attack systems starting with different initial conditions is achieved and stable [16]. (Largest CLE = -0.0232169 for $d = 0.67$). However for the values of d out of the given range, largest CLE is positive and identical synchronization is unstable.

Log $|e_x(t)|$, Log $|e_y(t)|$ and Log $|e_z(t)|$ are shown in Figs. 4, 5, and 6 respectively for $d = 0.71$ (where the synchronization effect is better than that of $d = 0.67$) which indicate that the identical synchronization is achieved in less than $340t$ (Largest CLE = -0.0661455 for $d = 0.71$).

Particularly, we have reported preliminary results of an other cryptanalysis in [18] where auto-synchronization scheme is used. In this work we recall this paper and further propose a novel attack system where both target random number generation mechanism and target chaotic system are different from the previous work [18].

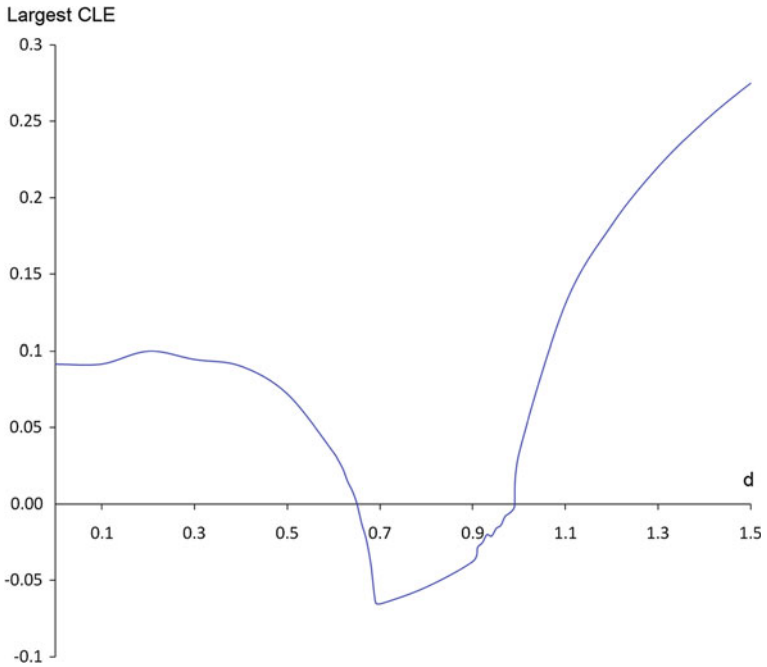

Fig. 3 Largest CLEs as a function of coupling strength d

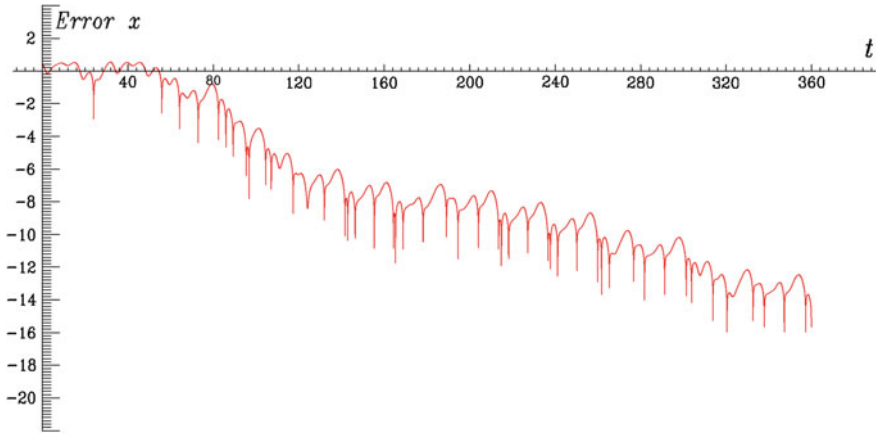

Fig. 4 Synchronization error Log $|e_x|$

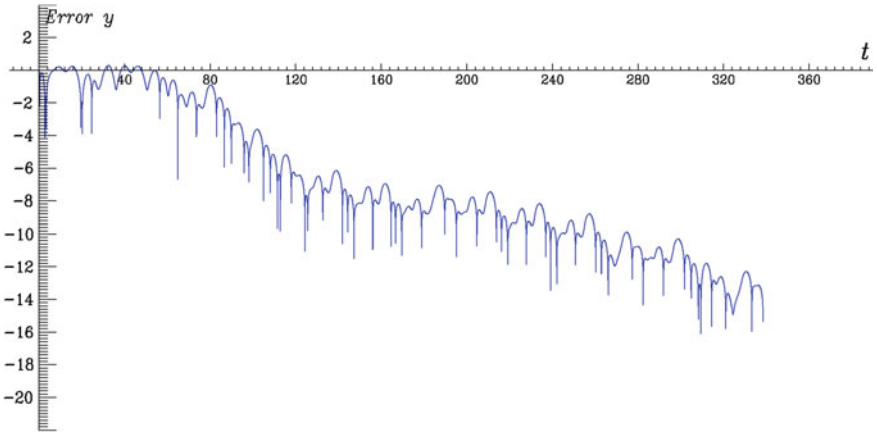

Fig. 5 Synchronization error Log $|e_y|$

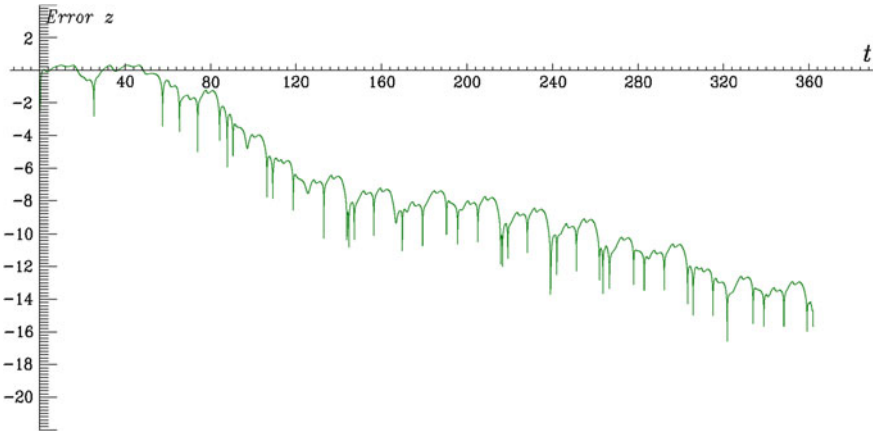

Fig. 6 Synchronization error Log $|e_z|$

4 Numerical Results

We numerically demonstrate the proposed attack system using a 4^{th}-order Runge–Kutta algorithm with fixed step size and its convergence is illustrated in Figs. 4, 5, and 6. Numerical results of $x_1 - x_2$, $y_1 - y_2$, and $z_1 - z_2$ are also given in Figs. 7, 8, and 9, respectively illustrating the unsynchronized behavior and the synchronization of target and attack systems.

It is observed from the given figures that, master slave synchronization is achieved and stable. As shown by black lines in these figures, no synchronous phenomenon is observed before $340t$. In time, the proposed attack system converges to the target

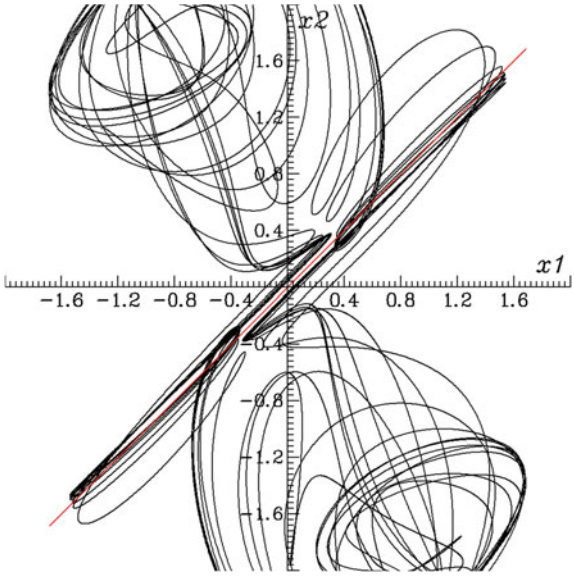

Fig. 7 Numerical result of $x_1 - x_2$ illustrating the unsynchronized behavior and the synchronization of target and attack systems

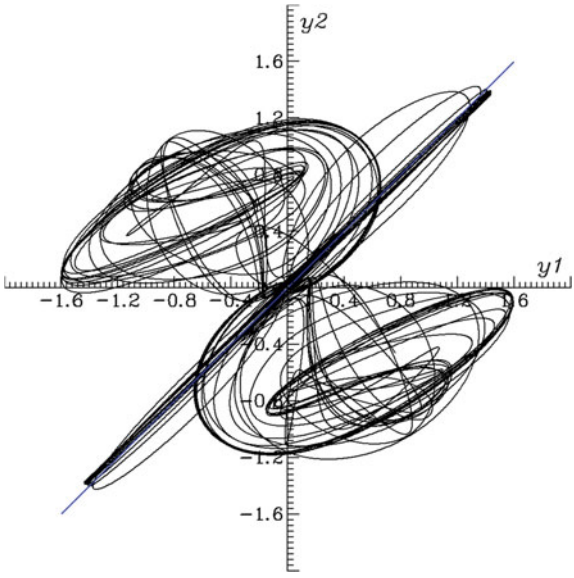

Fig. 8 Numerical result of $y_1 - y_2$ illustrating the unsynchronized behavior and the synchronization of target and attack systems

system and identical synchronization is achieved where colored lines depict synchronized behaviors of chaotic states in Figs. 7, 8, and 9, respectively.

Since the identical synchronization of attack and target systems is achieved $(x_2 \rightarrow x_1)$ in $340t$, the estimated value of $S_{()i}$ bit which is generated according to the procedure explained in Sect. 2 converges to its fixed value. As a result, it is obvious

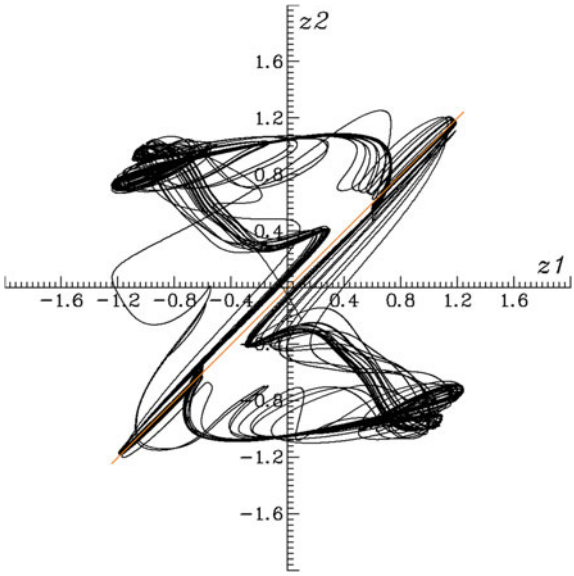

Fig. 9 Numerical result of $z_1 - z_2$ illustrating the unsynchronized behavior and the synchronization of target and attack systems

that identical synchronization of chaotic systems is achieved and hence output bit streams of target and attack systems are synchronized.

It is clearly shown that master slave synchronization of proposed attack system is achieved. Hence, output bit sequences of target and attack systems are synchronized. As a result, cryptanalysis of the target random number generation system not only predicts the previous and the next random bit but also demonstrates that the same output bit sequence of the target random number generation system can be reproduced. In conclusion, the target system [10] satisfies neither the second, nor the third secrecy criteria that a RNG must satisfy.

5 Conclusions

In this paper, we propose an algebraic attack on a random number generator (RNG) based on a chaotic oscillator. An attack system is introduced to discover the security weaknesses of the chaos-based RNG and its convergence is proved using master slave synchronization scheme. Although the only information available are the structure of the target RNG and a scalar time series observed from the target chaotic system, identical synchronization of target and attack systems is achieved and hence output bit streams are synchronized. Simulation and numerical results presented in this work not only verify the feasibility of the proposed attack but also encourage its use for the

security analysis of the other chaos-based RNG designs. Proposed attack, renders generated bit streams predictable, thereby qualifying the target RNG to be used as a not random but pseudo random source.

References

1. Jun, B., Kocher, P.: The intel random number generator. Cryptography Research, Inc., White Paper Prepared for Inter Corporation. http://www.cryptography.com/resources/whitepapers/IntelRNG.pdf (1999)
2. Schrift, A.W., Shamir, A.: On the Universality of the next bit test. In: Proceeding of the CRYPTO, pp. 394–408 (1990)
3. Schneier, B.: Applied Cryptography, 2^{nd} edn. Wiley, New York (1996)
4. Göv, N.C., Mıhçak, M.K., Ergün, S.: True random number generation via sampling from flat band-limited Gaussian processes. IEEE Trans. Circuits Syst. I **58**(5), 1044–1051 (2011)
5. Petrie, C.S., Connelly, J.A.: A noise-based IC random number generator for applications in cryptography. IEEE Trans. Circuits Syst. I **47**(5), 615–621 (2000)
6. Bucci, M., Germani, L., Luzzi, R., Trifiletti, A., Varanonuovo, M.: A high speed oscillator-based truly random number source for cryptographic applications on a smart card IC. IEEE Trans. Comput. **52**, 403–409 (2003)
7. Güler, Ü., Ergün, S.: A high speed IC random number generator based on phase noise in ring oscillators. In: Proceedings of the IEEE International Symposium on Circuits and Systems (ISCAS '10), pp. 425–428 (2010)
8. Stojanovski, T., Pihl, J., Kocarev, L.: Chaos-based random number generators-part II: practical realization. IEEE Trans. Circuits Syst. I **48**(3), 382–385 (2001)
9. Callegari, S., Rovatti, R., Setti, G.: Embeddable ADC-based true random number generator for cryptographic applications exploiting nonlinear signal processing and chaos. IEEE Trans. Signal Process. **53**(2), 793–805 (2005)
10. Tavas, V., Demirkol, A.Ş., Özoğuz, S., Kilinç, S., Toker, A., Zeki, A.: An IC random number generator based on chaos. In: Proceedings of the International Conference on Applied Electronics (AE'10), pp. 1–4 (2010)
11. Ergün, S., Güler, Ü., Asada, K.: A high speed IC truly random number generator based on chaotic sampling of regular waveform. IEICE Trans. Fundam. Electron. Commun. Comput. Sci. **E94-A**(1), 180–190 (2011)
12. Security Requirements for Cryptographic Modules. NIST, Boulder, CO (1994)
13. National Institute of Standard and Technology: A statistical test suite for random and pseudo random number generators for cryptographic applications. NIST-800-22. http://csrc.nist.gov/rng/SP800-22b.pdf (2001)
14. L'Ecuyer, P.: Universit'e de Montr'eal. Empirical Testing of Random Number Generators. http://www.iro.umontreal.ca/~lecuyer/ (2002)
15. Marsalgia, G.: Diehard: A Battery of Tests of Randomness. http://stat.fsu.edu/~geo/diehard.htm (1997)
16. Pecora, L.M., Carroll, T.L.: Synchronization in chaotic systems. Phys. Rev. Lett. **64**(8), 821–824 (1990)
17. Hasler, M.: Synchronization principles and applications. In: Toumazou, C. (ed.) Tutorials IEEE International Symposium on Circuits and Systems (ISCAS '94), London, England, pp. 314327 (1994)
18. Ergün, S.: Cryptanalysis of a double scroll based "True" random bit generator. In: Proceedings of the IEEE 58th International Midwest Symposium on Circuits and Systems (MWSCAS 15), pp. 1–4 (2015)

Part III
Networks

Experiments on Clustering and Synchronous Patterns in a Configurable Network of Chaotic Oscillators

Soudeh Yaghouti, Carlo Petrarca and Massimiliano de Magistris

Abstract We present new experimental results on a recently developed set-up, implementing a dynamically configurable network of chaotic oscillators with Chua's circuits as nodes. The set-up has been designed and tailored to easily perform real time experiments on complex networks with arbitrary topology. We focus here on the emergence of symmetry related synchronization patterns, as well as on the switching among different clusters due to modification of the network structure and/or coupling strength, that are experimentally analyzed for the first time in such type of networks. The observed behavior confirms basic theoretical expectations on small networks, as recently appeared in literature. Moreover the scalability to higher complexity network, as allowed by the considered set-up, is briefly discussed.

1 Introduction

The analysis of oscillatory networks, with possibly chaotic nodes, has received a plenty of scientific interest in the past and recent years (for an extensive review refer to [1, 2]). Their distinguishing characteristics from other modeling paradigms of real phenomena are: (i) collective behavior (better known as "emerging dynamics" differing substantially from individual "stand-alone" ones; (ii) the concept of complexity, that arises from proper combination of non linearity of single nodes and the richness of the interconnection structure. Such interest basically bases on the vast spectrum of potential application domains, ranging from biological systems to social

S. Yaghouti · C. Petrarca · M. de Magistris (✉)
Dipartimento di Ingegneria Elettrica e delle Tecnologie dell'Informazione,
University of Naples FEDERICO II, Via Claudio 21, 80125 Naples, Italy
e-mail: soudeh.yaghouti@unina.it

C. Petrarca
e-mail: carlo.petrarca@unina.it

M. de Magistris
e-mail: m.demagistris@unina.it

G. Mantica et al. (eds.), *Emergent Complexity from Nonlinearity, in Physics, Engineering and the Life Sciences*, Springer Proceedings in Physics 191,
DOI 10.1007/978-3-319-47810-4_9

networks or, in the specific area of circuit and systems, from electric power grids to neural networks.

Synchronization [3] of such networks is one of the most studied effects; in particular, complete synchronization, which implies the coincidence of all state variables, has been widely explored and can be analytically predicted using the Master Stability Function (MSF) [4]. At the same time, the transition from nonsynchronous to synchronous state is a fundamental question in order to understand the synchronization mechanisms [5]. For instance, it has been shown that during such a transition the system can undergo phase synchronization [6, 7] or can form clusters, i.e., groups of state variables in which states belonging to the same cluster are synchronized, while states belonging to different clusters are not correlated [8].

In this context it has been recognized the importance of electronic analog realizations of complex networks as prototypical models of different real systems [9], motivated by the availability of well developed simulation tools and, in principle, by the possibility of realizing prototypes as integrated structures. Nevertheless there are quite few experimental realizations, especially when high cardinality and reconfigurable systems are concerned. We designed and realized an "ad hoc" discrete electronic implementation of a re-configurable network of chaotic oscillators, based on an entirely settable set of interconnections and a robust implementation of Chua's circuits as nodes [10–14]. This unique experimental realization allows, besides the setting of the main node's dynamic parameters, a complete and dynamic control on the coupling network in terms of topologies, link type, direction and strength. A high number of data acquisition channels permits the recording and real time processing of the node's states. As a result, flexible experiments can be easily carried out and the setup can be viewed as an "analog simulator" of a quite general structure network, drastically reducing the time for getting results in realistic configurations, as compared to simulations. At the same time, the effects induced by the coexistence of non-perfectly identical oscillators, i.e., nodes realized with real components, are naturally taken into account.

In this work we use the above mentioned experimental set-up to describe the transition process towards synchronization in networks of non linear oscillators, when some property of the interconnection network is intentionally varied, or the topological structure is suddenly altered by removing or switching some link. In particular, we wish to explore the possible clustering of node's dynamics related to properly defined symmetries in the interconnecting network. We have experimentally found a complex transition from complete synchronization to the uncorrelated regime, with the emergence of clusters described by specific patterns. The results are compared with some theoretical findings as in [15].

2 The Experimental Setup

The structure and realization of the experimental setup has already been described in quite detail in previous papers [10, 11, 14], and will not be repeated. For the sake

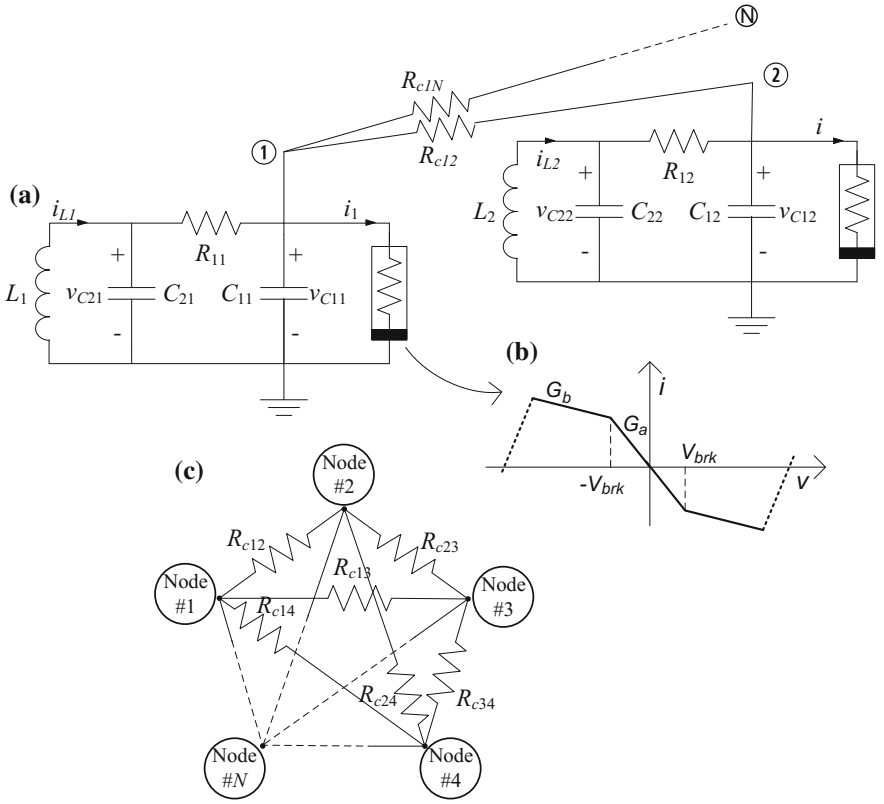

Fig. 1 **a** Chua's circuit typical schematic, reference parameters, **b** Chua's diode characteristic, **c** general schematic of the interconnecting network topology

of clarity only its major features will be briefly summarized hereafter. The network is based on a modular set of Chua's circuits whose dynamics can be individually settled onto periodic or chaotic trajectories. The network nodes are interconnected via a fully reconfigurable link network, with adjustable topologies. Figure 1 depicts a schematic draw of the Chua's nodes and the interconnecting links along with symbols and names of parameters used within the paper.

In the design and simulation phase, requirements in accuracies of realization have been determined, in order to ensure uniformity in the operating conditions between the circuits incorporated in the network. Components have been properly selected to fulfill such realization requirements, as described in [10]. Although the realized setup allows in principle arbitrary choice in determining the structure and the interconnected variables, we will consider in the following the specific case of linking the voltages v_{c1i} across capacitor C_{1i} ($i = 1, \ldots, N$, where N is the number of nodes), as schematically depicted in Fig. 1. The nodes are connected through diffusive links via settable resistance values R_{link}; in particular the link resistances span in the

range 100 Ω to 12.8 kΩ in 255 steps of 50 Ω, in order to properly scan the transition from complete synchronization to complete unsynchronized state, for the considered topologies.

A modular USB multi-channel acquisition system allows to measure and monitor the variables of interest (nodes' states) in real time. Up to 64 state variables can be synchronously acquired. The whole network is controlled via a USB interface from a PC running LabVIEW. A typical full range scan of the parameters range of 255 steps takes about 45 min, this time being mainly dominated by the setting time for the link network at each step.

Evaluation of the synchronization level of the acquired waveforms has been performed by introducing a suitable index I_{cc} calculated by extending at N waveforms the definition of the cross correlation index $I_{cc}(x_i, x_j)$ between two time series $x_i(k)$ and $x_j(k)$:

$$I_{cc}(x_i, x_j) = \frac{\sum_{k=1}^{N_s} \left[\left(x_i(k) - \overline{X_i} \right) \left(x_j(k) - \overline{X_j} \right) \right]}{\sqrt{\sum_{k=1}^{N_s} \left[x_i(k) - \overline{X_i} \right]^2 \left[x_j(k) - \overline{X_j} \right]^2}} \tag{1}$$

where N_s is the number of samples of the signal, $\overline{X_p} = \frac{1}{N_s} \sum_{k=1}^{N_s} x_p(k)$, $p = i, j$ is the mean value of the sequence $x_p(k)$. $I_{cc}(x_i, x_j)$ is 1 when the signals x_i and x_j are identical, it is -1 when they are opposite signals, it is 0 when they are uncorrelated.

In the case of N discrete signals x_p with $p = 1, \ldots, N$ the correlation index I_{cc} can be defined by first calculating the average trajectory as:

$$\overline{x(k)} = \frac{1}{N} \sum_{k=1}^{N} \left(x_p(k) - \overline{X_p} \right), \tag{2}$$

then defining N correlation coefficients $I_{cc}(x_p, \bar{x})$ and calculating their mean value

$$I_{cc} = \frac{1}{N} \sum_{p=1}^{N} I_{cc}(x_p, \overline{x}) \tag{3}$$

Again, the index is bounded in $[-1, 1]$, approaching 1 when all traces are fully synchronized. As will be shown in the following, the plotting of the index $(1 - I_{cc})$ will give a better and clearer resolution of the waveform synchronization.

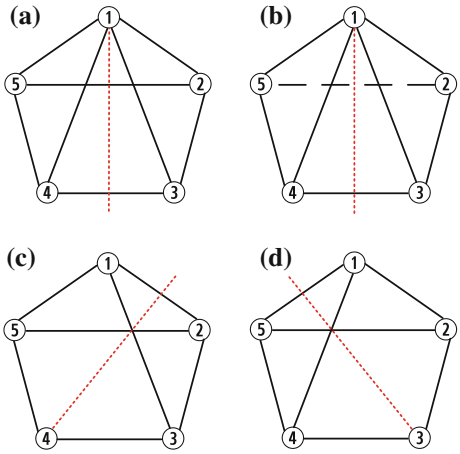

Fig. 2 The topologies considered in paper for a *5* nodes network (the *red-dashed lines* indicate some possible topological symmetries): **a** original network with node *1* connected to all the others; **b** same network with the link *2–5* different from the others; **c** link *1–4* removed from the network (**a**); **d** link *1–3* removed from the network (**a**)

2.1 Experimental Results

Recent articles have analyzed the transition towards synchronization and the possible growth of synchronous patterns in networks of coupled nonlinear oscillators [5–9, 15]. They have theoretically and numerically investigated the role of the network topology and the influence of special links between nodes beyond the complete synchronization regime [16]. In particular it has been demonstrated how also small size regular networks allow to analyze the emergence of topological clustering and synchronous patterns in the transition to complete synchronization. For our experiments we have here considered a simple five-Chua-nodes network, as depicted in Fig. 2a, in which all nodes, when uncoupled, are settled at identical nominal parameters with double scroll chaotic dynamics (for details about the set-up see [10]). In this reference network, we have investigated the transition towards complete synchronization both as a function of the coupling strength, as well as a function of some topological changes.

The main information regarding the interconnection network is well expressed by the rank $N-1$ coupling matrix $C=(c_{ij})$ (where c_{ij} represents the coupling strength between nodes i and j, with $c_{ii}=-\sum_{\forall j\neq i}(c_{ij})$), being it related to both topological and physical interconnection parameters. The analysis of its properties is used to predict the stability of the complete synchronization for linearly coupled identical nodes (via MSF method), as well as for analysis of partial synchronization (stability of clusters), as shown in [15, 16].

Topological symmetries, as resulting from invariant permutations in matrix C (and easily identified at a glance for small networks), are fundamental in the process of creation of symmetry related synchronous clusters in a regime of non complete synchronization, and for the analysis of their stability. Following the concepts of stability along the synchronous dynamics as defined in MSF theory, one can extend the

ideas to the case of partial (clustered) synchronous manifold, and the corresponding transverse manifold by linearizing the perturbed motion around synchronous dynamics. This is done, after defining a permutation matrix P leaving invariant the adjacency matrix A, and block diagonalizing C as:

$$\hat{C} = M^{-1} C M = \begin{bmatrix} C_{tran} & 0 \\ 0 & C_{syn} \end{bmatrix} \tag{4}$$

$$M : M^{-1} P M = \hat{P} = \text{diagonal}$$

In this way the eigenvalues set of C $(0 = \lambda_1 < \lambda_2 < \cdots < \lambda_N)$ is divided into two groups, each belonging to one diagonal block, C_{syn}, with dimension n_2, representing the synchronous subspace and C_{tran}, with dimension n_1, indicating the subspace of transverse motions (with 0 eigenvalue belonging to C_{syn}), satisfying the sorting relations $(0 = \lambda_{1syn} < \lambda_{2syn} < \cdots < \lambda_{n2syn})$, $(\lambda_{1tran} < \lambda_{2tran} < \cdots < \lambda_{n1tran})$ with $N = n_1 + n_2$.

In a network with equal coupling strength ε, the topological condition for getting stable clusters is given from the damping of all transverse motion modes, i.e., $\varepsilon\lambda_{ktran} > \sigma_c$ for all $k = 1, \ldots, n1$, where σ_c is the threshold obtained by MSF beyond which network is globally synchronized. At the same time, if we wish to avoid the trivial global synchronization, at least one of the synchronous modes (except the first one which represents the global synchronization manifold) should be unstable i.e., $\varepsilon\lambda_{2syn} < \sigma_c$, which consequently results in the inequality [15, 16]:

$$\lambda_{2syn} < \lambda_{1tran} \tag{5}$$

With reference to the five nodes network of Fig. 2a, a preliminary analysis has been carried out for the evaluation of the global cross correlation index as a function of the coupling resistance R_{link} (for the case of equally weighed links). At each R_{link} step the resulting waveforms have been recorded and the cross-correlation index I_{cc} calculated (referred to the state variable v_{c1}). The observed trend of $(1 - I_{cc})$ as a function of R_{link} is shown in Fig. 3: synchronized state is characterized by very low values (in the order of 10^{-6}) of the index, and complete synchronization is lost by a sudden and sharp jump of about two orders magnitude. The solid vertical line indicates the theoretical synchronization threshold ($R_{th} = 8843\ \Omega$) as calculated with the Master Stability Function approach, showing a very good agreement to what experimentally observed. After the sharp jump at the synchronization threshold, the curve trend exhibits a quite slow continuous increase to higher values towards unity, when the correlation becomes negligible. At such intermediate cross correlation levels one can expect that, although not completely synchronized, the waveforms still preserve some correlation. Figure 4 shows the waveforms corresponding to two topical points of Fig. 3: the complete synchronization just below the threshold, Fig. 4a ($R_{link} = 9442\ \Omega$), and its loss above the threshold ($R_{link} = 9478\ \Omega$) where the time behavior of v_{c1} at node 1 differs substantially from all other waveforms, whereas all

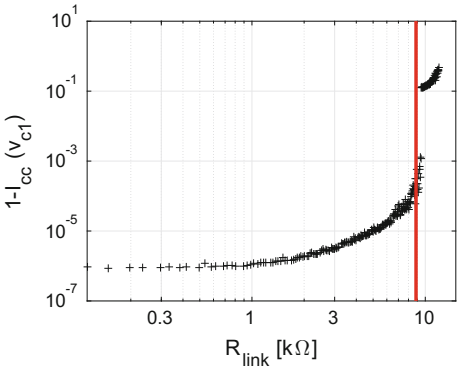

Fig. 3 Cross correlation index $(1 - I_{cc})$ versus R_{link} for network topology of Fig. 2a; *solid vertical line* represents the MSF theoretical threshold for complete synchronization

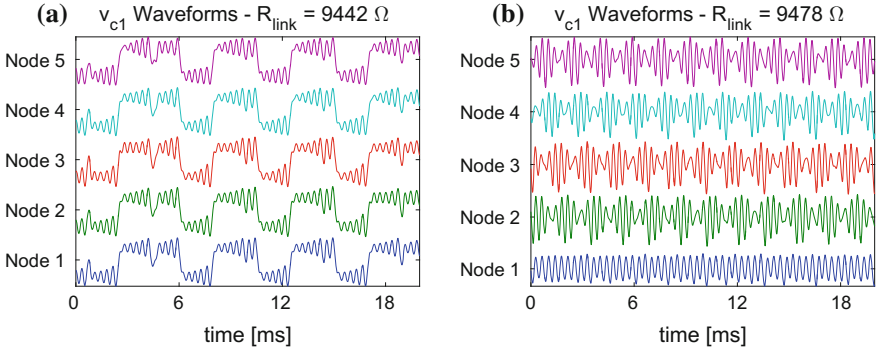

Fig. 4 v_{c1} waveforms for the network topology of Fig. 2a: **a** below the synchronization threshold; **b** above the synchronization threshold, showing lag synchronization among nodes *2*, *3*, *4* and *5* (node *1* is acting as "average" reference node)

the remaining nodes 2, 3, 4 and 5 exhibit some form of "lag" synchronized dynamics. Note that the absence of clustering, also observed at higher values of the coupling resistance, is in agreement, for the considered case, to theoretical results given in [15].

In order to show the effects of changes in topology the following experiments have been realized: the original network of Fig. 2a has been reconfigured twice, each time by removing one link. By removing the link between nodes 1 and 4 we get the network of Fig. 2c; by removing the link 1–3 we obtain the network of Fig. 2d. In both cases, as shown in Fig. 2, the symmetries of the network change and the transition from the synchronized state towards the unsynchronized state behaves differently, as shown in Fig. 5. Unlike the previous case, (Fig. 3) they do not exhibit a sudden loss of synchronization, but a smoother transition within a finite interval of coupling resistance values. The global behavior of the two topologies, from the

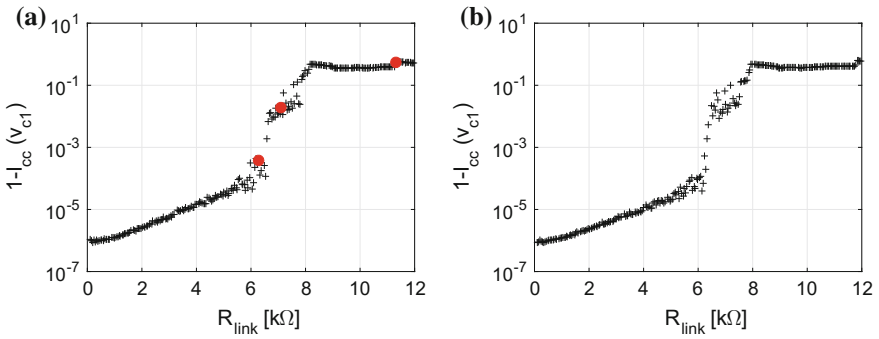

Fig. 5 Cross correlation index I_{cc} versus R_{link} the network topologies 2c (**a**) and 2d (**b**). *Red* topical points in Fig. 6a correspond to $R_{link} = 6278\ \Omega, 7106\ \Omega, 11306\ \Omega$, respectively

complete synchronization perspective, is very similar, as expected due to their dual symmetries.

With reference to the topology of Fig. 2c, we will show the waveforms corresponding to the topical points in Fig. 5a. At the first point the waveforms are well synchronized, corresponding to the low value of their average cross correlation $(1 - I_{cc})$ (Fig. 6a). At the second point they are no longer completely synchronized, whereas the network still keeps some coherence among the nodes by creating some clusters, formed by two couples of nodes (1–2) and (3–5) (Fig. 6b), that reflect the symmetry in the topology. Such clustered synchronization is definitively lost after a second jump in the index at the third point, as confirmed by the waveforms of Fig. 6c.

To better show the topology related clustering behavior, it is possible to calculate the relative correlation index $I_{cc}(x_i, x_j)$ between the two generic waveforms x_i and x_j, as defined in (1). For the considered case, in Fig. 7a, b we report such index as function of the link resistance, for the two considered topologies of Fig. 2c, d. With reference to the 2c topology, the correlation between nodes 3–5 and 1–2 are shown in Fig. 7a. It is possible to observe that the clustering of nodes 3–5 is maintained in quite a large resistance range, while the correlation between nodes 1–2 decreases continuously as the link resistance increases. Moreover, at a certain threshold ($R_{link} = 11300\ \Omega$) the cluster (3–5) suddenly disappears, whereas the cluster (1–2) is only partially recovered: as a consequence, the network undergoes a sudden jump towards the globally unsynchronized state. The analysis of Fig. 7b, referring to topology (2d), reveals the duality of the two cases, notwithstanding minor differences due to realization tolerances.

A last experiment has been considered, to study how the growth of synchronous patterns can be affected by varying the coupling strength (weight) of a single link, where all the rest stay unchanged, as theoretically discussed in [15]. The reference topology is that indicated in Fig. 2b in which, leaving the basic symmetry unaffected, we change the weight (that is the value of the link resistance) between the nodes (2–5), keeping all other link values fixed ($R_{link} = 10\ \text{k}\Omega$).

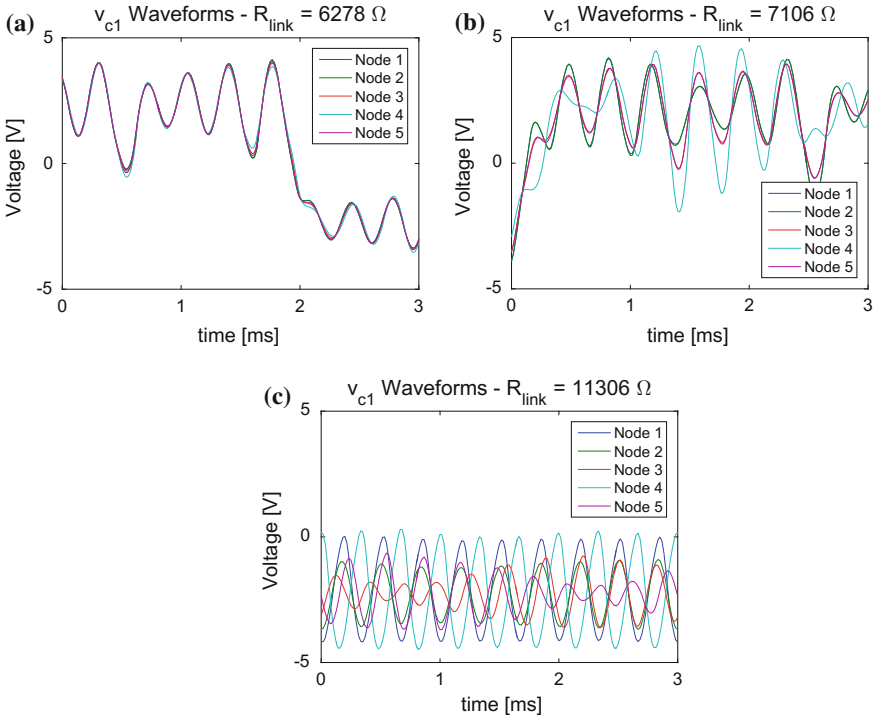

Fig. 6 Waveforms for topology (2c): **a** complete synchronization; **b** formation of clusters; **c** complete loss of synchronization

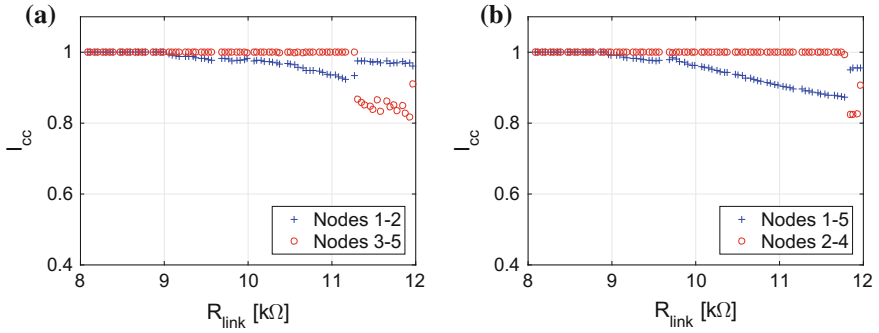

Fig. 7 Relative cross correlation index $I_{cc}(x_i, x_j)$ versus R_{link}: **a** for the topology (2c); **b** for the topology (2d)

First of all we observe that, even for very small value of the link resistance $R_{link(2-5)}$, the global synchronization is never achieved. However it is very interesting to observe that (Fig. 8), with increasing $R_{link(2-5)}$, clusters between nodes (2–5) and nodes (3–4) are first formed, then they disappear in the interval $[7.9 - 10.8]$ kΩ,

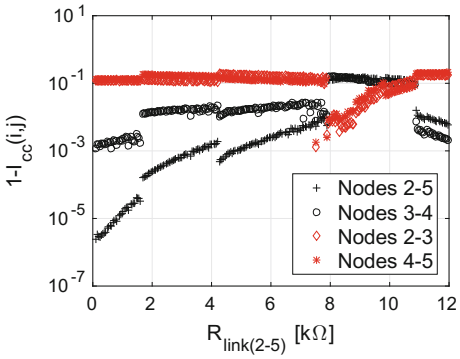

Fig. 8 Relative cross correlation index $I_{cc}(x_i, x_j)$ versus R_{link} for topology (2b), as a function of the link resistance $R_{link(2-5)}$ between nodes $(2-5)$

where they are substituted by different clusters formed by the couples of nodes (2–3) and (4–5). By further increasing the link resistance above 10.8 kΩ, the clusters (2–5) and (3–4) appear again while clusters (2–3) and (4–5) disappear. Such behavior is better brought to evidence by means of the oscillator's deviation [5] from the synchronous manifold of the corresponding cluster, defined as:

$$\Delta v_{c1i}(k) = (v_{c1i}(k) - \langle v_{c1}(k)\rangle) \tag{6}$$

where $\langle v_{c1}(k)\rangle$ is the mean value at k_{th} sample of the waveforms belonging to the cluster. It has been calculated both for cluster (2–5) and (2–3) in Fig. 9a at three different values of the link resistance. The mutually exclusive formation and disappearance of clusters is visually distinguishable.

We complete the analysis of this case by evaluating the eigenvalues of synchronous and transverse manifolds. In Fig. 9b their dependency on $R_{link(2-5)}$, within the considered range, is given. The clusters, previously evidenced experimentally, are now explained in terms of the reciprocal relation-ships between transverse and synchronous eigenvalues subsets, according to inequality (5).

At $R_{link(2-5)} = 10$ kΩ we have all equal links weight and the coupling strength ε value is below the MSF threshold, where complete synchronization is not possible. For smaller values of $R_{link(2-5)}$ we get $\lambda_{2syn} < \lambda_{1tran}$, in this way satisfying inequality (5) and, accordingly, having the possibility of stable clusters. For example, the vertical line R_1 in Fig. 9b is the value of $R_{link(2-5)}$ where the cluster formation between (2–5 and 3–4) is proved experimentally as reported in Fig. 9a. Interestingly, for $R_{link(2-5)}$ larger than 10 kΩ the appearance of a stable cluster is reported experimentally in some region where $\lambda_{2syn} > \lambda_{1tran}$, (i.e., $R_{link(2-5)} = R_3$ in Fig. 9b). This result is only apparently in contrast to results given in [15], since in that case linearization of the whole system is given about the global synchronous manifold.

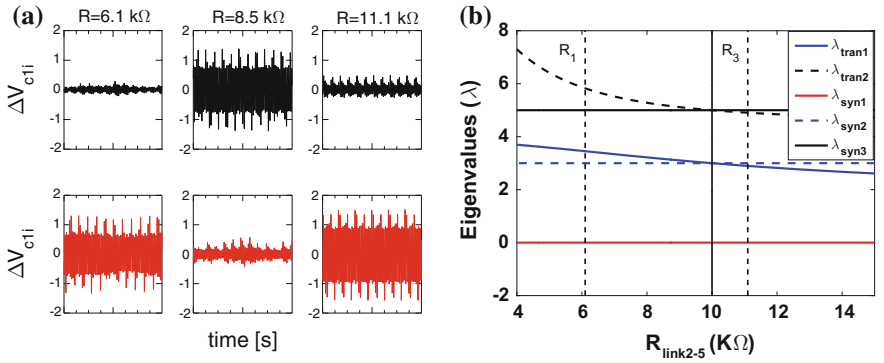

Fig. 9 **a** Oscillator's deviation Δv_{c1i} for clusters (2–5) (*red*) and cluster (4–5) (*black*); **b** coupling matrix eigenvalues dependency on the link resistance $R_{link(2-5)}$. The value $R_{link(2-5)} = 10$ kΩ represents the situation of equal links weights, with the network coinciding in this case to that of Fig. 2a

2.1.1 Conclusions

We have reported a new set of experiments on the transition from complete synchronization to patterns of clusters in complex networks with topological symmetries, as a function of topology and/or global/individual coupling strengths of the links. Emerging of some clusters have been observed, according to theoretical expectations, as well as the switching among possible clusters related to the modification of the network structure and/or coupling strength. This study, although preliminary and confined to small networks and few topologies, has revealed the wide potential of the considered experimental realization for such kind of investigations. The scalability of the setup to higher complexity network will be exploited in the future in wider experimental campaigns on the topologically induced clustering, in which of theoretical tools for their prediction could be validated. In particular we plan to explore complete networks of 6 and 7 nodes (that are in the full capability of the present set-up), in this way greatly enlarging the combinations of possible clusters to be evidenced.

References

1. Strogatz, S.H.: Exploring complex networks. Nature **410**(6825), 268–276 (2001)
2. Boccaletti, S., Latora, V., Moreno, Y., Chavez, M., Hwang, D.U.: Complex networks: structure and dynamics. Phys. Rep. **424**(4), 175–308 (2006)
3. Arenas, A., Diaz-Guilera, A., Kurths, J., Moreno, Y., Zhou, C.: Synchronization in complex networks. Phys. Rep. **469**(3), 93–153 (2008)
4. Pecora, L.M., Carroll, T.L.: Master stability functions for synchronized coupled systems. Phys. Rev. Lett. **80**(10), 2109 (1998)

5. Pecora, L.M., Sorrentino, F., Hagerstrom, A.M., Murphy, T.E., Roy, R.: Cluster synchronization and isolated desynchronization in complex networks with symmetries. Nat. Commun. **5**, 4079 (2014)
6. Rosenblum, M.G., Pikovsky, A.S., Kurths, J.: From phase to lag synchronization in coupled chaotic oscillators. Phys. Rev. Lett. **78**(22), 4193 (1997)
7. Zhou, C., Kurths, J.: Noise-induced phase synchronization and synchronization transitions in chaotic oscillators. Phys. Rev. Lett. **88**(23), 230602 (2002)
8. Zhou, C., Kurths, J.: Hierarchical synchronization in complex networks with heterogeneous degrees. Chaos: an Interdisciplinary. J. Nonlinear Sci. **16**(1), 015104 (2006)
9. Corinto, F., Biey, M., Gilli, M.: Nonlinear coupled CNN models for multiscale image analysis. Int. J. Circuit Theory Appl. **34**(1), 77–88 (2006)
10. de Magistris, M., di Bernardo, M., Di Tucci, E., Manfredi, S.: Synchronization of networks of non-identical Chua's circuits: analysis and experiments. IEEE Trans. Circuits Syst. I: Regul. Papers **59.5**, 1029–1041 (2012)
11. Colandrea, M., de Magistris, M., di Bernardo, M., Manfredi, S.: A fully reconfigurable experimental setup to study complex networks of Chua's circuits. In: Proceedings of NDES 2012 Nonlinear Dynamics of Electronic Systems (VDE), pp. 1–4 (2012)
12. Petrarca, C., Yaghouti, S., de Magistris, M.: Experimental dynamics observed in a configurable complex network of chaotic oscillators. In: Nonlinear Dynamics of Electronic Systems, pp. 203–210. Springer International Publishing, Berlin (2014)
13. Petrarca, C., Yaghouti, S., Corti, L., de Magistris, M.: Analogic realization of a non-linear network with re-configurable structure as paradigm for real time analysis of complex dynamics. In: Advances in Neural Networks: Computational and Theoretical Issues, pp. 375–382. Springer International Publishing, Berlin (2015)
14. de Magistris, M., di Bernardo, M., Manfredi, S., Petrarca, C., Yaghouti, S.: Modular experimental setup for real-time analysis of emergent behavior in networks of Chua's circuits. Int. J. Circuit Theory Appl. **44**, 8, 1551–1571 (2016)
15. Fu, C., Lin, W., Huang, L., Wang, X.: Synchronization transition in networked chaotic oscillators: the viewpoint from partial synchronization. Phys. Rev. E **89**(5), 052908 (2014)
16. Ao, B., Zheng, Z.: Partial synchronization on complex networks. EPL (Europhys. Lett.) **74**(2), 229 (2006)

Complex Structures and Behavior from Elementary Adaptive Network Automata

Daniel Wechsler and Ruedi Stoop

Abstract Adaptive networks are systems where a network structure evolves in interaction with, and depending on, node dynamics and where the node dynamics evolution depends on the actual network structure. This is a setting of fundamental relevance for neuronal culture development, for which often power law characteristics and indications of a critical state are found. Investigating an extremely simple instance of this computational paradigm of adaptive networks, we find particular rules and parameters for which power-law statistics emerge, which provides evidence that this fundamental framework is able to provide robust network structure evolution towards a critical state, an issue of great current interest.

1 Introduction

The paradigm of life at the edge of chaos [1] places the theory of Per Bak of nature self-organizing towards criticality [2] in an evolutionary context. The exact way how this may or even has to happen in a measure-theoretic sense, has, however, not been answered. If this theory is relevant to nature, we should be able to find fundamental computational principles that based on evolutionary principles would lead to such a state, where an asset would be if such computational paradigms could be related in some sense to biological data. Since the fitness landscape guiding evolution is, in terms of dimensions, variables and interrelation interdependencies, beyond what possibly could be described in a model without severe simplification (and hence the optimality function is not seizable), evolutionary optimization in its standard approach does not apply, and the question emerges, how this could be circumvented in a mathematical and physics framework.

D. Wechsler · R. Stoop (✉)
Institute of Neuroinformatics and Institute for Computational Science, University of Zürich, Winterthurerstr. 190, 8057 Zurich, Switzerland
e-mail: ruedi@ini.phys.ethz.ch

D. Wechsler · R. Stoop
ETH Zürich, Zurich, Switzerland

G. Mantica et al. (eds.), *Emergent Complexity from Nonlinearity, in Physics, Engineering and the Life Sciences*, Springer Proceedings in Physics 191,
DOI 10.1007/978-3-319-47810-4_10

This question could be pursued in various ways. One approach would be to consider network optimization based on some global measure, such as, e.g., a weighted convex combination of normalized averaged path length and normalized density of the network [3]. It can be shown that if such an optimization is implemented by genetic algorithms, the optimal network structures that we arrive at for a substantial interval of the convexity parameter, yields emergence of hubs, which can be associated with the often observed in nature presence of power laws.

One of the simplest, and yet most fundamental formulation of the problem to understand the routes along which these phenomena emerge, is, however, the adaptive network paradigm, in which the fitness landscape paradigm is mapped onto instances of computational rules. In this way, the development is guided by fixed rules that act locally, without having access to globally measured quantities. The rule itself can be interpreted as expressing fundamental properties of the network that is dealt with. In this work, we implement this paradigm in the computational model of an elementary adaptive automata [4]. Here, the situation is similar to the elementary cellular automaton (ECA) paradigm [5, 6], where only a small set of rules is able to generate a language of Turing power (in the sense of the Chomsky hierarchy of languages [7]), could be seen as a computational paraphrase of a critical state.

We will see that a few rules in our paradigm have the potential to generate a critical network state, if associated parameters are appropriately chosen. The in-depth analysis of one of these rules shows explicitly how from our simple model, an extremely rich interplay between topology and node dynamics emerges. As a result, it appears that we have found a minimal model of an adaptive network that can be used to study in more detail the properties of this class.

Our formulation links the notions of a network with that of a computational paradigm. Because of the fundamental nature of the network notion, networks arise in a variety of different scientific disciplines, where they have been mainly used to successfully describe collective and statistical features of ensembles consisting of coupled actors (the nodes of the network). Examples are traffic networks, power grids or the Internet, trade networks, phone call graphs, or collaboration networks. Other networks are the product of biological evolution and manifest themselves, for instance, in gene networks, food webs, or neural networks.

To demonstrate how the two viewpoints are related, a straightforward pathway is provided by the 2d-version of a cellular automaton, the game of life [8] (that also has been shown to host Turing power). If we consider the plane as a lattice of cells (squares) with each one having exclusively state spin up or state spin down property (cf. Fig. 1), the spin property may change according to some update rule. Conventionally, the new state will depend on the state the square had before, the states of the topologically neighboring squares (usually, the four-fold von Neumann neighborhood of range 1 or range 2 (12 neighbors in the latter case) is considered), and the implemented update rule. By connecting cells to the neighbors that are in the same state (or by looking at the system's adjacency matrix), we arrive in a natural manner at the structure of a network.

In rare cases (in terms of rules, parameters and initial conditions), we obtain networks that are in a sense 'invariant' under evolution by the rule, such as the 'glider'

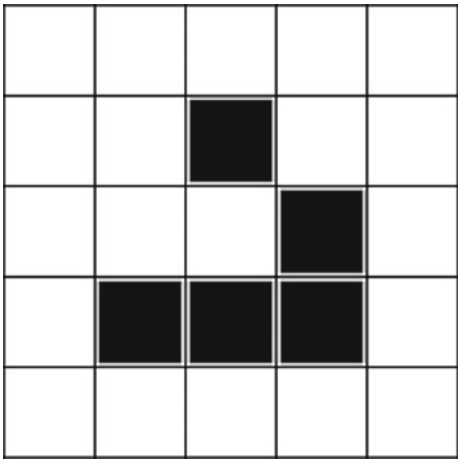

Fig. 1 Glider structure, able to move across a 2d-lattice, upon time evolution defined by the game-of-life automaton. During movement, such structures are often oscillating in their form

of Fig. 1. For such subnetworks, it was investigated how the dynamical behavior of the ensemble depends on the topology of the underlying network [9–13]. These investigations pointed out that the topology has a crucial influence on the dynamical processes occurring on the network [10, 11] and they led to a variety of well-established models of collective dynamics given a complex, such as scale-free, or a small-world network topology. For instance, small-world networks would lead to a faster convergence in opinion formation [14] or scale-free networks would entail a higher vulnerability of the spread and persistence of diseases [15].

Networks that change in time in configuration and size according to a nontrivial rule are the next level of complexity. In the literature, the terms 'adaptive' or 'co-evolutionary network' are used to refer to this class of dynamical networks [16]. This paradigm is becoming well-recognized as an important challenge to network science [9, 17, 18], as many real-world networks demonstrate instances where the evolution of the topology and the dynamical process on the network are deeply coupled (e.g., virus spreading). Due to the different time-scales that may distinguish network shaping and node dynamics, for providing sufficient variability of the evolving networks, a probabilistic notion may be necessary within the computational rule.

A noteworthy example of study of adaptive networks is in connection with self-organized criticality [2] of neural networks (Fig. 2). Self-organized criticality is a property of certain dynamical systems to evolve towards a critical state, where system observables have no characteristic scale and follow a power law distribution. This state has been found to be maximally efficient in terms of information-related measures, such as the storage and transmission of information [19–22] and sensitivity to sensory stimuli [20, 22]. In addition, empirical evidence has shown that the size of neural avalanches (phases of ongoing neural activity interrupted by phases of quiescence) follow a power law distribution [23], supporting a hypothesis that the brain 'operates at criticality'. The precise mechanisms that allow biological neural networks to converge to this critical state are, however, not known. The authors of [24]

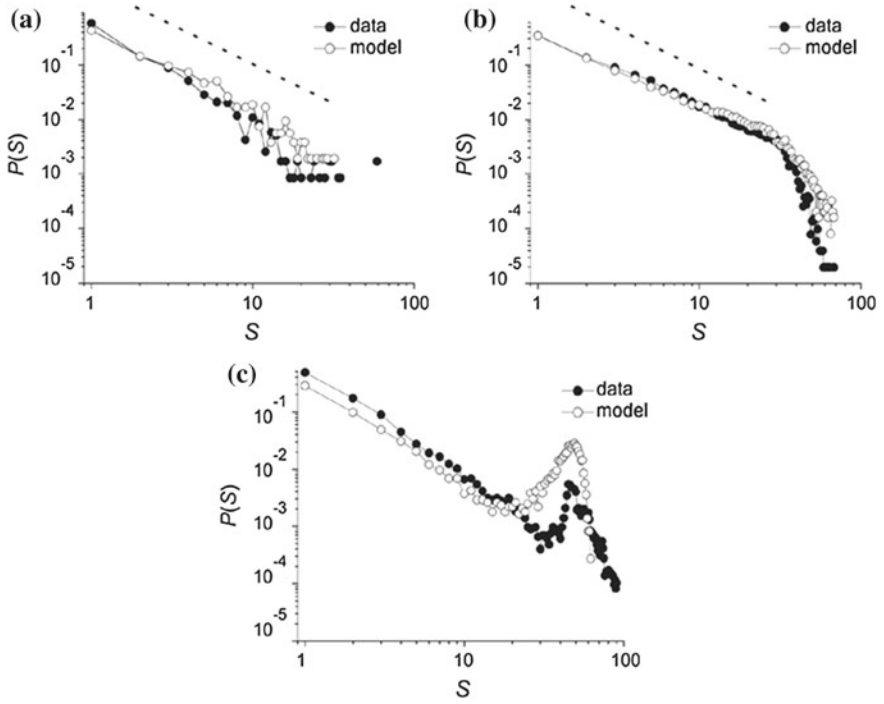

Fig. 2 Situation advocating the presence of a critical state: Tuning of the avalanche distribution in biological neural networks using pharmacological agents [19]. **a** Subcritical regime induced by excitatory antagonist CNQX. **b** Critical regime, normal network. **c** Supercritical regime induced by inhibitory antagonist PTX

proposed a model of an adaptive threshold network based on simple local rewiring rules, that robustly self-organizes towards a critical state. There are a number of other recent studies on adaptive networks covering topics such as consensus formation [25, 26], emergence of cooperation [27] or organization dynamics [28]. More recent contributions have emphasized the relation to critical branching processes [19, 29–33], which provides an improved correspondence between cortical experiments and exponents obtained at criticality.

A model of an adaptive network thus includes an evolving network, and a dynamical process that takes place on the network nodes and their interaction. It requires a coupling between the two evolutions, such that their temporal evolutions mutually depend on each other. The state of a node evolves according to a rule that depends on the states of its neighboring nodes. That way a dependence of the dynamical process on the network topology is achieved. Conversely, the network topology depends on node dynamics by modifying the connections through a rule that takes into account the dynamical state of the system. This general definition of an adaptive network model of course allows for various possible implementations.

As a side-note, from biology, this paradigm can be seen as a mapping of a process of evolving neural cultures. In a recent study of in vitro neuronal activity of dissociated hippocampal neurons recorded from micro-electrodes, we found that the spatiotemporal correlations decay, as a function of the time, in an exponential manner. For activity that consists of isolated bursts, this would be equivalent to an exponential decay of the spike frequency within the burst. We consequently modeled bursts by exponentially decaying spiking probability and found avalanche size distributions that are well-modeled by power laws. Also for inter-event interval distributions that in many respects are more natural observables than spike frequency distributions, we found avalanche-size power laws, for the experimental data, as well as for the data generated from our model. Moreover, we were able to calculate within this framework the power law exponents analytically and to compare them with the experimental data, resulting in a good agreement. In the present work, we exhibit evidence for even a simpler, computationally more direct process that may lead to power law distributions.

2 A Ring that Rules Them All

Automata are considered the simplest and the most generic form of complex systems; they have become the canonical examples for the emergence of complex collective behavior through local interactions of simple units [10, 34]. The success of cellular automata as an intuitive modeling paradigm for complex systems [34] inspired the design of the automaton used in this work. While for cellular automata the rules determine the states of its cells at the next time step, in the derived adaptive automaton paradigm the rules define the transformation of the network topology depending on the dynamical state, but, moreover, also on the current connectivity.

The evolving network is represented by a directed and unweighted graph with a fixed number of nodes N, so that it is at any time step t fully characterized by the $N \times N$ adjacency matrix A_t. The entries of $A_t(i, j) \in \{0, 1\}$ determine whether there exists a connection from node i to node j. Self-connections are not allowed; therefore $A(j, i) = 0, \forall i = j$. To distinguish between the source and the target node of a directed connection, the term 'input' or 'preceding' node will be used for the former, and 'successor' node to refer to the latter. The number of incoming connections of a node is its 'in-degree' k_{in} and the number of outgoing connections is its 'out-degree' k_{out}.

The dynamics of the nodes is binary: Each node can only be in one of two states $S \in \{0, 1\}$; usually, we will use the term 'active' if a node is in state 1 and 'inactive' for state 0. At any time t, the dynamical state of the automaton is fully defined by the vector S_t of size N, where entry $S_t(i)$ indicates the state of the node i.

The dynamical state is updated according to a probabilistic transition. Whether node i will be active at time $t + 1$ depends on the number k^i of active nodes projecting on node i at time t, $k^i = \sum_{j=1}^{N} S_t(j) A_t(j, i)$. Each of them can put node i into the active state with probability p_{ac}. The total probability of node i for being in the active

Fig. 3 Rule table of automaton 21

$S_t(j)$	$A_t(j,i)$	$S_t(i)$	$A_{t+1}(j,i)$
0	0	0	0
0	0	1	0
0	1	0	0
0	1	1	1
1	0	0	0
1	0	1	1
1	1	0	0
1	1	1	1

state at time $t + 1$ is therefore

$$P(S_{t+1}(i) = 1) = 1 - (1 - p_{ac})^{k^i}, \tag{1}$$

where all nodes in the network are updated simultaneously. If the node is not activated by at least one of its inputs, it will become inactive. The topology is thus updated by the removal and creation of edges. As the state of the system is determined by whether a link from node j is pointing to node i, which involves $S_t(j)$, $S_t(j)$ and $A_t(j, i)$, and since these tree values are all binary, there are in total eight possible configurations. For each of these eight configurations it can be specified whether an edge should be established, $A_{t+1}(i, i) = 1$, or not, $A_{t+1}(j, i) = 0$. This allows for $2^{2^3} = 256$ different mappings.

Each such mapping is called a 'rule', or an 'automaton'. It can be represented by a table that lists all possible $S_t(i)$, $A_t(j, i)$, $S_t(i)$ configurations together with the rule-specific value of $A_{t+1}(j, i)$. Figure 3 provides an example of a rule table.

A particular position in a rule table can be addressed by the short form

$$R_{S(j)A(j,i)S(j)} \in \{0, 1\}.$$

For a convenient way of referencing, each rule is named the decimal correspondent to the binary number $R_{000}R_{001}R_{010}R_{011}R_{100}R_{101}R_{110}R_{111}$. For example, the rule in Fig. 3 extracted as 00010101 evaluates to $0 \cdot 2^7 + 0 \cdot 2^6 + 0 \cdot 2^5 + 1 \cdot 2^4 + 0 \cdot 2^3 + 1 \cdot 2^2 + 0 \cdot 2^1 + 1 \cdot 2^0 = 21$, i.e. rule 21. This follows the standard enumeration of the rules found for elementary cellular automata [4, 6].

An important ingredient of our approach is that like in most real-world networks, the structure evolves much slower compared to the dynamics of the nodes. To account for this, the removal or creation of an edge is only effectuated with a probability p_{em} per each update step. In this way, for small p_{em}, the topology evolves much slower than the node state. For $p_{em} = 1$, topology and node dynamics evolve at the same

pace. The model that we look at is therefore an example of a probabilistic automaton [6], although of a somewhat particular kind.

3 Emerging Topologies

The model space is therefore characterized by the rules, by node activation probability p_{act} and by edge mutation probability p_{em}. Our aim still is to identify regions in model space where non-trivial network topologies and node dynamics can arise. The isolation of such regions requires a screening process; however, the following obvious distinction can be made:

- the network has converged to a state where all nodes are inactive. The only rule table positions that are effective in this situation are R_{000} and R_{010}. Their values consequently determine the resulting network topology. The four possible combinations and the resulting topologies are then defined by Fig. 3.
- the network has converged to a state where all nodes are persistently active. This happens if the topology is kept in a configuration with a high in-degree that lets the probability of the nodes to be active to be close to one. Whether this can happen depends in particular on R_{101} and on R_{111} (for more details see the next sections). Complex network topologies and complex dynamical behavior only arise in regions where the automaton is able to maintain an intermediate activity level. Therefore, of interest is the average activity level to which the network converges, under the action of the automaton, defined as the fraction of nodes that are active at a particular time step. Averages are denoted by the symbol $\langle . \rangle$.
- the network has converged to a static topology, $p_{em} = 0$. Here, the final activity level depends directly on the activation probability p_{act} and on the average in-degree $\langle k_{in} \rangle$ (note that $\langle k_{in} \rangle = \langle k_{out} \rangle$).
- we deal with a trivial rule:
  Rule 0 is the rule that only removes edges from the network. If $p_{em} > 0$, this leads to a completely disconnected and therefore inactive network.
  Rule 255, in contrast, only creates new edges and never removes existing ones. For $p_{em} > 0$, the network ends up fully connected with the final activity depending on the activation probability.
  Rule 51 is the static rule: Since for all positions in the rule table $A_t = A_{t+1}$, the connectivity of the network never changes and therefore its activity is determined by the initial connectivity and the activation probability.

The two dynamical extremes are separated by usually a narrow band in which the activity settles down to intermediate levels (e.g., Fig. 5). In such regions, one can expect to find a non-trivial interplay between topology and node dynamics, which might give rise to complex system level-properties. Since each rule, however, manifests a unique dependence of the topology on the dynamics, one can expect to encounter various characteristic situations of behavior in the $p_{em} \times p_{act}$ parameter space.

4 Classes of Emergent Behavior

With just a few exceptions, the behavior of an automaton is independent of the rule table positions R_{001}, R_{010} and R_{011}. Hence if only these entries are changed in a rule, the same dependence of the average activity on p_{act} and on p_{em} is observed. Grouping rules together that only differ in R_{001}, R_{010} and R_{011} leaves 32 groups of eight rules each. For 29 groups the dependence of the average activity on p_{act} and on p_{em} is almost identical. Only for three of these groups, the behaviors of the rules within the group are significantly different. According to this scheme, all rules can be assigned to eleven classes, corresponding to the eleven basic types with eight classes having eight rules, two classes having 32 rules and one class having 128 rules. According to the classifications logic, an x (='arbitrary') occurs wherever appropriate. Each class was given a name that reflects its general behavior in terms of average activity, evaluated by simulating each rule for p_{act} and p_{em} combinations covering the parameter space at regular intervals of $\Delta p_{act} = \Delta p_{em} = 0.025$. Due to the large number of simulations (430336 in total) required for a screening at this resolution, modest networks of $N = 50$ nodes were used. The networks were initialized with $p_{k_{init}} = 0.5$ and $p_{a_{init}} = 0.5$ and the automaton was iterated for $T = 1000$ time steps. These are the classes of emergent behavior (partial fulfillment):

- Trivial class:
  Pattern: 0xxx 0000
  Rules: 0, 16, 32, 48, 64, 80, 96, 112

One straight critical line

- One straight 'critical line' separates the region where activity dies out (inactive region) from the region where activity sustains (active region). For a large subset, the transition does not depend on p_{em}.

  Rules: 6, 7, 9, 11, 12, 13, 14, 15, 22, 23, 25, 27, 28, 29, 30, 31, 38, 39, 41, 43, 44, 45, 46, 47, 54, 55, 57, 59, 60, 61, 62, 63, 70, 71, 73, 75, 76, 77, 78, 79, 86, 87, 89, 91, 92, 93, 94, 95, 102, 103, 105, 107, 108, 109, 110, 111, 118, 119, 121, 123, 124, 125, 126, 127, 134, 135, 137, 139, 140, 141, 142, 143, 150, 151, 153, 155, 156, 157, 158, 159, 166, 167, 169, 171, 172, 173, 174, 175, 182, 183, 185, 187, 188, 189, 190, 191, 198, 199, 201, 203, 204, 205, 206, 207, 214, 215, 217, 219, 220, 221, 222, 223, 230, 231, 233, 235, 236, 237, 238, 239, 246, 247, 249, 251, 252, 253, 254, 255

- straight 'critical line', but overall gradient-like dependence on p_{em}
  Pattern: xxxx 10x1
  Rules: 8, 10, 24, 26, 40, 42, 56, 58, 72, 74, 88, 90, 104, 106, 120, 122, 136, 138, 152, 154, 168, 170, 184, 186, 200, 202, 216, 218, 232, 234, 248, 250

- straight 'critical line', but overall gradient-like dependence on p_{em}
  Pattern: 1xxx 0011
  Rules: 131, (147), 163, (179), (195), (211), (227), (243)

- inclined critical line, without gradient.
  Pattern: 0xxx 0011
  Rules: 3, 19, 35, (51), (67), (83), (99), (115)
- inclined critical line, with gradient.
  Pattern: 0xxx 0001
  Rules: 1, 17, 33, 49, 65, 81, 97, 113

One curved critical line

- curved critical line, almost no gradient, except for high p_{em}. The region where the average activity takes intermediate values is in this case limited to the vicinity of the critical line, getting slightly more pronounced towards higher p_{em}.
  Pattern: xxxx 010x
  Rules: 4, 5, 20, 21, 36, 37, 52, 53, 68, 69, 84, 85, 100, 101, 116, 117, 132, 133, 148, 149, 164, 165, 180, 181, 196, 197, 212, 213, 228, 229, 244, 245
- curved critical line, but with gradient.
  Pattern: 1xxx 0001
  Rules: 129, 145, 161, 177, 193, 209, 225, 241

Two critical lines

- Straight first critical line:
  Pattern: 1xxx 0010
  Rules: 130, 146, 162, 178, 194, 210, 226, 242 (straight first transition line)

  Pattern: 0xxx 0010
  Rules: (2), 18, (34), 50, 66, 82, 98, 114
- Curved first critical line, not fully developed
  Pattern: 1xxx 0000
  Rules: 128, 144, 160, 176, 192, 208, 224, 240

5 Exemplary Discussion of a Class with Critical Behavior

In the following, we investigate the 1xxx 0001 pattern class, by focusing, specifically, on rule 209.

5.1 Rule 209

This class is an exception to the regularity that mainly rules having $R_{101} = 0$ and $R_{111} = 1$ exhibit, by showing large regions of intermediate activity. This fact together with the inspection of results of individual simulations suggested an in-depth analysis of rule 209, the rule table of which is shown in Fig. 4. Figure 5 shows the activity heat map for rule 209. It was obtained from simulations based on networks of size $N = 100$.

$S_t(j)$	$A_t(j,i)$	$S_t(i)$	$A_{t+1}(j,i)$
0	0	0	1
0	0	1	1
0	1	0	0
0	1	1	1
1	0	0	0
1	0	1	0
1	1	0	0
1	1	1	1

Fig. 4 Rule table of automaton 209

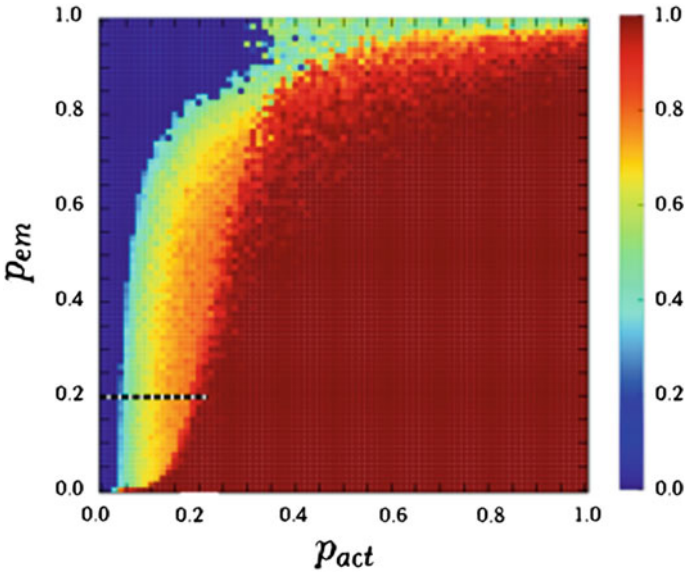

Fig. 5 Activity heat map for rule 209. The *color* indicates the average activity of the last 50 iterations of simulations over $T = 1000$ time steps in the p_{act}, p_{em} parameter space. For all simulations the network size was $N = 100$. The resolution is 80×80 simulations ($\Delta p_{act} = \Delta p_{em} = 0.0125$). The *dashed line* indicates the cut along which we will sample the behavior of the rule

We will focus in the following on the cross section indicated in Fig. 5 by a dashed line at $p_{em} = 0.2$. For all simulations in the subsequent investigations, networks of size $N = 100$ were considered. In Fig. 6 we compare the average activities exhibited by the rules 129 (a), 177 (b), 209 (c) and 225 (d) along the cross section (dots). The average was extracted from the last 50 iterations of simulations over 4000 time steps. The sharp transition apparent there is an artifact caused by the limited simulation

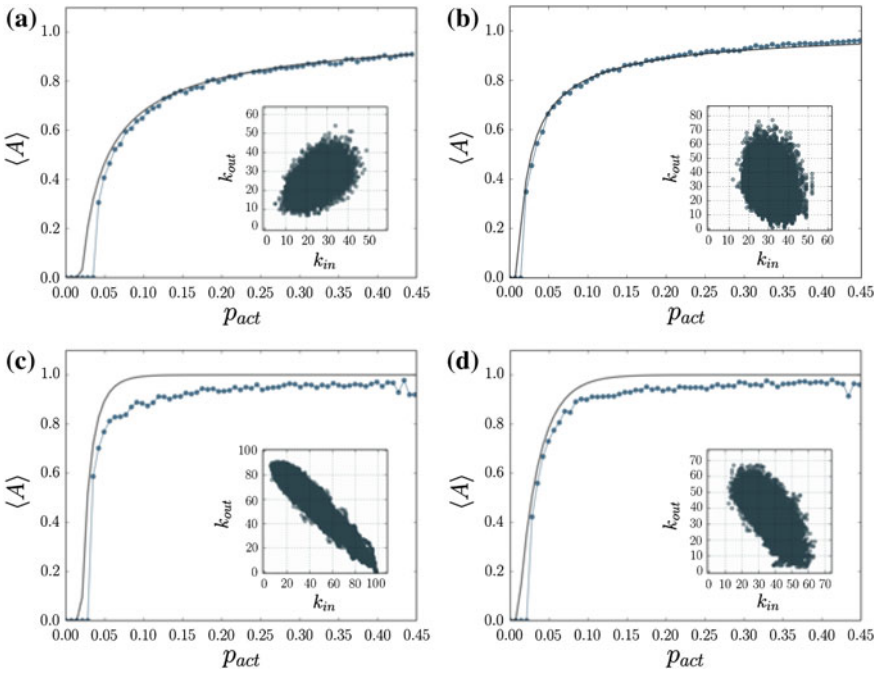

Fig. 6 Average activity along a cross section parallel to the p_{act} axis at $p_{em} = 0.2$ for the rules 129 (**a**), 177 (**b**), 209 (**c**) and 225 (**d**) (*dots*). *Solid lines*: Average activity predicted by the mean field model. *Insets*: In- versus the out-degree of all nodes in the last 50 iterations ($p_{act} = 0.06$)

duration. The larger p_{act}, the longer the automaton initially stays in a phase of full activity, until it eventually converges to its equilibrium activity level.

5.2 Node Dynamics of Rule 209

The three raster plots shown in Fig. 7 exhibit the obtained node dynamics. They show the states of 50 nodes over 100 time steps, from simulations at $p_{act} = 0.03$ (a), $p_{act} = 0.079$ (b) and $p_{act} = 0.14$ (c). The nodes are aligned horizontally, and their state at a certain time step (vertical axis) is indicated by a single dot in the image (black = active, white = inactive). There are notable qualitative differences in the behavior of the node dynamics. In (a) all nodes erratically switch from active to inactive. This results in a rather disordered and random raster plot. In (c) only about half of the nodes switch between active and inactive. The remaining nodes are constantly active during the considered time window. The resulting vertical stripes make the raster plot look fairly ordered. The behavior in (b) appears to lie somewhere between (a) and (c).

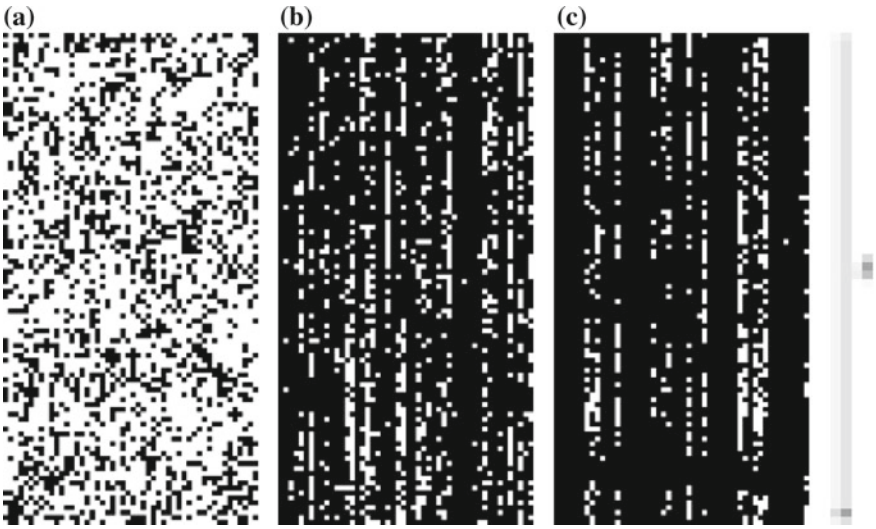

Fig. 7 Node dynamics of rule 209 at $p_{act} = 0.03$ (**a**), $p_{act} = 0.079$ (**b**) and $p_{act} = 0.14$ (**c**) ($p_{em} = 0.2$). The raster plots show the states of 50 nodes (horizontal direction) over 100 time steps (vertical direction). *Black* = activated node, *white* = inactive node

To estimate the Lyapunov exponent for the adaptive network automaton, a method proposed in [35] was used. The automaton is initialized at $t = 0$ with a random state and a random network. To account for a convergence phase, the automaton is iterated for t_0 time steps. Hereafter, the state of the automaton at the next time step $t_0 + 1$ is computed for the original state S_{t_0} and a minimally perturbed state $\hat{S}_{t_0}$. Of interest is the change of the initially minimal distance $H(S_{t_0}, \hat{S}_{t_0})$ upon iteration of both. As distance function H, the normalized Hamming distance is used (computed as the fraction of entries in the two state vectors that are not identical). The minimal perturbation corresponds to the flip of a single entry in the state vector; this results in a Hamming distance of $1/N$. To get a reliable estimate, the procedure is repeated m times and an average $\langle H(S_{t_0+1}, \hat{S}_{t_0+1})\rangle$ is calculated. This finally yields an estimate of the Lyapunov exponent as

$$\lambda = \log \frac{H(S_{t_0+1}, \hat{S}_{t_0+1})}{H(S_{t_0}, \hat{S}_{t_0})}.$$

Figure 8 shows the convergence behavior of the method for the three activation probabilities from above. The vertical axis is the Lyapunov exponent λ and the horizontal axis corresponds to the number of samples m used to compute the average distance at the next time step. The method nicely converges, after a few thousand repetitions. According to the obtained results the node dynamics are chaotic at $p_{act} = 0.03$ ($\lambda \approx 0.95$) and stable (or ordered) at $p_{act} = 0.14$ ($\lambda \approx -0.29$). For $p_{act} =$

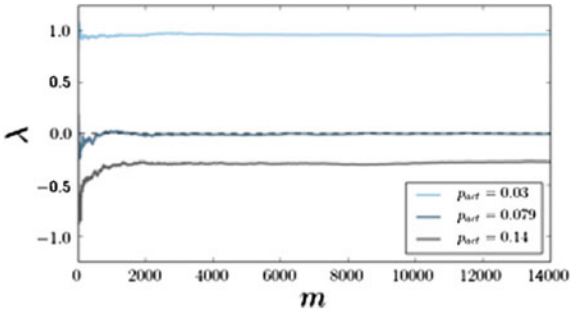

Fig. 8 Convergence of the Lyapunov exponent λ. The horizontal axis indicates the number of samples used to compute the average distance $\langle H(S_{t_0+1}, \hat{S}_{t_0+1})\rangle$. The *three curves* show the convergence for three activation probabilities for rule 209 at $p_{em} = 0.2$. Resulting Lyapunov exponents: $\lambda = 0.954680$ for $p_{act} = 0.03$, $\lambda = -0.007172$ for $p_{act} = 0.079$, $\lambda = -0.285562$ for $p_{act} = 0.14$

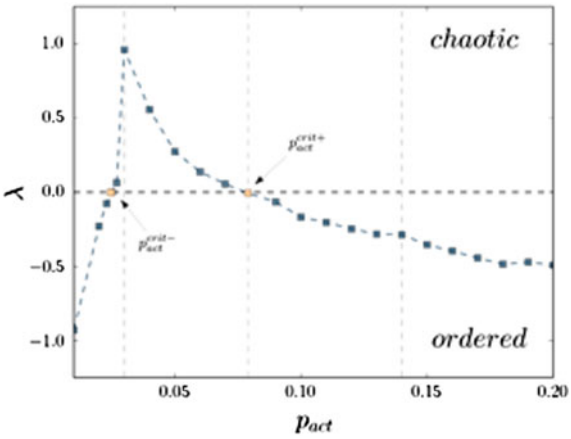

Fig. 9 Dependence of the Lyapunov exponent on activation probability (edge mutation rate $p_{em} = 0.2$). There are two ordered ($\lambda < 0$) and a chaotic ($\lambda > 0$) regime, separated by two critical points $p_{act} \approx 0.025$ and $p_{act} \approx 0.079$

0.079, the Lyapunov exponent is close to zero, indicating that the node dynamics might be determined by a critical state of the network and its update rules.

5.2.1 Mean-Field Approximation of Node Dynamics

In what follows, we exhibit the mean field approximation of the adaptive network automaton is exhibited. The idea is to analytically infer the time evolution of the average activity $\langle A\rangle$ and the average in-degree $\langle k_{in}\rangle$ for a network of size N (note $\langle k_{in}\rangle = \langle k_{out}\rangle$). The approximation is based on the assumption that correlations between in- and the out-degree are negligible or cancel out. Hence it is expected that on average for a particular node i it holds that $k_{in}(i) = k_{out}(i)$. The mean field model is implemented using a two dimensional iterated map with $\langle A\rangle$ and $\langle k_{in}\rangle$ defining its state at

time t. Given the average in-degree $\langle k\rangle := \langle k_{in}\rangle \in [0, N-1]$ and the average activity $\langle A\rangle \in [0, 1]$ at time t, the expected number of active preceding nodes a randomly chosen node i has is $\langle k\rangle\langle A\rangle$. By substituting this expression for k^i into the activation function (1) we get the following approximation for the average activity at the next time step:

$$\langle A\rangle_{t+1} = 1 - (1 - p_{ac})^{\langle k\rangle_t \langle A\rangle_t} \tag{2}$$

The change $\Delta\langle k_{in}\rangle$ of the average in-degree in a single time step depends on the probability $P(m)$ with which position m in the rule table is applied for a randomly chosen pair $\{j, i\}$ of nodes. The probability that there is a connection from node j to node i is given by $P(A_t(j,i){=}1) = \langle k_{in}\rangle_t (N-1)^{-1}$. The likelihood that a randomly chosen node is active is equal to $P(S_t(j){=}1) = P(S_t(i){=}1) = \langle A\rangle_t$. Using these approximations, $P(m)$ can be written as

$$P(m) = P(S_t(j){=}m_j) \cdot P(A_t(j,i){=}m_{j,i}) \cdot P(S_t(i){=}m_i), \tag{3}$$

with

$$\begin{aligned}
P(S_t(j){=}m_j) &= m_j\langle A\rangle_t + |m_j - 1|(1 - \langle A\rangle_t),\\
P(A_t(j,i){=}m_(j,i)) &= m_{j,i}\langle k\rangle_t (N-1)^{-1} + |m_{j,i} - 1|(1 - \langle k\rangle_t (N-1)^{-1}),\\
P(S_t(i){=}m_i) &= m_i\langle A\rangle_t + |m_i - 1|(1 - \langle A\rangle_t),
\end{aligned}$$

$m_j, m_{j,i}, m_i \in \{0, 1\}$ being the values of $S_t(j)$, $A_t(j,i)$ and $S_t(i)$ of position m in the rule table.

Given the probability $P(m)$ with which each position in the rule table is applied for a randomly chosen pair of nodes, one can calculate the expected connectivity change of that node pair. This change depends on the particular rule. For a single position m in the rule table it equals to $P(m) \cdot (R_m - m_{j,i}) \cdot p_{em}$. Here, R_m is the value $A_{t+1}(j,i)$ defined for the particular rule at position m in the rule table. Summing over all eight rule table positions and accounting for the number of nodes N, the expected change of the average in-degree $\Delta\langle k_{in}\rangle_t$ is given by

$$\Delta\langle k_{in}\rangle_t = (N-1) \cdot \sum_{m=0}^{7} P(m) \cdot (R_m - m_{j,i}) \cdot p_{em}. \tag{4}$$

From this, the final map is defined by

$$\begin{aligned}\langle A\rangle_{t+1} &= 1-(1-p_{act})^{\langle k_{in}\rangle_t\langle A\rangle_t}\\ \langle k_{in}\rangle_{t+1} &= \langle k_{in}\rangle_t + (N-1)\cdot\sum_{m=0}^{7} P(m)\cdot(R_m - m_{j,i})\cdot p_{em}.\end{aligned} \tag{5}$$

The mean-field equations, used in Fig. 6, are useful when systematically searching for non-trivial topologies, since we expect those to occur when we observe a deviation between mean field approximation and the simulations.

5.3 Two Critical Points in Dependence of p_{act}

The dependence of λ across the cross section is exhibited in Fig. 9. In the considered range of activation probabilities three dynamical regimes can be identified, which are separated by the two critical points $p_{act}^{crit-} \approx 0.025$ and $p_{act}^{crit+} \approx 0.079$. Below p_{act}^{crit-} and above p_{act}^{crit+}, the node dynamics are ordered. Between the two critical points a chaotic regime extends with a maximum at $p_{act} = 0.03$. The two critical points were found by manually tuning the activation probability and repeatedly measuring the Lyapunov exponent.

At p_{act}^{crit-}, the activation probability is too low for a sustained activity: Independent of the initial connectivity, after a certain number of iterations, activity dies out. Only the targeted reactivation of a node in the dead state triggers an avalanche of activity that lasts for a variable number of time steps.

Figure 10a shows a log-log histogram of the distribution of the durations of such avalanches. The data were acquired from a simulation over 106 time steps. As soon as the automaton reached a dead state, a randomly chosen node was reactivated and the duration d of the triggered avalanche was recorded. The distribution follows a power law with an exponential cutoff. The exponent was estimated to be $\alpha \approx 1.734$ for data in the range $d_{min} = 8$ to $d_{max} = 80$, using a maximum likelihood method [36].

At p_{act}^{crit+}, the activity, however, is sustained. Therefore the duration for which individual nodes were continuously active was considered. Figure 10 shows a log-log histogram of the frequency with which sequences of continuous activity of length l occur in a simulation over 16×103 time steps. This distribution also follows a power law over a large range of the data. The critical exponent was estimated to be $\alpha \approx 2.06$ for data of $l_{min} \geq 11$.

The two critical points are qualitatively different. The point p_{act}^{crit-} corresponds to the critical activation probability below which activity dies out and above which a certain level of activity sustains. Such a point can be expected to occur at every transition from an inactive region to an active region and thus cannot be seen as a particularity of the interplay between topology and node dynamics. At p_{act}^{crit+}, however, the case is different: It is clearly the adaptive nature act of the system

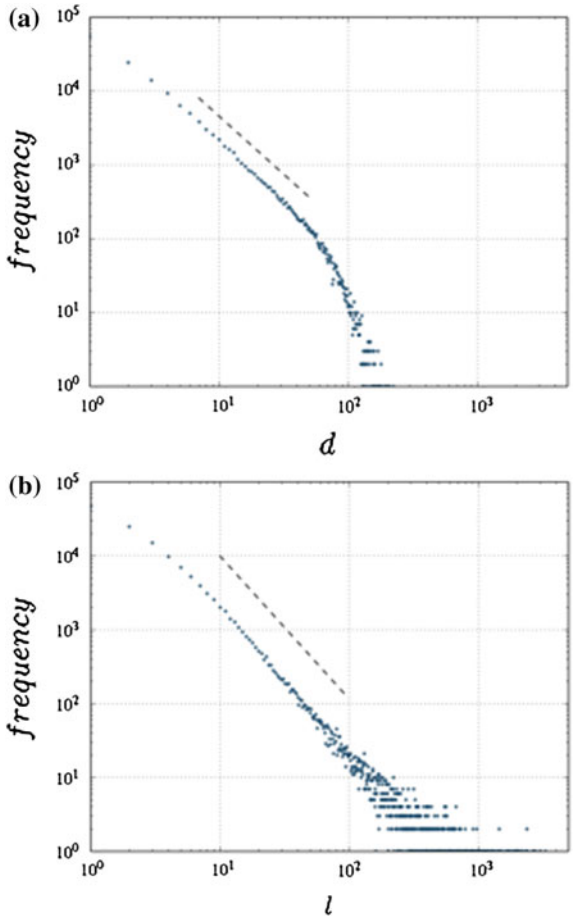

Fig. 10 Power law distributions occurring at the critical points **a** p_{act}^{crit-} and **b** p_{act}^{crit+}. The log-log histogram for p_{act}^{crit+} shows the frequency of avalanches of activity of duration d acquired from a simulation over 10^6 time steps. The critical exponent was estimated to be $\alpha = 1.7341$ ($\sigma = 0.0039$) using a maximum likelihood method (for the range $d_{min} = 8$ to $d_{max} = 80$). For p_{act}^{crit+} the log-log histogram shows the frequency of sequences of continuous activity of length l of individual nodes. The critical exponent was estimated to be $\alpha = 2.06527$, for a simulation over 16×10^3 iterations

that allows the node dynamics to operate at the border between ordered and chaotic behavior. As a consequence, in the subsequent analysis, let us exclusively focus on the behavior at p_{act}^{crit+}.

5.4 Network Topology at the Critical Point p_{act}^{crit+}

Figure 11 shows the distribution of the in-degrees (a) and the out-degrees (b) of a typical network evolving at p_{act}^{crit+}. The distributions were generated by including the degrees of all nodes in the last 100 time steps of a simulation over $T = 1000$ iterations. Two things are worth noting. First, the symmetry; the two distributions are almost mirror images of each other. Second, recalling that the in-/out-degrees are negatively correlated, it is apparent that the nodes tend to separate into two distinct

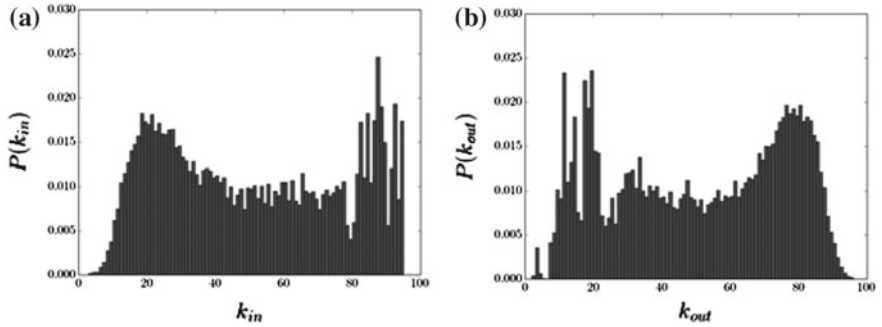

Fig. 11 **a** In- and **b** out-degree distributions of a typical network evolving at p_{act}^{crit+}. Distributions are based on the degrees of all nodes in the last 100 iterations of a simulation over 1000 time steps. The two-peaked histogram structures reflect the basic ingredients of complex behavior as the competition between (here: two) rivaling attracting states

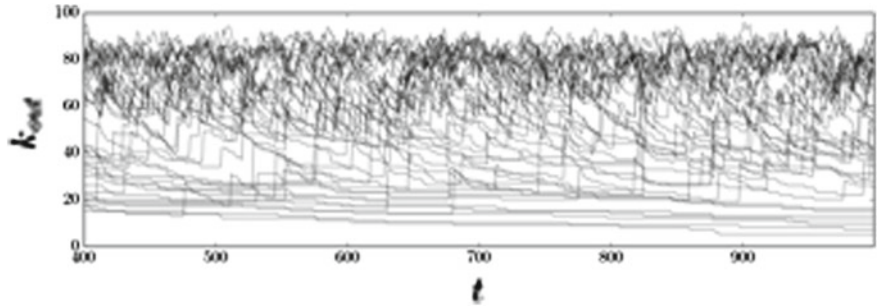

Fig. 12 Time evolution of the out-degrees of 40 nodes over a duration of 900 time steps at p_{act}^{crit+}

groups. One group consists of nodes with a low in-degree and a high out-degree. These nodes cause the smooth peaks of the distributions. The other group is made of nodes with a high in-degree and a low out-degree, found in the distorted tails of the distributions.

Figure 12 exhibits the dynamical behavior of the network topology. It shows the time evolution of the out-degrees of 40 nodes over 900 iterations. The dense and erratic region at high k_{out} corresponds to the smooth peak in Fig. 11b. The steady region around $k_{out} = 20$ accounts for the peaks in the tail. The area in-between is characterized by a transient behavior of the out-degrees. The degrees either slowly approach the steady region or they erratically climb towards the dense region. The corresponding plot for the in-degrees looks almost identical. The only difference is that the dense region is found at low values and the steady region at high values of k_{in}. The dynamical behavior of the degrees implies that nodes occasionally migrate between the high in-degree/low out-degree group and the low in-degree/high out-degree group.

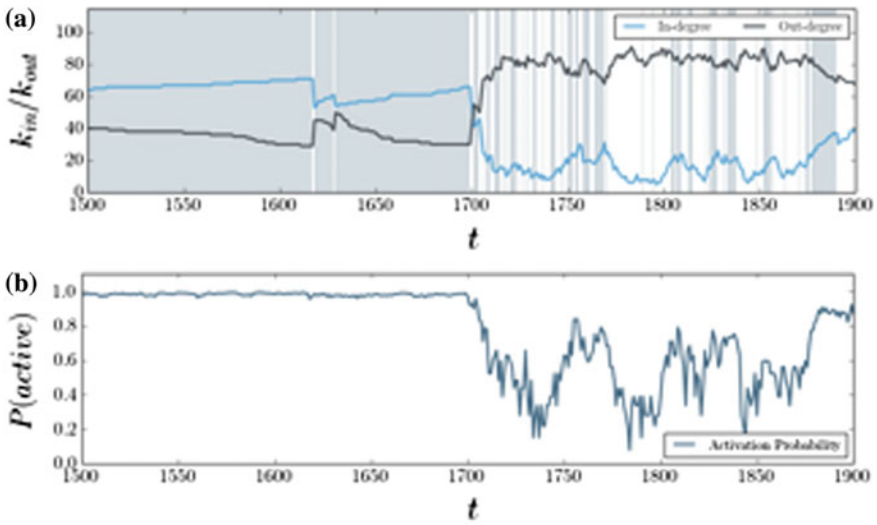

Fig. 13 **a** Time evolution of the in-degree, the out-degree and the dynamical state of a single node at p_{act}^{crit+}. The state is indicated by the *background color* (*gray* = active, *white* = inactive). **b** The probability with which the considered node was activated during the observed period

5.5 Critical Behavior at p_{act}^{crit+} as the Interplay Between Topology and Node Dynamics

The critical node dynamics and the non-trivial structure observed at p_{act}^{crit+} are interdependent phenomena. The underlying mechanism can be best understood by analyzing the behavior of a single node. Figure 13a shows the time evolution of the in-degree, the out-degree (lines) and the state of a particular node (gray background = active, white = inactive).

The degrees almost symmetrically oscillate with respect to each other around the mean in- /out-degree ($\langle k_{in} \rangle = \langle k_{out} \rangle \approx 50$). Two different phases are recognizable. In the first phase the node is mostly active and characterized by a high in-degree and a low out-degree. At around $t = 1700$, the behavior changes. The node enters a phase of sporadic activity that goes along with a low in-degree and a high out-degree. The strong fluctuations in this phase are a consequence of the low in-degree that reduces the likelihood of the node of being activated. Figure 13b illustrates the drop of the activation probability as the node enters the phase. The two phases correspond to two topologically different node groups. The transition therefore designates a switch of the node between the two groups. To understand the mechanism causing the symmetric oscillation, we consider the change of the degrees of a node i caused by a single application of the edge mutation rules Fig. 4.

If node i is active, the only positions in the rule table that cause a change of its degrees are $R_{001} = 1$ and $R_{110} = 0$. Hence only connections to and from inactive

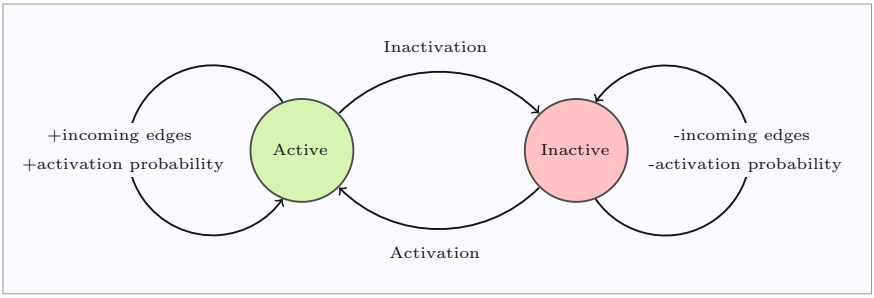

Fig. 14 Scheme of the emergent behavior of rule 209: Two feedback loops dominate the behavior of a single node. Consecutive activity leads to an increase of the in-degree and consequentially promotes subsequent activation (self-loop/*green circle*). In contrast, consecutive inactivity lowers the in-degree and therefore reduces the likelihood of subsequent activation (self-loop/*red circle*)

nodes are modified. R_{001} affects all inactive nodes that have no outgoing connection to node i. In a single time step, on average a fraction of p_{em} of these nodes will establish a connection to node i. R_{110} affects all inactive nodes to which node i currently has an outgoing connection. In a single time step on average, a fraction p_{em} of these connections will be lost. Since the set of inactive nodes changes with every iteration, an active node constantly acquires incoming and loses outgoing connections. Consequentially, if one would force a node into the active state for a sufficient duration, it would eventually end up having incoming connections from all other nodes, and no outgoing connections. The smoothness of the change of the degrees is because the fraction of inactive nodes is low ($\langle A \rangle \approx 0.84$), and therefore only a few connections are modified at once. If, however, node i is inactive, the major changes of the degrees are caused by the positions $R_{001} = 1$ and $R_{110} = 0$. Both modify the connections to and from active nodes. $R_{001} = 1$ affects all active nodes to which node i has no outgoing connection. In one time step, node i establishes a fraction p_{em} connections of those nodes. $R_{110} = 0$ affects all active nodes that have a connection to node i. In a single time step, an average of a fraction p_{em} of these connections are removed. Since most nodes are active, more connections are created and removed at once. This explains the jumps in the degrees observed if nodes turn inactive. The positions $R_{000} = 1$, $R_{010} = 0$ also affect the degrees of i in the case it is inactive. They cause the creation and removal of connections from and to active nodes. Since the two positions are counteracting each other, their effect on the degree fluctuations is only marginal. The described mechanisms describe two positive feedback processes counteracting each other: First: The longer a node is continuously active, the higher is the probability that it will be active in the next time step. That is because active nodes acquire incoming edges and the more incoming edges a node has the more likely it is subsequently active. Second: The longer a node is continuously inactive, the lower is the chance that it will be active in the next time step. This because inactive nodes lose incoming edges and the fewer incoming edges a node has the less likely it will be active in the next time step. This effect is

slightly damped since inactive nodes can gain incoming edges from other inactive nodes ($R_{000} = 1$). The first feedback process explains the presence of the power law in the length distribution of sequences of continuous activity of single nodes. This is essentially the realization of a rich get richer mechanism well known to result in heavy tail distributions [37]. Investigations on the robustness of this mechanism have revealed that the typical degree distribution and the critical node dynamics evolve almost independently of the initial configuration of the network. As long as the initial density of connections is enough to sustain activity, the automaton robustly self-organizes toward that peculiar configuration. This behavior can be comprised in the schematic Fig. 14.

6 Conclusion

Here we have introduced the adaptive network automaton as a minimalistic model of an adaptive network. The main object of this work was to clarify whether this concept is a suitable research framework to shed light on the relation between local rules and emerging global behaviors in adaptive networks.

Through systematic simulations of the 256 rules, we could identify those parameter space regions that favor the emergence of complex structure and behaviors. Inherent regularities in the rule space further allowed to derive a rule classification scheme that served as a guideline for more in-depth investigations. The detailed analysis of rule 209 revealed that the interplay between topology and node dynamics generates a complex network topology with a robust convergence towards a critical state. This behavior was shown to arise from the manifestation of two counteracting positive feedback processes, causing a separation of the nodes into two topologically distinct groups. The results demonstrate that simple binary node dynamics in combination with local edge mutation rules are sufficient to produce behavior characteristic of adaptive networks. However, the present results give only a glimpse on the full behavioral repertoire of the automaton. For most of the rules and parameter combinations, it is currently unknown to what type of topologies or dynamical behavior they give rise to. In order to eliminate these blind spots, additional simulations covering the interesting parameter space regions will be necessary. With efforts along our approach and by employing the observables used in our work, the regions in the parameter space where the automata might operate at criticality can be extracted with some effort. We also introduced a mean-field approximation based on an iterated map. It adequately predicts the behavior of the automaton in the cases whenever the network is not strongly correlated. This approach turns out to be useful when searching for non-trivial topologies, since we expect them to occur when we observe a deviation between mean field approximation and the simulations. A screening based on such quantities would render a more detailed picture of the parameter space, allowing to devise a comprehensive map relating the rules to the emerging global behaviors. Such a map could be the starting point to investigate more specific questions, like for instance: What are the necessary conditions under

which the automaton converges towards a critical state? Or: Which rules and parameter combinations promote the formation of specific network topologies, like for example, scale-free networks?

We have shown that our model is even amenable to analytical treatment and also allows for an intuitive understanding of the emerging behaviors. Therefore, the adaptive network automaton opens up promising new perspectives for research on adaptive networks. While we believe our model to provide a solid framework for studying adaptive network behavior, further investigations will be needed to clarify to what extent the generality of the approach is limited by the implementation chosen by us.

References

1. Langton, C.G.: Computation at the edge of chaos. Phys. D **42**, 12–37 (1990)
2. Bak, P., Tang, C., Wiesenfeld, K.: Self-organized criticality: an explanation of the $1/f$ noise. Phys. Rev. Lett. **59**, 381 (1987)
3. Novelli, L:. Genetic algorithms for multi-objective optimization on network topology. ETHZ Term Work (2015)
4. von Neumann, J.: Theory of Self-Reproducing Automata. University of Illinois Press, Urbana (1966)
5. Wolfram, S.: University and complexity in cellular automata. Phys. D **10**, 1–35 (1984)
6. Schuele, M., Stoop, R.: A full computation-relevant topological dynamics classification of elementary cellular automata. Chaos **22**, 043143 (2012)
7. Chomsky, N.: On certain formal properties of grammars. Inf. Control **9**, 137–167 (1959)
8. Gardner, M.: The fantastic combinations of John Conway's new solitaire game "life". Sci. Am. **223**, 120–123 (1970)
9. Barabási, A.-L., Albert, R.: Statistical mechanics of complex networks. Rev. Mod. Phys. **74**, 47–97 (2002)
10. Boccaletti, S., Latora, V., Moreno, Y., Chavez, M., Hwang, D.-U.: Complex networks: structure and dynamics. Phys. Rep. **424**, 175–308 (2005)
11. Motter, A., Albert, R.: Networks in motion. Phys. Today **65**(4), 43–48 (2012)
12. Newman, M.: The structure and function of complex networks. SIAM Rev. **45**, 167–256 (2003)
13. Vespignani, A.: Modelling dynamical processes in complex socio-technical systems. Nat. Phys. **8**, 32–39 (2012)
14. Li, P.-P., Zheng, D.-F., Hui, P.: Dynamics of opinion formation in a small-world network. Phys. Rev. E **73**, 056128–056132 (2006)
15. Pastor-Satorras, R., Vespignani, A.: Epidemic spreading in scale-free networks. Phys. Rev. Lett. **86**, 3200 (2001)
16. Gross, T., Blasius, B.: Adaptive coevolutionary networks: a review. J. R. Soc. Interface **5**, 259–271 (2008)
17. Perra, N., Baronchelli, A., Mocanu, D., Gonçalves, B., Pastor-Satorras, R., Vespignani, A.: Random walks and search in time-varying networks. Phys. Rev. Lett. **109**, 238701 (2012)
18. Sayama, H., Pestov, I., Schmidt, J., Bush, B., Wong, C., Yamanoi, J., Gross, T.: Modeling complex systems with adaptive networks. Comput. Math. Appl. **65**, 1645–1664 (2013)
19. Haldeman, C., Beggs, J.M.: Critical branching captures activity in living neural networks and maximizes the number of metastable states. Phys. Rev. Lett. **94**, 058101 (2005)
20. Kinouchi, O., Copelli, M.: Optimal dynamical range of excitable networks at criticality. Nat. Phys. **2**, 348–351 (2006)

21. Levina, A., Herrmann, J.M., Geisel, T.: Dynamical synapses causing self-organized criticality in neural networks. Nat. Phys. **3**, 857–860 (2007)
22. Shew, W., Yang, H., Petermann, T., Roy, R., Plenz, D.: Neuronal avalanches imply maximum dynamic range in cortical networks at criticality. J. Neurosci. **29**, 15595–15600 (2009)
23. Beggs, J., Plenz, D.: Neuronal avalanches in neocortical circuits. J. Neurosci. **23**, 11167–11177 (2003)
24. Bornholdt, S., Rohlf, T.: Topological evolution of dynamical networks: global criticality from local dynamics. Phys. Rev. Lett. **84**, 6114 (2000)
25. Holme, P., Newman, M.E.J.: Nonequilibrium phase transition in the coevolution of networks and opinions. Phys. Rev. E **74**, 056108 (2006)
26. Kozma, B., Barrat, A.: Consensus formation on adaptive networks. Phys. Rev. E **77**, 016102 (2008)
27. Zschaler, G., Traulsen, A., Gross, T.: A homoclinic route to asymptotic full cooperation in adaptive networks and its failure. New J. Phys. **12**, 093015 (2010)
28. Buskens, V., van de Rijt, A.: Dynamics of networks if everyone strives for structural holes. Am. J. Sociol. **114**, 371–407 (2008)
29. Petermann, T., Thiagarajan, T.C., Lebedev, M.A., Nicolelis, M.A.L., Chialvo, D.R., Plenz, D.: Spontaneous cortical activity in awake monkeys composed of neuronal avalanches. Proc. Natl. Acad. Sci. USA **106**, 15921 (2009)
30. Eguiluz, V.M., Chialvo, D.R., Cecchi, G., Baliki, M., Apkarian, A.V.: Scale free brain functional networks. Phys. Rev. Lett. **94**, 018102 (2005)
31. Eurich, C.W., Herrmann, J.M., Ernst, U.: Finite-size effects of avalanche dynamics. Phys. Rev. E **66**, 066137 (2002)
32. Lombardi, F., Herrmann, H.J., Perrone-Capano, C., Plenz, D., de Arcangelis, L.: Balance between excitation and inhibition controls the temporal organization of neuronal avalanches. Phys. Rev. Lett. **108**, 228703 (2012)
33. de Arcangelis, L., Herrmann, H.J.: Learning as a phenomenon occurring in a critical state. Proc. Natl. Acad. Sci. USA **107**, 3977 (2010)
34. Hoekstra, A., Kroc, J., Sloot, P. (eds.): Simulating Complex Systems by Cellular Automata. Springer, Heidelberg (2010)
35. Büsing, L., Schrauwen, B., Legenstein, R.: Connectivity, dynamics, and memory in reservoir computing with binary and analog neurons. Neural Comput. **22**, 1272–311 (2010)
36. Alstott, J., Bullmore, E., Plenz, D.: powerlaw: a python package for analysis of heavy-tailed distributions. PLoS One **9**, e85777 (2014)
37. Lorimer, T., Gomez, F., Stoop, R.: Two universal physical principles shape the power las statistics of real-world networks. Sci. Rep. **5**, 12353 (2015)

Hebbian Learning Clustering with Rulkov Neurons

Jenny Held, Tom Lorimer, Carlo Albert and Ruedi Stoop

Abstract The recent explosion of high dimensional, high resolution 'big-data' from automated bioinformatics measurement techniques demands new methods for unsupervised data processing. An essential analysis step is the identification of groups of similar data, or 'clusters', in noisy high-dimensional data spaces, as this permits to perform some analysis steps at the group level. Popular clustering algorithms introduce an undesired cluster shape bias, require prior knowledge of the number of clusters, and are unable to properly deal with noise. Manual data gating, often used to assist these methods, is based on low-dimensional projection techniques, which is prone to obscure the underlying data structure. While Hebbian Learning Clustering successfully overcomes all of these limitations (by using only local similarities to infer global structure), previous implementations were unsuited to deal with big data sets. Here, we present a novel implementation based on realistic neuronal dynamics that removes also this obstacle. By a performance that scales favourably compared to all standard clustering algorithms, unbiased large data analysis becomes feasible on standard desktop hardware.

1 Introduction

Data analysis begins with detecting structure. High-dimensional big-data has changed the face of this fundamental step. Biological experiments now routinely produce automated high-throughput, high-dimensional measurements of unknown data elements,

J. Held · C. Albert
Eawag, Swiss Federal Institute of Aquatic Science and Technology,
8600 Dübendorf, Switzerland

J. Held · T. Lorimer · R. Stoop (✉)
Institute of Neuroinformatics and Institute for Computational Science,
University of Zürich, 8057 Zurich, Switzerland
e-mail: ruedi@ini.phys.ethz.ch

J. Held · T. Lorimer · R. Stoop
ETH Zürich, Zurich, Switzerland

G. Mantica et al. (eds.), *Emergent Complexity from Nonlinearity, in Physics, Engineering and the Life Sciences*, Springer Proceedings in Physics 191,
DOI 10.1007/978-3-319-47810-4_11

which can no longer be feasibly analysed manually. The large data volume requests an unsupervised simplification by partitioning the data into groups of similar data items, which are expected to manifest on high dimensional structures in the space of measured features [4]. As a result, clustering algorithms have become a standard tool in the analysis of such data sets. The goal of such algorithms is to autonomously infer structure from the similarity between data items and find classes, or 'clusters', of similar data. An automated clustering procedure, however, faces several difficulties. First, the data may contain clusters of any shape, where generally the global cluster shape depends on the point-to-point proximity of data items in a non-trivial way. In particular, it is well known that stable periodic solutions of non-linear dynamic systems are distributed over convex-concave shrimp-like regions in parameter space [14, 15] and that this distribution is generally preserved in the feature space of the system [4]. Therefore, shape biases that preclude the identification of such complex, non-convex clusters need to be avoided. Second, the number of clusters is generally unknown and may even change over time, and should thus be found in an autonomous, unbiased way. And third, the measurements usually include noise, which asks for a method to classify data as outliers.

Traditional clustering algorithms, such as the partitional k-means [11] and the hierarchical Ward's [18] algorithms, or variations of these, are now widely used in the bioinformatics community [2, 3, 19]. Both methods, however, introduce strong biases that make them infeasible choices for unknown data sets. The k-means algorithm is based on an optimisation procedure, where the distances between points and their respective cluster centres is minimised globally. This requires the repeated computation of distances between points and representations of sets of points, which are obtained through an averaging process. In averaging over all points in a cluster, however, information about the shape of the set is lost and as a result a convex shape bias is imposed. Moreover, the k-means algorithm intrinsically imposes a bias on the number of clusters, which has to be pre-specified, and cannot deal with outliers, since all data items have to be assigned to a cluster. Ward's algorithm, at first sight, seems to avoid bias resulting from to global distance measures, as it constructs a hierarchy of clusters by recursively merging points and groups of points based on their separation. Although at a low hierarchical level this only takes into account local measurements of distance, on higher hierarchical levels it still involves the measurement of global distances between sets of points. This once more prevents the identification of convex-concave shapes, independently of the distance measure used [4]. Similar to the k-means algorithm, outliers cannot be dealt with properly, and the number of clusters remains dependent on the hierarchy level, so that none of the above mentioned criteria for unbiased clustering are met.

In this paper, we exhibit a solution to these issues. The key to successfully clustering data in an unbiased way is to use local information only, and from this to infer the global data structure. Neural network inspired algorithms, such as Sequential Superparamagnetic Clustering (SSC) [12] and Integrate-and-Fire Hebbian Learning Clustering (I&F HLC) [8], perform this inference in a natural way, mapping the computational task on a problem addressed in the cortical learning context with the Hebbian learning principle. In the HLC procedure, data items (i.e. points in the space

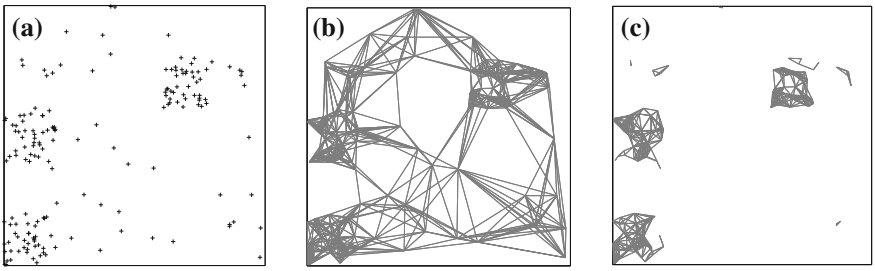

Fig. 1 **a** A two-dimensional synthetic data distribution. **b** The initial HLC network structure. **c** Evolved HLC network structure, exposing three main clusters, were points identified as outliers are not shown [8]

of measured features) are interpreted as neurons with an internal dynamics and the ability to interact with each other via nearest neighbour coupling. Local structure is initially extracted from the data by translating pair-wise distances between data items into similarities. This topological similarity is then converted into dynamical similarity by constructing a network of pair-wise coupled neurons and imposing a coupling strength that is positively correlated with the synchrony between neurons. The Hebbian learning principle, which uses the bio-inspired rule that only the coupling between neurons with highly correlated dynamics is strengthened, can now be used to let the global structure emerge in a self-organised way: The coupling between highly synchronous neurons will be increased at the cost of the coupling strength between less synchronous neurons, so that initial fluctuations in similarity are amplified in such a way that only intra-cluster connections are strengthened. An example of an initial and final state of such a network extracted from an example data set is shown in Fig. 1. As a result of this procedure, clusters will emerge as groups of strongly coupled, synchronised neurons. The principle of preferential reinforcement of some connections at the cost of others reflects the fundamental homeostatic tendencies of natural physical systems with sparse resources, and has been linked to the occurrence of power law distributions in the network connectivity and the emergence of community structures in networks at mesoscopic scales [5, 9].

Previous implementations of the HLC, however, were computationally too expensive to be effectively applied to large data sets. Our new implementation of the HLC principle improves upon the I&F HLC algorithm by making use of the biologically more realistic and lean Rulkov neuron dynamics as well as the inherently sparse nature of the network. Fast nearest neighbour and graph searching algorithms as well as our sparse implementation, using the local nature of the interactions, now allow a linear scaling of computation time with the number of data items, as well as the clustering of data sets with more than 10^5 measurements, which was not possible previously.

We will first describe the structure and behaviour of the algorithm, demonstrate its stability and time performance, and validate its ability to identify clusters without shape bias with several synthetic data sets. We then analyse a biological mass

cytometry data set of human bone marrow cells and point out potential drawbacks of manual and standard algorithmic clustering procedures.

2 The Rulkov Neuron Hebbian Learning Clustering Algorithm (RHLC)

The aim of a clustering algorithm is to extract global structure from local density information in an unbiased way. The HLC succeeds in this by using exclusively local (i.e. point-to-point) topological similarities between data items to impose dynamic similarity between representative neurons, which is then used in the Hebbian learning procedure to identify groups of similar data. In order to achieve this, local structure needs to be extracted from the data first. We can encode this local information in a weighted network that favours connections between data items that are similar, where this similarity is interpreted as pair-wise proximity in the feature space. A natural way to construct such a network from the original set of measurements, with N data items of dimension d, is to impose a nearest neighbour coupling. Therefore, as a first step, the k nearest neighbours of each item i are found based on the pair-wise distances d_{ij}, where an appropriate distance measure, for instance Euclidean distance, is chosen. Thus, a sparse non-symmetric adjacency matrix $\mathbf{A}$ is constructed, where $A_{ij} = 1$ if j is a nearest neighbour of i and $A_{ij} = 0$ otherwise. An example 2D data set and the graph representing the initial adjacency of points are shown in Fig. 1a and b respectively, where the direction of the connections is omitted. A weighting that encodes pair-wise similarity can then be realised in the choice of an initial coupling strength g_{ij} between the two neurons, at time $t = 0$:

$$g_{ij,t=0} = A_{ij} \exp\left[-\varepsilon \left(\frac{d_{ij}}{d_0}\right)^2\right], \tag{1}$$

where d_0 is the average distance between all neighbours in the network and $\varepsilon \in \mathbb{R}_{>0}$ is a scaling constant. A different measure that results in an increase in similarity for decreasing distance may also be feasible.

The similarity encoded statically in these weights can now be translated into a dynamic similarity. To this end, the data items are interpreted as neurons with internal dynamics, on which the coupling imposes dynamic correlation, or 'synchrony'. The input to a neuron, which is coupled only to its neighbours, also contains information about the dynamics of more distant parts of the network, mediated by the dynamics of structures of neurons connecting these parts. Thus, intermediate- and large-scale synchronisation patterns may emerge even though not all neurons within these groups are coupled directly. In order for the final weight structure to represent these large-scale correlations, Hebbian learning is used to adjust the weights to represent the 'true' similarity between data points. In this process, the neuron group interactions allow for initial local variations in similarity to be either amplified or smoothed out.

For instance, groups of neurons may collectively behave synchronised despite small variations in the weights, so that all intra-group connections may be strengthened. On the other hand, the lack of similar driving inputs will cause neurons from different groups or outliers to behave less similarly, so that their initial dissimilarity can be amplified in the learning process. The final weight structure, as shown for instance in Fig. 1c, therefore essentially represents global dynamic similarity, as opposed to topological proximity.

Here, the dynamics imposed on the nodes is given by the Rulkov neuron model [13], which in contrast to the I&F model used in earlier implementations is realistic in the sense that it is capable of producing any real-life neuron behaviour, including spiking, bursting, and silent phases. Each node has two time-discrete state variables, a fast evolving (membrane) potential $x_{i,t}$ and a slowly evolving (phase) potential $y_{i,t}$, given by

$$x_{i,t+1} = f(x_{i,t}, y_{i,t} + \beta_{i,t}), \tag{2}$$

$$y_{i,t+1} = y_{i,t} - \mu(x_{i,t} + 1) + \mu(\widetilde{\sigma}_i + \sigma_{i,t}), \tag{3}$$

where $\widetilde{\sigma}_i$ represents a constant input current driving the uncoupled neuron, and the evolution of the fast variable is given by

$$f(x, y) = \begin{cases} \frac{\alpha}{1-x} + y & \text{if } x \leq 0, \\ \alpha + y & \text{if } 0 < x < \alpha + y, \\ -1 & \text{if } x \geq \alpha + y. \end{cases} \tag{4}$$

where μ and α are constants. Nodes can interact via the Rulkov coupling equations, with a strength proportional to the coupling $g_{ij,t}$:

$$\beta_{i,t} = \beta_c \frac{1}{k} \sum_{j=1}^{k} g_{ij,t}(x_{j,t} - x_{i,t}), \tag{5}$$

$$\sigma_{i,t} = \sigma_c \frac{1}{k} \sum_{j=1}^{k} g_{ij,t}(x_{j,t} - x_{i,t}), \tag{6}$$

where the parameters β_c, $\sigma_c \in [0, 1]$ are constants that may be used to weight the influence of the coupling on the fast and slow potentials.

The currents $\beta_{i,t}$ and $\sigma_{i,t}$ allow the neurons to communicate and synchronise for large coupling strengths. In the Hebbian learning procedure, this dynamic similarity needs to be quantified. It is essential that such a measure of synchrony and the coupling strength between neurons interact appropriately. This includes the direction of change, i.e. an increase in synchrony as a result of an increase in coupling strength (and vice versa), and a preferably small time scale on which the synchrony reacts to a

change in coupling. These requirements are realised in a measure of phase synchrony, where the synchrony $S_{ij,t}$ at time t, measured over a preceding time period τ, is given by means of the population Pearson correlation between the slow potentials of the neurons:

$$S_{ij,t} = \frac{\sum_{\ell=t-\tau}^{t} \left(y_{i,\ell} - \overline{y}_i\right)\left(y_{j,\ell} - \overline{y}_j\right)}{\sqrt{\sum_{\ell=t-\tau}^{t} \left(y_{i,\ell} - \overline{y}_i\right)^2 \sum_{\ell=t-\tau}^{t} \left(y_{j,\ell} - \overline{y}_j\right)^2}}, \tag{7}$$

where $\overline{y}_i$ is the average potential of the ith neuron over the period τ.

A single Hebbian update rule, that comprises both a tendency for global synchronisation and a restriction of the same due to resource sparsity, can now be realised. These two counteracting principles, mediated locally, eventually result in the formation of global and mesoscopic structures, from which clusters can be extracted. With this aim, the learning rule is formulated such that the coupling between two neurons will be increased or decreased depending on the nodes' synchrony relative to the average synchrony in the network, such that high synchrony results in an increase in coupling and low synchrony in a decrease:

$$g_{ij,t+1} = g_{ij,t} + \frac{\tau}{t}\left(c_1 S_{ij,t} - c_2 \overline{S}\right), \tag{8}$$

where $c_1, c_2 \in [0, 1]$ and $\overline{S}$ is the average synchrony in the network, given by

$$\overline{S} = \sum_{i,j \in \mathbb{N}, A_{ij}=1} S_{ij,t}. \tag{9}$$

An example of the development of some weights between different neurons is shown in Fig. 2. It can be seen that the weights settle to an equilibrium where only neurons within a cluster will maintain their strong connections.

Finally, the clusters are to be extracted from the resulting global weight structure. Towards the end of the learning process, the system will be driven into state where the number of strong weights does not change significantly any more (i.e. all strong connections are found) while the number of intermediate-strength connections becomes small (due to a strong increase or decrease in the learning procedure). That is, it has become clear whether two neighbours do have a strong correlation or not. At this stage, the final structure is found and the learning procedure can be stopped. To determine when this stage is reached, a stopping coefficient κ, which is given by the ratio of still-learning connections n_ℓ to the total number of strong connections n_s in the network, is defined:

$$\kappa = \frac{n_\ell}{n_s}. \tag{10}$$

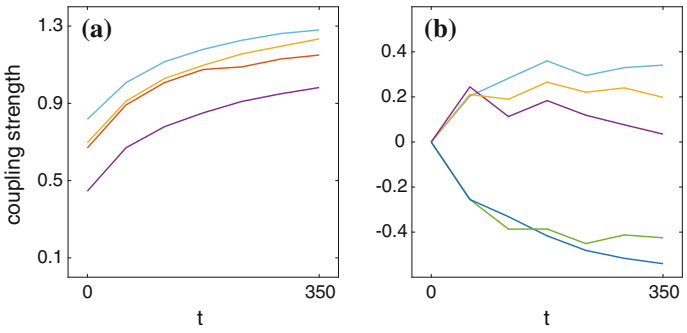

Fig. 2 **a** Development of several weights within a cluster, where all weights are increased in the Hebbian learning procedure. **b** Development of weights among low-density noise data (*top three* weights) and the weights with neurons from an adjacent cluster. The weights among noise data are increased initially, due to the fact that the nodes are in an environment of similar density, but overall remain small in compensation for the increase in coupling strengths within clusters

The number of connections that are still learning is determined using two thresholds θ_1 and θ_2. Still-learning connections are said to have weights in the intermediate range with $\theta_1 < g_{ij} < \theta_2$, while strong connections have a high coupling strength $g_{ij} > \theta_2$. The learning process is stopped when κ falls below a small threshold, $\kappa \leq \omega$, indicating a low number of still-learning weights compared to already settled weights.

In the final step, clusters are defined as structures of strongly coupled nodes. These can be extracted from the network as subgraphs of nodes with weights above a certain threshold. In our implementation, this is done by applying the fast Tarjan's algorithm [16] in the graph of weights above threshold θ_2.

3 Stability and Computational Complexity of the RHLC

3.1 Stability of the RHLC Results

While the numerical values of some parameters used in the algorithm have biological or computational motivation and the algorithm is stable towards changes in others, mainly two parameters directly influence the clustering result and may be used for tuning. These are the coupling initialisation parameter ε and the number of nearest neighbours k. For a synthetic data set, where the ideal clustering result is known, we can measure the quality of any RHLC clustering for ranges of these parameters. In Fig. 3, we present an example outcome of such an experiment, where we measure the quality of a clustering result using the Jaccard index ([6, 7], see Appendix), a measure of similarity between sets, where an index close to 1 indicates a good clustering result.

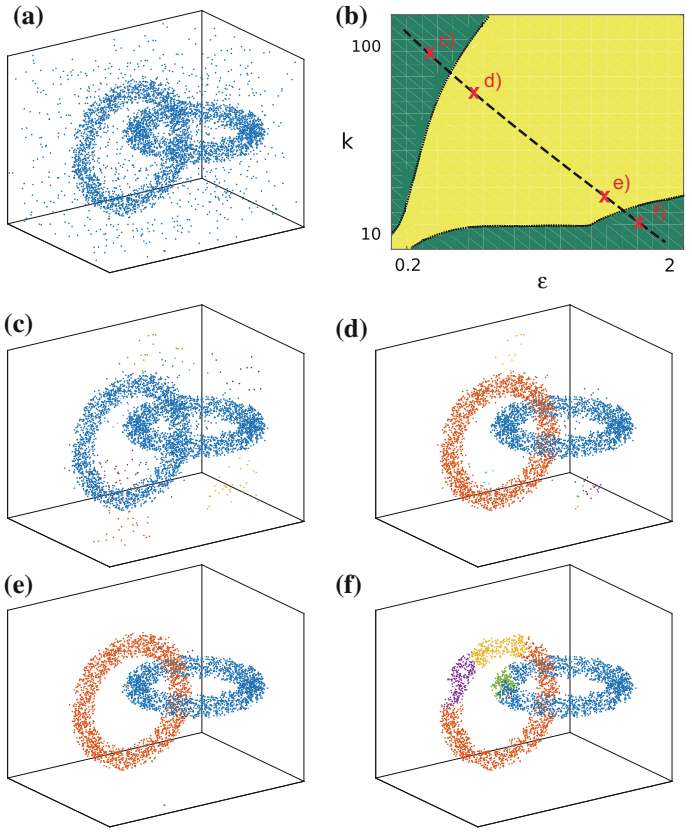

Fig. 3 **a** A synthetic 3D data set with two intertwined rings that represent convex-concave-shaped clusters, and background noise data, simulating outliers. **b** The clustering result quality as function of the parameters k and ε, where a Jaccard index close to 1 (*yellow region*, points **d** and **e**) marks a good clustering result, while low Jaccard indices (*green region*, points **c** and **f**) indicate poor results. In the *top left* parameter region a tendency towards large clusters is observed, in the *bottom right* region a tendency towards small clusters, where the specific results are displayed in **c**–**f** respectively

It is clear that there is a region of stability, where changes in the parameters do not alter the clustering result significantly. However, with more extreme values, a preference for larger or smaller clusters can be induced, as shown in Fig. 3c and f. A large number of nearest neighbours or a low value of ε, which increases the average similarity between neurons, favours larger clusters, whereas low similarity and few neighbours effectively splits clusters up into smaller clusters. A hierarchy becomes apparent, and the naturalness of a cluster can be inferred from its stability, where the most natural clusters will be the most robust with respect to changes in these parameters.

The numerical values of the other parameters and initial conditions used in this implementation are motivated by simulations with toy data sets or theoretical arguments, and are presented for completeness in the Appendix.

3.2 *Computational Complexity of the RHLC*

Our HLC implementation makes use of the computationally lean (discrete) Rulkov neuron dynamics and the local nature of the interactions (and therefore sparse form of the interaction matrices), and is thus able to achieve a favourable scaling of computation time with respect to the number of data items. From Fig. 4, a practical estimation of the complexity of the RHLC (Matlab implementation) reveals a scaling of $\approx O(N)$, similar to the k-means algorithm (Matlab implementation) and the k-means related algorithm 'flowPeaks' (R implementation) [3], which is used in the flow cytometry community. The I&F HLC (C implementation, of which no sparse version exists at this time) and Ward's algorithm (Matlab implementation) show a scaling of $\approx O(N^2)$.

The HLC algorithms have an offset in computation times compared to classical algorithms, due to the network initialisation and repeated computation of the neuron potentials and synchrony, but due to the local nature of interactions, a linear scaling can be achieved. In the RHLC algorithm, the k-nearest neighbour search requires $O(kN\log(N))$ and the connected components search $O(N+kN)$. The computation of synchrony and the weight updates occur with $O(kN)$, multiplied by the number

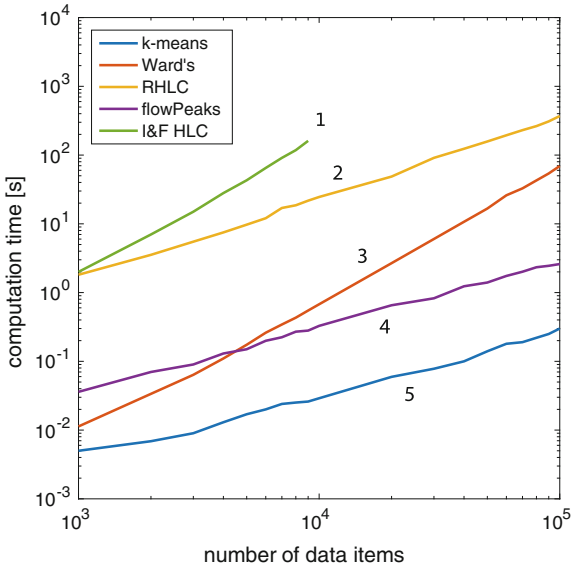

Fig. 4 Computation times of several clustering algorithms. The estimated slope values indicate a favourable behaviour of the RHLC (*2*) which scales with $O(N)$, similar to the flowPeaks (*4*) and k-means (*5*) algorithms. The I&F HLC (*1*) and Ward's (*3*) algorithms scale with $O(N^2)$. The offset of the HLC algorithms due to the network initialisation and repeated neuron potential computation may be reduced further by parallelisation

of weight updates required until the learning procedure is stopped. With our learning rule and the Rulkov neuron dynamics, we were able to reduce the number of updates required by a factor of ≈0.5 compared to the I&F HLC. The limiting factor for very large data sets will thus be the network initialisation. The local interaction rules, however, also open up the possibility of parallelisation, which would further reduce the total computation times and therefore the computation time offset.

4 Application to Data

We first analyse a biologically relevant clustering paradigm [4] that is ideal for testing the requirements for an unbiased clustering algorithm posed in the beginning. The data set, shown in Fig. 5a, contains two convex-concave shapes of different sizes as well as noise data. The dataset illustrates the complex relationship between local and global similarity, where the membership of a point to a cluster is mediated by local connectivity, not necessarily global proximity. As a result it can be seen in Fig. 5b that Ward's algorithm, which implicitly uses the assumption of global proximity, is unable to identify the clusters, while the RHLC finds them in a natural way (Fig. 5c).

A promising real-life application of our automated clustering approach is the identification of cell types. Many diseases, such as acute myeloid leukemia, manifest themselves in functionally and phenotypically diverse cells, the classification of which is essential for disease identification and relapse prevention. Human bone marrow, containing a variety of distinct and well-characterized immunological cell types, presents an ideal benchmark case for phenotypic clustering [10]. We therefore analyse here a mass cytometry dataset of healthy human bone marrow cells (data and description of experimental method: [1]). In the analysis, 13 different surface marker expressions were used as cell features. These are the integrated elemental reporter signals recorded in a time-of-flight mass cytometer, induced by transition element antibody tags labelled with elemental isotopes. A standard method for cell type

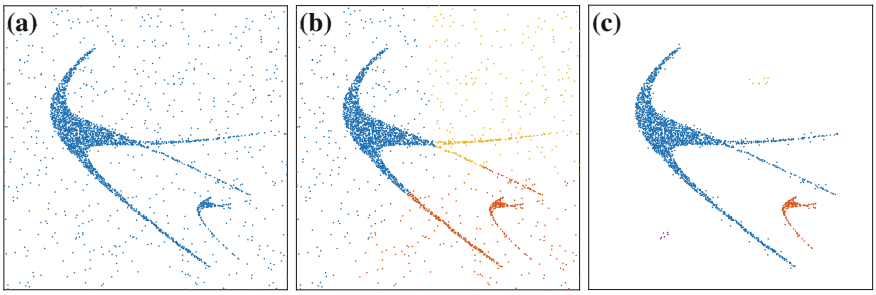

Fig. 5 **a** The initial 2D convex-concave synthetic data set, with background noise data items. **b** Ward's clustering result, where the clusters are not identified correctly. **c** With the RHLC, a close-to-ideal clustering result is obtained

identification in mass cytometry data is an expert manual gating procedure, where constant thresholds are introduced in a series of biaxial plots to separate classes of cells (this procedure is described in detail in [1]). Here, we compare the expert cluster labels, resulting from this manual low-dimensional gating procedure, with the results of the analysis of the gated dataset in higher dimensions with Ward's and the RHLC algorithms. For the visualisation of the results, t-SNE projections [17] have become a standard tool, allowing the mapping of high dimensional data to a low-dimensional space while aiming to preserve relative inter-item distances.

The classification results on the manually gated dataset are presented in Fig. 6, where Ward's clustering was given, a priori, the number of clusters found by manual gating. With the benefit of this strong additional information, Ward's clustering performs generally well, but fails to correctly identify some clusters, and splits some clusters that are identified by RHLC and manual gating as one cluster. RHLC merges some of the clusters that are distinguished by the manual gating (such as the three clusters in Fig. 6a surrounded by a dashed line, which as the most striking example, become a single cluster in the RHLC clustering, Fig. 6c). Searching for features that give rise to the distinction missed by RHLC, we look at the two-dimensional orthogonal projections in Fig. 7, which reveal thin, linear, separating gaps, that were introduced by the gating procedure. However, these two-dimensional projections may be misleading regarding the significance of the gap in the full high-dimensional feature space. Comparing the size of the gaps with the average nearest neighbour distance in the high-dimensional space, we find that the average size of the gap is roughly equal to (or in some cases even smaller than) the average nearest neighbour distances within the respective clusters. RHLC, therefore, does not perceive these gaps as significant, and the most reasonable clustering configuration is the one where these clusters are merged. We note that RHLC, through specific choices of k and ε,

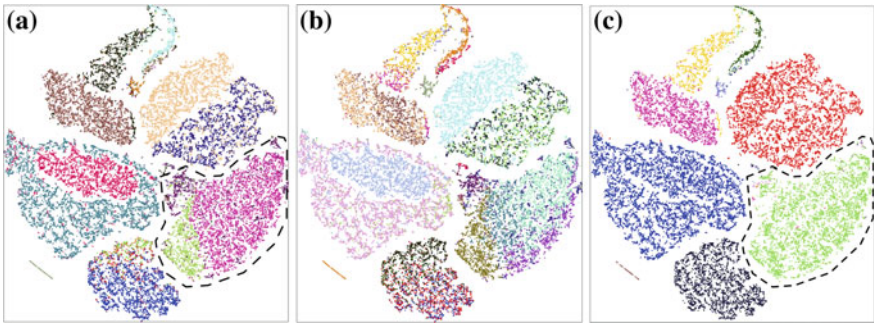

Fig. 6 The t-SNE projections [17] of 30000 cells from the gated healthy human bone marrow benchmark data [1], where *colours* encode cluster labels. **a** Expert cluster labels, which were found by biaxial manual gating [1]. **b** Ward's cluster labels, where the ideal number of clusters (24) was supplied. **c** Most stable RHLC clustering result. While Ward's clustering is very sensible to small separations and density gradients, the very stable RHLC result suggests generally larger clusters

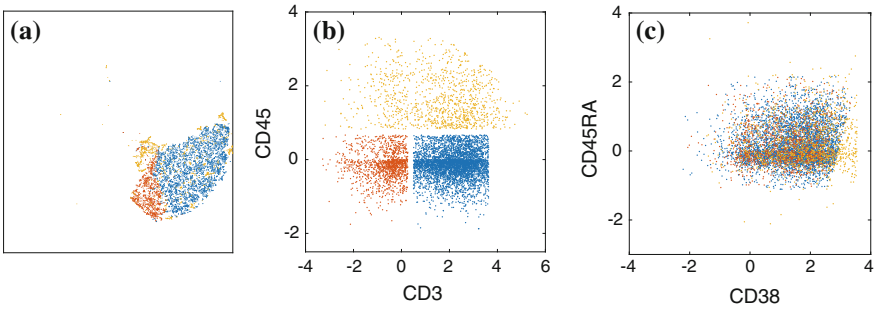

Fig. 7 **a** The t-SNE map of three manually labelled clusters. **b** The two-dimensional projection of the same clusters in the only two separating dimensions. **c** In all other dimensions, the clusters occupy roughly the same ranges, such as demonstrated with these example features. Here, the standard mass cytometry data transformation, $asinh$ of the data divided by 5, was applied

can be tuned to separate these clusters as well. However, the computational stability with respect to parameter variation of the result shown in Fig. 6c emphasises that even in the gated data set the involved cell types are perceived as very similar.

5 Conclusions

We presented the basic principles, implementation, and results of a neuronal network based clustering algorithm that combines the robust, self-organised design of the Hebbian learning clustering with the biologically realistic Rulkov neuron dynamics and an efficient sparse implementation. By using unsupervised learning in an artificial neural network based on local interactions, global information about the cluster membership can be extracted avoiding the shape biases of standard clustering algorithms. Additionally, its hierarchical response to changes in certain parameters allows the evaluation of the stability and thus naturalness of a cluster.

We demonstrated the algorithm's ability to identify convex-concave clusters in the presence of noise data with several synthetic data sets. For a high-dimensional biological bone marrow data set, we showed that RHLC, by using information from all dimensions simultaneously, may provide insights that are not accessible by manual clustering procedures.

The use of Rulkov neuron dynamics and our sparse implementation now allows the fast analysis of large data sets, where the possibility for further optimisation by parallelisation is given. This opens up new possibilities to analyse large, high-dimensional, unknown data sets, without prior knowledge about the number, shape, or density of clusters.

Appendix

Parameters and Initial Conditions

The initial potentials of the neurons are randomised around $\{x_i, y_i\} = \{-1, -3\}$, which are values that a standard uncoupled neuron will visit naturally in its cycle. The algorithm is stable with respect to this random initialisation. The parameter ranges that may in principle be used are presented in Table 1.

We find that generally, the best results are obtained with the initialisation parameters $k \in \{10 \ldots 100\}$ and $\varepsilon \in [0.5, 2]$, where the clustering result is in general stable for ranges of these parameters, as shown in Fig. 3. The Rulkov neuron parameters are set to allow all types of neuron dynamical behaviours, a fast evolution of the potentials, and non-weighted coupling ($\alpha = 8$, $\mu = 0.1$, and $\beta_c\,, \sigma_c = 1$). The parameter τ is chosen $\tau = 50$, which was found to be the minimum time required for the synchrony to be measured reliably. Higher values are equally suitable but increase the computation time. The parameters c_1 and c_2 were chosen $c_1 = \frac{1}{2}$ and $c_2 = \frac{1}{3}$ to allow for a global increase in coupling strength in the initially generally weakly coupled network. The thresholds θ_1 and θ_2 define what is a weak and a strong connection, respectively. Two Rulkov neurons generally behave synchronously for large values of g_{ij} and less synchronous for low values, so here we choose $\theta_1 = 0.2$ and $\theta_2 = 0.9$. The value of ω has to be chosen small to ensure that the number of still-learning connections has become small enough compared to the number of already-settled connections. In our implementation, motivated by experiments with toy data sets, we choose $\omega = 0.4$.

The constant parameters $\widetilde{\sigma}_i$ are computed by

$$\widetilde{\sigma}_i = \frac{G_i}{\max\limits_i G_i}\,, \tag{11}$$

Table 1 Parameters and their ranges in the Rulkov HLC algorithm

Parameter	Range	Description
k	$\{1, 2, \ldots, N-1\}$	Number of nearest neighbours
ε	$\mathbb{R}_{>0}$	Coupling initialisation parameter
β_c,σ_c	$[0, 1]$	Rulkov neuron dynamical parameters
μ	$(0, 1)$	Rulkov neuron dynamical parameter
α	$\mathbb{R}_{>0}$	Rulkov neuron dynamical parameter
τ	$\mathbb{N}$	Time over which synchrony is measured
θ_1, θ_2	$\mathbb{R} \mid \theta_1 < \theta_2$	Thresholds for weak and strong weights
c_1, c_2	$[0, 1]$	Weight update parameters
ω	$\mathbb{R}_{>0}$	Stopping criterion

where the total coupling strength G_i of a neuron is given by the sum over all initial coupling strengths to all its neighbours, normalised by the number of neighbours,

$$G_i = \frac{1}{k} \sum_{j=1}^{k} g_{ij,0} \,. \tag{12}$$

This initialisation of $\widetilde{\sigma}_i$ ensures that neurons in similarly dense regions have a similar constant input current and tend to behave synchronously from the beginning.

We note that further deparametrisation may be possible by altering the Hebbian learning rule to include a local measure of the average synchrony, so that it is of the form $g_{ij,t+1} = g_{ij,t} + \frac{\tau}{t}\left(S_{ij,t} - \overline{S}_i\right)$, where $\overline{S}_i$ is the average synchrony in the neighbourhood of neuron i only. This would complement the algorithms local nature and provide the possibility of a further increase in stability.

Jaccard Similarity

The Jaccard index is for two clusterings c_r and c_o is given by

$$J(c_r, c_o) = \frac{a(c_r, c_o)}{a(c_r, c_o) + e(c_r, c_o) + e(c_o, c_r)} \,, \tag{13}$$

where $a(c_r, c_o)$ is the number of observation pairs that are in the same cluster in c_r as well as c_o, and $e(c_r, c_o)$ is the number of observation pairs that are in the same cluster in c_r but not in c_o. The Jaccard index is thus large ($J(c_r, c_o) \approx 1$) for high similarity between the clusterings, and low ($J(c_r, c_o) \approx 0$) for low similarity. Therefore, if a given clustering result c_r is compared to some optimal clustering result c_o, a Jaccard index close to 1 indicates a good clustering result.

References

1. Bendall, S.C., Simonds, E.F., Qiu, P., Amir, el-AD., Krutzik, P.O., Finck, R., Bruggner, R.V., Melamed, R., Trejo, A., Ornatsky, O.I., Balderas, R.S., Plevritis, S.K., Sachs, K., Peer, D., Tanner, S.D., Nolan, G.P.: Single-cell mass cytometry of differential immune and drug responses across a human hematopoietic continuum. Science **332**, 687–696 (2011)
2. Bréhélin, L., Gascuel, O., Martin, O.: Using repeated measurements to validate hierarchical gene clusters. Bioinformatics **24**, 682–688 (2008)
3. Ge, Y., Sealfon, S.C.: FlowPeaks: a fast unsupervised clustering for flow cytometry data via k-means and density peak finding. Bioinformatics **28**, 2052–2058 (2012)
4. Gomez, F., Stoop, R.L., Stoop, R.: Universal dynamical properties preclude standard clustering in a large class of biochemical data. Bioinformatics **30**, 1–8 (2014)

5. Gutiérrez, R., Amann, A., Assenza, S., Gómez-Gardeñes, J., Latora, V., Boccaletti, S.: Emerging meso- and macroscales from synchronization of adaptive networks. Phys. Rev. Lett. **107**, 234103 (2011)
6. Jaccard, P.: Lois de distribution florale dans la zone alpine. Bull. Soc. Vaud. Sci. Nat. **38**, 67–130 (1902)
7. Jaccard, P.: The distribution of the flora in the alpine zone. New Phytol. **11**, 37–50 (1912)
8. Landis, F., Ott, T., Stoop, R.: Hebbian self-organizing integrate-and-fire networks for data clustering. Neural Comput. **22**, 273–288 (2010)
9. Lorimer, T., Gomez, F., Stoop, R.: Two universal physical principles shape the power-law statistics of real-world networks. Sci. Rep. **5**, 12353 (2015)
10. Levine, J.H., Simonds, E.F., Bendall, S.C., Davis, K.L., Amir, el-AD., Tadmor, M.D., Litvin, O., Fienberg, H.G., Jager, A., Zunder, E.R., Finck, R., Gedman, A.L., Radtke, I., Downing, J.R., Peer, D., Nolan, G.P.: Data-driven phenotypic dissection of AML reveals progenitor-like cells that correlate with prognosis. Cell **162**, 184–197 (2015)
11. McQueen, J.B.: Some methods for classification and analysis of multivariate observations. Proc. Fifth Berkeley Symp. Math. Statist. Prob. **1**, 281–297 (1967)
12. Ott, T., Kern, A., Schuffenhauer, A., Popov, M., Acklin, P., Jacoby, E., Stoop, R.: Sequential superparamagnetic clustering for unbiased classification of high-dimensional chemical data. J. Chem. Inf. Comput. Sci. **44**, 1358–1364 (2004)
13. Rulkov, N.F.: Modeling of spiking-bursting neural behavior using two-dimensional map. Phys. Rev. E **65**, 041922 (2002)
14. Stoop, R., Benner, P., Uwate, Y.: Real-world existence and origins of the spiral organization of shrimp-shaped domains. Phys. Rev. Lett. **105**, 074102 (2010)
15. Stoop, R., Martignoli, S., Benner, P., Stoop, R.L., Uwate, Y.: Shrimps: occurrence, scaling and relevance. Intl. J. Bif. Chaos **22**, 1230032 (2012)
16. Tarjan, R.E.: Depth first search and linear graph algorithms. SIAM J. Comput. **1**, 146–160 (1972)
17. Van der Maaten, L., Hinton, G.: Visualizing data using t-SNE. J. Mach. Learn. Res. **9**, 2579–2605 (2008)
18. Ward Jr., J.H.: Hierarchical grouping to optimize an objective function. J. Am. Stat. Assoc. **58**, 236–244 (1963)
19. Wong, D.S.V., Wong, F.K., Wood, G.R.: A multi-stage approach to clustering and imputation of gene expression profiles. Bioinformatics **23**, 998–1005 (2007)

Part IV
Biological Dynamics

Network Physiology: From Neural Plasticity to Organ Network Interactions

Plamen Ch. Ivanov, Kang K.L. Liu, Aijing Lin and Ronny P. Bartsch

Abstract The fundamental question in the new field of Network Physiology is how physiologic states and functions emerge from networked interactions among diverse physiological systems. We present recent efforts in developing new methodology and theoretical framework adequate to identify and quantify dynamical interactions among systems with very different characteristics and signal outputs. In this chapter, we demonstrate the utility of the novel concept of time delay stability and a first Network Physiology approach: to investigate new aspects of neural plasticity at the level of brain rhythm interactions in response to changes in physiologic state; to characterize dynamical features of brain-organ communications as a new signature of neuroautonomic control; and to establish basic principles underlying hierarchical reorganization in the network of organ-organ communications for different physiologic states and functions. The presented results are initial steps in developing an atlas of dynamical interactions among key organ systems in the human body.

P.Ch. Ivanov (✉) · K.K.L. Liu · A. Lin · R.P. Bartsch
Keck Laboratory for Network Physiology, Department of Physics, Boston University, Boston, MA 02215, USA
e-mail: plamen@buphy.bu.edu

P.Ch. Ivanov
Harvard Medical School and Division of Sleep Medicine, Brigham and Women's Hospital, Boston, MA 02115, USA

K.K.L. Liu
Department of Neurology, Beth Israel Deaconess Medical Center, Harvard Medical School, Boston, MA 02115, USA
e-mail: kangliu@buphy.bu.edu

A. Lin
Department of Mathematics, Beijing Jiaotong University, Beijing, China
e-mail: ajlin@bjtu.edu.cn

R.P. Bartsch
Department of Physics, Bar-Ilan University, Ramat Gan, Israel
e-mail: bartsch.ronny@gmail.com

G. Mantica et al. (eds.), *Emergent Complexity from Nonlinearity, in Physics, Engineering and the Life Sciences*, Springer Proceedings in Physics 191,
DOI 10.1007/978-3-319-47810-4_12

1 Introduction

The human organism comprises various physiological organ systems, each with its own structural organization and functional complexity, leading to transient, fluctuating and nonlinear output dynamics [20, 22]. The state and function of the human organism is defined by the characteristics of individual organ systems, and by how systems' dynamics change in response to neuroautomomic regulation and external or pathologic perturbations [10, 23, 25, 27, 39, 40]. Another key feature of the human organism is the presence of complex signaling and interaction processes between organ systems and sub-systems. These interactions occur through different coupling feedbacks, at multiple levels of integration and across spatio-temporal scales to optimize and coordinate physiologic organ functions. In addition to the state of individual organ systems, coordinated network interactions among organ systems are essential to maintain health and generate distinct physiologic states, e.g., wake and sleep; light and deep sleep; dreams; consciousness and unconsciousness. Disrupting these communications can lead to dysfunction of individual systems or to a collapse of the entire organism as observed in coma and multiple organ failure [8]. Yet, despite the importance to basic physiology and clinical medicine, we do not have established analytic and computational methodology and theoretical framework to probe emergent physiologic state and function out of networked interactions among diverse organ systems.

Recent developments in the new field, Network Physiology [6, 19], which focuses on inferring coupling and dynamical interactions among organ systems based on continuous streams of synchronized recordings of key physiologic parameters, may help overcome limitations in the current state-of-the-art. In contrast to traditional complex network theory, where edges/links are constant and represent static graphs of association, novel approaches in Network Physiology focus on dynamical aspects of organ communications in real time, on the evolution of organ interactions and the collective network behavior in response to changes in physiologic state and condition.

While initial steps were made in this direction [6, 30], major challenges remain that would require a coordinated interdisciplinary effort spanning from statistical physics, applied mathematics to biomedical signals processing, human physiology and clinical medicine. These challenges arise from several levels of complexity inherent to the dynamics of organ systems: (i) each organ is a multi-component system with its own structural complexity and regulatory mechanism leading to complex emerging dynamics characterized by fluctuating, intermittent and non-linear output signals [21, 24]; (ii) organ systems operate on a broad range of time scales from ms to hours and exhibit different types of output dynamics – oscillatory, stochastic or mixed – and thus, earlier concepts of treating them as chaotic oscillators need to be extended [1, 12, 47]; (iii) interactions between organ systems vary in time and moreover, certain pairs of organ systems can communicate through multiple forms of coupling [2–4]. Most importantly, global network dynamics of the entire organism can not be simply expressed as a sum of the behaviors of individual systems, and can

be strongly influenced by minor changes in the relative strength of their interactions, even when the network topology between these systems remains unchanged.

To address these challenges, recent nonlinear methods based on phase synchronization [2, 3, 41], coherence [7, 13, 33, 35], mutual information [15], transfer entropy [14, 16, 45, 46] and Granger causality [43] have been proposed to infer nonlinear interactions between pairs of dynamical systems. Efforts have focused on extending these methods to quantify direct or indirect interactions, the strength and directionality of links and the functional forms of coupling in physiological networks. In this chapter, we present a first Network Physiology approach based on the novel concept of time delay stability, which is suitable to identify and quantify physiologic interactions among diverse organ systems with distinct output dynamics. We report first findings utilizing this new framework to (1) investigate brain-brain network interactions across distinct brain rhythms and locations, and their relation to new aspects of neural plasticity in response to changes in physiologic state; (2) characterize dynamical features of brain-organ communications as a new signature of neuroautonomic control; (3) to establish basic principles underlying coordinated organ-organ communications, and construct first atlas (maps) of dynamical organ interactions across distinct physiologic states.

2 Time-Delay Stability Method: A New Approach to Physiologic Network Interactions

The structural and neuronal networks that control physiological systems lead to a high degree of complexity, which is further compounded by various coupling and feedback interactions that continuously vary in time, and the nature of which is not understood. These systems operate on different time scales, from msec to hours, and exhibit multiple coexisting forms of coupling. To quantify these interactions and characterize how they change in time under different physiological conditions, we study the time delay with which modulations in the output dynamics of a given system are consistently followed by corresponding modulations in the signal output of another system (time delay stability, TDS). Periods with constant time delay indicate a stable physiological interaction, and stronger coupling between systems results in longer periods of TDS [6].

Our TDS approach is a natural extension of previous efforts to develop methods sensitive to infer bivariate and multivariate interactions between dynamical systems based on cross-correlation, cross-coherence [35], Granger causality and mutual information [15, 16, 43], aiming to quantify linear and nonlinear characteristics of dynamical coupling [14, 42]. Measures derived from each of these methods reflect specific aspects of dynamical coupling and physiological regulation including the detection of direct or indirect links, the hierarchy of network interactions and directionality of links. While the sign of the time delay is naturally related with the

directionality of interactions [31, 32], here we focus on time delay stability as a measure of coupling strength between dynamical systems.

In our analyses, physiological output signals are first re-sampled at 1 Hz and normalized to zero mean and unit standard deviation within overlapping time windows of $\Delta t = 60$s with a moving step of 30 s (effectively de-trending the signals), as shown in Fig. 1a. Synchronous bursts in the normalized signals lead to pronounced cross-correlation calculated in windows of $\Delta t = 60$s and in steps of 30s (Fig. 1b). The time delay τ_0 is determined by the position of the maximum of the cross-correlation function in each moving window Δt. We identify two systems as linked if their corresponding signals exhibit a time delay that does not change by more than ± 1 s for several consecutive time windows Δt. Specifically, we track the values of τ_0 along the series $\tau_0(\Delta t)$ — when for at least four out of five consecutive time windows Δt (corresponding to a period of 5×30 s) the time delay remains in the interval $[\tau_0 - 1, \tau_0 + 1]$ these segments are labeled as stable (Fig. 1c). The procedure for determining intervals with stable time delay is repeated for a sliding time window with a step size one along the entire series $\tau_0(\Delta t)$.

Longer periods of TDS between the output signals of two systems reflect more stable interaction/coupling between these systems. Such interpretation is analogous to quantification of coupling strength between nonlinear chaotic oscillators based on the concept of phase synchronization — higher value of the coupling constant has been theoretically linked with increased percent of phase synchronization between the output signals of the oscillators [34, 37, 38]. Thus, the strength of coupling in our analysis is determined by the percentage of time in the recordings when TDS is observed: higher percentage of TDS corresponds to stronger coupling. The % TDS is calculated as the fraction of segments with stable time delay out of the entire time series $\tau_0(\Delta t)$. We obtained % TDS for each pair of physiological systems and we construct a TDS matrix to derive the dynamical network of organ interactions, as shown in Fig. 1d, e. The TDS measure focuses on the stability of coordinated modulation between dynamical systems and provides complimentary information on physiological coupling to alternative measures based on spectral coherence, mutual information or transfer entropy [15, 16, 33]. We note that in the context of TDS, strong physiologic coupling is defined as long periods of time delay stability, which can result only from active coordination (i.e., strong links) between physiologic systems.

We analyze continuously recorded multi-channel physiological data obtained from 36 healthy young subjects (18 female, 18 male, with ages between 20–40, average 29 years) during night-time sleep (average record duration is 7.8 h). We focus on physiological dynamics during sleep as sleep stages are well-defined physiological states, and external influences due to physical activity or sensory inputs are reduced during sleep. Sleep stages are scored in 30 s epochs by sleep lab technicians based on standard criteria [36]. Specifically, we analyze EEG data from six scalp locations (frontal left - Fp1, frontal right - Fp2, central left - C3, central right - C4, occipital left - O1, and occipital right - O2), the electrocardiogram (ECG), respiration, the electrooculogram (EOG), and the electromyogram (EMG) of the chin and leg. In order to compare these very different signals with each other and to study

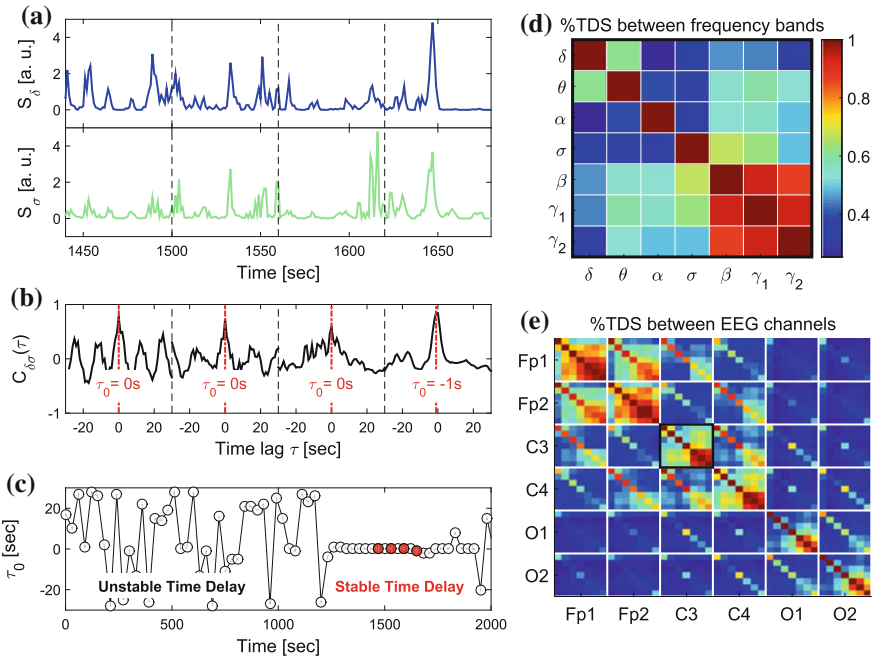

Fig. 1 Schematic presentation of the time delay stability (TDS) method and TDS matrix representing the degree of coupling between different frequency bands across brain locations. **a** Segments of brain EEG power spectra S_δ and S_σ for the δ- and σ-band shown for four consecutive 60 s time windows. **b** Coordinated bursts in S_δ and S_σ lead to pronounced cross-correlation $C_{\delta\sigma}$ within each time window. The time lag τ_0 that corresponds to the peak in the cross-correlation function $C_{\delta\sigma}(\tau)$ represents the time delay between the two signals. **c** Time delay τ_0 between S_δ and S_σ plotted as a function of time for consecutive 60 s windows moving with a step of 30 s. *Four red dots* represent τ_0 for the four windows shown in the above panels. Note the transition at ~1200 s from a segment with strongly fluctuating τ_0 to a stable time delay regime with $\tau_0 \approx$ constant. Such regime of time delay stability (TDS) indicates the onset of physiological coupling. The fraction of time when TDS is observed in the EEG recording, i.e. % TDS, quantifies the degree of coupling strength. Longer periods of TDS between S_δ and S_σ reflect stronger coupling. **d** TDS matrix representing the degree of coupling between different physiologically relevant EEG frequency bands (δ , θ , α , σ , β , γ_1 , γ_2) derived from the C3 channel. Matrix elements represent %TDS, where the *color code* is shown in the vertical bar. **e** Block-matrix representing the degree of TDS coupling between EEG channels (Fp1, Fp2, C3, C4, O1, O2) and between EEG frequency bands. Each off-diagonal block element corresponds to a specific pair of EEG channels and each diagonal block element represents the coupling between different frequency bands within the same EEG channel, as shown in **d**

interrelations between them, we extract the following time series from the raw signals: the spectral power of seven frequency bands of the EEG in moving windows of 2 s with a 1 s overlap: δ (0–4 Hz), θ (4–8 Hz), α (8–12 Hz), σ (12–16 Hz), β (16–20 Hz), γ_1 (20–34 Hz) and γ_2 (34–100 Hz) [11]; the variance of the EOG and EMG signals in moving windows of 2 s with a 1 s overlap; heartbeat RR intervals and interbreath

intervals are both re-sampled to 1 Hz (1 s bins) after which values are inverted to obtain heart rate and respiratory rate. Thus, all time series have the same time resolution of 1 s before the analysis.

To confirm that the TDS method captures physiologically relevant information about the endogenous interactions between systems, we perform a surrogate test where we pair physiological signals from different subjects, thus eliminating physiological coupling. Applying the TDS method to these surrogate data, we obtain almost uniform rank distributions with significantly decreased link strength due to the absence of physiological interactions. The results of this surrogate test indicate a significant ten-fold decline (outside 5 standard deviations) compared to real physiologic coupling between organ systems across all physiologic states (sleep stages). In contrast, the same surrogate test applied to traditional cross-correlation analysis does not show a difference between the rank distributions from surrogate and real data, indicating that the TDS measure extracts hidden information that is not accessible to the traditional linear cross-correlation analysis. The details of these statistical tests are presented in an earlier work [6].

3 Brain-Brain Networks: New Aspects of Neural Plasticity in Response to Change in Physiologic State

Research work on brain structure and brain dynamics in last decades has actively focused on structural, dynamical and functional brain maps constructed from fMRI, MEG, or BOLD signals [9]. Dynamics of brain wave rhythms and their distribution across brain areas have been studied in the context of different physiologic states under healthy conditions [13, 17, 44], in relation to cognitive and memory function [28], and under pathological deviations [7].

Our approach based on the TDS method focuses on the coordinated bursting activity of brain waves in different frequency domains, specifically focusing on cross-brain-wave interactions at the same location and same-brain-wave coordination across brain areas. Generally, this integrative approach allows us to investigate how multi-component dynamical systems self-organize as a result of network interactions among components in order to generate complex functions, and to elucidate mechanisms underlying the evolution of systems dynamics across states and conditions.

3.1 Hierarchical Reorganization of Brain Wave Interactions

Utilizing our TDS method and network approach, we identify and quantify coupling between brain waves defined by physiologically-relevant EEG frequency bands. We build a network of brain wave interactions, where network nodes represent diverse

brain waves at different brain locations and network links represent the strength of TDS coupling between brain waves across the entire brain.

We find that brain-wave network links exhibit complex patterns in the coupling strength between frequency bands across different brain locations, as represented by the TDS block-matrix elements (Fig. 1e). Moreover, we find that during distinct physiologic states (sleep stages) the entire brain adjusts the configuration and strength of network connections (defined by % TDS) between brain waves, leading to a hierarchical network re-organization with transitions across physiologic states [29]. This demonstrates a remarkable neural plasticity in the way brain waves coordinate their bursting activity at the integrated system level to produce physiologic functions associated with each physiologic state [29]. Specifically, the network of brain wave interactions undergoes a pronounced transition from a less connected state during Deep Sleep and REM to a highly connected state in Light Sleep and Wake (Fig. 2).

Generally, the strongest links in the network structure of brain wave interactions are those links between brain waves of different frequencies at the same EEG-channel location (i.e., intra-channel interactions), as represented by the diagonal matrix blocks in the TDS matrix. In contrast, interactions among brain waves from different EEG-channel locations (i.e., inter-channel links) are weaker, as represented by the off-diagonal matrix blocks (Fig. 1e). Further, considering all inter-channel links those that represent interactions between the same brain waves exhibit strongest coupling, as shown by the dominant diagonal elements in each off-diagonal matrix block (Fig. 1e).

We find that these network features are consistently observed for all sleep stages, indicating a universal and robust structure in brain wave interactions independent of physiologic states. Moreover, our results show that a significant part of the brain wave interactions across different brain areas is mediated through the coupling between brain waves in the same frequency bands (Fig. 2).

We uncover that different dominant structures ("building blocks") underlie general network connectivity and link strength during different sleep stages [5]. Specifically during DS, we find that the network is characterized by strong Frontal-Frontal (Fp1-Fp2) and Central-Central (C3-C4) links. In contrast, Occipital-Occipital (O1-O2) links are less prominent and weaker in strength. In addition, same hemisphere Frontal-Central interactions (Fp1-C3 and Fp2-C4) are more dominant, with higher connectivity and stronger links, compared to Central-Occipital (C3-O1 and C4-O2) interactions. Further, same-hemisphere Frontal-Occipital (Fp1-O1 and Fp2-O2) interactions and cross-hemisphere interactions (diagonal links) are not pronounced during DS (Fig. 2, where interactions with link strength $>45\%$ TDS are shown).

Notably, the majority of brain-brain interactions during DS are parallel links between same frequency bands in the Frontal, Central and Occipital locations, while inter-channel interactions across different frequency bands are much weaker and mainly present in the Frontal area. These complex brain-brain inter-channel interactions topologically form a network structure similar to an upper half of a hexagon. This half-hexagon structure is typical for all DS episodes throughout the night and remains present as a building block across all sleep stages (Fig. 2).

Expanding our analysis to REM sleep episodes, we find a similar structure of inter-channel interactions across various frequency bands as observed during DS episodes,

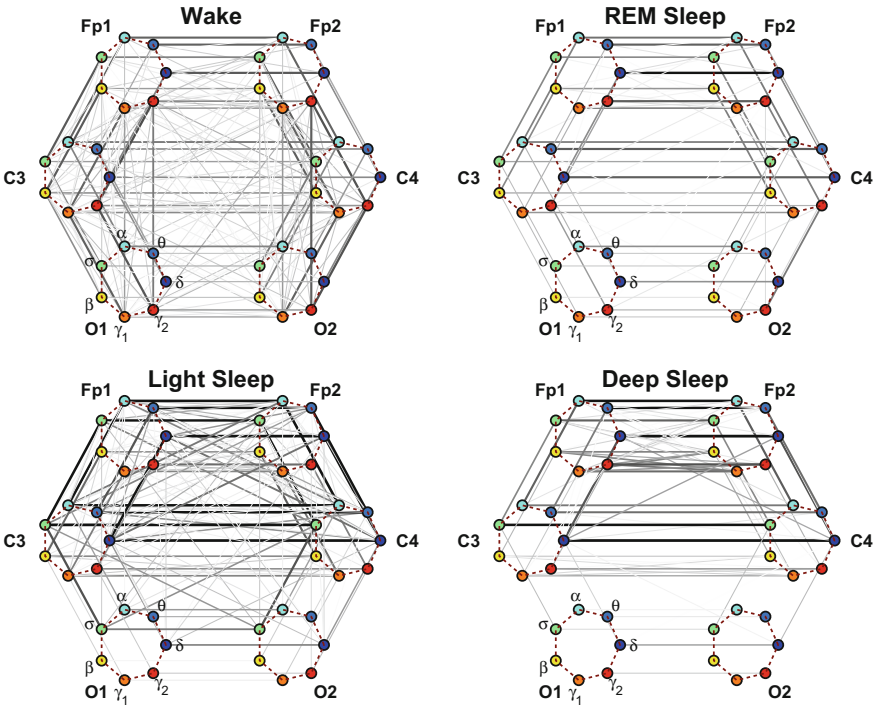

Fig. 2 Inter-channel brain networks during different physiologic states. Network nodes with different colors represent seven different frequency bands (δ , θ , α , σ , β , γ_1 , γ_2) derived from EEG signals, and each set of seven nodes ordered as a heptagon forms a vertex on the hexagon representing six EEG channels from particular brain locations: 2 Frontal areas (Fp1 and Fp2), 2 Central areas (C3 and C4) and 2 Occipital areas (O1 and O2). Coupling strength between frequency bands of signals from different EEG channels (i.e., inter-channel networks) is quantified as the fraction of time (out of the total duration of a given sleep stage throughout the night) when TDS is observed (% TDS). While during quiet W and LS the network of inter-channel brain interactions exhibits high connectivity and strong links between frequency bands of different EEG channels, the networks during REM and DS are more sparse with weaker links. Links between two nodes represent the group averaged coupling strength between frequency bands over all subjects. Inter-channel links strength is plotted in linear scale with *gray color code and line* thickness — strong links with high %TDS are represented by *dark thick lines*

however, with more pronounced Occipital-Occipital (O1-O2) and same-hemisphere Central-Occipital (C3-O1 and C4-O2) interactions with higher link strength. Similar to DS, all inter-channel interactions during REM are characterized by dominant interactions between the same frequency bands (parallel links), while links across different frequency bands are much weaker and mainly located in the Frontal area. The increased involvement of Occipital-Occipital and Central-Occipital interactions during REM lead to a network structure that extends the half-hexagon topology (basic building block) observed in DS to a full hexagon configuration. In addition to this hexagonal topology, the inter-channel network of brain interactions during REM is

characterized by higher number of weak cross-hemisphere links that are not present in DS (Fig. 2).

Investigating brain-brain interactions during LS, we find that the typical network structure characterized by full-hexagon topology observed for REM is reinforced by stronger links. Moreover, the transition to LS is characterized by a dramatic increase in cross-hemisphere connectivity mediated through much stronger diagonal links, and by the emergence of same-hemisphere Frontal-Occipital links of intermediate strength that are absent in REM and DS. Further, we note that the brain network dynamics during LS are characterized by a significant increase in interactions across different frequency bands not only in the Frontal area (Fp1-Fp2) as observed in REM and DS, but also in the Central area (C3-C4) as well as Frontal-Central interactions (Fp1-C3, Fp2-C4, Fp1-C4 and Fp2-C3). In contrast, interactions across different frequency bands are not observed in the Occipital area (O1-O2) or in Central-Occipital interactions (C3-O1, C4-O2, C4-O1 and C3-O2). Thus our analyses indicate that on top of the typical for REM hexagon topology, the brain-brain network during LS is characterized by additional degrees of cross-hemisphere and cross-frequency bands connectivity in the Frontal and Central areas.

During Wake, we find that brain-brain interactions are characterized by a topology similar to the one observed during LS. However, network connectivity during W is reinforced by additional and stronger links in the Occipital area (O1-O2) as well as by same-hemisphere Central-Occipital (C3-O1 and C4-O2) links. Moreover, in contrast to all other sleep stages, same-hemisphere Frontal-Occipital (Fp1-O1 and Fp2-O2) interactions are characterized by strong network links. Notably, inter-channel brain-brain interactions during W involve a high number of cross-hemisphere and cross-frequency links (Fig. 2), leading to a homogenous network with the highest connectivity and the highest average link strength compared to all other sleep stages [5].

Comparing inter-channel brain networks for different sleep stages, we find that the most significant change in the network of brain wave interactions occurs for links which represent interactions between brain waves of different frequencies (Fig. 2). Such dramatic reorganization in network connectivity and link strength between different brain waves indicates high degree of neural plasticity and modulation of global cooperative behavior of brain wave interactions to accommodate physiologic function during different physiologic states.

3.2 Specific Roles of Different Brain Areas in Brain Wave Network Interactions

To better understand the role of individual brain areas in the network of brain wave interactions, we consider subnetworks associated with specific brain locations. We consider six subnetworks associated with the six EEG channels in the experimental setup, where each subnetwork represents the set of network links between different

frequency bands (network nodes) derived from a given EEG channel (brain location) and brain waves at all other brain areas (EEG locations).

Our results show a strong and robust symmetry between the left and right hemisphere in both network topology and link strength configurations. For example, we find that for each physiologic state, the subnetwork associated with the C3 channel is almost identical to the one associated with the C4 channel. Thus, we only present and discuss the results obtained for the C3 channels located in the left hemisphere. The choice of C3 channel is also motivated by traditional sleep-stage classification rules which utilize EEG signals derived from the C3 channel. Our analyses of brain-wave subnetworks associated with other channels (reported elsewhere [29]) show a similar stratification across sleep stages in the average link strength and number of network links as shown here for the C3 channel.

3.2.1 Intra-channel Network at C3

The intra-channel network represents flow of communication (as measured by %TDS) carried by the spectral power of different frequency bands of the EEG signal recorded at one specific channel location. We find that the connectivity of the intra-channel network at C3 channel changes significantly across distinct physiologic states [29] — we observe a lowest connectivity in REM, a higher one in Wake and Light Sleep and the highest connectivity during Deep Sleep. Notably, in Deep Sleep we observe that most links are associated with high frequency β , γ_1 , γ_2 bands, which form a dark triangle in Fig. 3.

3.2.2 Inter-channel Network Associated with C3

The inter-channel network represents interactions between one channel location and all other brain areas. By investigating the inter-channel network associated with C3, we find that the network undergoes a very pronounced reorganization with transition across sleep stages. This network reorganization, both in network structure and link strength, is more pronounced compared to the reorganization we observe in the intra-channel network of C3 (Fig. 3).

Central-Central interaction: Our analyses show that inter-channel links that connect same frequency bands (i.e., same-frequency links) at different central channel locations remain strong (>45%TDS) during all sleep stages. In contrast, inter-channel links that connect different frequency bands (i.e., cross-frequency links) at the two Central channels C3 and C4 change significantly across different sleep stages. Central-Central cross-frequency links are weak with <45%TDS during REM (not visible on the network graph), stronger during Deep Sleep and Wake, and reach their maximum strength during Light Sleep as shown in Fig. 3.

Central-Frontal interaction: We find that inter-channel links representing connections observed between brain waves at the Central and Frontal channels have lower con-

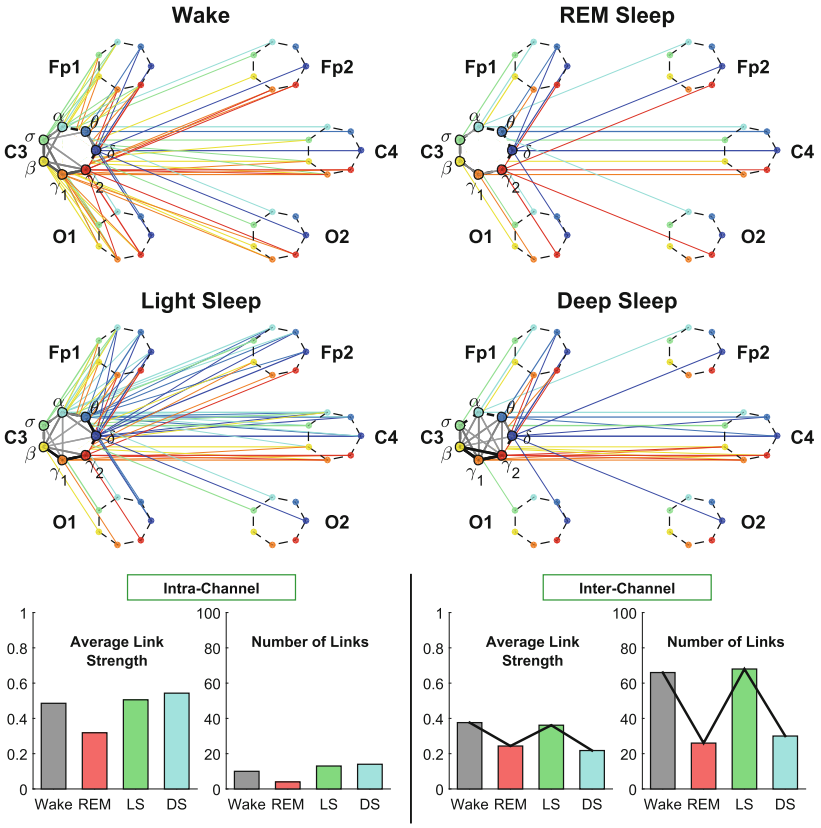

Fig. 3 Neural plasticity represented by transitions in the sub-networks of brain wave interactions centered at the Central C3 channel. Network nodes with different colors represent seven different frequency bands (δ , θ , α , σ , β , γ_1 , γ_2) derived from EEG signals. Each set of seven nodes ordered as a heptagon forms a vertex on the hexagon representing six EEG channels from particular brain locations: Two Frontal areas (Fp1 and Fp2), two Central areas (C3 and C4) and two Occipital areas (O1 and O2). Interactions between frequency bands derived from the C3 channel (intra-channel links) are color-coded in *gray scale*. Interactions between frequency bands derived from the C3 channel and network nodes in all other EEG channels are represented by inter-channel links shown with the same color as the corresponding frequency band (network node) at C3. Line thickness represents the group-averaged link strength as measured by %TDS, and only links with %TDS$\geq$ 45% are shown. Both the intra-channel networks (involving links between the frequency nodes at C3) and inter-channel networks (colored links between nodes at C3 and nodes at all other channels) undergo complex hierarchical reorganization across sleep stages, indicating pronounced plasticity in the way frequency bands communicate locally within the C3 Central area and with frequency bands at other brain areas. The intra-channel subnetwork at C3 exhibits low connectivity during REM, medium connectivity during Wake and Light Sleep, and becomes highly connected during Deep Sleep. A similar sleep-stage pattern is also observed for the intra-channel links strength. In contrast, the inter-channel subnetwork between C3 and other brain areas undergoes a very different transition in network connectivity and link strength – from low connectivity in REM and Deep Sleep to high connectivity in Light Sleep and Wake. Note that an identical network structure and reorganization across sleep stages is observed for the Central C4 channel (not shown), indicating a robust symmetry between the left and right hemisphere

nectivity in REM and Deep Sleep, higher connectivity in Wake and become highly connected during Light Sleep. In general, we find that inter-channel links within the same hemisphere (C3-Fp1) are stronger than cross-hemisphere links (C3-Fp2) in all sleep stages.

Central-Occipital interaction: Further we observe that Central-Occipital brain wave interactions are much weaker (lower network connectivity) compared to Central-Central or Central-Frontal brain wave interactions, a behavior which is consistent for all sleep stages (Fig. 3). Nonetheless, the connectivity of Central-Occipital subnetwork follows a similar sleep-stage stratification pattern as all other inter-channel subnetworks associated with C3 — lower connectivity during Deep Sleep and REM, and higher connectivity during Light Sleep and Wake (Fig. 3).

In summary, our results show that each brain area follows its own rule with respect to the intra-channel communications between different frequency bands. In contrast, brain wave inter-channel interactions across different locations (Frontal, Central and Occipital) exhibit a robust sleep-stage stratification pattern in network connectivity and average link strength [29]. These observations suggest the possible presence of two distinct mechanisms of neural plasticity, within a brain location and between brain areas, that regulate the network of brain-wave communications across different physiologic states.

3.3 Network Interactions of the Same Brain Rhythm Across Brain Areas

Our investigations show that brain wave interactions between different frequency bands at different brain locations exhibit strong sleep-stage specificity — as represented by dramatic change in the cross-frequency links in the Central, Frontal and Occipital subnetwork during different sleep stages (Fig. 3) [29].

In contrast, brain wave interaction mediated through the same frequency band (e.g., parallel diagonal lines in the TDS block matrices in Fig. 1e) are stronger in all sleep stages compared to the cross-frequency links, indicating an important role of same-frequency links in facilitating communications between different brain locations.

To better understand the role of same-frequency interactions across brain areas and how these interactions respond to change in physiologic states, we obtain frequency-specific networks (Fig. 4) as the ensemble of inter-channel links connecting a specific frequency band at different brain locations (network nodes). We find that brain interactions mediated through specific frequency bands are (i) associated with very different network structure within a given physiologic state, and (ii) exhibit distinct patterns of hierarchical reorganization with transition across physiologic states (Fig. 4).

Comparing frequency-specific networks within the same physiologic state, we find very different degree of network connectivity and link strength for the different bands.

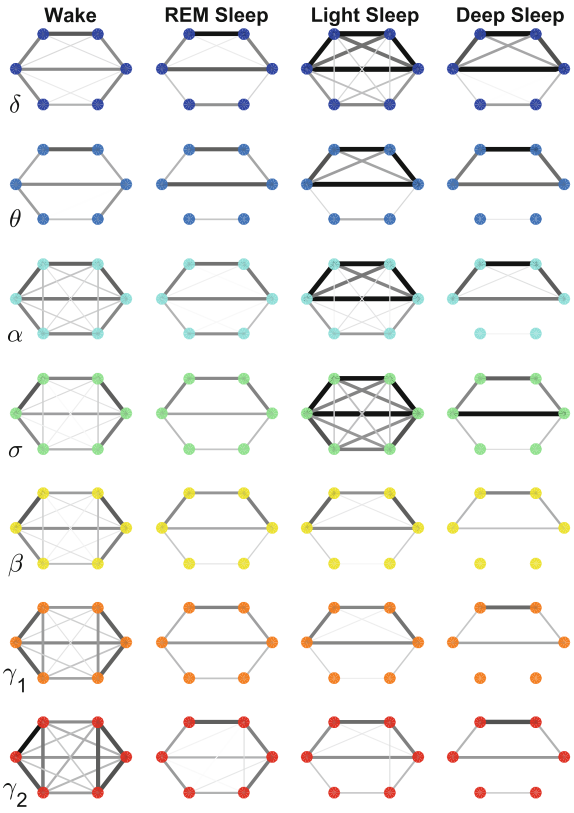

Fig. 4 Neural plasticity in the frequency domain represented by reorganization of network interactions across brain areas mediated through a specific frequency band across physiologic states. Network nodes represent six different brain areas: Frontal Fp1 and Fp2 (*top vertices* of the hexagon), Central C3 and C4 (*middle vertices*) and Occipital O1 and O2 (*bottom vertices*). Node colors indicate different frequency bands through which the inter-channel brain interactions are mediated. Group-averaged TDS links strength is represented by line thickness and by different color on *gray scale*. Only links with %TDS $\geq$45% are shown. Brain interactions mediated through specific frequency bands are associated with very different network structure within a given physiologic state, and exhibit distinct patterns of hierarchical reorganization with transition across physiologic states. Specifically, networks representing brain interactions in the δ and σ band are highly connected and with stronger links in Light Sleep, whereas networks representing brain interactions in the α , γ_1 and γ_2 band are highly connected and with stronger links during Wake. Notably, network characteristics during Deep Sleep and REM are similar for almost all frequency bands

During Deep and Light Sleep, the inter-channel interactions are mainly mediated through the δ and σ band. However, during Deep Sleep the network of δ band is dominant where as during Light Sleep the network of σ band is dominant (Fig. 4). Further, during REM we find that networks of all frequency bands have comparable contributions to the inter-channel brain wave communications, with slight prevalence of network interactions in the α and γ bands (Fig. 4). In contrast, the high-frequency γ_1 and γ_2 bands dominates the inter-channel interactions during Wake.

Our investigation reveals that each frequency-specific network is characterized by a different signature pattern of sleep-stage stratification in average link strength, reflecting different neural plasticity of brain activation in different frequency bands.

4 Brain-Organ Networks: New Signatures of Neuroautonomic Control

To better understand the neurophysiologic control of key organ systems, we next focus our investigation on identifying and quantifying the networks of interactions between the brain and individual organ systems. Specifically we consider the cardiac system. There are several key questions related to the nature of brain-organ interactions: (i) how different areas of the brain as represented by different EEG-channel locations are involved in the communications and control of each organ system, (ii) which brain-wave frequency bands mediate the brain-organ communications, and (iii) how the networks representing brain-organ interactions across brain areas and different brain-wave frequency bands evolve with transitions across physiologic states [5, 15, 16].

To this end, we apply the TDS method to identify and quantify dynamical links in the networks of brain-heart interactions, and we develop radar-charts to graphically represent these complex communications, and how they change with physiologic states. The obtained networks serve as unique physiological maps of brain-organ interactions [5].

Our analysis of the network of brain-heart interactions shows a relatively symmetric distribution of the average links strength for different brain areas, with a slight prevalence in strength for the links between the heart and the Central brain areas (C3 and C4), as indicated by the radar chart inside the heart hexagon in Fig. 5. We find this spatial symmetry in the average brain-heart link strength to hold for all sleep stages [5].

Next, we study the frequency profile for the strength of the brain-heart links. We find that for a given physiologic state, the frequency profile of brain-heart links remains stable for all brain areas (Frontal, Central and Occipital) [5]. However, comparing different physiologic states we find markedly different frequency profiles for the strength of brain-heart links. Specifically, during W the frequency profiles for the links to the Frontal, Central and Occipital areas are characterized by strongest links for the highest-frequency γ_1 and γ_2 bands and a gradual decrease in links strength for the lower-frequency bands (β , σ , α , θ), followed by a slight increase in link strength for the lowest-frequency δ band. With transition to REM, the frequency profiles for all brain areas are modulated, where the relative difference in links strength between different frequency bands is reduced compared to W, and the shape of the profile changes — stronger links for high-frequency bands (γ_1 , γ_2 , β , σ) and much weaker links for low-frequency (α , θ , δ). In contrast, during both LS and DS, we find that for all brain areas (Frontal, Central and Occipital) the frequency profiles of

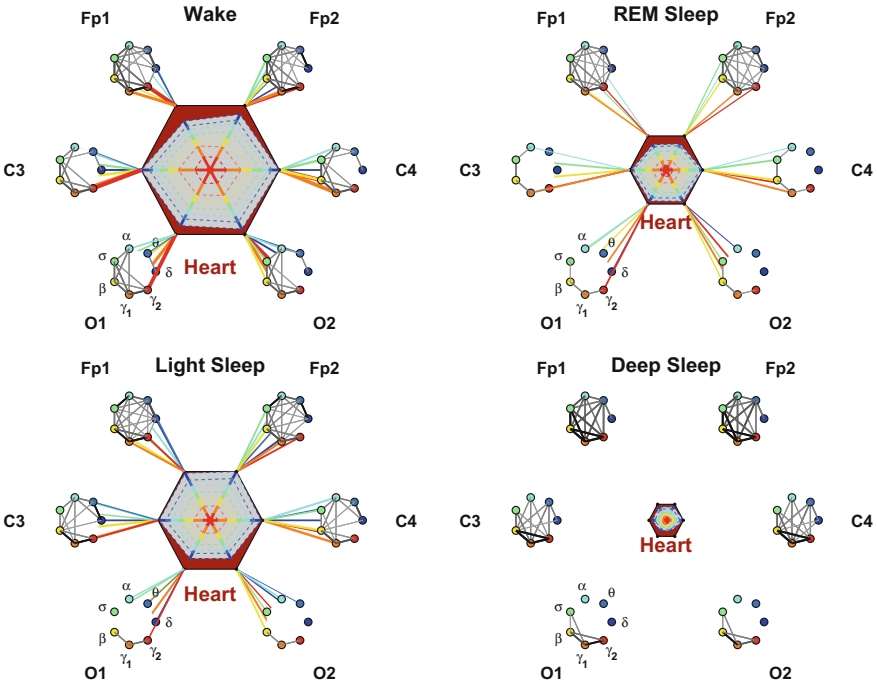

Fig. 5 Networks of brain-heart interactions during different physiologic states. Brain areas are represented by Frontal (Fp1 and Fp2), Central (C3 and C4) and Occipital (O1 and O2) EEG channels. Network nodes with different colors represent seven frequency bands (δ , θ , α , σ , β , γ_1 , γ_2) in the spectral power of each EEG channel. Within each brain area (EEG channel), intra-channel network links between frequency bands are plotted in linear gray color code. Network links between the heart (*red hexagon*) and EEG frequency nodes at different locations are determined based on the TDS measure, and brain-heart links strength is illustrated by the line thickness (shown are links with strength $\geq$5%TDS). Radar-charts centered in each hexagon represent the relative contribution of brain control from different brain areas to the strength of network links during different sleep stages. The length of each segment along each radius in the radar-charts represents TDS coupling strength between the heart and each frequency band at each EEG channel location. These segments are shown in the same color as the corresponding EEG frequency nodes. During W and REM, the brain-heart network interactions are mediated mainly through high-frequency γ_1 and γ_2 bands (*orange* and *red links*), while during LS and DS, the interactions are mediated uniformly through all frequency bands. The brain-heart network is characterized by relatively symmetric links strength to all six brain areas, as shown by the symmetric radar-charts in each hexagon. A pronounced stratification pattern is observed for the overall strength of network links — stronger links during W and LS (*larger hexagons*) and weaker links during REM and DS (*smaller hexagons*)

links strength are practically homogeneous with an almost flat distribution across all frequency bands.

Systematically investigating the links strength in the brain-heart network for all 7 frequency bands and different sleep stages, we find that the average link strength for the entire network of brain-heart interactions is highest during W and LS, lower

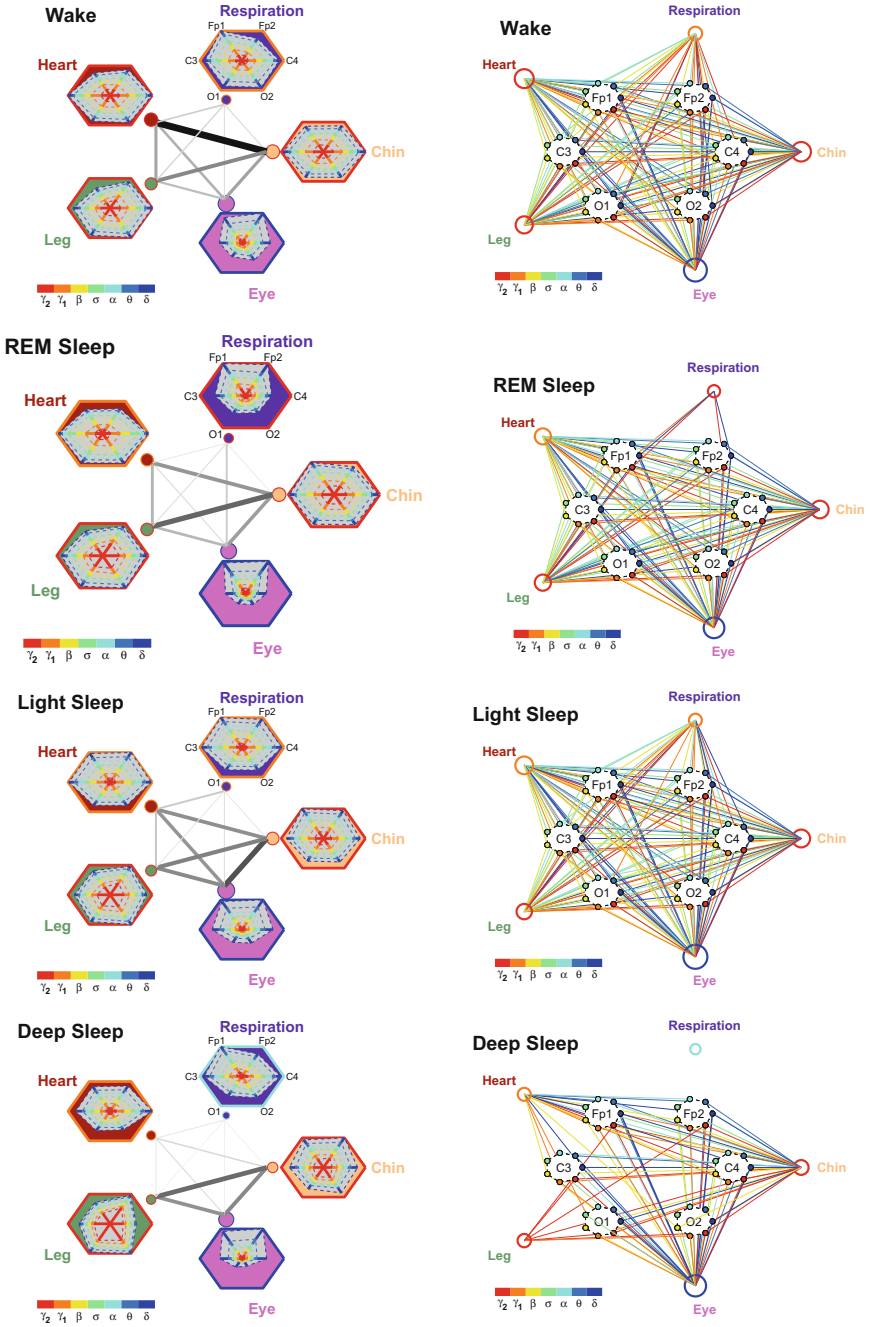

Fig. 6 (Continued)

◀**Fig. 6 Networks of physiologic interactions among key organ systems during different physiologic states**. (*Left column*) Interactions among organ systems are represented by weighted undirected graphs, where links reflect the strength of dynamic coupling as measured by % TDS. *Darker* and *thicker links* between organ systems correspond to stronger interaction with higher %TDS. (*Right column*) Brain-organ interactions are represented by links between each organ and different frequency bands at six brain locations: (Fp1, Fp2, C3, C4, O1 and O2) EEG channels. The size of each organ node in the network is proportional to the strength of the overall brain-organ interaction as measured by the summation of the TDS links strength for all frequency bands and EEG channel locations. Hexagons representing individual organs in the networks are obtained in the same way as in Fig. 5; and are normalized to the same size. Color bars represent different physiologically relevant frequency bands in the EEG spectral power and are used in the radar-charts for the brain-organ interactions shown in each hexagon. The color of each organ node as well as the edge color of the organ hexagon corresponds to the dominant frequency band in the coupling of the organ system with the brain. Notably, larger organ nodes representing stronger brain-organ interactions are consistently connected by stronger organ-organ links (*thicker* and *darker lines*)

during REM and lowest during DS (Fig. 5). Further, this sleep-stage stratification pattern is consistently observed for all three sub-networks representing the Frontal-heart, Central-heart and Occipital-heart links across all frequency bands (Fig. 5).

Our analysis show that the observed hierarchical reorganization in the network of brain-heart interactions across different sleep stages is accompanied by a parallel reorganization in the topology of intra-channel networks representing brain rhythms interaction within the same brain location (EEG channel). Notably, during Deep Sleep where the strength of brain-heart interaction is greatly reduced, intra-channel brain networks at all EEG channel locations exhibit hight connectivity. This intra-channel network connectivity is more pronounced for the Frontal and Central locations compared to the Occipital areas – a pattern that is consistently observed for all sleep stages [5].

5 Organ-Organ Networks: New Maps of Dynamical Organ Interactions

We develop a novel approach to analyze and graphically present the complex behavior of organ-organ interactions. Integrating information obtained from our investigation of brain-organ interactions, we focus on how organ-to-organ interactions are influenced by neural regulation through different brain areas. We combine radar-charts representing the characteristics of brain-organ interactions with the network of links between all organ systems obtained thought TDS analysis of the output signals for each pair of organ systems (Fig. 6) [5].

We observe that, with transitions from one sleep stage to another there is a pronounced structural re-organization in the topology and links strength of the organ-organ network. This demonstrates a clear association between organ-to-organ network structure and physiologic function of the entire organism. The result in Fig. 6 shows how physiologic states influence the dynamics of horizontal integration among

organ systems through changing the configuration of links strength in the organ-to-organ network.

Specifically, we find that eye, chin and leg are always strongly connected despite the very different characteristics in their interactions with the brain — i.e., different dominating frequency bands (shown by different color rim of the organ hexagons) and different involvement of the brain areas (shown by different shape of radar-charts in each hexagon) and different overall strength of their network interaction with the brain (shown by different size of the nodes representing each organ), in Fig. 6. In contrast, the heart and respiratory system significantly vary their degree of coupling with the rest of the network across physiologic states (Fig. 6). Further, we note that even when two organ systems predominately interact with the same brain areas, their coupling strength in the organ-to-organ network can still exhibit a complex transition across different physiologic state — for example, both heart and chin predominately interact with the Central brain areas, however, the strength of the heart-chin link in the organ network dramatically change across different sleep stages [5].

Interestingly, we discover that strong organ-to-organ links often occur between large nodes in the network that represent strong brain-organ interactions, suggesting our TDS network approach captures significant cerebral component in organ-organ interactions. Notably, the reduced link strength of the heart and respiratory system in the organ-to-organ network during LS and DS compared to REM and W is consistent with earlier findings of reduced sympathetic input and corresponding loss of long-range auto-correlation in cardiac and respiratory dynamics during LS and DS [18, 25, 26, 39, 40].

6 Summary

The findings reported here are first steps in understanding how organ systems synchronize and coordinate their output dynamics as a network to produce distinct physiologic functions [5, 29, 30]. Our investigations reveal basic rules that underlie (i) the dynamics of network interactions among organ systems, and (ii) the hierarchical reorganization of organ network interactions in response to changes in physiologic state. The uncovered association between physiologic network structure and specific physiologic states (sleep stages) demonstrates the utility of the proposed integrative approach as a necessary step to more comprehensively understand fundamental mechanisms of neurophysiologic regulation at the organism level. In addition, our investigations lead to the identification of new set of physiologic parameters (link strength and network connectivity based on %TDS) that characterize the variability and strength of organ network interactions during different physiologic states under healthy conditions. The discovered dynamical networks of organ interactions are a unique signature and hallmark of physiologic states and functions. This will impact the current paradigm of defining health and physiologic states, shifting the focus from structure and function of individual systems to the coordination and communication among organ systems as a network.

Finally, in a more general context, these are important first steps in the development of an adequate analytic formalism and theoretical framework to study network interactions among diverse complex dynamical systems with multiple coexisting forms of coupling. Such framework will be necessary for the development of the new field, Network Physiology, with focus on understanding physiologic function through the prism of horizontal integration of physiologic systems in the organism. The uncovered maps of organ network interactions are initial building blocks of a more comprehensive dynamical atlas of the human organism under health and disease with broad clinical applications.

Acknowledgements We acknowledge support from W.M. Keck Foundation, National Institutes of Health (NIH Grant 1R01- HL098437), the Office of Naval Research (ONR Grant 000141010078), the US-Israel Binational Science Foundation (BSF Grant 2012219), EC-FP7 Marie Curie Fellowship (IIF 628159).

References

1. Ashkenazy, Y., Hausdorff, J., Ivanov, P.Ch., Stanley, H.E.: A stochastic model of human gait dynamics. Phys. A **316**(1–4), 662–670 (2002). doi:10.1016/S0378-4371(02)01453-X
2. Bartsch, R.P., Ivanov, P.Ch.: Coexisting forms of coupling and phase-transitions in physiological networks. Commun. Comput. Inf. Sci. **438**, 270–287 (2014)
3. Bartsch, R.P., Schumann, A.Y., Kantelhardt, J.W., Penzel, T., Ivanov, P.Ch.: Phase transitions in physiologic coupling. Proc. Natl. Acad. Sci. USA **109**(26), 10181–10186 (2012). doi:10.1073/pnas.1204568109
4. Bartsch, R.P., Liu, K.K.L., Ma, Q.D.Y., Ivanov, P.Ch.: Three independent forms of cardio-respiratory coupling: transitions across sleep stages. Comput. Cardiol. **41**, 781–784 (2014)
5. Bartsch, R.P., Liu, K.K.L., Bashan, A., Ivanov, P.C.: Network physiology: how organ systems dynamically interact. PLoS ONE **10**(11), e0142,143 (2015). doi:10.1371/journal.pone.0142143
6. Bashan, A., Bartsch, R.P., Kantelhardt, J.W., Havlin, S., Ivanov, P.Ch.: Network physiology reveals relations between network topology and physiological function. Nat. Commun. **3**, 702 (2012)
7. Bian, Z., Li, Q., Wang, L., Lu, C., Yin, S., Li, X.: Relative power and coherence of EEG series are related to amnestic mild cognitive impairment in diabetes. Front Aging Neurosci. **6**, 11 (2014). doi:10.3389/fnagi.2014.00011
8. Buchman, T.G.: Complex systems science in biomedicine. In: Physiologic Failure: Multiple Organ Dysfunction Syndrome, pp. 631–640. Kluwer Academic/Plenum Publishers, New York (2006)
9. Bullmore, E., Sporns, O.: Complex brain networks: graph theoretical analysis of structural and functional systems. Nat. Rev. Neurosci. **10**(3), 186–198 (2009). doi:10.1038/nrn2575
10. Bunde, A., Havlin, S., Kantelhardt, J.W., Penzel, T., Peter, J.H., Voigt, K.: Correlated and uncorrelated regions in heart-rate fluctuations during sleep. Phys. Rev. Lett. **85**(17), 3736–3739 (2000). doi:10.1103/PhysRevLett.85.3736
11. Carskadon, M.: Principles and practice of sleep medicine. In: Guidelines for the Multiple Sleep Latency Test (MSLT): A Standard Measure of Sleepiness, pp. 962–966. WB Saunders Company, Philadelphia (1994)
12. Chen, Z., Hu, K., Stanley, H.E., Novak, V., Ivanov, P.Ch.: Cross-correlation of instantaneous phase increments in pressure-flow fluctuations: applications to cerebral autoregulation. Phys. Rev. E **73**(3 Pt 1), 031,915 (2006)

13. Chorlian, D.B., Rangaswamy, M., Porjesz, B.: EEG coherence: topography and frequency structure. Exp. Brain Res. **198**(1), 59–83 (2009). doi:10.1007/s00221-009-1936-9
14. Dumont, M., Jurysta, F., Lanquart, J.P., Migeotte, P.F., van de Borne, P., Linkowski, P.: Interdependency between heart rate variability and sleep EEG: linear/non-linear? Clin. Neurophysiol. **115**(9), 2031–2040 (2004). doi:10.1016/j.clinph.2004.04.007
15. Faes, L., Nollo, G., Jurysta, F., Marinazzo, D.: Information dynamics of brain–heart physiological networks during sleep. New J. Phys. **16**, 105,005 (2014)
16. Faes, L., Marinazzo, D., Jurysta, F., Nollo, G.: Linear and non-linear brain-heart and brain-brain interactions during sleep. Physiol. Meas. **36**(4), 683–698 (2015). doi:10.1088/0967-3334/36/4/683
17. Ferri, R., Rundo, F., Bruni, O., Terzano, M.G., Stam, C.J.: The functional connectivity of different EEG bands moves towards small-world network organization during sleep. Clin. Neurophysiol. **119**(9), 2026–2036 (2008). doi:10.1016/j.clinph.2008.04.294
18. Ivanov, P.Ch.: Scale-invariant aspects of cardiac dynamics - observing sleep stages and circadian phases. IEEE Eng. Med. Biol. **26**(6), 33–37 (2007). doi:10.1109/MEMB.2007.907093
19. Ivanov, P.Ch., Bartsch, R.P.: Network Physiology: Mapping Interactions Between Networks of Physiologic Networks, pp. 203–222. Springer International Publishing, Switzerland (2014)
20. Ivanov, P.Ch., Rosenblum, M.G., Peng, C.K., Mietus, J., Havlin, S., Stanley, H.E., Goldberger, A.L.: Scaling behaviour of heartbeat intervals obtained by wavelet-based time-series analysis. Nature **383**, 323–327 (1996)
21. Ivanov, P.Ch., Amaral, L.A.N., Goldberger, A.L., Stanley, H.E.: Stochastic feedback and the regulation of biological rhythms. Europhys. Lett. **43**, 363–368 (1998)
22. Ivanov, P.Ch., Amaral, L.A.N., Goldberger, A.L., Havlin, S., Rosenblum, M.G., Struzik, Z.R., Stanley, H.E.: Multifractality in human heartbeat dynamics. Nature **399**(6735), 461–465 (1999). doi:10.1038/20924
23. Ivanov, P.Ch., Bunde, A., Amaral, L.A.N., Havlin, S., Fritsch-Yelle, J., Baevsky, R.M., Stanley, H.E., Goldberger, A.L.: Sleep-wake differences in scaling behavior of the human heartbeat: analysis of terrestrial and long-term space flight data. Europhys. Lett. **48**(5), 594–600 (1999). doi:10.1209/epl/i1999-00525-0
24. Ivanov, P.Ch., Amaral, L.A.N., Goldberger, A.L., Havlin, S., Rosenblum, M.G., Stanley, H.E., Struzik, Z.: From 1/*f* noise to multifractal cascades in heartbeat dynamics. Chaos **11**, 641–652 (2001)
25. Kantelhardt, J.W., Ashkenazy, Y., Ivanov, P.Ch., Bunde, A., Havlin, S., Penzel, T., Peter, J.H., Stanley, H.E.: Characterization of sleep stages by correlations in the magnitude and sign of heartbeat increments. Phys. Rev. E **65**(5), 051,908 (2002). doi:10.1103/PhysRevE.65.051908
26. Kantelhardt, J.W., Havlin, S., Ivanov, P.Ch.: Modeling transient correlations in heartbeat dynamics during sleep. Europhys. Lett. **62**(2), 147–153 (2003)
27. Karasik, R., Sapir, N., Ashkenazy, Y., Ivanov, P.Ch., Dvir, I., Lavie, P., Havlin, S.: Correlation differences in heartbeat fluctuations during rest and exercise. Phys. Rev. E **66**(6), 062,902 (2002). doi:10.1103/PhysRevE.66.062902
28. Klimesch, W.: EEG alpha and theta oscillations reflect cognitive and memory performance: a review and analysis. Brain Res. Rev. **29**(2–3), 169–195 (1999)
29. Liu, K.K.L., Bartsch, R.P., Lin, A., Mantegna, R.N., Ivanov, P.C.: Plasticity of brain wave network interactions and evolution across physiologic states. Front. Neural Circuits **9**, 62 (2015). doi:10.3389/fncir.2015.00062
30. Liu, K.K.L., Bartsch, R.P., Ma, Q.D.Y., Ivanov, P.Ch.: Major component analysis of dynamic networks of physiologic organ interactions. J. Phys.: Conf. Ser. **640**(1), 012,013 (2015). http://dx.doi.org/10.1088/1742-6596/640/1/012013, http://stacks.iop.org/1742-6596/640/i=1/a=012013
31. Lin, A., Liu, K.K.L., Bartsch, R.P., Ivanov, P.C.: Delay-correlation landscape reveals characteristic time delays of brain rhythms and heart interactions. Philos. Trans. R. Soc. A: Math. Phys. Eng. Sci. **374**(2067), 20150,182 (2016). doi:10.1098/rsta.2015.0182
32. Long, X., Arends, J.B., Aarts, R.M., Haakma, R., Fonseca, P., Rolink, J.: Time delay between cardiac and brain activity during sleep transitions. Appl. Phys. Lett. **106**(14), 143,702 (2015). doi:10.1063/1.4917221

33. McCraty, R., Atkinson, M., Tomasino, D., Bradley, R.T.: The coherent heart: heart-brain interactions, psychophysiological coherence, and the emergence of system-wide order. Integral Rev. **5**(2), 10–115 (2009)
34. Pikovsky, A.S., Rosenblum, M.G., Kurths, J.: Synchronization: A Universal Concept in Nonlinear Sciences. Cambridge University Press, Cambridge (2001)
35. Piper, D., Schiecke, K., Pester, B., Benninger, F., Feucht, M., Witte, H.: Time-variant coherence between heart rate variability and EEG activity in epileptic patients: an advanced coupling analysis between physiological networks. New J. Phys. **16**(11), 115,012 (2014)
36. Rechtschaffen, A., Kales, A.: A manual of standardized terminology, techniques and scoring system for sleep stages of human subjects. US Department of Health, Education, and Welfare, Bethesda, MD (1968)
37. Rosenblum, M.G., Pikovsky, A.S., Kurths, J.: Phase synchronization of chaotic oscillators. Phys. Rev. Lett. **76**(11), 1804–1807 (1996)
38. Rosenblum, M.G., Pikovsky, A.S., Kurths, J.: From phase to lag synchronization in coupled chaotic oscillators. Phys. Rev. Lett. **78**(22), 4193–4196 (1997). doi:10.1103/PhysRevLett.78.4193
39. Schmitt, D.T., Stein, P.K., Ivanov, P.Ch.: Stratification pattern of static and scale-invariant dynamic measures of heartbeat fluctuations across sleep stages in young and elderly. IEEE Trans. Biomed. Eng. **56**(5), 1564–1573 (2009). doi:10.1109/TBME.2009.2014819
40. Schumann, A.Y., Bartsch, R.P., Penzel, T., Ivanov, P.Ch., Kantelhardt, J.W.: Aging effects on cardiac and respiratory dynamics in healthy subjects across sleep stages. Sleep **33**(7), 943–955 (2010)
41. Song, L.Z., Schwartz, G.E., Russek, L.G.: Heart-focused attention and heart-brain synchronization: energetic and physiological mechanisms. Altern. Ther. Health Med. **4**(5), 44–52, 54–60, 62 (1998)
42. Stankovski, T., Ticcinelli, V., McClintock, P.V.E., Stefanovska, A.: Coupling functions in networks of oscillators. New J. Phys. **17**, 035,002 (2015)
43. Stramaglia, S., Cortes, J.M., Marinazzo, D.: Synergy and redundancy in the granger causal analysis of dynamical networks. New J. Phys. **16**, 105,003 (2014)
44. Tanaka, H., Hayashi, M., Hori, T.: Topographical characteristics and principal component structure of the hypnagogic EEG. Sleep **20**(7), 523–534 (1997)
45. Valenza, G., Greco, A., Gentili, C., Lanata, A., Sebastiani, L., Menicucci, D., Gemignani, A., Scilingo, E.P.: Combining electroencephalographic activity and instantaneous heart rate for assessing brain-heart dynamics during visual emotional elicitation in healthy subjects. Philos. Trans. R. Soc. A **374**, 20150176 (2016)
46. Valenza, G., Toschi, N., Barbieri, R.: Uncovering brain-heart information through advanced signal and image processing. Philos. Trans. R. Soc. A **374**, 20160020 (2016)
47. Xu, L., Chen, Z., Hu, K., Stanley, H.E., Ivanov, P.Ch.: Spurious detection of phase synchronization in coupled nonlinear oscillators. Phys. Rev. E **73**(6 Pt 2), 065,201 (2006)

Temporal Excitation Patterns on the Cerebral Cortex as a Result of Migraine Modeling

Julia M. Kroos, Ibai Diez, Jesus M. Cortes, Sebastiano Stramaglia and Luca Gerardo-Giorda

Abstract The complex, highly individual, geometry of the cerebral cortex in humans presents a major challenge in studying the spreading of spontaneous neuronal activity. Recent computational advances [1] allow to simulate the propagation of depolarization waves on the macroscale and for individual geometries, reconstructed from accurate medical imaging as MRI, with high levels of detail. In this paper we take advantage of such technique to study the temporal excitation patterns that follow the passage of a depolarization wave on the cerebral cortex.

J.M. Kroos (✉)
Basque Center for Applied Mathematics, Basque Country, Bilbao, Spain
e-mail: jkroos@bcamath.org

I. Diez
Biocruces Health Research Institute, Cruces University Hospital, Barakaldo, Spain
e-mail: ibaidiez85@gmail.com

J.M. Cortes
Biocruces Health Research Institute Barakaldo, Barakaldo, Spain
e-mail: jesus.m.cortes@gmail.com

J.M. Cortes
Departamento de Biologia Celular e Histologia, University of the Basque Country, Leioa, Spain

J.M. Cortes
Ikerbasque: The Basque Foundation for Science, Bilbao, Spain

S. Stramaglia
Dipartimento di Fisica, Università di Bari, Bari, Italy
e-mail: sebastiano.stramaglia@ba.infn.it

S. Stramaglia
INFN, Sezione di Bari, Bari, Italy

L. Gerardo-Giorda
Basque Center for Applied Mathematics,, Basque Country Bilbao, Spain
e-mail: lgerardo@bcamath.org

G. Mantica et al. (eds.), *Emergent Complexity from Nonlinearity, in Physics, Engineering and the Life Sciences*, Springer Proceedings in Physics 191,
DOI 10.1007/978-3-319-47810-4_13

1 Introduction

One of the most intriguing phenomenon related to reaction-diffusion processes in complex geometries is the spreading depression of spontaneous activity, initially discovered and characterized in animal cortices [2, 3]. Nowadays these phenomena are believed to be relevant in a plethora of brain pathologies, such as cerebral ischemia-infarction, transient global amnesia, epilepsy or migraine auras, the situation we focus on here. Several experiments suggest that a propagating depolarization wave on the cortex is underlying migraine, see [4–6] and references therein. This wave, named cortical spreading depression (CSD), causes a drastic failure of the brain homeostasis and is followed by a wave of inhibition. CSD is characterized by relevant increases in both extracellular K^+ and glutamate, as well as rises in intracellular Na^+ and Ca^{2+}. These ionic shifts result in slow direct current potential shifts that can be recorded extracellularly. Starting in the visual cortex, CSD propagates to the peripheral areas. It is worth mentioning that, whilst CSD has been experimentally demonstrated in animal models, the strongest evidences for CSD in humans are the migraine aura itself, and the spreading oligemia phenomenon observed in migraine patients, consisting in a decrease of the cerebral blood flow in the posterior part of the brain at the beginning of the attack, followed by the spreading of the low flow region at a speed which is similar to those found for CSD in animals. Some electrophysiological evidences that human grey matter in vivo supports CSD have also been reported (see, e.g., [7]). A deeper understanding of CSD phenomenology would be useful to test current and novel prophylactic drugs, while providing knowledge on mechanisms of action relevant for migraine [8]. The role played by the peculiar geometry of the brain cortex in supporting or blocking CSD is far from being satisfactorily understood. In a recent paper [1] we investigated several aspects of the brain geometry which favor or disfavor the propagation of CSD. In particular, by using a computational neuronal model distributed throughout a realistic cortical mesh, we have found significant differences in the propagation traveling patterns of CSD, both intra and inter-hemispherically, and revealed important asymmetries in the propagation profile. Moreover we identified brain regions displaying a peculiar behavior during CSD propagation, in particular, some regions that appear to trap the propagating action potentials for a longer time. Those regions play a key role in the CSD propagation (and possibly would be able to stop it). These results are relevant to identify target structures for therapies using stereotactic cortical neuromodulation, see e.g., [9].

In the present work we will concentrate on another feature of the propagating CSD wave, still exploiting the computational frame of simulations on the realistic cortical mesh. In the specific, we will study the temporal patterns of excitation associated with the propagation of the CSD by analyzing the percentage of cortex that can get excited at the same time. The paper is organized as follows. In Sect. 2 we describe the distributed model for CSD propagation, its numerical approximation and the characteristics of the realistic cortical computational grid. In Sect. 3 the temporal

activity we study in this paper is introduced. Finally, numerical results from the simulation of the distributed model are collected in Sect. 4.

2 Modeling and Numerical Simulation of CSD on Real Geometries

2.1 A Distributed Computational Model for CSD Propagation

A key property of neural cells is to produce an action potential (AP). It consists in a sudden variation in the transmembrane potential, called spike, followed by a recovering of the resting condition through a refractory period, during which the cell cannot be excited. In agreement with previous computational studies [10], we consider neurons at rest to have a background firing rate of 4 Hz while excited neurons fire with an average frequency of 64 Hz.

In [1] we introduced a slow variables model for the firing rate to describe the neuronal activity, where the state variable $u(x,t)$ represents the average firing rate of neurons at location x and time t (in seconds). Such model is locally a temporal mean field one with respect to the finer scale of the action potential, and represents the typical all-or-nothing response of a single excited cell in a simplified manner [11]. The model is a modification of the Roger-McCulloch variant of the Fitzhugh-Nagumo model [12], that has been adapted to reproduce the characteristic neuronal activity, with a resting state of 4 Hz, a firing rate of 64 Hz in the excited state, and the plateau length matching the duration of the neuron excitation after the passage of the CSD (around 10 min, [13]).

A diffusion term accounts for the spatial propagation of the excitation on the cortex, and the complete model reads:

$$\begin{aligned} \frac{\partial u}{\partial t} &= -I(u,w) + \operatorname{div}(D\nabla u) \\ I(u,w) &= G(u-u_0)\left(1-\frac{u}{u_{th}}\right)\left(1-\frac{u}{u_p}\right) + \eta_1(u-u_0)w \\ \frac{\partial w}{\partial t} &= \eta_2\,(u-u_0-\eta_3 w)\,, \end{aligned} \tag{1}$$

where $u(x,t)$ is the firing rate at time $t \geq 0$, and $w(x,t)$ is the recovery variable, u_{th} and u_p are threshold and peak values for u, u_0 is the background firing rate and $D \in \mathbf{R}^{3\times 3}$ is the conductivity tensor, while η_1, η_2, η_3 and G are parameters, whose values are given in Table 1. The coupled PDE-ODE system (1) is defined on the computational domain $\Omega \times (0,T)$, $\Omega \subset \mathbf{R}^3$. To ensure that problem (1) is mathematically well posed, initial conditions $u^0(x) = u(x,0)$, $w^0(x) = w(x,0)$ must be imposed in Ω and boundary conditions on $\partial\Omega$. If the computational domain is a 2D surface $\Sigma \subset \mathbf{R}^3$ the classical divergence and gradient operators are replaced by their

Table 1 Model parameters

Parameter	Value	Description
G	0.2667	
u_0	4	Resting value of the firing rate
u_{th}	11.8	Threshold value for excitation
u_p	64	Peak value of the firing rate
η_1, η_2, η_3	0.4806, 3.3333e−5, 60	

tangential counterparts div_Σ and ∇_Σ. Boundary conditions are not necessary if the surface Σ is closed, as in the case of the reconstructed cortical geometry we consider in the numerical simulations of this paper.

2.2 Numerical Approximation

We discretise problem (1) by $\mathbf{P}_1$ finite elements in space and finite differences in time (for an introduction to finite element methods see, e.g., [14]). Let $t^n = n\Delta t$, for $n = 0, \ldots, N$, be a discretisation of the time interval $(0, T)$: we denote with u^n and w^n the approximation of u and w at time t^n. We use an implicit-explicit (IMEX) scheme to advance from time t^n to t^{n+1}. The recovery variable w^{n+1} can be solved explicitly and is used in the expression $I(u, w)$ to compute u^{n+1}. The overall scheme reads:

$$\begin{aligned}
&\text{update:} \quad w^{n+1} = \frac{u^n - u_0}{\eta_3} + \left(w^n - \frac{u^n - u_0}{\eta_3} \right) \exp\left(-\eta_2 \eta_3 \Delta t\right) \\
&\text{update:} \quad I^{n+1} = I(u^n, w^{n+1}) \\
&\text{solve:} \quad A u^{n+1} = M u^n - \Delta t\, M I^{n+1}
\end{aligned}$$

where $A := M + \Delta t\, S$, while M and S are the classic finite elements mass and stiffness matrices.

2.3 Computational Domain

A crucial aspect in studying the behaviour of an individual brain relies on the use of personalized computational domains. The cortical geometry we used in this study has been reconstructed from a MRI scan with FreeSurfer image analysis suite (http://surfer.nmr.mgh.harvard.edu/): for further details, see [15] and references therein. This data set was already acquired and published in [16], and used in [1], and its acquisition was approved by the Ethics Committee at the Cruces University Hospital:

all the methods employed were in accordance to approved guidelines. The data set corresponds to one healthy subject, male, age 28, and was acquired with a Philips Achieva 1.5T Nova scanner. The cortical mesh was obtained from a high-resolution anatomical MRI, acquired using a T1-weighted 3D sequence with the following parameters: TR = 7.482 ms, TE = 3.425 ms; parallel imaging (SENSE) acceleration factor =1.5; acquisition matrix size = 256 × 256; FOV = 26 cm; slice thickness = 1.1 mm; 170 contiguous sections.

The computational grid is a triangulation of the reconstructed cortex, consisting of 140, 208 nodes and 280, 412 triangles for the left hemisphere and 139, 953 nodes and 279, 902 triangles for the right hemisphere.

2.3.1 Regions of Interest

We consider a subdivision of the brain cortex into different regions of interest (ROIs): we base our study on the anatomical subdivision of each hemisphere into 34 ROIs, which is a generalised version of the Brodmann atlas [17] (included in the MRIcro software http://www.mricro.com).

2.4 Simulation Protocol

The numerical simulations of (1) are performed with a self-developed code in Matlab (MathWorks Inc., Natick, MA), taking advantage of its Parallel Computing Toolbox to speed up the computations on multicore processors. We chose a uniform time step of $\Delta t = 0.6$ seconds, and an isotropic diffusion tensor $D = \delta\,\mathrm{Id}$, with $\delta = 0.7174\,\mathrm{mm^2 s^{-1}}$. The conductivity coefficient has been tuned to ensure that a wave is actually propagating across the cortex, at a velocity comparable with the one of the CSD.

The finite element matrix A associated with the problem is poorly conditioned, entailing high costs in terms of CPU time. In order to speed up the computation, a proper preconditioning strategy can be implemented, such as an incomplete Cholesky factorisation with threshold, pivoting and properly chosen drop tolerance [18]. Since the linear system is symmetric, a Preconditioned Conjugate Gradient (PCG) is the natural choice as a solver.

CSD is known to originate from the visual cortex, but to gain deeper insight in the effect of geometry on the propagation we simulate, in both hemispheres, the spread of excitation waves between all the regions of the anatomical classification. In each simulation, we consider as initial condition one fully depolarized region out of the 34 in the anatomical subdivision. Each simulation is run until all remaining regions have been fully activated. The only compartment that is not considered as initially activated is the corpus callosum as it constitutes the intersection between the two hemispheres and obeys different rules for diffusion.

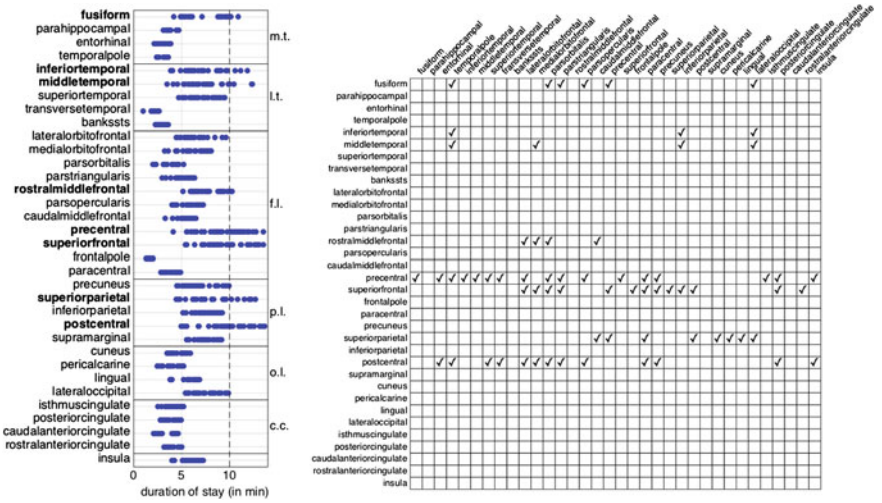

Fig. 1 Duration of stay of the depolarisation wave and regions of the *left* hemisphere featuring a long residence time. The duration of stay of the excitation wave in the different regions for all the initially excited regions possible (*left*). The *dashed line* draws the 10 min threshold; regions featuring waves staying longer than 10 min are marked in *bold*. The abbreviations give the affiliation to the lobes: m.t. medialtemporal lobe, l.t. lateraltemporal lobe, f.l. frontal lobe, p.l. parietal lobe, o.l. occipital lobe, c.c. cingulate cortex. A detailed description of the initially activated regions causing the wave to stay for longer than 10 min are marked with a tick (*right*). Rows represent the arrival regions, columns the initially activated ones

3 Temporal Activity

We are interested in studying the pattern of excited regions over the course of time. Although CSD is originating in the visual cortex, we aim for a deeper understanding of the geometry impact on the propagation when a depolarization wave is starting from another area. In that order, we initialise the excitation in one of the 34 different regions of the brain, and observe the number of regions that is excited at every point in time. The first aspect to consider is the definition of an activated region. Since the duration of the excitation following the passage of CSD is about 10 min [13], some caution is mandatory with regions that are either big or feature a large aspect ratio. In such regions, it might occur that some of the points initially excited have already gone back to resting state before every remaining point in the region gets excited. In view of these remarks, we consider a region as excited at a given moment in time if 80 % of the grid points located in it are excited. Before taking a more detailed look at any excitation pattern we thus have to verify that every region we are considering can be deemed excited at a given moment in time, independently from the initially activated area.

As done in [1], we record, for all simulations, the minimum and the maximum activation times (in minutes) for each of the 33 regions that were not excited at

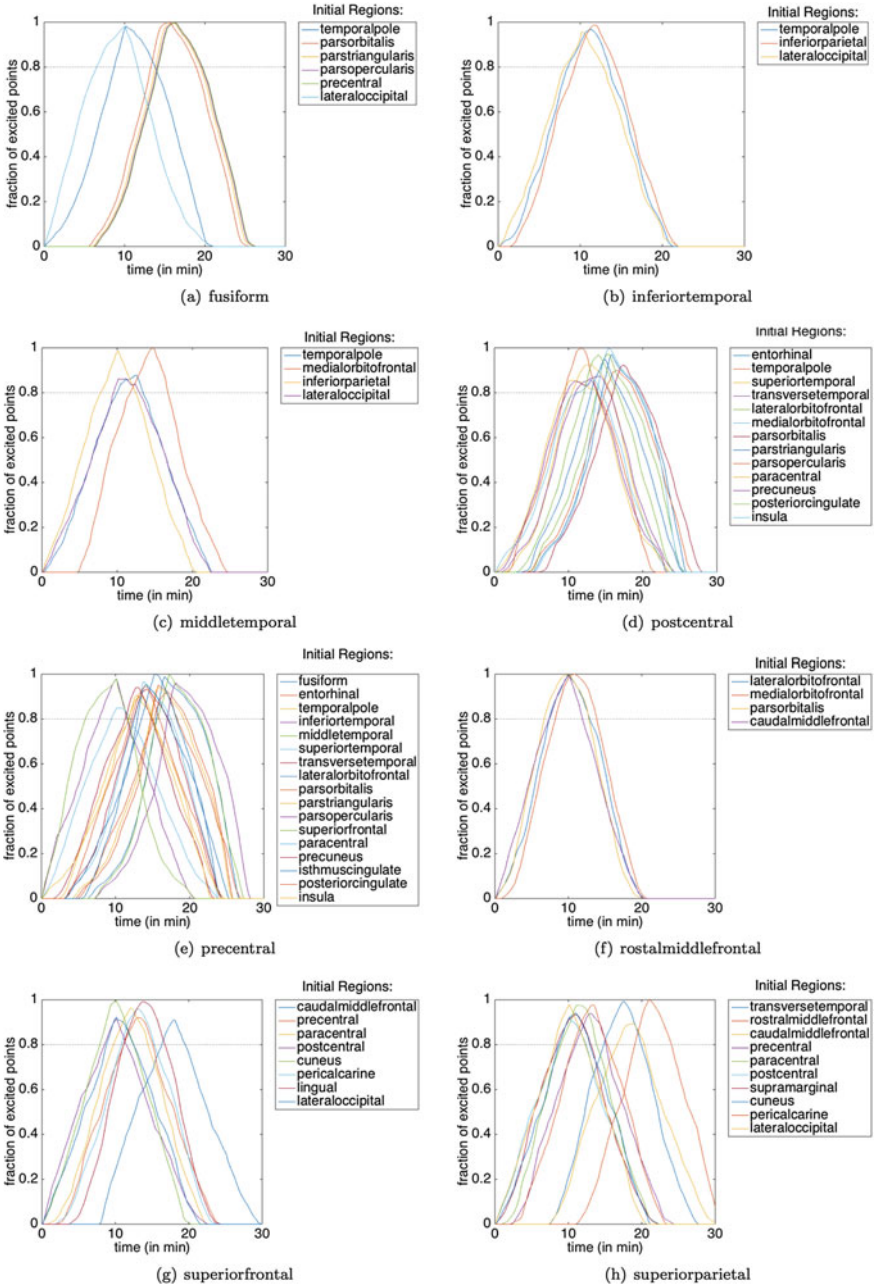

Fig. 2 Detailed excitation patterns for the regions of the *left* hemisphere featuring a long residence time. The percentage of excited points in time in the regions (**a**)–(**h**) identified in Fig. 1 for the different initially excited regions. The *dotted line* marks the threshold value of 80%, at which the whole region is considered excited

$t = 0$. The minimum activation time is the moment when the first point of the region at hand gets excited, while the maximum activation time is the moment at which the last point of the region gets excited. Such values are collected into four 34×34 matrices, that we denote by L_{min}, L_{max}, R_{min} and R_{max}, where L and R refer to the left and right hemisphere, respectively. To emphasize the spatial connection between the regions, the ordering of the regions is arranged according to their affiliation to lobes. Regions belonging to one lobe are then clustered according to the mutual distance of their centroids in the Euclidean norm. In all of the above matrices, rows represent the starting region of the wave propagation, while columns the arrivals: as an example, the (i, j)-th element of L_{min} represents the arrival time in region j of a wave originated in region i. We also introduce the depolarization residence matrices by considering the difference between the maximum and minimum activation times (or equivalently, the time elapsed between the depolarization of the first and the last point of the region), as

$$D^L = L_{max} - L_{min} \qquad D^R = R_{max} - R_{min}. \tag{2}$$

Again, rows represent the starting region of the wave propagation, while columns the difference between activation times: the (i, j)-th element of D^L and D^R represents the residence time in region j of a wavefront originating from region i. For illustrative purpose, we focus here on the left hemisphere, but results and conclusions similar to the ones we present in the following can be drawn for the right hemisphere as well. Whenever $D^L_{i,j} > 10$, the region j might not be considered as excited by a wave originating in region i. In Fig. 1 (left), we plot the columns of the residence matrix D^L, where the different markers in each row of the plot correspond to different initially excited regions. The threshold of 10 min, after which a region might not get excited as a whole at any given time, is highlighted by a dashed line, and the 8 regions featuring residence time longer than 10 min are marked in bold. These regions are fusiform, inferiortemporal, middletemporal, rostralmiddlefrontal, precentral, superiorfrontal, superiorparietal, and postcentral. In Fig. 1 (right) we pair these 8 peculiar regions with the corresponding initially activated ones: rows indicate the arrival regions, columns the initially activated areas, while checkmarks highlight the occurrencies when the depolarisation wave lasts longer than 10 min. The regions so identified in Fig. 1 require a more detailed analysis to check whether 80 % of their grid points are excited at any point in time. For each of these regions, we computed the percentage of activated points along time for a depolarization originating in the areas identified in Fig. 1 (right). A detailed visualisation of these patterns is given in Fig. 2, from which we can infer that all the regions feature a period in time where at least 80 % of their points is excited, independently of the origin of the initial excitation. Analogous results hold for the 9 regions of the right hemisphere (the same as the ones in the left hemisphere, plus the precuneus one) featuring a residence time longer than 10 min.

Since we ensured that all regions get fully excited independently from the initially activated region, we can focus on the temporal activation patterns. Given an initially activated region, we simulate the propagation of the depolarization wave and monitor

along time the percentage of excited points in every arrival region, thus identifying the number of excited region at every moment in time.

4 Results

A comparison between the two hemispheres for all the possible initially excited regions can be performed. Although the two hemispheres globally feature similar excitation schemes in the course of time, some differences can be spotted. In order to exhibit the typology of such differences, we display in Fig. 3 the comparison between the two hemispheres for 6 representative regions, one per lobe: fusiform, middletemporal, medialorbitofrontal, postcentral, lingual and rostralanteriorcingulate. The major differences we observe are in the guise of similar excitation patterns that are shifted in time, where one of the two hemispheres features a faster activation than the other, like for the medialorbitalfrontal (c) and the rostralanteriorcingulate (f), or in the form of similar temporal patterns, but pretty different excitation ones, like in the case of fusiform (a), middletemporal (b), postcentral (d), and lingual (e).

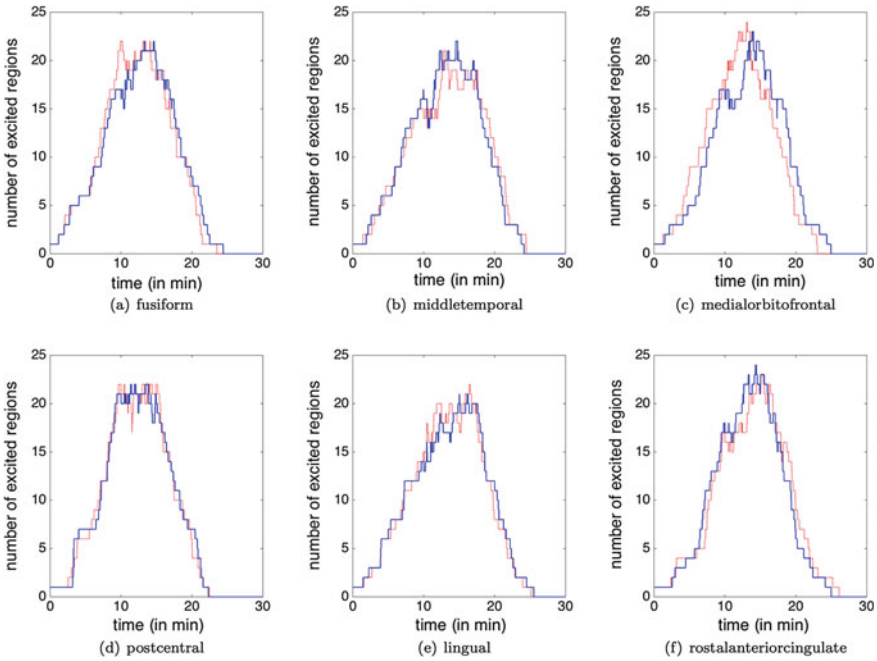

Fig. 3 Number of excited regions. The number of excited regions with initially activated regions (**a**)–(**h**) for the *left* (*red*) and *right* (*blue*) hemisphere; each one is chosen exemplarily for each lobe

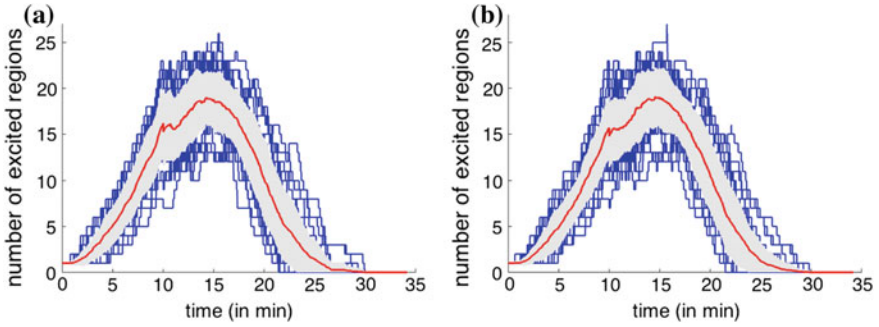

Fig. 4 Average number of excited regions. The average number of excited regions (*red*) - averaged over all initially activated regions - for the *left* (**a**) and *right* (**b**) hemisphere. For all initially excited regions the number of excited regions is plotted in *blue* and the *grey* area marks the standard deviation around the average

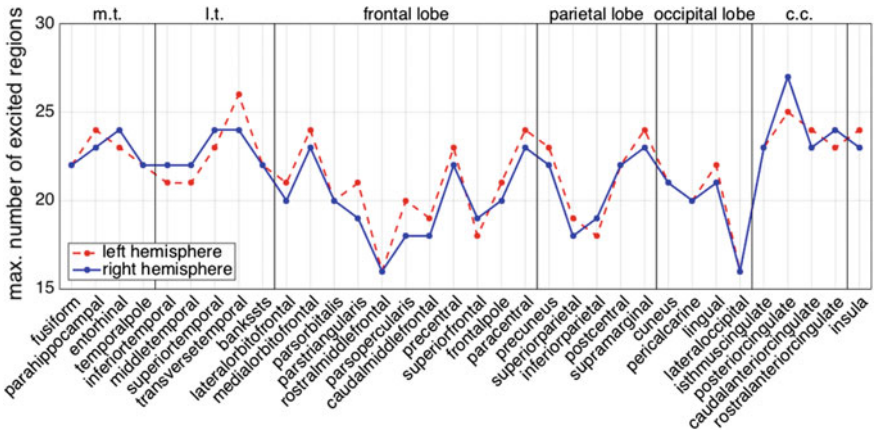

Fig. 5 Maximum number of excited regions. The maximum amount of excited regions for all the initially activated regions for the *left* (*red dashed*) and *right* (*blue solid*) hemisphere. The abbreviations give the affiliation to the lobes

For a more global approach, we average the number of excited regions over all the initially excited areas at each time step, obtaining a temporal excitation pattern for the left and right hemisphere. These temporal excitation patterns are shown in Fig. 4. We display in the background (in blue) the excitation patterns for every initial region and we highlight (in grey) the standard deviation around the mean. The temporal excitation patterns of the two hemispheres are globally very similar, but show some differences in the vicinity of 10 min after the start of the wave propagation.

The maximum number of excited regions for each initially activated area highlights their impact on the excitation pattern of the cortex. A comparison of the left and right hemisphere is given in Fig. 5, where a significant variation in the maximum number of activated regions is more evident intra-hemispherically than inter-

hemispherically. As an example, a depolarization wave originating from the lateraloccipital area will excite at once only up to 16 regions (in both hemispheres), whereas a wave originating from the posteriorcingulate area can activate up to 27 regions in the left hemisphere (25 in the right hemisphere). Left and right hemisphere exhibit a difference of up to 2 regions, but 10 areas feature exactly the same maximum number of excited regions in the two hemispheres.

5 Conclusions

It has been recently proposed that thalamocortical dysrhythmia may be responsible for the altered synchronicity in migraine; CSD is expected to play a central role in migraine pathogenesis being the cause of the aura phenomenon. In order to gain further insights of the role of geometry in the temporal excitation patterns following the passage of a depolarization wave on the cerebral cortex, here we have adopted a distributed computational model for CSD, and studied the temporal pattern connected to the propagation of CSD on the real geometry of human brain. Our results may also be useful for the automatic identification of CSD from electrophysiological recordings [19].

Acknowledgements This work was supported by the Bizkaia Talent and European Commission through COFUND under the grant BRAhMS – Brain Aura Mathematical Simulation– (AYD-000-285), and also by the Basque Government through the BERC 2014–2017 program, and by the Spanish Ministry of Economics and Competitiveness MINECO: BCAM Severo Ochoa excellence accreditation SEV-2013-0323. JMC acknowledges financial support from Ikerbasque: The Basque Foundation for Science and Euskampus at UPV/EHU.

References

1. Kroos, J.M., Diez, I., Cortes, J.M., Stramaglia, S., Gerardo-Giorda, L.: Geometry shapes propagation: assessing the presence and absence of cortical symmetries through a computational model of cortical spreading depression. Front. Comput. Neurosci. **10**, 6 (2016). doi:10.3389/fncom.2016.00006
2. Leão, A.: Spreading depression of activity in the cerebral cortex. J. Neurophysiol. **7**, 391–396 (1944)
3. Leão, A.: Further observations on the spreading depression of activity in the cerebral cortex. J. Neurophysiol. **10**, 409–414 (1947)
4. de Tommaso, M., Ambrosini, A., Brighina, F., Coppola, G., Perrotta, A., Pierelli, F., Sandrini, G., Valeriani, M., Marinazzo, D., Stramaglia, S., Schoenen, J.: Altered processing of sensory stimuli in patients with migraine. Nat. Rev. Neurol. **10**, 144–155 (2014)
5. Hadjikhani, N., Sanchez del Rio, M., Wu, O., Schwartz, D., Bakker, D., Fischl, B., Kwong, K.K., Cutrer, F.M., Rosen, B.R., Tootell, R.B.H., Sorensen, A.G., Maskowitz, M.A.: Mechnisms of migraine aura revealed by functional MRI in human visual cortex. Proc. Natl. Acad. Sci. USA **98**, 4687–4692 (2001). doi:10.1073/pnas.071582498

6. Richter, F., Lehmenkühler, A.: Cortical spreading depression (csd):a neurophysiological correlate of migraine aura. Der Schmerz **22**, 544–550 (2008). doi:10.1007/s00482-008-0653-9
7. Sramka, M., Brozek, G., Bures, J., Nadvornik, P.: Functional ablation by spreading depression: possible use in human stereotactic neurosurgery. Appl. Neurophysiol. **30**, 589–596 (1977)
8. Costa, C., Tozzi, A., Rainero, I., Cupini, L.M., Calabresi, P., Ayata, C., Sarchielli, P.: Cortical spreading depression as a target for anti-migraine agents. J. Headache Pain **14**, 62 (2013). doi:10.1186/1129-2377-14-62
9. Dahlem, M., Schmidt, B., Bojak, I., Boie, F., Kneer, S., Hadjikhani, N., Kurths, J.: Cortical hot spots and labyrinths: why cortical neuromodulation for episodic migraine with aura should be personalized. Front Comput. Neurosci. **9** (2015). doi:10.3389/fncom.2015.00029
10. Cortes, J., Marinazzo, D., Series, P., Oram, M., Sejnowski, T., van Rossum, M.: The effect of neural adaptation on population coding accuracy. J. Comput. Neurosci. **32**, 387–402 (2012). doi:10.1007/s10827-011-0358-4
11. Rogers, J., McCulloch, A.: A collocation - galerkin finite element model of cardiac action potential propagation. IEEE Trans. Biomed. Eng. **41**, 743–757 (1994). doi:10.1109/10.310090
12. FitzHugh, R.: Impulses and physiological states in theoretical models of nerve membrane. Biophys. J. **1**, 445–466 (1961)
13. Porooshani, H., Porooshani, A., Gannon, L., Kyle, G.: Speed of progression of migrainous visual aura measured by sequential field assessment. Neuro-Ophthalmol. **28**, 101–105 (2004). doi:10.1076/noph.28.2.101.23739
14. Quarteroni, V., Valli, A.: Numer. Approx. Partial Differ. Equ. Springer, Berlin (1994)
15. Fischl, B.: Freesurfer. Neuroimage **62**, 774–781 (2012)
16. Diez, I., Bonifazi, P., Escudero, I., Mateos, B., Muñoz, M.A., Stramaglia, S., Cortes, J.M.: A novel brain partition highlights the modular skeleton shared by structure and function. Sci. Rep. **5**, 10532 (2015)
17. Brodmann, K.: Brodmann's Localisation in the Cerebral Cortex - The Principles of Comparative Localisation in the Cerebral Cortex Based on Cytoarchitectonics. Springer, Heidelberg (2006)
18. Saad, Y.: Iterative Methods for Sparse Linear Systems. SIAM (2003)
19. Yoshida, K., Xu, M., Natsubori, A., Mimura, M., Takata, N., Tanaka, K.F.: Identification of the extent of cortical spreading depression propagation by Npas4 mRNA expression. Neurosci. Res. **98**, 1–8 (2015). doi:10.1016/j.neures.2015.04.003

Persistent Memories in Transient Networks

Andrey Babichev and Yuri Dabaghian

Abstract Spatial awareness in mammals is based on an internalized representation of the environment, encoded by large networks of spiking neurons. While such representations can last for a long time, the underlying neuronal network is transient: neuronal cells die every day, synaptic connections appear and disappear, the networks constantly change their architecture due to various forms of synaptic and structural plasticity. How can a network with a dynamic architecture encode a stable map of space? We address this question using a physiological model of a "flickering" neuronal network and demonstrate that it can maintain a robust topological representation of space.

1 Introduction

It is believed that mammalian ability to navigate, to escape from predators, to find its nest, to plan hunting strategies and so forth, is based on an internalized neuronal representation of space—a cognitive map of the environment [1–3]. Neurophysiologically, this map is encoded via timed sequences of quick electrical discharges of the neurons—neuronal spikes—in various parts of the brain. A particularly important role in producing this map is played by the hippocampus—one of the oldest parts of the mammalian brain in evolutionary terms. The spike times of the hippocampal principal neurons—so called place cells—are defined by the animal's spatial location: in rodents, each place cell fires when the animal visits a specific location—this cell's place field [3] (Fig. 1a). Why a given place cell fires only when an animal is "here" rather than "there" is still a mystery, and how the ensemble of place cells

A. Babichev · Y. Dabaghian (✉)
Jan and Dan Duncan Neurological Research Institute, Baylor College of Medicine,
Houston, TX 77030, USA
e-mail: dabaghia@bcm.edu

A. Babichev · Y. Dabaghian
Department of Computational and Applied Mathematics, Rice University,
Houston, TX 77005, USA
e-mail: babichev@bcm.edu

G. Mantica et al. (eds.), *Emergent Complexity from Nonlinearity, in Physics, Engineering and the Life Sciences*, Springer Proceedings in Physics 191,
DOI 10.1007/978-3-319-47810-4_14

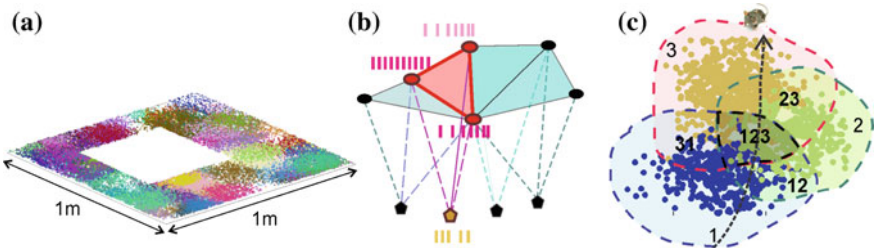

Fig. 1 Place cells and cell assemblies. **a** Simulated place fields in a small planar environment containing a *square hole*: *dots* of different *color* mark the locations where the corresponding place cells produced spikes. The *dots* of a particular *color* form spatial clusters—the place fields. **b** Schematic representation of four overlapping third-order cell assemblies by four third order simplexes (*triangles*). The vertexes (shown by *small circles*) represent place cells synaptically connected to their respective readout neurons (*pentagons*). A cell assembly σ "ignites" (*red triangle*) when all of its place cells become simultaneously active, thus eliciting a response from the readout neuron n_σ (active cells have *colored centers*). **c** A coactivity of the place cells c_1, c_2 and c_3 occurs when the rat crosses through the overlap of the corresponding place fields—the domain 123

forms a hippocampal map of the environment is equally mysterious. In particular, it remains largely unknown how the spike trains produced by the place cells are processed downstream from the hippocampus.

Experimental evidence points out that groups of coactive place cells form functionally interconnected "assemblies" [4, 5] that together drive their respective "read-classifier" or "readout" neurons in the downstream networks (Fig. 1b). Since coactivity of the place cells marks the overlap of their respective place fields (Fig. 1c), the activity of a readout neuron actualizes a connectivity relationship between the regions encoded by the individual place cells. This suggests that the hippocampus provides a qualitative representation of space, based on connectivity, adjacency and containment relationships, i.e., that the hippocampal cognitive map is topological in nature—a hypothesis that receives an increasing amount of experimental support [6–10].

In [11, 12] we proposed a theoretical model that showed that hippocampal cell assembly network can indeed capture the spatial connectivity of the environment in a biologically plausible time, given that the place cells operate within biological parameters of firing rate and place field size. However, the approach of [11, 12] was based on analyses of the ever-growing pool of spike trains, i.e., it ignored that, in physiological networks, the connectivity information may not only accumulate, but also decay. In particular, the physiological cell assemblies may not only form, but also disband as a result of deterioration of synaptic connections [13], then reappear as a result of subsequent learning, then disband again and so forth. Electrophysiological studies suggest that the lifetime of the cell assemblies ranges between tens of milliseconds to minutes or longer [4, 5, 14, 15], whereas spatial memories in rats can last for days and months [16–18]. How can the large-scale spatial representation of the environment be stable if the neuronal stratum that computes this representation changes on a much faster timescale? Below we discuss a model of a

transient hippocampal network and use methods of Algebraic Topology to demonstrate that the topological characteristics of the large-scale spatial representation of the environment encoded by this network can remain stable.

2 Model

The way place fields cover an environment $\mathscr{E}$ (Fig. 1a) calls to mind a basic theorem of algebraic topology due to P. Alexandrov [19] and E. Čech [20]: it is possible to reconstruct the topology of a space X from the pattern of overlaps between the regions that cover it. The model proposed in [11, 12, 21] is based on the observation that this theorem can not only be applied to the place fields themselves, but also implemented via spiking signals of cells that represent these place fields. In this approach, groups of coactive place cells, c_1, c_2, …, c_n, are viewed as abstract simplexes, $\sigma = [c_1, c_2, \ldots, c_n]$, which together form a simplicial "cell assembly complex," $\mathscr{T}_{CA}$ (for definitions and details see [22, 23] and Methods in [11]).

This construction provides a connection between the local (cellular) and the global (system-level) scales: the individual cell assemblies, just like simplexes, provide local information about the space, but together, as a neuronal ensemble, they represent space as whole—as the simplicial complex. Thus, $\mathscr{T}_{CA}$ provides a schematic representation of the cell assembly network and of its rewiring dynamics: formation of new place cell assemblies and disbanding of some old ones are represented, respectively, by the appearance and disappearance of their counterpart (maximal) simplexes in $\mathscr{T}_{CA}$. On the other hand, the cell assembly complex $\mathscr{T}_{CA}$ provides semantics for describing the global spatial memory map in topological terms [24]. For example, a sequence of cell assemblies ignited along a path γ navigated by the rat corresponds to a chain of simplexes $\Gamma \in \mathscr{T}_{CA}$—a "simplicial path" (Fig. 2). The structure of $\mathscr{T}_{CA}$ allows to establish certain qualitative properties of the simplicial paths and to relate them to the properties of the physical paths in $\mathscr{E}$. For example, a simplicial path that closes onto itself in $\mathscr{T}_{CA}$ may represent a closed physical path, a pair of topologically equivalent simplicial paths $\Gamma_1 \sim \Gamma_2$ may represent physical paths γ_1 and γ_2 that can be deformed into one another, a hole in $\mathscr{T}_{CA}$ may represent a physical obstacle and so forth. However, establishing these correspondences requires learning: as the animal begins to explore the environment, only a few place cells would have time to (co)activate, and only a few cell assemblies would have time to form; as a result, a newly developing complex $\mathscr{T}_{CA}$ consists of only a few maximal simplexes and contains many holes, some of which correspond to physical obstacles or to regions that have not yet been visited by the animal, and others are "spurious", i.e., reflecting transient information about place cell coactivity. As shown in [11, 12], the spurious holes tend to disappear as more spatial information accumulates.

In [25] we suggested two methods for constructing the cell assembly network and hence producing the simplicial cell assembly complex $\mathscr{T}_{CA}$ that represents this network, by selecting the most frequent combinations of spiking place cells.The key

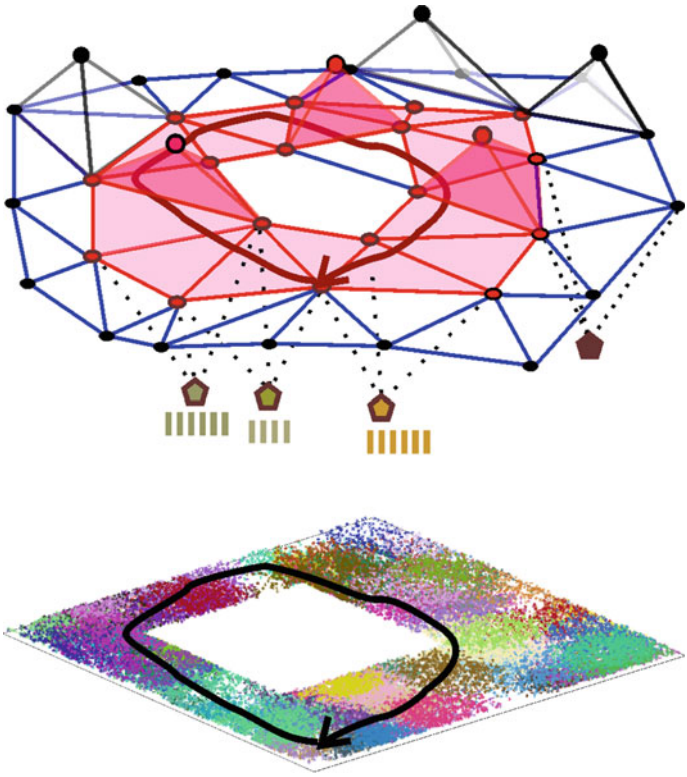

Fig. 2 Schematic representation of place cell coactivity in the cell assembly complex $\mathscr{T}_{CA}$. The topological structure of $\mathscr{T}_{CA}$, induced from the place field layout in $\mathscr{E}$, provides a topological representation of $\mathscr{E}$. For example, the *hole* in the *middle* of $\mathscr{T}_{CA}$, which produces non-contractible simplicial paths (topological loops) corresponds to the central hole in the environment $\mathscr{E}$, which produces non-contractible navigation paths γ (e.g., a sample path is shown at the *bottom*). As the animal travels along γ, the hippocampal place cell assemblies ignite in a certain order, which corresponds to a chain of maximal simplexes in $\mathscr{T}_{CA}$—a simplicial path Γ, shown by *red triangles* and *tetrahedrons*

observation of [25] was that in bounded environments, the coactive cell combinations eventually become repetitive, and it is therefore possible to identify the cell assemblies from the most frequent coactivity patterns. However, the frequency of a given cell assembly's activation, f_σ, was evaluated from the total number of its appearances over the entire navigation period, and then the selected cell assemblies were presumed to have existed for as long as the navigation continued. In other words, the cell assemblies were "perennial" by construction. In the following, we model a transient hippocampal network by limiting the time during which a cell assembly σ can form to a smaller time interval—"a memory window" $W^{(\sigma)}$. Physiologically, $W^{(\sigma)}$ defines the period during which readout neuron n_σ can identify the combination σ of coactive place cells, connect to it synaptically, retain these connections and respond to subsequent ignitions of σ.

To simplify the approach, we consider the case in which the entire ensemble of readout neurons is characterized by a single parameter $W^{(\sigma)} = W$, and proceed as follows. First, we identify the cell assemblies that emerge within the first W-period after the onset of the navigation, W_1, and then repeat the algorithm for the subsequent windows W_2, W_3,..., obtained by shifting the W_1 over small time steps. As a result, a cell assembly σ that was identified in the window W_{t_1}, based on the local place cell coactivity rate $f_\sigma(W_{t_1})$, may disappear at a certain step W_{t_2}, then reappear in a later window, W_{t_3}, disappear again and so forth. The ensemble of appearing and disappearing cell assemblies can then be schematically represented by a "flickering" simplicial complex, $\mathscr{F}_W$, with appearing and disappearing maximal simplexes. Our task is to study the net topological properties of $\mathscr{F}_W$, e.g., whether the lifetimes of its topological loops can be longer than the lifetimes of its typical maximal simplex.

3 Results

We studied the dynamics of the flickering complex $\mathscr{F}_W$ and the topological information encoded in it, as a function of the discrete time $t_n = n\Delta t$, $\Delta t = 2.5\,\mathrm{s}$, for the memory window width $W = 5\,\mathrm{min}$. The results produced by a typical neuronal ensemble containing $N_c = 300$ simulated place cells are shown on Fig. 3. First, we observe that the fluctuations of the number of the maximal simplexes in $\mathscr{F}_W$, N_σ, remain confined within about 20 % from the mean, $220 \leq N_\sigma \leq 300$, so that the simulated hippocampal network contains about 260 fluctuating cell assemblies on average (Fig. 3a). However, while the size of the flickering complex remains bounded, the pool of the maximal simplexes changes significantly: as temporal separation $\Delta_{ij} = |t_i - t_j|$ between the memory windows increases, the corresponding complexes $\mathscr{F}_W(t_i)$ and $\mathscr{F}_W(t_j)$ become more and more dissimilar (Fig. 3b). After about 50 time steps ($\sim$120 s), the set of simplexes in $\mathscr{F}_W$ is essentially renewed, which implies that the cell assembly network, as described by the model, is completely rewired (Fig. 3c).

A typical maximal simplex lasts on average about 10 discrete time steps ($\tau_\sigma \approx 25\,\mathrm{s}$), which is close to the range of values established experimentally [5]. Such rapid rate of the simplex renewal in the flickering cell assembly complex allows us to address our main question: what is the dynamics of the topological characteristics of $\mathscr{F}_W$ and how do they correspond to the topology of the environment?

The topology of the environment can be described in terms of the Betti numbers—roughly speaking, a Betti number b_n defines the number of n-dimensional topological loops in $\mathscr{F}_W$ (i.e., closed surfaces counted up to topological equivalence). In the case of the environment shown on Fig. 1a, the Betti numbers are as follows: $b_0 = 1$ (i.e., the environment is connected), $b_1 = 1$ (i.e., there is one $1D$ topological loop that encircles the hole in the middle), while $b_{n>1} = 0$ (no topological loops in higher dimensions). Using the methods of Persistent Homology [26–28], we evaluated these numbers for the flickering cell assembly complex for the sequence of windows, and found that $\mathscr{F}_W$ does, in fact, reliably capture the topological properties

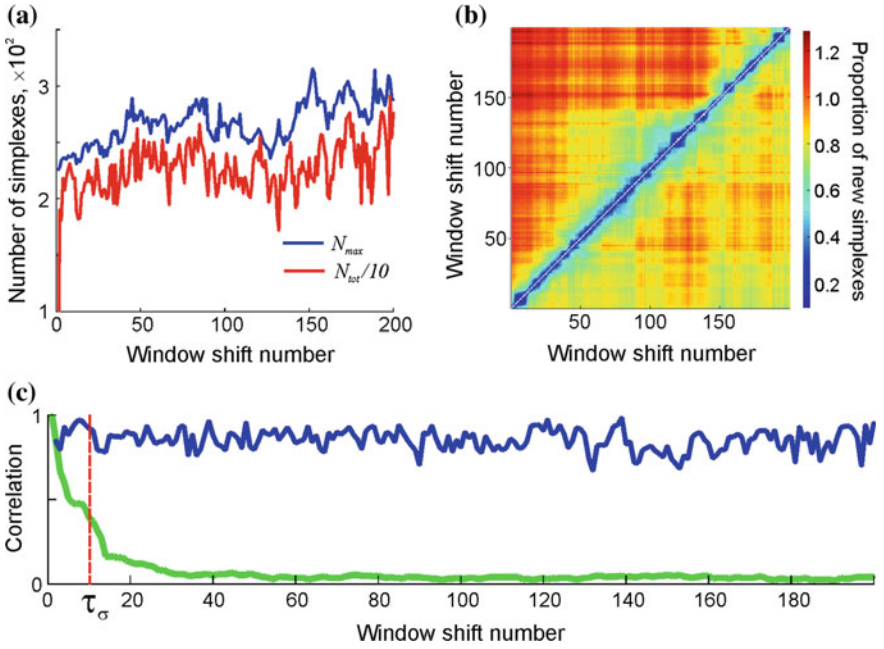

Fig. 3 Time evolution of the cell assembly complex. **a** The number of maximal simplexes (*blue trace*) and the total number of all simplexes, scaled down by a factor of 10 (*red*) in the flickering simplicial complex $\mathscr{F}_W$. The memory window spans over $W = 5$ min, shifting over $\Delta t = 2.5$ s at a time. Shown are first 200 shifts. **b** The matrix of similarity coefficients, r_{ij}, between the pairs of flickering cell assembly complexes $\mathscr{F}_W(t_i)$ and $\mathscr{F}_W(t_j)$ defined as the proportion of the maximal simplexes contained in $\mathscr{F}_W(t_i)$ but not in $\mathscr{F}_W(t_j)$. For close moments t_i and t_j, the differences are small, but as time separation grows, the differences becomes larger. **c** At every moment of time t_i, the *blue line* shows the fraction of the maximal simplexes that were also present at the previous moment, t_{i-1}. The *green line* shows the fraction of the original maximal simplexes (from $\mathscr{F}_W(t_1)$) remaining in $\mathscr{F}_W(t_i)$. The population of simplexes changes entirely (by about 0.95 %) in about 60 steps. The *dashed line* marks the mean simplex decay rate, $\tau_\sigma = 10$ window shifts (about 25 s)

of the environment over long periods, which significantly exceed both the simplexes' lifetimes, τ_σ, and the width of the memory window, W.

As illustrated on Fig. 4a, the first and the second Betti numbers almost never deviate from their respective physical values ($b_1 = 1$ and $b_2 = 0$). The occasional changes of b_1 and b_2 can be viewed as short-time "topological fluctuations" in the hippocampal map. For example, an occurrence of $b_1 = 2$ value indicates the appearance of an extra (non-physical) $1D$ loop, and at the moments when $b_1 = 0$, all $1D$ loops in $\mathscr{F}_W$ are contractible, i.e., the central hole (Fig. 1a) is not represented in the hippocampal map. Similarly, the moments when $b_2 \neq 0$ indicate times when the flickering complex $\mathscr{F}_W$ contains non-physical, non-contractible $2D$ bubbles (one can speculate about the cognitive effects that these fluctuations may produce). The 0-th and the third Betti number always came out correct, $b_0 = 1$, $b_3 = 0$, implying that despite the fluctuations of its simplexes, the cell assembly complex $\mathscr{F}_W$ does not

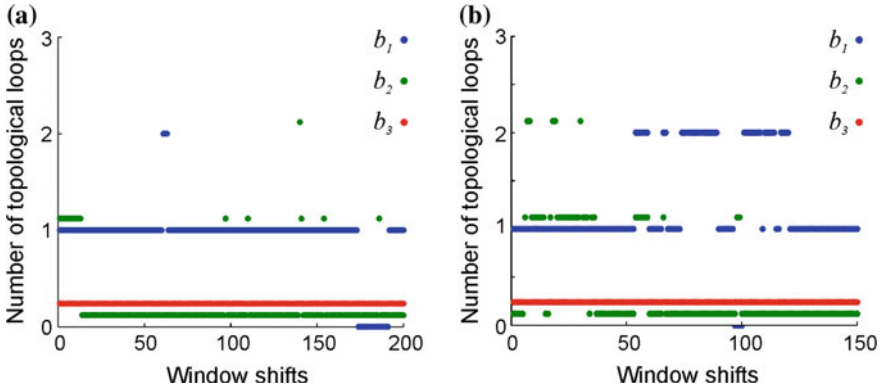

Fig. 4 Stability of the topological information. **a** The low-dimensional Betti numbers, b_1, b_2, b_3 as a function of the discrete time, computed using 5 min wide memory window W. The 0th Betti number ($b_0 = 1$ at all times) is not shown. **b** As the memory window *decreases* to $W = 3$ min, the frequency and the number of the topological fluctuations *increases*: the flickering complex repeatedly produces an extra (spurious) $1D$ topological loop and up to two spurious *bubbles*

disintegrate into pieces and remains contractible in higher ($D > 2$) dimensions, i.e., that the topological fluctuations in the hippocampal map are bounded to $1D$ paths and $2D$ surfaces.

Further numerical analyses demonstrate that, as the memory window increases, the Betti numbers b_1 and b_2 become more stable. In contrast, as the memory window shrinks, the fluctuations of the topological loops intensify (Fig. 4b). This implies that if the characteristic timescale of the network's transience is sufficiently large, then the corresponding coactivity complex remains fixed and topologically equivalent to the "perennial" cell assembly complex, $\mathscr{F}_{W=\infty} = \mathscr{T}_{CA}$. On the other hand, if the simplexes are too unstable, then the cell assembly complex $\mathscr{T}_{CA}$ fails to acquire the correct physical structure, no matter how long is the learning period.

4 Discussion

In physical literature, fluctuating simplicial complexes have been previously used in the context of Simplicial Quantum Gravity theories for discretizing quantum fluctuations of the space-time [29, 30]. A natural requirement for these theories is that the quantum fluctuations at the micro-scale should average out in the thermodynamic limit, yielding a smooth space-time continuum at the macroscale.

There are certain parallels with cognitive representations of space that emerge from the spiking activity of neuronal ensembles. At the micro level, the encoded spatial information is naturally discrete at the cellular level and allows a schematic representation in terms of simplicial complexes [11, 12, 24, 25]. Moreover, since the various place cell assemblies that spike at different locations are transient struc-

tures, these auxiliary simplicial complexes fluctuate. On the macro level, the emergent hippocampal maps provide a stable topological representation of the physical environment over long periods [10, 16–18], enabling topological reasoning during animals' spatial navigation [8, 9].

Our model provides one explanation for how these two experimentally established aspects of hippocampal neurophysiology can coexist. According to the model, while the simplexes of the flickering simplicial complex $\mathscr{F}_W$ fluctuate at the physiological timescale, its Betti numbers can keep their physical values indefinitely. The fact that the simplex fluctuations can average out at the scale of the entire complex suggests that rapid rewiring of the cell assemblies can preserve the stability of the cognitive map as a whole.

Although these results were obtained using a simple computational model, we hypothesize that the observed effect reflects a more general phenomenon that might apply to physiological mechanisms of synaptic and structural plasticity in the hippocampal network.

5 Methods

Place cell spiking activity is modeled as a stationary temporal Poisson process with a spatially localized rate [31] that is characterized by the spatial location of the peak, r_c, the peak firing amplitude, f_c, and the place field size, s_c. We simulated an ensemble of $N_c = 300$ place cells with log-normally distributed peak firing amplitudes, with the mean $\langle f_c \rangle = 14$ Hz, log-normally distributed place field sizes with the mean $\langle s_c \rangle = 17$ cm (for details see Methods in [11]). Spiking is modulated by the 8 Hz θ-oscillations—the basic rhythm of the extracellular field in the hippocampus [32]. Neuronal coactivity is defined as firing that occurred over two consecutive θ cycles—a computationally established optimal value [12], which corresponds to the parameters estimated from experimental data [32, 33]. The topological analyses were implemented using the JPlex package [34].

Acknowledgements The work was supported by the NSF 1422438 grant and by Houston Bioinformatics Endowment Fund.

References

1. O'Keefe, J., Nadel, L.: The Hippocampus as a Cognitive Map, vol. xiv, p. 570. Clarendon Press; Oxford University Press, New York (1978)
2. Tolman, E.C.: Cognitive maps in rats and men. Psychol. Rev. **55**, 189–208 (1948)
3. Tolman, P.J., White, A.M., Minai, A.: Spatial processing in the brain: the activity of hippocampal place cells. Ann. Rev. Neurosci. **24**, 459–486 (2001)
4. Harris, K.D., Csicsvari, J., Hirase, H., Dragoi, G., Buzsaki, G.: Organization of cell assemblies in the hippocampus. Nature **424**, 552–556 (2003)

5. Buzsaki, G.: Neural syntax: cell assemblies, synapsembles, and readers. Neuron **68**, 362–385 (2010)
6. Gothard, K.M., Skaggs, W.E., McNaughton, B.L.: Dynamics of mismatch correction in the hippocampal ensemble code for space: interaction between path integration and environmental cues. J. Neurosci. **16**, 8027–8040 (1996)
7. Leutgeb, J.K., Leutgeb, S., Treves, A., Meyer, R., Barnes, C.A., et al.: Progressive transformation of hippocampal neuronal representations in "morphed" environments. Neuron **48**, 345–358 (2005)
8. Alvernhe, A., Sargolini, F., Poucet, B.: Rats build and update topological representations through exploration. Anim. Cogn. **15**, 359–368 (2012)
9. Poucet, B., Herrmann, T.: Exploratory patterns of rats on a complex maze provide evidence for topological coding. Behav. Process. **53**, 155–162 (2001)
10. Dabaghian, Y., Brandt, V.L., Frank, L.M.: Reconceiving the hippocampal map as a topological template. eLife 10.7554/eLife.03476 (2014)
11. Dabaghian, Y., Mmoli, F., Frank, L., Carlsson, G.: A topological paradigm for hippocampal spatial map formation using persistent homology. PLoS. Comput. Biol. **8**, e1002581 (2012)
12. Arai, M., Brandt, V., Dabaghian, Y.: The effects of theta precession on spatial learning and simplicial complex dynamics in a topological model of the hippocampal spatial map. PLoS Comput. Biol. **10**, e1003651 (2014)
13. Wang, Y., Markram, H., Goodman, P.H., Berger, T.K., Ma, J., et al.: Heterogeneity in the pyramidal network of the medial prefrontal cortex. Nat. Neurosci. **9**, 534–542 (2006)
14. Bi, G-q., Poo, M-m.: Synaptic modification by correlated activity: Hebb's postulate revisited. Ann. Rev. Neurosci. **24**, 139–166 (2001)
15. Magee, J.C., Johnston, D.: A synaptically controlled, associative signal for hebbian plasticity in Hippocampal neurons. Science **275**, 209–213 (1997)
16. Meck, W.H., Church, R.M., Olton, D.S.: Hippocampus, time, and memory. Behav. Neurosci. **127**, 655–668 (2013)
17. Clayton, N.S., Bussey, T.J., Dickinson, A.: Can animals recall the past and plan for the future? Nat. Rev. Neurosci. **4**, 685–691 (2003)
18. Brown, M.F., Farley, R.F., Lorek, E.J.: Remembrance of places you passed: social spatial working memory in rats. J. Exper. Psychol. **33**, 213–224 (2007)
19. Alexandroff, P.: Untersuchungen Uber Gestalt und Lage Abgeschlossener Mengen Beliebiger Dimension. Ann. Math. **30**, 101–187 (1928)
20. Čech, E.: Theorie generale de lhomologie dans une space quelconque. Fundamenta mathematicae **19**, 149–183 (1932)
21. Curto, C., Itskov, V.: Cell groups reveal structure of stimulus space. PLoS Comput. Biol. **4**, e1000205 (2008)
22. Hatcher, A.: Algebraic Topology. Cambridge University Press, Cambridge (2002)
23. Aleksandrov, P.: Elementary Concepts of Topology, p. 63. F. Ungar Pub, Co, New York (1965)
24. Babichev, A., Cheng, S., Dabaghian, Y.: Topological Schemas of Cognitive Maps and Spatial Learning in the Hippocampus. In submition (2015). arXiv:1509.00171
25. Babichev, A., Memoli, F., Ji, D., Dabaghian, Y.: Combinatorics of Place Cell Coactivity and Hippocampal Maps. In submition (2015). arXiv:1509.01677
26. Ghrist, R.: Barcodes: the persistent topology of data. Bull. Am. Math. Soc. **45**, 61–75 (2008)
27. Zomorodian, A.J.: Topology for Computing, vol. xiii, p. 243. Cambridge University Press, UK (2005)
28. Edelsbrunner, H., Harer, J.: Computational Topology: An Introduction, vol. xii, p. 241. American Mathematical Society, Providence, R.I. (2010)
29. Ambjørn, J., Carfora, M., Marzuoli, A.: The Geometry of Dynamical Triangulations, vol. viii, p. 197. Springer, Berlin (1997)
30. Hamber, H.W.: Quantum gravitation: the Feynman path integral approach, vol. xvii, p. 342. Springer, Berlin (2009). (Nuclear Physics B - Proceedings Supplements **94**, 689–692)
31. Barbieri, R., Frank, L.M., Nguyen, D.P., Quirk, M.C., Solo, V., et al.: Dynamic analyses of information encoding in neural ensembles. Neural Comput. **16**, 277–307 (2004)

32. Buzsaki, G.: Theta oscillations in the hippocampus. Neuron **33**, 325–340 (2002)
33. Buzsaki, G.: Theta rhythm of navigation: link between path integration and landmark navigation, episodic and semantic memory. Hippocampus **15**, 827–840 (2005)
34. http://comptop.stanford.edu/u/programs/jplex. JPlex freeware was developed by ComTop group, Stanford University

A Multiplex Network Model to Characterize Brain Atrophy in Structural MRI

Marianna La Rocca, Nicola Amoroso, Roberto Bellotti, Domenico Diacono, Alfonso Monaco, Anna Monda, Andrea Tateo and Sabina Tangaro

Abstract We developed a multiplex network approach for the description and recognition of structural brain changes in the context of the early diagnosis of Alzheimer disease (AD). Our techniques can supply a convenient mathematical framework to model structural inter- and intra-subject brain similarities in magnetic resonance images (MRI) within Alzheimer disease studies. We used a set of 100 structural T1 brain scans, from subjects of the Alzheimer's Disease Neuroimaging Initiative, including AD patients, normal controls (NC) and mild cognitive impairment (MCI) subjects. We evaluated the classification performances including the comparison of two state-of-the-art techniques, Random Forests (RF) and Support Vector Machines (SVM). Our results show that multiplex networks can significantly improve the classification performance obtained only with the use of structural features. They can also effectively distinguish NC, MCI and AD patterns with an *area under the receiver-operating-characteristic curve* (AUC) $\geq 0.89 \pm 0.04$.

M. La Rocca · N. Amoroso (✉) · R. Bellotti · A. Tateo
Dipatimento di Fisica "M. Merlin", Università Degli Studi di Bari "A. Moro", Istituto Nazionale di Fisica Nucleare, sez. di Bari, Via Orabona, 4, Bari, Italy
e-mail: nicola.amoroso@ba.infn.it

D. Diacono · S. Tangaro
Istituto Nazionale di Fisica Nucleare, sez. di Bari, Via Orabona, 4, Bari, Italy

A. Monaco
Dipatimento di Fisica "M. Merlin", Istituto Nazionale di Fisica Nucleare, sez. di Bari, Via Orabona, 4, Bari, Italy

A. Monda
Department of Basic Medical Sciences, Neuroscience and Sense Organs, Università degli Studi di Bari "Aldo Moro", Bari, Italy

G. Mantica et al. (eds.), *Emergent Complexity from Nonlinearity, in Physics, Engineering and the Life Sciences*, Springer Proceedings in Physics 191,
DOI 10.1007/978-3-319-47810-4_15

1 Introduction

The number of elder people affected by dementia (in 2010 $\sim$ 35.6 million) is dramatically increasing.[1] This is particularly evident for the Alzheimer's disease (AD). Therefore, it is fundamental to find new instruments, methods and strategies to describe these pathologies. In recent years, machine learning algorithms and multivariate data analysis methods have been widely utilized. In particular, several validation strategies and classifiers, several feature extraction and selection methods, applied especially to MRI measures, have been explored [1–4].

Graph theory can be a suitable tool to reveal differences between healthy controls and patients or quantify them through topological network properties [5]. The investigation of which measurements and graph properties can better capture and model these alterations, eventually furnishing a direct interpretation of the disease etiology, depends on the data used and the connectivity definition adopted.

In our case the attention was focused to model the single-subject variations, to outline brain atrophy and consequently predict neurodegeneration onset. Multiplex approach, that recent study have demonstrated to be more informative than a single-graph approach, was naturally adopted here to include in this model the context information obtainable only considering the other subjects and the related networks [6, 7].

We compared the classification performances obtained with structural and multiplex network features. Moreover, we quantified the add-on value carried by multiplex. Finally, we evaluated the robustness of the informative content with respect of the different features included in the description and the classification techniques adopted.

2 Materials

Data used in this study was obtained from the ADNI database (adni.loni.usc.edu). In particular, a data set $\mathscr{D}_{ADNI}$ of 100 MRI scans, including normal controls (NC), mild cognitive impairment (MCI) and Alzheimer's disease (AD) subjects, from the ADNI database, was used in preparation of this work. $\mathscr{D}_{ADNI}$ set consisted of MPRAGE MRI brain scans with a resolution of $1 \times 1 \times 1$ mm^3 or 1 voxel. Data size, clinical detail, age and sex information of $\mathscr{D}_{ADNI}$ are summarized in Table 1. The $\mathscr{D}_{ADNI}$ was chosen to result balanced from the clinical and demographic point of view.

[1] http://www.alz.co.uk/research/world-report-2014.

Table 1 Image demographics. Group size, range age, sex and clinical composition of normal controls (NC), mild cognitive impairment (MCI) and Alzheimer's disease (AD) subjects of the $\mathscr{D}_{ADNI}$ data set are provided

Data	Size	Age (years)	M/F	NC-MCI-AD
$\mathscr{D}_{ADNI}$	100	60–90	56/44	29–33–38

3 Multiplex Model

The $\mathscr{D}_{ADNI}$ MRI scans were spatially and intensity normalized with FSL [8]. In particular, the scans were both linearly and non-linearly registered to the MNI152 template, then parceled into smaller volumes called *supervoxels* (of dimension equal to 3000 *voxels*). The supervoxels were used for two main reasons: we wanted a robust description of the brain, thus we chose to perform our analyses on a dimensional scale far higher than the voxel; at the same time, we did not want a ROI description, because of its well known limitations in perceiving small or multi-site effects involved in brain atrophy [9–11].

As scans had been spatially and intensity normalized, we hypothesized that corresponding supervoxels:

1. contained the same anatomical districts;
2. shared analogous gray level distributions unless substantial morphological variations.

This hypothesis yields a crucial aspect. In fact, the comparison of the similarity of two supervoxels in different subject scans, can model important changes occurring in grey matter volume of a diseased brain, that would be neglected within a single subject perspective. Besides, as Alzheimer disease does not uniformly involve the whole brain, it is reasonable to assume that supervoxels, including brain regions affected by atrophy, manifest different similarity patterns that can be captured by the proposed approach.

A graph $\mathscr{G} = (\mathscr{N}, \mathscr{E})$ is by definition a couple of two sets $\mathscr{N}$ and $\mathscr{E}$, respectively representing the *nodes* and the *edges* of the graph. We built a multiplex network considering each MRI scan as a multiplex layer α, that is a network where each supervoxel represents a node i (549 nodes). To build our model, the last step required, was the network edge definition. Many structural MRI studies, adopting graph theory, define the network nodes as anatomical regions and establish the link presence between them, when they covary in thickness or volume across subjects, within an individual or longitudinally [12, 13]. However, this edge choice needs and relies upon an accurate brain mapping and a preliminary knowledge of the anatomical areas to extract. In the present study, instead, connections and the related weights were obtained measuring the Pearson's correlation, in absolute value, between each supervoxel. We discarded correlations lower than moderate ($|r| < 0.3$). This metric was chosen because simple to interpret and computationally fast. In this way a multiplex, formed by undirected and weighted networks, was obtained. To extract

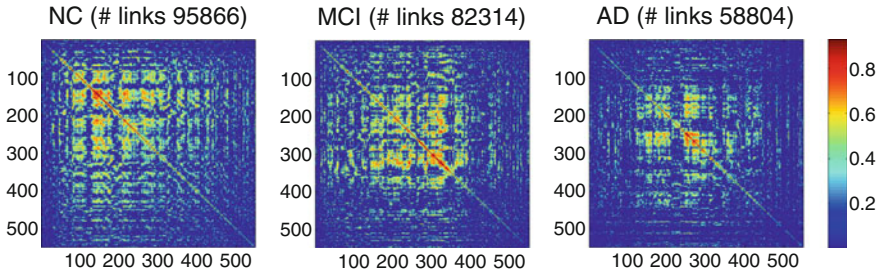

Fig. 1 Representative networks for each group: NC (*left*), MCI (*middle*) and AD (*right*). Correlations are sorted as a function of the node strength. *Color bar* shows the value of the Pearson's correlation coefficient. This figure suggests that the loss of connections could be a marker of the disease

significant features for the classification, for each layer α and for each node i of the multiplex network, two topological properties were computed:

1. *strength* s_i^α,
2. *inverse participation ratio* Y_i^α.

These quantities are usually used to portray weighted networks. In particular, the first one is the sum of the weights of the links incident upon node i in layer α and the second one indicates how evenly the weights of the links of node i are distributed in layer α [14]:

$$\begin{aligned} s_i^\alpha &= \sum_j a_{ij}^\alpha \\ Y_i^\alpha &= \sum_j \left(\frac{a_{ij}^\alpha}{s_i^\alpha}\right)^2 \quad with \quad \left(Y_i^\alpha\right)^{-1} \in \left(1, k_i^\alpha\right) \end{aligned} \tag{1}$$

the previous sums are calculated over all nodes connected with node i. Then for each layer also the *conditional means of the strength* and the *inverse participation ratio* of the nodes with the same degree k were evaluated. Correlation matrices are shown in Fig. 1 as an example of each group (NC, MCI, AD).

To obtain topological features encoding the information content of the whole multiplex network, it was necessary to consider the aggregate adjacency matrix $\mathscr{A} = \{a_{ij}\}$ where:

$$a_{ij} = \{1 \; if \; \exists\alpha | w_{ij}^\alpha > 0 \quad \wedge \quad 0 \quad otherwise\} \tag{2}$$

The matrix $\mathscr{A}$ allowed the previous network measurements to be introduced within an inter-layer perspective. Thus, for each network $8N$ features were obtained. The overall multiplex network resulted in a $M \times 8N$ (100×4392) feature matrix that could be used to feed a classifier and study specific disease patterns. A fundamental step of the analysis was then the feature selection and classification.

4 Feature Selection and Classification

Feature selection techniques are usually distinguished in three classes: *filter*, *embedded* and *wrapper* approaches. The first one measures the single feature relevance. This method is particularly appropriate for high dimensional datasets as it is robust against overfitting, independent from the classification and computationally easy and fast. Both *wrapper* and *embedded* methods select feature subsets using a machine learning and taking inter-connections among features into account. *Wrapper* methods explore the space of all possible feature subsets using a search technique and assessing every time the chosen subsets repeating classification process. *Embedded* methods select features evaluating, for each one, the chosen metric values without retraining the classifier [15].

We compared these different approaches with 1000 5-fold cross validations, using standards techniques, to find the best feature configuration for the multiplex features. For the *filter* method, the *Kruskal–Wallis* (KW) non-parametric statistic test was used. Only the $p < 0.01$ significant features were selected. For the *wrapper* method we chose as search algorithm the *Sequential Forward Selection* (SFS). SFS starts from an empty set and for each step, it adds a new feature evaluating the feature combination with the highest performance. At the end, the subset with the configuration providing the best accuracy are selected. For the *embedded* method we trained a RF (Random Forest) classifier and used it to measure the feature importance. In this case only those features whose importance exceeded the third quartile of the whole normalized importance distribution were selected. Finally, we trained two distinct models with RF and SVM (Support Vector Machine). The RF was trained with 500 trees, SVM model consisted of a radial kernel with cost $C = 1$ and the free parameter of the Gaussian radial basis function $\gamma = 0.01$. Classifiers parameters were set with typical values as our study was aimed at assessing the informative difference between the several sets of features, more than refining the method performances.

In Fig. 2 the classification performance is shown. It can be noticed that the best method was the *Embedded* one with a reduction to 43 features and an accuracy of 0.88 ± 0.01. Successively with the chosen features we performed these two distinct evaluations:

1. *one versus one* classification: with this test we studied the separation of the classes (NC, MCI, AD) along with the discriminant power of the selected features. We studied separately the groups NC/MCI, NC/AD and MCI/AD.
2. *one versus others*: for each cross-validation round, training examples were divided in three binary groups, each one consisting of the elements of one class, e.g., NC, and considering the remaining two classes as an other class, e.g., not-NC ($\neg$NC). Accordingly, for each cross-validation round three different classifiers were trained, whose scores allowed us to assign the class to each test example.

Performance for the binary classification problems were measured in terms of accuracy, sensitivity and specificity. For the three class prediction we measured the *area under the receiver operating characteristic* (AUC) with the relative standard

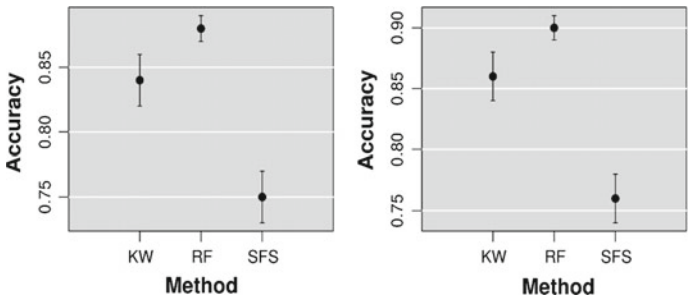

Fig. 2 The figure shows the performances in terms of accuracy and standard error obtained respectively with RF (on the *left*) and SVM (on the *right*) for the three different chosen feature selection methods: the *Kruskal–Wallis* (KW) non-parametric statistic test, the *Random Forest* (RF) feature importance selection and the *sequential forward selection* (SFS)

error [16]. The same procedure was also adopted with the FreeSurfer [17] features and with the combination of the structural and topological ones.

5 Results

5.1 Binary Classification

Our first test aimed to demonstrate if multiplex features were able to capture the differences between NC, MCI and AD. Besides, we assessed if the base of knowledge provided by the multiplex framework allowed classification performances to be compared favorably with those obtained using structural FreeSurfer features. A comprehensive overview, with the three cases NC/AD, NC/MCI and MCI/AD is shown in the following Fig. 3.

Higher performances, in terms of accuracy, were reached by SVM for all three cases NC/AD, NC/MCI and MCI/AD, RF always performed worst. In particular, these SVM accuracy values and standard errors were found (in parenthesis the corresponding sensitivity/specificity): 0.90 ± 0.01 (0.92/0.89) for NC/AD, 0.90 ± 0.02 (0.89/0.91) for NC/MCI and 0.81 ± 0.02 (0.85/0.86) for MCI/AD. Finally, no significant improvement could be obtained using both kinds of features.

5.2 Three Class Evaluation

A second test was performed to establish whether the discriminating power, previously assessed, could be suitably adopted for the three class classification problem of distinguishing NC/MCI/AD.

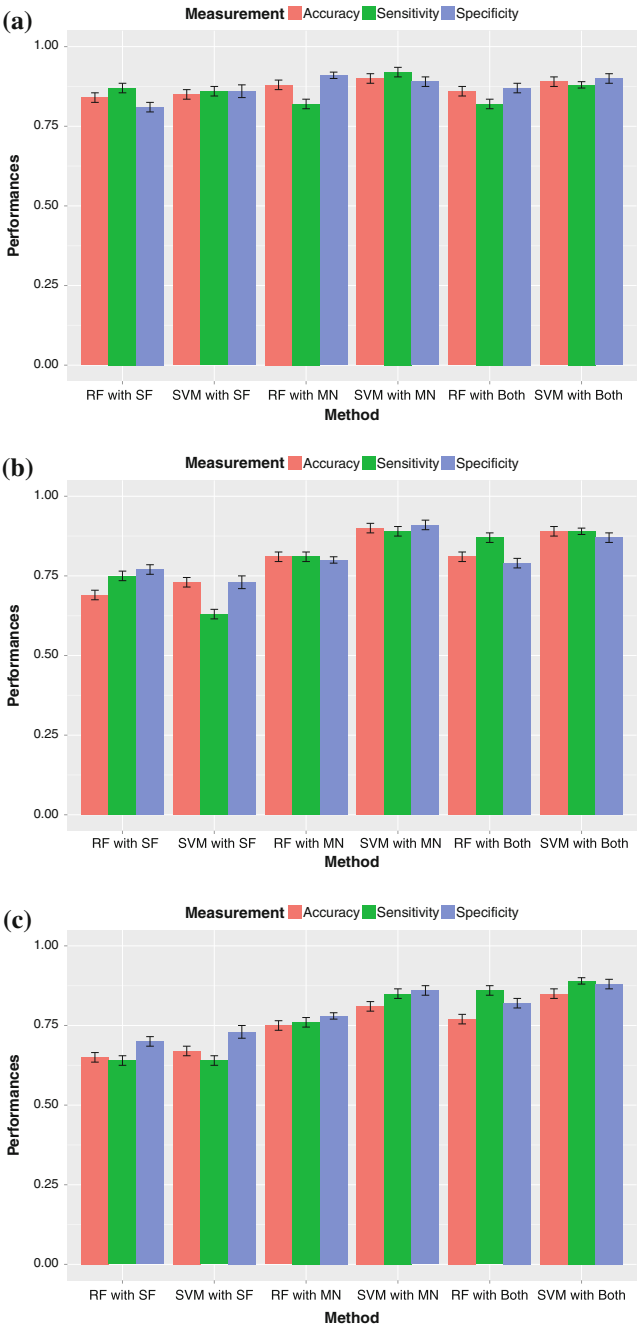

Fig. 3 Accuracy, sensitivity and specificity are shown for each classifier and for each binary classification: NC/AD (**a**), NC/MCI (**b**) and MCI/AD (**c**). SVM performs better than RF and multiplex network features (MN) allow higher performances than structural features (SF)

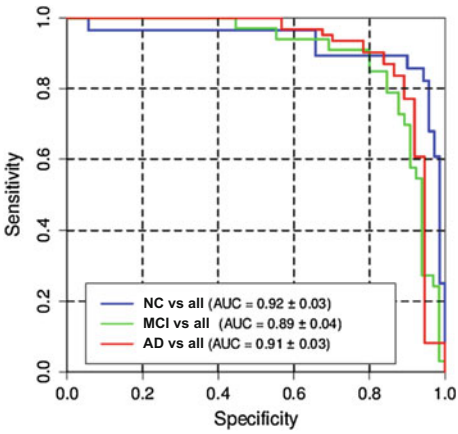

Fig. 4 The figure shows the three class classification performances for NC (*blue*), MCI (*green*) and AD (*red*)

We adopted a *one versus others* approach using SVM to perform three class classification, as the previous test had already demonstrated its effectiveness.

Performances were measured in terms of area under the curve and the relative standard error. We found an AUC of 0.92 ± 0.03 for NC/¬NC, 0.89 ± 0.04 for MCI/¬MCI and 0.91 ± 0.03 for AD/¬AD. As expected the best performances were achieved for NC and AD classes. A Kruskal–Wallis test established that no significant difference could be found for the three AUC values ($p < 0.05$). A performance overview is presented in the Fig. 4

6 Conclusions and Discussion

We have extensively studied the multiplex network use for describing brain changes due to neurological diseases. We showed that this approach suitably reveals important bio-markers, such as the grey matter loss in Alzheimer's disease patients, and can outline them independently from other adopted structural measures (FreeSurfer features).

Notably, the proposed method can be used for predictive purpose in the context of the early diagnosis of Alzheimer disease. Accordingly, we considered three classes: controls, AD and MCI subjects and found: (i) MCI subjects can be accurately distinguished from the others ($AUC = 0.89 \pm 0.04$); (ii) the remaining classes have classification performances not significantly different ($AUC = 0.92 \pm 0.03$ for NC, $AUC = 0.91 \pm 0.03$ for AD), confirming the multiplex network approach robustness; (iii) the multiplex-based features outperform the structural ones in two-class classification problems; (iv) it is worthwhile to note that the use of both kinds of feature does not yield any significant enhancement.

This study could be improved evaluating which MCI converts to AD or increasing the dataset size. Other machine learning techniques, such as neural networks, that

can provide richer models when multiple layer are included and there is a large number of samples could be explored. Further important investigations can arise from the introduction of longitudinal informations and from the use of other imaging modalities, such as diffusion MRI, within the described framework.

References

1. Lebedev, A., Westman, E., Van Westen, G., Kramberger, M., Lundervold, A., Aarsland, D., Soininen, H., Kloszewska, I., Mecocci, P., Tsolaki, M., et al.: Random forest ensembles for detection and prediction of alzheimer's disease with a good between-cohort robustness. NeuroImage: Clin. **6**(115), 237–125 (2014)
2. Amoroso, N., Errico, R., Bellotti, R.: PRISMA-CAD : Fully automated method for computer-aided diagnosis of dementia based on structural MRI data. In Proceedings of the Computer-aided Diagnosis of Dementia Based on Structural MRI Data, MICCAI 2014, pp. 16–24 (2014)
3. Magnin, B., Mesrob, L., Kinkingnéhun, S., Pélégrini-Issac, M., Colliot, O., Sarazin, M., Dubois, B., Lehéricy, S., Benali, H.: Support vector machine based classification of alzheimer's disease from whole-brain anatomical mri. Neuroradiology **51**(2), 73–83 (2009)
4. Bellotti, R., Pascazio, S.: Advanced physical methods in brain research. Eur. Phys. J. Plus **127**(145) (2012)
5. Tijms, B.M., Wink, A.M., De Haan, W., van der Flier, W.M., Stam, C.J., Scheltens, P., Barkhof, F.: Alzheimers disease: connecting findings from graph theoretical studies of brain networks. Neurobiol. Aging **34**, 2023–2036 (2013)
6. Szell, M., Lambiotte, R., Thurner, S.: Multirelational organization of large-scale social networks in an online world. Proc. Natl. Acad. Sci. USA **107**, 13636–13641 (2010)
7. Battiston, F., Nicosia, V., Latora, V.: Structural measures for multiplex networks. Phys. Rev. E **89** (2014)
8. Jenkinson, M., Beckmann, C.F., Behrens, T.E., Woolrich, M.W., Smith, S.M.: Fsl. NeuroImage **62**(2), 782–790 (2012)
9. Ishii, K., Kawachi, T., Sasaki, H., Kono, A.K., Fukuda, T., Kojima, Y., Mori, E.: Voxel-based morphometric comparison between early- and late-onset mild Alzheimer's disease and assessment of diagnostic performance of z score images. Am. J. Neurorabiol. **26**, 333–340 (2005)
10. Bron, E.E., Smits, M., van der Flier, W.M., Vrenken, H., Barkhof, F., Scheltens, P., Papma, J.M., Steketee, R.M., Orellana, C.M., Meijboom, R., et al.: Standardized evaluation of algorithms for computer-aided diagnosis of dementia based on structural mri: The caddementia challenge. NeuroImage **111**, 562–579 (2015)
11. Suk, H.I., Shen, D.: Deep learning-based feature representation for AD/MCI classification. Med. Image Comput. Comput. Assist. Interv. MICCAI **8150**, 583–590 (2013)
12. Yao, Z., Zhang, Y., Lin, L., Zhou, Y., Xu, C., Jiang, T.: Alzheimer's Disease Neuroimaging Initiative. Abnormal cortical networks in mild cognitive impairment and Alzheimer's disease. PLoS Comput. Biol. **6** (2010)
13. Li, Y., Wu. Y., Wang, G., Shi, F., Zhou, L., Lin, W., Shen, D.: Discriminant analysis of longitudinal cortical thickness changes in Alzheimer's disease using dynamic and network features. Neurobiol. Aging **33** (2012)
14. Manichetti, G., Remondini, D., Panzarasa, P., Mondragón, R.J., Bianconi, G.: Weighted multiplex networks. PLOS ONE **9**(6) (2014)
15. Tangaro, S., Amoroso, N., Brescia, M., Cavuoti, S., Chincarini, A., Errico, R., Inglese, P., Longo, G., Maglietta, R., Tateo, A., Riccio, G., Bellotti, R.: Feature selection based on machine learning in MRIs for hippocampal segmentation. In: Computational and Mathematical Methods in Medicine (2015)

16. DeLong, E.R., DeLong, D.M., Clarke-Pearson, D.L.: Comparing the areas under two or more correlated receiver operating characteristic curves: a nonparametric approach. Biometrics 837–845 (1988)
17. Fischl, B.: FreeSurfer. NeuroImage **62**(2), 774–781 (2012)

Topological Complex Networks Properties for Gene Community Detection Strategy: DRD2 Case Study

Anna Monda, Nicola Amoroso, Teresa Maria Altomare Basile, Roberto Bellotti, Alessandro Bertolino, Giuseppe Blasi, Pasquale Di Carlo, Annarita Fanizzi, Marianna La Rocca, Tommaso Maggipinto, Alfonso Monaco, Marco Papalino, Giulio Pergola and Sabina Tangaro

Abstract Gene interactions can suitably be modeled as communities through weighted complex networks. However, the problem to efficiently detect these communities, eventually gaining biological insight from them, is still an open question. This paper presents a novel data-driven strategy for community detection and tests it on the specific case study of *DRD2* gene coding for the D2 dopamine receptor, which plays a prominent role in risk for Schizophrenia. We adopt a combined use of centrality and topological properties to detect an optimal network partition. We find that 21 genes belongs with our target community with probability $P \geq 90\,\%$. The robustness of the partition is assessed with two independent methodologies: (i) fuzzy c-means and (ii) consensus analyses. We use the first one to measure how strong the membership of these genes to the *DRD2* community is and the latter to confirm the stability of the detected partition. These results show an interesting reduction ($\sim$80 %) of the target community size. Moreover, to allow this validation on different case studies, the proposed methodology is available on an open cloud infrastructure, according to the Software as a Service paradigm (SaaS).

A. Monda · A. Bertolino · P. Di Carlo · M. Papalino · G. Pergola
Dipartimento di Scienze Mediche di Base, Neuroscienze e Organi di Senso, Università Degli Studi di Bari "Aldo Moro", Piazza Giulio Cesare 11, 70124 Bari, Italy

N. Amoroso (✉) · T.M.A. Basile · R. Bellotti · A. Fanizzi · M. La Rocca · T. Maggipinto
Dipartimento Interateneo di Fisica "Michelangelo Merlin", Università Degli Studi di Bari "Aldo Moro", Via G. Amendola 173, 70126 Bari, Italy
e-mail: nicola.amoroso@ba.infn.it

N. Amoroso · T.M.A. Basile · R. Bellotti · M. La Rocca · T. Maggipinto · A. Monaco · S. Tangaro
Istituto Nazionale di Fisica Nucleare - Sezione di Bari, Via Orabona 4, 70125 Bari, Italy

A. Bertolino · G. Blasi
Azienda Ospedaliero-Universitaria Consorziale Policlinico, 70124 Bari, Italy

A. Bertolino
pRED, NORD DTA, F. Hoffman-La Roche Ltd., 4070 Basel, Svizzera

G. Mantica et al. (eds.), *Emergent Complexity from Nonlinearity, in Physics, Engineering and the Life Sciences*, Springer Proceedings in Physics 191,
DOI 10.1007/978-3-319-47810-4_16

1 Introduction

Gene coexpression network analysis arises from the merge of network theory and transcriptome analysis techniques [1]. Its pertinence to formalize, include and manage all the information originated from the genetic data, especially for the characterization of complex diseases, is manifest [2]. Therefore, explaining the widespread use of this methodology has gained. However, no general consensus exists as to an unambiguous interpretation of all the knowledge that could be extracted from a graph [3] and yet the choice of the data analysis technique is a crucial element depending both on the data and on the aims of the experiment [4–6]. Furthermore, it is well known that biological networks tend to self-organize into many small, highly connected topological modules, generally difficult to detect, that gradually tend to combine in a hierarchical manner into larger, less cohesive units [7].

In the present work, we designed and implemented a data-driven analysis for community detection in weighted graphs, specifically, we adopted this methodology for the study of *DRD2* gene. This gene could play a relevant role, as a dopamine receptor, in several psychiatric disorders, such as Schizophrenia, as it is known that dopaminergic transmission is altered in this kind of disease.

Several approaches have been proposed to investigate weighted gene coexpression networks. In particular, the Weighted Gene Coexpression Network Analysis (WGCNA) [8] allows us to suitably generalize to weighted networks important properties of binary networks. Nevertheless, weighted graphs suffer from an intrinsic variability, as no *a priori* considerations allow to establish which gene correlations are biologically meaningful. This issue especially affects community detection strategies. Accordingly, our work aims to tackle some questions: (i) we try to determine the existence of a suitable and robust threshold for weighted graphs; (ii) then we perform a data-driven community detection, whose robustness is granted by iterated cross-validation analyses; (iii) finally, we refine our analysis by assigning to each gene a community membership degree by means of fuzzy c-means. Finally, we deployed this methodology on the Bari ReCaS computer farm[1] as an available Service, to ensure wider opportunities to validate our methodology on new case studies.

2 The *DRD2* Community Detection

WGCNA is a framework based on the concept of correlation networks, i. e. networks whose edges are represented by correlation measurements. This approach has been widely adopted in genetic studies to summarize coexpression profiles and identify communities of interacting genes. On the contrary, it would seem counterintuitive to have just one gene regulating highly complex phenomena, as those involving pathologic conditions [9]. Thus, in preparation of this manuscript we used the Braincloud dataset, publicly available at http://braincloud.jhmi.edu/, consisting of 85 gene

[1] http://recasgateway.ba.infn.it.

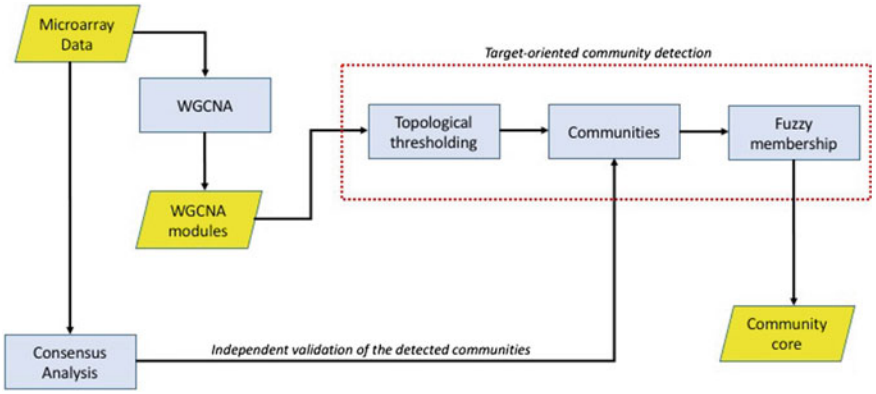

Fig. 1 This figure shows a schematic overview of the proposed approach. The target oriented strategy is mainly composed of three steps: topological thresholding, community detection and measurement of membership degree with a fuzzy approach. An independent assessment of the communities detected is provided with a consensus analysis

expressions x_i from 199 subjects [10] and measured the absolute value of Pearson's pairwise correlations s_{ij} to define the network:

$$s_{ij} = \left| cor\left(x_i, x_j\right) \right|. \tag{1}$$

Since we're interesting in the strength of the relationship between pairs of genes, the sign of the correlation value became non influential. After constructing the network, we detected the WGCNA modules and selected the subgraph including *DRD2*, our gene of interest. The subgraph, as the original graph, can be interpreted as network of interacting genes. We studied the possibility to further divide the WGCNA module. In this work we propose a data-driven approach to detect a further partition. We also assessed the quality of the partition with a consensus analysis and for each gene of the *DRD2* community we measured a degree of membership (see Fig. 1 for a schematic overview).

The essential hypothesis of the proposed approach is that a varying threshold for pairwise correlations can be used to prove the existence of network communities. The presence of network communities should be closely related to centrality and topological measurements, therefore we expect it should also affect their measured values. Thus, we explored several properties, namely: degree, betweenness, diameter and eccentricity.

The degree, k_i, indicates the amount of connections that the node i have, with respect to all other nodes in the networks j, for $j = 1, ..., N$. It is defined as:

$$k_i = \sum_{j \in N} a_{ij}, \tag{2}$$

where a_{ij} are the elements of the adjacency matrix, A.

In weighted networks, this quantity is straightforwardly a degree generalization. For each node i it represents the sum of the weights extended to the node connected neighbors and expresses the overall strength of the node connectivity.

The matrix A is defined by $a_{ij} = f(s_{ij})$, so they are derived by the correlation measurements. This matrix formally represents the graph and it is differently defined depending on the case we are implementing a weighted networks:

$$a_{ij} = power(s_{ij}, \beta) = \left|s_{ij}\right|^{\beta}, \tag{3}$$

with $\beta \geq 1$. This is the case of *soft thresholding*, otherwise, for unweighted networks, we employ a so called *hard thresholding*:

$$a_{ij} = signum(s_{ij}, t) = \begin{cases} 1 & \text{if } s_{ij} \geq t \\ 0 & \text{if } s_{ij} < t. \end{cases} \tag{4}$$

Another centrality measure applied in this work is the betweenness b_i. This topological property emphasizes the paths including the considered node instead than the number of its connections:

$$b_i = \sum_{j,k \in N, j \neq k} \frac{n_{jk}(i)}{n_{jk}} \tag{5}$$

In this case n_{jk} represents the number of geodesics between node j and k, while $n_{jk}(i)$ is the number of geodesics between the same genes, passing through node i.

A geodesic between two nodes j and k is the shortest path connecting a node j with a node k. The diameter is the maximum geodesic of a graph, thus it can be considered as a size measure of the graph itself. The last property we considered was the eccentricity. For each node i, the eccentricity is defined as the maximum geodesic starting from node i. This quantity can be considered a geometrical alternative measure of centrality. All these properties except the diameter which is already a global network property, were considered on average to characterize the network behavior in order to analyze their trends. Figure 2 shows these four properties varying with the correlation threshold. The network reveals an interesting structure in a moderate correlation ranges ([0.40, 0.55]). For lower threshold values it is reasonable to assume that noisy relationships prevent the emergence of significant structures. On the other hand, for higher correlations the loss of information is too much. Interestingly, the same considerations arose from all the adopted measures.

There is an abundant literature (see for example [11–13]) on the importance of betweenness for graph characterization and also in our case the betweenness seemed to be the more informative property. Accordingly, we chose to maximize its value to define the optimal threshold. A qualitative inspection of the network partition can be useful in this case. Figure 3 shows how low threshold values yielded a rough two-class partition. On the contrary, with the optimal threshold values an underlying

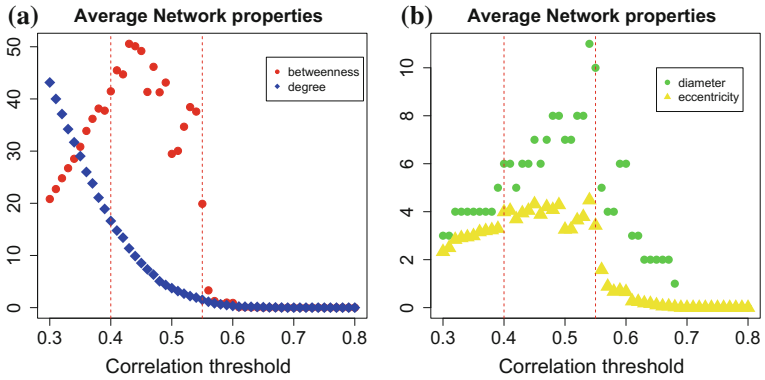

Fig. 2 The plots show the average network properties of degree, betweenness, diameter and eccentricity, for different threshold values

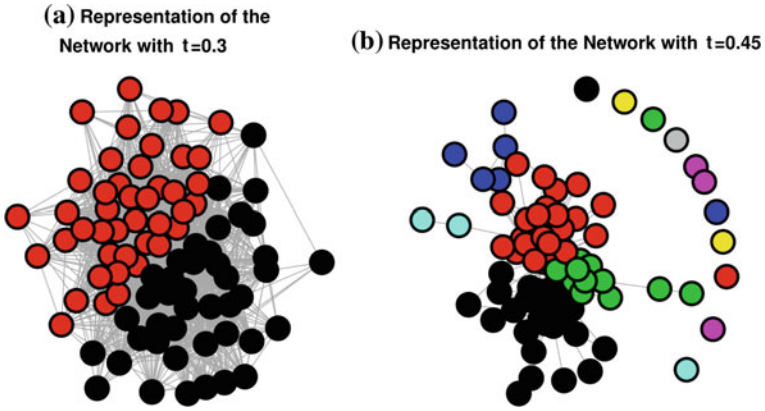

Fig. 3 The graphs illustrate the communities detected with two different values of threshold: **a** t = 0.3 and **b** t = 0.45. The case (**b**) suggest the presence of underlying communities within the WGCNA module

community structure of the WGCNA module was manifest. For higher threshold values there is a continuous increasing of isolated points.

Once the optimal threshold had been fixed, an edge-betweenness based community detection algorithm was used [14]. It is notable here that, after performing a WGCNA, with clearly a soft threshold method employed, we use an hard thresholding analysis. Therefore, what we implemented indeed is an integrated procedure of the previous techniques. Chosen the threshold, we decided to use the edge-betweenness algorithm to detect communities. However, we highlight that this is only one of the available procedures, so there is not an univocal clustering for the network now examined. We found a 6-class partition of the whole network. In particular a community of 28 genes including our target *DRD2* was found. This reduction was not trivial, as

the WGCNA included initially 85 genes. This subsetting represents an overall reduction of about 67 %, nonetheless we performed further tests to better characterize this community and eventually identify smaller yet significant communities.

3 Results

3.1 Methodological Assessment

A cross-validation analysis was carried out on the subjects to check the meaningfulness of the detected communities, focusing on our target gene *DRD2*. Consequently, we assessed to what extent the *DRD2* community depended on the subjects selected, i.e., its robustness. For each cross-validation round, up to $n = 199$, we checked which genes belonged to the *DRD2* community and summarized this information by introducing a dedicated *Coexistence* index for each gene i:

$$Coexistence_i = \frac{1}{n} \sum_{j=1}^{n} I_{i,j} \tag{6}$$

where:

$$I_{i,j} = \begin{cases} 1 & \text{if } gene_i \in DRD2\ cluster \\ 0 & \text{if } gene_i \notin DRD2\ cluster \end{cases} \tag{7}$$

$I_{i,j}$ values, for each iteration, depend on membership of the $gene_i$ to the *DRD2* cluster, as detailed in Formula 7. The number of occurrences of $gene_i$ within the target community is represented by $I_{i,j}$ values summed over j. This quantity were then scaled by n to define the *Coexistence*, see Formula 6.

We additionally performed a *leave-k-out* cross-validation, with k increasing in the range [1, 150]. The k value is the number of subjects left out of the sample in each cross-validation round. The results of these analyses are presented in Fig. 4.

Importantly, the stability test concerning the variation of the subjects in the sample showed the existence of a robust core within the target community. Figure 4 shows two distinct and important aspects: (i) the *DRD2* community is seemingly composed of about 28 genes, (ii) this composition remains stable even when the sample size is reduced, notably suppressing 75% of the original dataset. Results suggested the existence of a definitely stable community core with 21 genes, for an overall 80 % reduction, being present in 90% of cross-validation rounds. Consequently, a quantitative analysis to determine which genes should be considered to be part of the *DRD2* community is presented in the following.

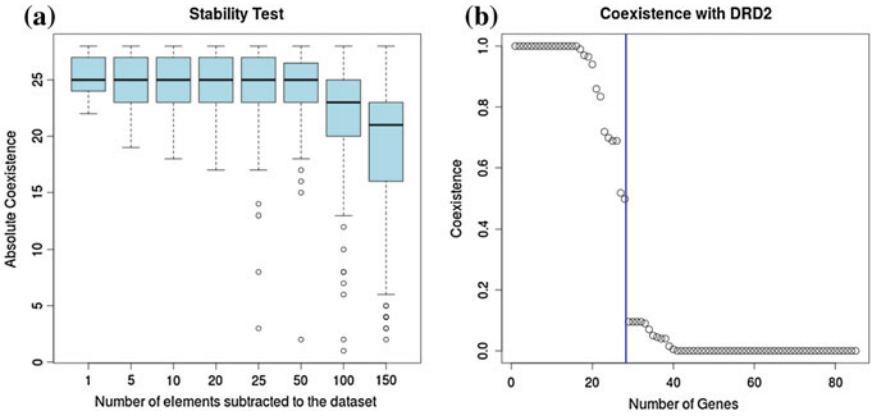

Fig. 4 The figure displays how the Coexistence between all genes and *DRD2* is nicely independent from the sample subjects (*case a*). Interestingly, the leave-one-out analysis suggests the existence of a stable *DRD2* community, with 28 genes detected in 50 % of cases (*vertical line*)

3.2 Consensus Analysis

It is demonstrated that the combination of different algorithms can improve the community detection. We performed a consensus analysis to test and validate the community structure detected as suggested in recent studies [15]. We considered 5 different community detection algorithms: edge betweenness, fast-greedy modularity optimization, label propagation, leading eigenvector and multi-level to define the *consensus* adjacency matrix.

Each community detection algorithm gives a network partition. For two generic nodes x_i and x_j, the consensus adjacency matrix takes into account how many times they belong to the same community, so that a new connectivity measure ranging from 0 (for nodes never found in the same community) to 1 (always in the same community) can be defined. The procedure is then iterated until a unique partition is reached by all methods.

Interestingly, this analysis confirmed the *DRD2* core community was composed of 21 genes. The quality of the partitioning was measured in terms of modularity and the consensus matrix led to the modularity maximization. In fact for the previously mentioned techniques modularity ranged from 0.483 to 0.488, while the consensus matrix had modularity 0.55 (see Fig. 5). This analysis confirmed the robustness of the network partition and the *DRD2* community.

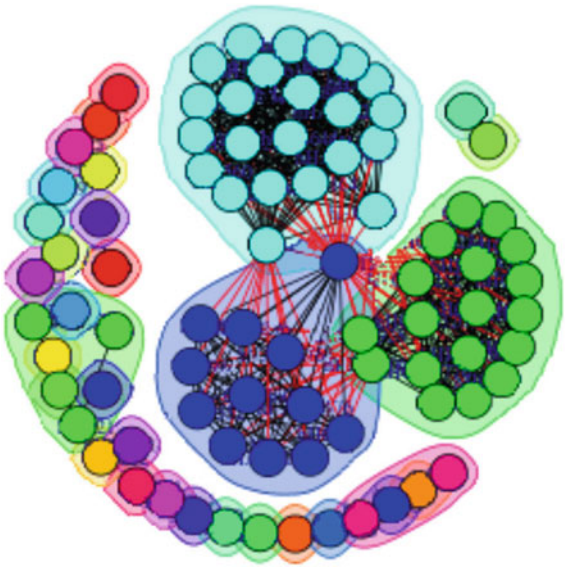

Fig. 5 This figure shows the consensus analysis results. The presence of three main communities is manifest. In particular, the *DRD2* community resulted composed by 21 genes, in agreement with the fuzzy membership

3.3 A Membership Degree Measurement

Previous results have shown how a stable *DRD2* community does exist. Nonetheless, it is also important to measure how strong its the community membership for each gene. In this section we pursue this aim with the fuzzy c-means.

In general, fuzzy clustering techniques assign to each data point a membership score. This score evaluates how strong is the degree of membership of a generic data point to each cluster. The degree of membership μ_{ig} of the i-*th* gene $x(i = 1, 2, \ldots, n)$ to the g-*th* cluster $(g = 1, 2, \ldots, k)$, in such a way that it satisfies the following two constraints: $0 \leq \mu_{ig} \leq 1$ and $\sum_{g=1}^{k} \mu_{ig} = 1$. Given the number of k groups, the non-hierarchical technique known as fuzzy c-means [16] estimates the values of minimizing the object function:

$$\sum_{g=1}^{k} \sum_{i=1}^{n} \mu_{ig}^2 \left|\left|x_{ig} - c_g\right|\right|^2 \tag{8}$$

where

$$c_g = \frac{\sum_{i=1}^{n} \mu_{ig}^2 x_i}{\sum_{i=1}^{n} \mu_{ig}^2} \tag{9}$$

is the centroid of the g-*th* cluster. As in the analogous non-fuzzy c-means technique, such expression represents the sum of squares within-group. In this case, the distance are weighted by the (squared) membership degrees of each observation to the different

Table 1 Number of genes belonging to *DRD2* community with maximum membership

Number of fuzzy partitions	Maximum membership genes
From 2 to 3	30
From 2 to 4	30
From 2 to 5	21
From 2 to 6	21

clusters. In other words, such object function is a measure of overall heterogeneity within the clusters.

Different fuzzy partitions were computed with the previously mentioned technique, in particular by varying the expected number of partitions from 2 to 6, as suggested from network's threshold analyses. It is worthwhile to note that the number of maximum membership genes depended on the number of fuzzy partitions. This is the reason why we performed a consensus analysis to independently assess the number of communities to be 6 (Table 1).

In conclusion, the fuzzy approach shows a *DRD2* community consisting of 21 genes. It is worthwhile to note that, if a data partition is a meaningless data samples, the degree of membership assigned could be the same for different clusters, thus these measurements could be meaningless. Accordingly, it is of paramount importance to assess the robustness and meaningfulness of the communities detected.

4 Conclusion

In this work we presented a data driven approach to refine the community detection performed by state-of-the-art tool such as WGCNA. We applied our methodology to the *DRD2* case, a gene of interest for its involvement in several psychiatric disorders. A stable *DRD2* community of 21 genes was detected with the proposed approach. This community represented a consistent reduction (of about 80 %) if compared with the original WGCNA module, but at the same time these genes achieve a probability $P \geq 90\,\%$ to belong with our target gene *DRD2*, tested by several and different methods.

In order to assess the robustness of the methodology from two distinct perspectives, we performed: (i) a consensus analysis and (ii) a fuzzy clustering. The consensus analysis confirmed the partition obtained with our method, thus suggesting that the detected *DRD2* community did not depend on the adopted community detection algorithm. The fuzzy clustering on the other hand was adopted to measure how strong was the community membership of each gene to the *DRD2* community. Notably, the 21 genes previous detected resulted to be those belonging to the *DRD2* community with maximum membership, so also the fuzzy membership is well-defined.

Finally, we assessed the stability of the results with respect of the sample size. Specifically, we performed repeated cross-validation analyses, with a decreasing sample size. This analysis quantified how the *DRD2* community depended on the

particular subjects composing the data. Notably, we found that even suppressing 75 % of the original subjects the *DRD2* community remained unchanged.

These results suggest *DRD2* being strongly related to a small, robust and stable community of 21 genes. Nonetheless, further investigations could be of interest. In particular, we intend to introduce a significance measurement for the detected communities, a possibility could be for example the adoption of the OSLOM algorithm [17]. Furthermore, a clinical validation on independent data sets is fundamental to understand whether the detected *DRD2* community caries a biological meaning. In this sense, a possibility could be the study of intermediate phenotypes [18].

References

1. Horvath, S., Dong, J.: Geometric interpretation of gene coexpression network analysis. PLoS Comput. Biol. **4**(8), e1000117 (2008)
2. Sieberts, S.K., Schadt, E.E.: Moving toward a system genetics view of disease. Mamm. Genome **18**(6–7), 389–401 (2007)
3. Aittokallio, T., et al.: Computational strategies for analyzing data in gene expression microarray experiments. J. Bioinf. Comput. Biol. **1**(03), 541–586 (2003)
4. Hudson, T.J., et al.: International network of cancer genome projects. Nature **464**(7291), 993–998 (2010)
5. Nicotri, S., et al.: Complex networks and public funding: the case of the 2007–2013 Italian program. EPJ Data Sci. **4**(1), 1 (2015)
6. Amoroso, N., et al.: Hippocampal unified multi-atlas network (HUMAN): protocol and scale validation of a novel segmentation tool. Phys. Med. Biol. **60**(22), 8851 (2015)
7. Ravasz, E.: Detecting hierarchical modularity in biological networks. Comput. Syst. Biol. 145–160 (2009)
8. Langfelder, P., Horvath, S.: WGCNA: an R package for weighted correlation network analysis. BMC Bioinf. **9**(1), 1 (2008)
9. Barabási, A.-L., Gulbahce, N., Loscalzo, J.: Network medicine: a network-based approach to human disease. Nat. Rev. Genet. **12**(1), 56–68 (2011)
10. Colantuoni, C., et al.: Temporal dynamics and genetic control of transcription in the human prefrontal cortex. Nature **478**(7370), 519–523 (2011)
11. Dunn, R., Dudbridge, F., Sanderson, C.M.: The use of edge-betweenness clustering to investigate biological function in protein interaction networks. BMC Bioinf. **6**(1), 1 (2005)
12. Brandes, U.: On variants of shortest-path betweenness centrality and their generic computation. Soc. Netw. **30**(2), 136–145 (2008)
13. Pinney, J.W., David, R.W.: Betweenness-based decomposition methods for social and biological networks. Interdiscip. Stat. Bioinf. 87–90 (2006)
14. Newman, M.E.J., Michelle, G.: Finding and evaluating community structure in networks. Phys. Rev. E **69**(2), 026113 (2004)
15. Lancichinetti, A., Santo, F.: Consensus clustering in complex networks. Sci. Rep. **2** (2012)
16. Kaufman, L., Peter, J.R.: Finding Groups in Data: An Introduction to Cluster Analysis, vol. 344. Wiley, New Jersey (2009)
17. Lancichinetti, A., et al.: Finding statistically significant communities in networks. PloS one **6**(4), e18961 (2011)
18. Meyer-Lindenberg, A.: The future of fMRI and genetics research. NeuroImage **62**(2), 1286–1292 (2012)

Power Laws in Neuronal Culture Activity from Limited Availability of a Shared Resource

Damian Berger, Sunghoon Joo, Tom Lorimer, Yoonkey Nam and Ruedi Stoop

Abstract We record spontaneous activity from a developing culture of dissociated rat hippocampal neurons in vitro using a multi electrode array. To statistically characterize activity, we look at the time intervals between recorded spikes, which, unlike neuronal avalanche sizes, do not require the selection of a time bin. The distribution of inter event intervals in our data approximate power laws at all recorded stages of development, with exponents that can be used to characterize the development of the culture. Synchronized bursting emerges as the culture matures, and these bursts show activity that decays approximately exponentially. From this, we propose a model for neuronal activity within bursts based on the consumption of a shared resource. Our model produces power law distributed avalanches in simulations, and is analytically demonstrated to produce power law distributed inter event intervals with an exponent close to that observed in our data. This indicates that power law distributions in neuronal avalanche size and other observables, can be also an artefact of exponentially decaying activity within synchronized bursts.

1 Introduction

In the recent global push to understand brain function, it has become clear that an experimental paradigm is required where the interaction between neuronal network structure and function can be understood. In vitro studies of neuronal cultures

D. Berger · T. Lorimer · R. Stoop (✉)
Institute of Neuroinformatics and Institute for Computational Science, University of Zürich, Winterthurerstr. 190, 8057 Zurich, Switzerland
e-mail: ruedi@ini.phys.ethz.ch

S. Joo · Y. Nam
Department of Bio and Brain Engineering, Korea Advanced Institute of Science and Technology (KAIST), 291 Daehak-ro, Yuseong-gu, Daejeon 34141, Republic of Korea

D. Berger · T. Lorimer · R. Stoop
ETH Zürich, Zurich, Switzerland

G. Mantica et al. (eds.), *Emergent Complexity from Nonlinearity, in Physics, Engineering and the Life Sciences*, Springer Proceedings in Physics 191,
DOI 10.1007/978-3-319-47810-4_17

on multi-electrode arrays (MEA) provide a window onto the relationship between growth and activity, from the individual neuron to the ensemble level, both during development and in the mature state. During development, neuronal structures undergo several structural changes, and these are reflected in the statistical properties of their spontaneous activity. One major approach in the analysis of neuronal culture recordings has been to focus on these statistical properties, considering neuronal cultures as ensembles of coupled items linked by an interaction paradigm. This approach opens up a connection to similar abstract situations that have been greatly analyzed in statistical physics. Generally the predictions made by models in statistical physics depend on the specific law of interaction, which may not sufficiently reflect the poorly understood laws governing neuronal interaction. There is, however, a particular situation where the details of these laws should cease to be of importance. This is in the presence of a second order phase transition, or the ensemble being at 'criticality' or in a 'critical state', leaving open a parameter from which all other statistical parameters could be inferred [1]. A fingerprint of such a process to be at work is power law distributions of local descriptors evaluated across the ensemble.

Historically, the connection between neuronal tissue and statistical physics was sparked by the observation of power law distributed neuronal 'avalanches' of activations in the neural tissue, from recordings of local field potentials (LFP) on a MEA by Beggs and Plenz [2, 3]. Even before these observations, the potential connection between criticality and activity in neural networks was recognized or suggested [4, 5]. The power law observations of Beggs and Plenz [2, 3] were made from mature cultures, where activity is often characterized by synchronized bursting activity separated by quiet periods [6], by studying the sub-structure of such bursts. Other work has claimed to observe 'sub-critical', 'critical' and 'super-critical' avalanche statistics at different stages of development [7], or under chemically altered neuronal connectivity states [8], though the more general principles underlying power law distribution deviations are still in the process of being explained [9].

It often remains elusive, by exactly which process and mechanism power laws are generated. In physics, there are typical situations in which power laws emerge: Generally in systems that exhibit self-similarity, and more particularly in second order phase transition critical regimes (involving models of branching and percolation processes). Whereas these represent rather distinct physical situations, in the context of the neuronal avalanche size power law distributions, they have all been used to provide interpretations with the hope of gaining a grip on the phenomenon from a physics point of view [10, 11].

A further challenge arises when inferring the origin of power laws in neuronal avalanches: It is not clear exactly how an avalanche should be defined. Avalanches are generally defined as periods of uninterrupted neuronal activity with respect to a given time binning, but it is well known that changing the bin size changes the exponent of the power law; i.e. changes the key piece of information used to infer the generating process [2]. It is perhaps not so surprising, for example, that selecting the time bin size as the average inter event interval in neuronal LFP recordings results in an exponent close to the theoretical exponent of the branching process universality class, as in this way each event will be followed by, on average, one more event in the next bin. This

raises the question whether the avalanche power laws observed in neuronal cultures, in the absence of other evidence, are best explained by an underlying critical state, or whether there could be a simpler explanation. Furthermore, the activity patterns often discussed in terms of critical dynamics occur in mature cultures. During culture development, activity patterns undergo striking qualitative changes, but a quantitative statistical characterization is still missing.

Here we investigate the emergence of power law statistics in neuronal activity from new recordings of unsorted spikes from dissociated rat hippocampus neurons and propose both a simple, unambiguous statistical characterization of development, and an alternative, simpler model for the emergence of power law statistics in mature neuronal culture activity.

2 Power Law Statistics in Development Characterization

We analyzed one culture of dissociated hippocampal rat neurons grown on a 60-channel MEA (for details, see Methods). Between 9 and 15 days in vitro (DIV), each day recordings of two hours were sampled for further analysis. From the sixty channels of the MEA some measured no or very little activity; for simplicity and reliability, we will consider for plotting and calculations only channels with a mean firing rate above 0.1 Hz. The recorded activity across the development is visualized in Fig. 1. The raster plots show a clear evolution in the spiking characteristics from rather unsynchronized firing (9 and 10 DIV), towards distinct synchronized bursts. Such synchronized bursts, separated by periods with little activity, are typical for mature neuronal networks grown in isolation [6].

Similar synchronized bursts were the object of study in [2]. Following the same avalanche size distribution analysis procedure on our data from 15 DIV, we define avalanches to be a consecutive sequence of time steps of size Δt with at least one recorded event (in any channel) in each time step, ended by a time step of no activity. The size of an avalanche is then defined by the number of spike events in the avalanche. The resulting avalanche size distributions for the measurements at 15 DIV are presented in Fig. 2, showing reasonable agreement to a power law for different bin sizes Δt. However, Fig. 2 also highlights the earlier mentioned difficulty in producing an unbiased characterization of neuronal culture activity data from avalanche size distribution power law exponents: different exponents and distribution forms are observed for different time bin sizes. Arguments have been made justifying the average inter event interval as the appropriate bin size [2] by claiming that this relates to the rate of signal propagation between electrodes. We find this argument to be not sufficiently strong to justify setting such a sensitive parameter.

If we wish to resolve the ambiguity arising from time bin selection, and moreover to statistically characterize neuronal culture development, we require a non-parametric measure applicable also to the less synchronized activity seen from 9 to 12 DIV. We propose, as such a measure, the distribution of inter event intervals (IEI). IEI, defined as the time difference between two successive events at any channels, are

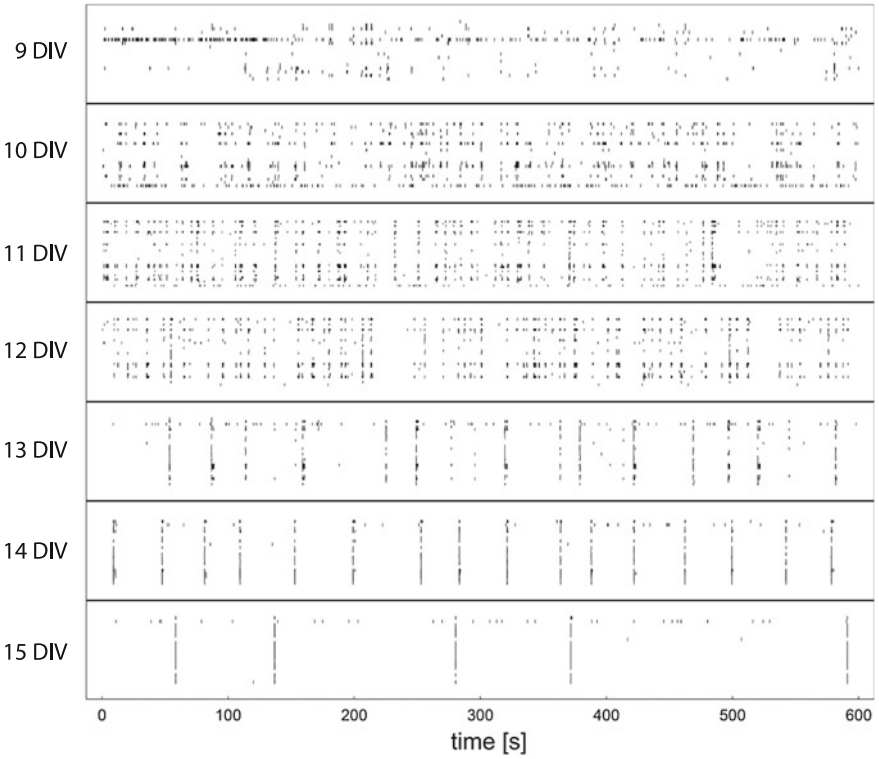

Fig. 1 Raster plots for the first 10 min of the recorded activity from 9 to 15 DIV. The 19 active channels are arranged vertically within each recording day. Each event within each channel is represented by a *short vertical black line*

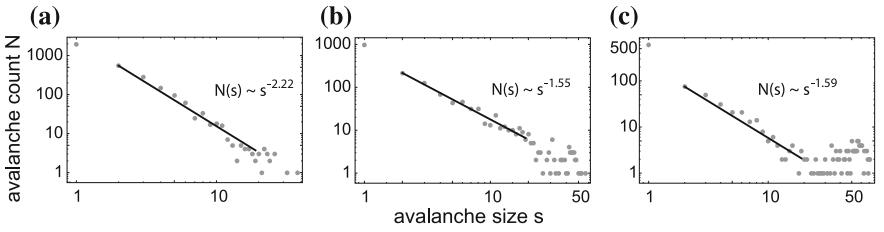

Fig. 2 Avalanche size distribution of experimental data from 15 DIV, using different binning sizes: **a** $\Delta t = 1$ ms; **b** $\Delta t = 2$ ms; **c** $\Delta t = 4$ ms. Power law exponents were fit using maximum-likelihood (see Methods) over a data-range from $s_{min} = 2$ to $s_{max} =$ number of active channels $= 19$

also approximately distributed according to a power law in our data (Fig. 3). Moreover, looking at IEI reveals that a fractal structure exists not only as a substructure of the synchronized bursts seen in mature cultures, but also in the time series throughout the culture's development from 9 to 15 DIV. We also observe a clear, almost perfectly

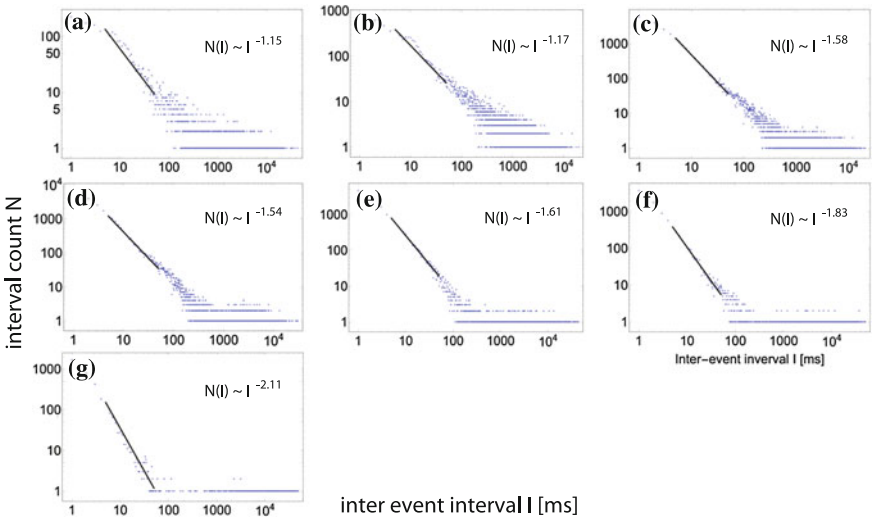

Fig. 3 IEI distributions for: **a** 9 DIV; **b** 10 DIV; **c** 11 DIV; **d** 12 DIV; **e** 13 DIV; **f** 14 DIV; **g** 15 DIV. Least-squares power law fits are shown for the range $I = 5\,\text{ms}$ to $I = 50\,\text{ms}$

monotonic increase in the exponent of the power law in our data, from an exponent close to 1 at 9 DIV to an exponent close to 2 at 15 DIV, which suggests this may be an appropriate quantitative measure of development. Furthermore, IEI distributions reveal in a simple way the emergence of synchrony as the culture matures. For example, at 14 and 15 DIV (Fig. 3f, g) we see the distribution split into two parts, with the power law decay reflecting the within-burst structure, and the high density of IEI above 1000 ms reflecting the quiet inter-burst periods. This can be seen without the need to define a threshold of discrimination between 'burst' and 'inter-burst' prior to analysis.

3 Structure Within Bursts of Mature Cultures

Returning now to our question about the origin of the power law distributions in neuronal avalanches, we limit ourselves to the synchronized activity of mature cultures, and look in more detail at the structure within bursts at 15 DIV. The recordings at 15 DIV show strongly synchronized activity, and all bursts have roughly the same size of about 60 spikes. A zoom into a single burst reveals how the activity is distributed (Fig. 4). The number of spikes is highest at the beginning of the bursts and then after is reduced. Looking at a histogram of events within all bursts aligned by the first spike (Fig. 5), we see an initial increase in activity during the first 20 ms followed by a roughly exponential decay.

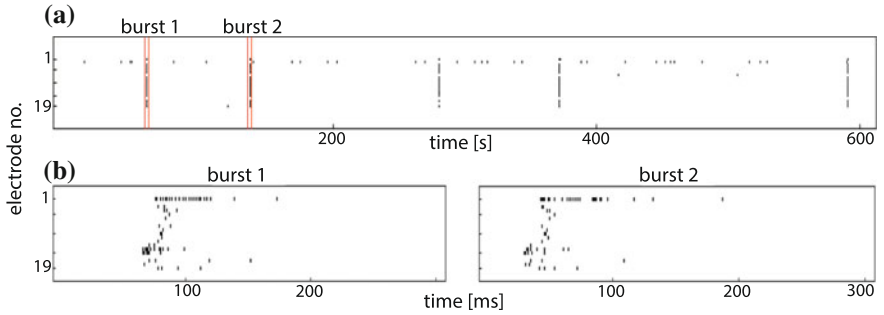

Fig. 4 **a** Raster plot for the first ten minutes of the recorded activity at 15 DIV showing strongly synchronized activity. **b** A closer look at two of the bursts in **a**, revealing a similar temporal pattern

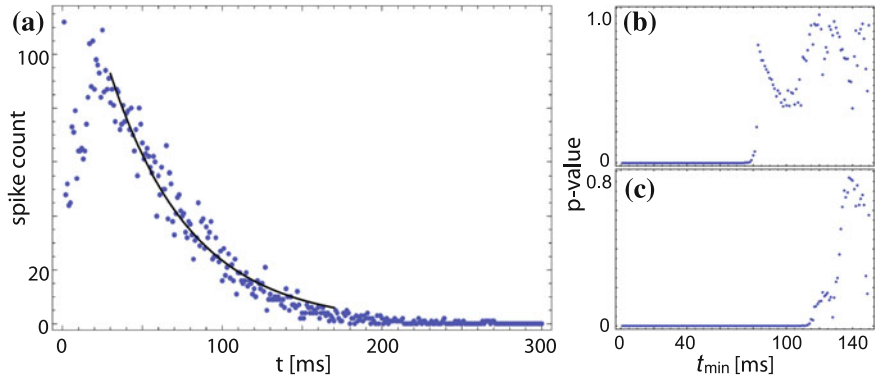

Fig. 5 **a** Stacking of all bursts, aligned at the first spike of each burst and counting the number of spikes per millisecond. The activity increases during the first 20 ms and decreases then after exponentially. **b** p-value for the exponential fit as a function of the lower bound t_{min} ($t_{max} = 300$). For $t_{min} \geq 82$ the p-values are greater than 0.1. **c** p-value for the power law fit as a function of the lower bound t_{min} ($t_{max} = 300$). For $t_{min} \geq 117$ the p-values are greater than 0.1

Even though visually the exponential seems to provide a plausible fit, we wish to use this observation as the basis of our later modeling, so we must clarify this statistically, and moreover, clarify that the fit is plausible over a greater range than a power law alternative. To this end, we fit each distribution over a variable range, and follow the procedure outlined in [12]. For each range $[t_{min}, t_{min} + 1, \ldots, t_{max}]$, the distribution parameters were estimated using maximum likelihood (see Methods) and these estimated parameters were used to generate 1000 surrogate datasets. The surrogates were then fit using maximum likelihood, and for each fit, the Kolmogorov–Smirnov distance was calculated. As a measure of plausibility of fit for a given distribution type, p-values were calculated as the fraction of surrogate data sets with a higher Kolmogorov–Smirnov distance (a worse fit) than the corresponding experimental data fit. We chose a p-value greater than 0.1 as a criterion for the plausibility of the hypothesized fit, and limited our fitting range by $t_{max} = 300$ ms.

In the exponential case, a plausible fit is achieved over a greater range than for the power law case ($t_{min} \geq 82$ vs. $t_{min} \geq 117$, Fig. 5) so we suggest that this justifies, as a first approximation, treating the decay of activity within a burst in our dataset as exponential. Further, our observations of the shape of bursting activity in vitro from our recordings of rat hippocampus neurons are at least qualitatively consistent with previous in vivo results from bursts of spikes in the thalamic reticular nucleus in anesthetized cats, which show a similar fast buildup followed by an exponential decay [13].

4 Exponential Resource Decay Model for Power Law Activity Statistics

The observation that burst activity decays exponentially suggests defining a model whereby spikes are generated stochastically, with probability proportional to an exponentially decaying 'resource' or 'potential'. We model bursts by simulating recording channels that have no direct interaction, and are linked only by a shared probability density p of recording a spike. An approximate exponential decay of p in our model is provided in a natural way by the spikes themselves: each spike reduces p by a constant amount c (Fig. 6).

Bursts modelled in this way lead to power law avalanche size distributions. Modeling small bursts of 60 spikes using this method produces power law distributed avalanche sizes, that, like the avalanches in our data, are sensitive to bin size. Modeling larger avalanches moves the power law exponent close to -2, and reduces the sensitivity to binning (Fig. 7).

For IEI distributions arising from our model we can derive a power law analytically for the case of one channel. Let $p\mathrm{d}t$ be the probability of a spike in the time interval $\mathrm{d}t$. After each spike, p will be reduced by $c \ll 1$; the starting probability is $p_0 \leq 1$. For known p, the probability of an interval with no spike with a length between L and $L + \mathrm{d}L$ is given by

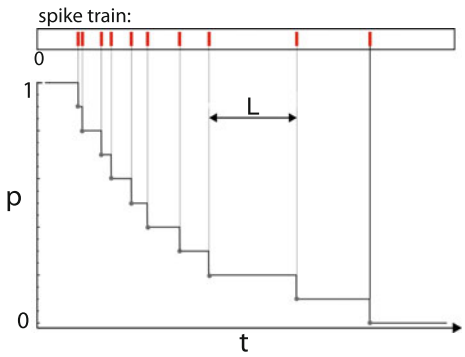

Fig. 6 Example time series of spikes generated by our model and its corresponding decay in p, in the case of only one channel

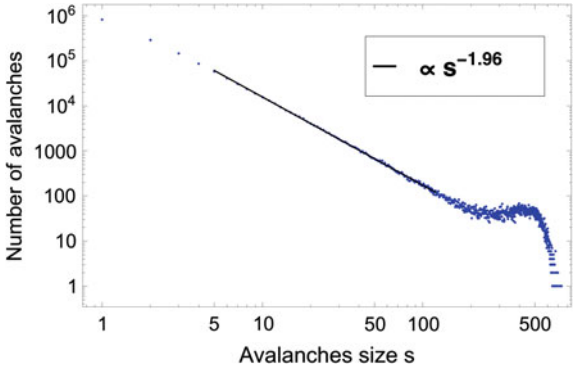

Fig. 7 Avalanche size distribution of modeled bursts: The distribution follows a power law with exponent close to −2. 14803 bursts of 1000 spikes each were generated using a 10 channel model

$$\mathrm{P}(L \mid p)\mathrm{d}L = \left(\lim_{\Delta t \to 0}(1 - p\Delta t)^{\frac{L}{\Delta t}}\right) \cdot p\mathrm{d}L = \left(\lim_{x \to \infty}\left(1 - \frac{p}{x}\right)^{Lx}\right) \cdot p\mathrm{d}L = e^{-pL} \cdot p\mathrm{d}L. \tag{1}$$

To make the IEI-distribution $\mathrm{P}(L)$ independent of p, one needs to know the probabilities for the occurrence of the different values of p, which we denote by $\mathrm{P}(p)$. We may then write $\mathrm{P}(L, p) = \mathrm{P}(L \mid p)\mathrm{P}(p)$ and $\mathrm{P}(L) = \int_0^1 \mathrm{P}(L, p)\mathrm{d}p$. The distribution of $\mathrm{P}(p)$ can be found easily: there will be exactly one IEI for each $p \in \{c, 2c, \ldots, p_0 - c, p_0\}$, so each possible value of p as a starting point for an IEI, appears with the same frequency, and $P(p)$ is constant. Thus

$$\mathrm{P}(L, p)\mathrm{d}L = \mathrm{P}(L \mid p)\mathrm{P}(p)\mathrm{d}L \propto e^{-pL} \cdot p\mathrm{d}L\,, \tag{2}$$

from which it follows that

$$\mathrm{P}(L) = \int_0^{p_0} \mathrm{P}(L, p)\mathrm{d}p \propto \int_0^{p_0} e^{-pL} p\mathrm{d}p = \frac{1}{L^2} - e^{-p_0 L}\left(\frac{1}{L^2} + \frac{p_0}{L}\right) \xrightarrow{L \to \infty} \frac{1}{L^2} \tag{3}$$

and so our simple model predicts an unambiguous IEI distribution power law exponent within bursts of $\alpha = 2$, very close to the observed exponent in our data.

5 Conclusions and Outlook

It is well known that power law distributions can be generated from exponentials [14, 15]. However, to our knowledge, so far no explicit model calculations exhibiting this in a realistic neuronal context were put forward. The presented model shows that this can be achieved in the most natural way. Our prediction of a power law exponent of $\alpha = 2$ holds only for the case of isolated bursts, that all have the same size. The

measurements at 14 and 15 DIV roughly fulfil these requirements; their power law exponents are indeed close to $\alpha = 2$ ($\alpha = 1.83$ for 14 DIV and $\alpha = 2.11$ for 15 DIV). How to describe the situation in the earlier stages, where the correlations also decrease exponentially but the activity does not consist of isolated bursts, is still unclear. We could speculate that in the earlier stages (9–12 DIV), the potential that we use for our modeling, does not completely recover before it decays. We found that in these earlier stages, the exponent is much lower, indicating a much slower activity decay. This may be taken as a fingerprint for an exponential decay that often starts before the previous one has finished.

Our results do not contradict the more general hypothesis that a critical state underlies brain activity [16], and nor do they contradict earlier observations and claims based on neuronal cultures, such as those made by Beggs and Plenz [2]. The bursts generated by our model are not intended to reproduce the finer structure which can be seen in our data (Fig. 4). Our intention is simply to demonstrate that an exponential decay in activity may be sufficient to produce power laws in MEA recordings; i.e. that power law distributed neuronal avalanche statistics can simply arise as an artefact of the partitioning of an exponential decay of activity within mature culture bursts. This would mean that these power law distributions are weaker evidence for a critical state than previously thought, and highlights the importance of looking at other evidence (e.g. [17, 18]).

On a more general level, it remains somewhat unclear to us how a partitioning of isolated, roughly stereotypical bursts into avalanches should be related to critical phenomena. Avalanches, such as those in the sandpile model [19], are distinct events with a clear definition. If an avalanche sub-structure exists within bursts, the avalanches need not even necessarily be separated in time, and if they result in a temporal structure which is fractal, this structure should be insensitive to time bin selection for sufficiently large bursts. The IEI distributions in our data suggest that a fractal temporal activity structure may be a stable property of neuronal cultures throughout development, and not only a substructure of mature bursts, opening a window toward a quantitative statistical characterization of development.

6 Methods

6.1 Neuronal Culture Preparations

Hippocampi were micro-surgically separated from E18 (embryonic day 18) Sprague–Dawley (SD) rat (Koatech, Republic of Korea). Dissected tissues were dissociated with pipetting in HBSS buffer solution and centrifuged at 1000 rpm for 2 min. Supernatant was then removed, and settled cell pellet was resuspended in plating medium (Neurobasal medium supplemented with B27, 2 mM GlutaMAX, 12.5 μM L-glutamate, and penicillin-streptomycin). After being sieved through a cell strainer (BD Falcon, NJ, USA), cells were plated on a chip at the density of 1500 cells/mm^2.

Cultured neurons were kept in a humidified incubator maintained with 37 °C and 5% CO_2. Half of the medium was changed twice a week with maintenance medium (plating medium without L-glutamate). All experiments were performed in accordance with the guidance of the Institutional Animal Care and Use Committee (IACUC) of Korea Advanced Institute of Science and Technology (KAIST) and all experimental protocols were approved by IACUC of KAIST.

6.2 Neural Recordings

A microelectrode array (MEA) was purchased from Multi Channel Systems (Reutlingen, Germany). It was composed of 59 microelectrodes (TiN, 30 μm in diameter, 200 μm spacing) and 1 reference electrode. In order to promote cell adhesion to the chip surface, the MEA was coated with poly-D-lysine (100 μg/mL) and sterilized with 70% ethanol. To measure neural signals, the MEA was connected with a 60-channel preamplifier (MEA 1060-BC, Multi Channel Systems) and placed in a recording incubator (5% CO_2). To prevent the evaporation of cell culture medium, the MEA was capped with FEP-membrane sealed Teflon ring. The preamplifier was connected with an MEA workstation (Plexon Inc., Dallas, USA) and digitized at 40 kHz. The overall gain factor was 14,000 and the bandwidth 250 Hz–6 kHz. For spike detection, the threshold level was set to six times the standard deviation of the background noise. At 8 DIV, the MEA was transferred to the recording incubator and neural spikes were continuously recorded for 7 days (9–15 DIV). To extract spike times for the data analysis, NeuroExplorer (Nex Technologies, Madison, USA) was used.

6.3 Fitting Using Discrete Maximum-Likelihood

Maximum likelihood estimation of a distribution parameter, α begins from the assumption that the observed data, in this case, spike times, $\mathbf{t}$, were sampled independently from a distribution, $p(t|\alpha)$. The likelihood, $\mathscr{L}$ of α is then the probability of the observations $\mathbf{t}$, given α, i.e.

$$\mathscr{L}(\alpha|\mathbf{t}) = p(\mathbf{t}|\alpha) = \prod_i p(t_i|\alpha)\,. \tag{4}$$

Since the logarithm is a monotonic function, the α which maximises the log likelihood, l, will also maximise the likelihood, which allows us to replace the product with a sum:

$$argmax_\alpha\big[\mathscr{L}(\alpha|\mathbf{t})\big] = argmax_\alpha\big[l(\alpha|\mathbf{t})\big] = argmax_\alpha\big[\sum_i ln\ p(t_i|\alpha)\big]\,. \tag{5}$$

For the discrete, truncated power law in t, with scaling exponent α, lower bound t_{min} and upper bound, t_{max}, the properly normalised probability mass function is

$$p(t|\alpha) = \frac{t^{-\alpha}}{\sum_{j=t_{min}}^{t_{max}} j^{-\alpha}}, \tag{6}$$

which gives the log likelihood

$$l(\alpha|\mathbf{t}) = -N\ ln \sum_{j=t_{min}}^{t_{max}} j^{-\alpha} - \alpha \sum_{i=1}^{N} ln\ t_i\,, \tag{7}$$

where N is the number of spike times t_i in the interval $[t_{min}, t_{max}]$.

For the discrete, truncated exponential distribution in t, with scaling exponent $\lambda \neq 0$, lower bound t_{min} and upper bound, t_{max}, the properly normalised probability mass function is

$$p(t|\lambda) = \frac{e^{-\lambda t}}{\sum_{j=t_{min}}^{t_{max}} e^{-\lambda j}}, \tag{8}$$

which gives the log likelihood

$$l(\lambda|\mathbf{t}) = -\lambda \sum_i t_i - N\ ln \sum_{j=t_{min}}^{t_{max}} e^{-\lambda j}\,. \tag{9}$$

Dividing by the constant factor N does not affect the maximisation of $l(\lambda|\mathbf{t})$, so we can write

$$l_N(\lambda|\mathbf{t}) = -\lambda \bar{t} - ln \sum_{j=t_{min}}^{t_{max}} e^{-\lambda j}\,, \tag{10}$$

where $\bar{t}$ is the arithmetic mean of spike times t_i in the interval $[t_{min}, t_{max}]$.

We find that maximising these log likelihood expressions is generally a one dimensional convex optimisation problem which can be solved numerically with any standard method.

Acknowledgements This work was supported by a joint Swiss-South Korea collaboration grant (IZKS2_162190).

References

1. Stanley, H.E.: Introduction to Phase Transitions and Critical Phenomena. Oxford University Press, Oxford (1987)
2. Beggs, J.M., Plenz, D.: Neuronal avalanches in neocortical circuits. J. Neurosci. **23**, 11167–11177 (2003)

3. Beggs, J.M., Plenz, D.: Neuronal avalanches are diverse and precise activity patterns that are stable for many hours in cortical slice cultures. J. Neurosci. **24**, 5216–5229 (2004)
4. Corral, A., Perez, C.J., Diaz-Guilera, A., Arenas, A.: Self-organized criticality and synchronization in a lattice model of integrate-and-fire oscillators. Phys. Rev Lett. **74**, 118–121 (1995)
5. Herz, A.V., Hopfield, J.J.: Earthquake cycles and neural reverberations: collective oscillations in systems with pulse-coupled threshold elements. Phys. Rev. Lett. **96**, 1222–1225 (1995)
6. Orlandi, J.G., Soriano, J., Alvarez-Lacalle, E., Teller, S., Casademunt, J.: Noise focusing and the emergence of coherent activity in neuronal cultures. Nat. Phys. **9**, 582–590 (2013)
7. Pasquale, V., Massobrio, P., Bologna, L.L., Chippalone, M., Martinoia, S.: Self-organization and neuronal avalanches in networks of dissociated cortical neurons. Neuroscience **153**, 1354 (2008)
8. Shew, W.L., Yang, H., Petermann, T., Roy, R., Plenz, D.: Neuronal avalanches imply maximum dynamic range in cortical networks at criticality. J. Neurosci. **29**, 15595 (2009)
9. Lorimer, T., Gomez, F., Stoop, R.: Two universal physical principles shape the power-law statistics of real-world networks. Sci. Rep. **5**, 12353 (2015)
10. Haldeman, C., Beggs, J.M.: Critical branching captures activity in living neural networks and maximizes the number of metastable states. Phys. Rev. Lett. **94**, 058101 (2005)
11. Breskin, I., Soriano, J., Moses, E., Tlusty, T.: Percolation in living neural networks. Phys. Rev. Lett **97**, 188102 (2006)
12. Deluca, A., Corral, A.: Fitting and goodness-of-fit test of non-truncated and truncated power-law distributions. Acta Geophys. **61**, 1351–1394 (2013)
13. Marlinski, V., Beloozerova, I.N.: Burst firing of neurons in the thalamic reticular nucleus during locomotion. J. Neurophysiol. **112**, 181–192 (2014)
14. Reed, W.J., Hughes, B.D.: From gene families and genera to incomes and internet file sizes: Why power laws are so common in nature. Phys. Rev. E **66**, 067103 (2002)
15. Newman, M.E.J.: Power laws, Pareto distributions, and Zipf's law. Contemp. Phys. **46**, 323–351 (2005)
16. Chialvo, D.: Emergent complex neural dynamics. Nat. Phys. **6**, 744–450 (2010)
17. Friedman, N., Ito, S., Brinkman, B.A.W., Shimono, M., DeVille, R.E.L., Dahmen, K.A., Beggs, J.M., Butler, T.C.: Universal critical dynamics in high resolution neuronal avalanche data. Phys. Rev. Lett. **108**, 208102 (2012)
18. Beggs, J.M., Timme, N.: Being critical of criticality in the brain. Front. Physiol. **3**, 163 (2012)
19. Bak, P., Tang, C., Wiesenfeld, K.: Self-organized criticality: an explanation of the 1/f noise. Phys. Rev. Lett. **59**, 381 (1987)

Index

G. Mantica et al. (eds.), *Emergent Complexity from Nonlinearity, in Physics, Engineering and the Life Sciences*, Springer Proceedings in Physics 191,
DOI 10.1007/978-3-319-47810-4